


Journal of
Mechanics of
Materials and Structures

Volume 1, N° 6

June 2006

 mathematical sciences publishers

JOURNAL OF MECHANICS OF MATERIALS AND STRUCTURES

<http://www.jomms.org>

EDITOR-IN-CHIEF Charles R. Steele

ASSOCIATE EDITOR Marie-Louise Steele
Division of Mechanics and Computation
Stanford University
Stanford, CA 94305
USA

SENIOR CONSULTING EDITOR Georg Herrmann
Ortstrasse 7
CH-7270 Davos Platz
Switzerland

BOARD OF EDITORS

D. BIGONI University of Trento, Italy
H. D. BUI École Polytechnique, France
J. P. CARTER University of Sydney, Australia
R. M. CHRISTENSEN Stanford University, U.S.A.
G. M. L. GLADWELL University of Waterloo, Canada
D. H. HODGES Georgia Institute of Technology, U.S.A.
J. HUTCHINSON Harvard University, U.S.A.
C. HWU National Cheng Kung University, R.O. China
IWONA JASIUK University of Illinois at Urbana-Champaign
B. L. KARIHALOO University of Wales, U.K.
Y. Y. KIM Seoul National University, Republic of Korea
Z. MROZ Academy of Science, Poland
D. PAMPLONA Universidade Católica do Rio de Janeiro, Brazil
M. B. RUBIN Technion, Haifa, Israel
Y. SHINDO Tohoku University, Japan
A. N. SHUPIKOV Ukrainian Academy of Sciences, Ukraine
T. TARNAI University Budapest, Hungary
F. Y. M. WAN University of California, Irvine, U.S.A.
P. WRIGGERS Universität Hannover, Germany
W. YANG Tsinghua University, P.R. China
F. ZIEGLER Technische Universität Wien, Austria

PRODUCTION

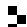
PAULO NEY DE SOUZA Production Manager
SILVIO LEVY Senior Production Editor
NICHOLAS JACKSON Production Editor

See inside back cover or <http://www.jomms.org> for submission guidelines.

Regular subscription rate: \$500 a year.

Subscriptions, requests for back issues, and changes of address should be sent to Mathematical Sciences Publishers, 798 Evans Hall, Department of Mathematics, University of California, Berkeley, CA 94720-3840.

©Copyright 2007. Journal of Mechanics of Materials and Structures. All rights reserved.

 mathematical sciences publishers

A NEW MODEL TO PREDICT THE BEHAVIOR AT THE INTERFACES OF MULTILAYER STRUCTURES

M. KARAMA, K. S. AFAQ AND S. MISTOU

One of the current problems connected with multilayer composite structures concerns the analysis of the distribution of the stresses around peculiarities (free edge and loaded edge) and at the interfaces of each layer. This work presents a new shear stress function in the form of the exponential function to predict the mechanical behavior of multilayered laminated composite structures. As a case study, the mechanical behavior of a laminated composite beam ($90^\circ/0^\circ/0^\circ/90^\circ$) is examined. The results are compared with the Touratier model *sine* and the two-dimensional finite element method studied. Results show that this new model is more precise than older ones when compared with results obtained by finite element analysis. To introduce continuity on the interfaces of each layer, the new exponential model is used with Ossadzow kinematics. The equilibrium equations and natural boundary conditions are derived from the principle of virtual power.

Notations

- h beam thickness or height
 h_1 transverse shear function
 H Heaviside step function
 L beam length
 m layer number
 P^* virtual power
 u_α membrane displacement
 \ddot{U} differentiation with respect to time $= \partial^2 U / \partial t^2$
 $U_{1,1}$ differentiation with respect to $x_1 = \partial U_1 / \partial x_1$
 U^* virtual displacements
 U^{*T} the vector of virtual displacements transposed
 w transverse displacement
 $\bar{\bar{D}}^*$ virtual tensor of the deformations
 \vec{f} vector forces of volume
 \vec{F} vector forces of surface

Keywords: boron fiber, laminate theory, interface, stress transfer, finite element analysis.

Greek letters

γ, ϕ	transverse shear rotation
ε	strain
σ	stress
$\bar{\sigma}$	stress tensor

1. Introduction

One of the major challenges in computational structural mechanics is the development of the advanced models and numerical techniques in order to provide efficient tools exhibiting good interior and edge solutions.

In this paper we are introducing an *exponential function* as a shear stress function; the exponential functions are found to be much richer than trigonometric sine and cosine functions in their development series. According to the definition of the transverse shear stress function, the existing laminated composite beam is divided into two broad categories: the global approximation models and the discrete layer approximation models. The equivalent single-layer laminate theories are those in which a heterogeneous laminated plate is treated as a statically equivalent single layer having a complex constitutive behavior, enabling the three-dimensional continuum problem to be considered as a two-dimensional one.

The equivalent single layer models are:

- The [Kirchhoff 1850; Love 1934] theory (or classical theory) in which deformation due to transverse shear is neglected, implies that the normal to the mid-plane remains straight and normal at mid-surface after deformation. This theory can be used for thin beams.
- The [Reissner 1945; Mindlin 1951] theory (or first-order theory). The first-order deformation theory increases the kinematics of the classical laminated plate theory by including a gross transverse shear deformation in its kinematical assumption. That the transverse shear strain remains constant with respect to the thickness coordinate implies that the normal to the mid plane remains straight but not normal at mid-surface after deformation due to the shear effect. The first-order theory requires shear correction factors, which are difficult to determine for arbitrary laminated composite plates.
- The higher-order models are based on the hypothesis of nonlinear stress variation through thickness [Reddy 1984; Touratier 1991]. These models are able to represent the section warping in the deformed configuration.

However, these theories do not satisfy the continuity conditions of transverse shear stress at layer interfaces. Although the discrete layer approximation theories are accurate, they are rather complex for problem solving because the order of their governing equations depends on the number of layers.

DiSciuva [1987; 1993] and Touratier [1991; 1992] proposed simplified discrete layer models with only five variational unknowns (two membrane displacements, a transverse displacement and two rotations), making it possible for the section in the deformed configuration to be represented by warping in the [Touratier 1992] model. Nevertheless, in these two cases compatibility conditions, both for layer interfaces and boundaries, cannot be satisfied. From Touratier's work, [Beakou 1991] and [Idlbi 1995]

proposed, respectively, shell and plate models which satisfy both the stress continuity at the interfaces and the zero stress conditions at the free boundaries.

Finally, He [1994] introduced the Heaviside step function which enables automatic satisfaction of the displacement continuity at interfaces between different layers. The new discrete layer model presented comes from the work of [Di Sciuva 1993; He 1994; Ossadzow et al. 1995]. The displacement field is assumed to be of the form:

$$\begin{aligned}
 U_1(x_1, x_3, t) &= u_1^0(x_1, t) - x_3 w_{,1}(x_1, t) + h_1(x_3)\phi_1(x_1, t), \\
 U_2 &= 0, \\
 U_3(x_1, t) &= w(x_1, t),
 \end{aligned}
 \tag{1}$$

with the transverse shear function

$$h_1(x_3) = g(x_3) + \sum_{m=1}^{N-1} \lambda_1^{(m)} \left(-\frac{1}{2}x_3 + \frac{1}{2}f(x_3) + (x_3 - x_3^{(m)})H(x_3 - x_3^{(m)}) \right),$$

where $H(x_3 - x_3^{(m)})$ is the Heaviside Step function defined as

$$H(x_3 - x_3^{(m)}) = \begin{cases} 1 & \text{for } x_3 \geq x_3^{(m)}, \\ 0 & \text{for } x_3 < x_3^{(m)}, \end{cases}
 \tag{2}$$

$f(x_3)$ is the shear refinement function, $g(x_3)$ is the membrane refinement function, and $\lambda_I^{(m)}$ are continuity coefficients.

1.1. New multilayered laminated composite structures model (“KAM”). In this work a new multilayered laminated composite structure model representing the shear and membrane functions using exponential functions as follows:

$$f(z) = ze^{-2(z/h)^2}, \quad g(z) = -ze^{-2(z/h)^2},
 \tag{3}$$

for a multilayered beam of uniform thickness h defined on the domain Ω , which refers to the coordinate system $R = (0/x_1, x_2, x_3 = z)$, with z being normal at plate mid-surface Σ , and Γ as the boundary of Ω . Then, the domain Ω is such that

$$\Omega = \left\{ \Sigma \times \left(-\frac{h}{2}, \frac{h}{2} \right) \mid -\frac{h}{2} \leq z \leq \frac{h}{2M(x_1, x_2, z)} \in \Omega, M_o(x_1, x_2, 0) \in \Sigma, \phi \gg \text{Max}(z) \right\} \subset R^3,$$

where ϕ is the diameter of the Ω and the closed domain $\bar{\Omega}$ is set by

$$\bar{\Omega} = \{ \Omega \cup \Gamma / \Gamma = \Gamma_{\text{edge}} \cup \Gamma_{z=\pm h/2} \}.$$

From the beginning our objective was clear, namely, to find the transverse shear stress function $f(z)$ that gives the mechanical behavior of the composite laminated structures as close as possible to that of the exact three-dimensional solution [Pagano 1970] or the finite element analysis in two dimensions (stress, strain plane), and with better representation of the transverse shear stress in the thickness of the laminated structure. Several different higher-order polynomial and trigonometric functions already had been tried:

- [Ambartsumian 1958]: $f(z) = \frac{z}{2} \left(\frac{h^2}{4} - \frac{z^2}{3} \right)$,
- [Kaczkowski 1968; Panc 1975; Reissner 1975]: $f(z) = \frac{5}{4}z \left(1 - \frac{4z^2}{3h^2} \right)$,
- [Levinson 1980; Murthy 1981; Reddy 1984]: $f(z) = z \left(1 - \frac{4z^2}{3h^2} \right)$,
- [Touratier 1991]: $f(z) = \frac{h}{\pi} \sin \left(\frac{\pi z}{h} \right)$.

We began with an exponential function, since that function has all even and odd powers in its expansion (see the present model) unlike sine functions (see the Touratier model), which have only odd powers. Then an exponential function is much richer than a sine function. If we take a look at the expansions of different transverse shear stress functions,

- [Reddy 1984]: $f(z) = z \left(1 - \frac{4z^2}{3h^2} \right) = z - 1.33 \frac{z^3}{h^2}$,
- [Touratier 1991]: $f(z) = \frac{h}{\pi} \sin \left(\frac{\pi z}{h} \right) = z - 1.645 \frac{z^3}{h^2} + 0.812 \frac{z^5}{h^4} - 0.191 \frac{z^7}{h^6} + 0.0261 \frac{z^9}{h^8}$,
- Present Model: $f(z) = ze^{-2(z/h)^2} = z - 2 \frac{z^3}{h^2} + 2 \frac{z^5}{h^4} - 1.333 \frac{z^7}{h^6} + 0.666 \frac{z^9}{h^8}$,

it is clear from expansions of the transverse shear stress functions that the coefficient of successive terms in sine functions decreases more rapidly than the present exponential function. These expansions are the main influences for the different mechanical behaviors of laminated structures.

For the transverse shear stress behavior, it is very important that the first derivative of the transverse shear stress function provide a parabolic response in the thickness direction of the laminate and that it satisfy the boundary conditions.

2. Governing equations

From the virtual power principle, the equations of motion and the natural boundary conditions can be obtained. The calculations are made in small perturbations. According to the principle of virtual power,

$$P_{(a)}^* = P_{(i)}^* + P_{(e)}^*, \tag{4}$$

where $P_{(a)}^*$, $P_{(i)}^*$, $P_{(e)}^*$ correspond to virtual power of the acceleration quantities, virtual power of internal work and the virtual power of external loading.

The virtual power of the acceleration quantities is:

$$P_{(a)}^* = \int_{\Omega} \rho U^{*T} \ddot{U} d\Omega, \tag{5}$$

where U^* and U^{*T} are virtual displacements and the vector of virtual displacements transposed.

Assuming

$$\begin{aligned} I_w &= \int_{-h/2}^{h/2} \rho dx_3, & I_{uw'} &= - \int_{-h/2}^{h/2} \rho x_3 dx_3, \\ I_{w'} &= \int_{-h/2}^{h/2} \rho x_3^2 dx_3, & I_{u\omega} &= \int_{-h/2}^{h/2} \rho h_1(x_3) dx_3, \\ I_{\omega} &= \int_{-h/2}^{h/2} \rho h_1^2(x_3) dx_3, & I_{\omega w'} &= - \int_{-h/2}^{h/2} \rho x_3 h_1(x_3) dx_3, \end{aligned} \tag{6}$$

Equation (5) becomes

$$P_{(a)}^* = \int_0^L (\Gamma^{(u)} u_1^{0*} + \Gamma^{(w)} w^* + \Gamma^{(\phi)} \phi_1^*) dx_1 + \bar{\Gamma}^{(w)} w^*, \quad (7)$$

where,

$$\begin{aligned} \Gamma^{(u)} &= I_w \ddot{u}_1^o + I_{uw'} \ddot{w}_{,1} + I_{u\omega} \ddot{\phi}_1, & \Gamma^{(w)} &= -I_{uw'} \ddot{u}_{1,1}^o + I_w \ddot{w} - I_{w'} \ddot{w}_{,11} - I_{\omega w'} \ddot{\phi}_{1,1}, \\ \Gamma^{(\phi)} &= I_{u\omega} \ddot{u}_1^o + I_{\omega w'} \ddot{w}_{,1} + I_{\omega} \ddot{\phi}_1, & \bar{\Gamma}^{(w)} &= I_{uw'} \ddot{u}_1^o + I_{w'} \ddot{w}_{,1} + I_{\omega w'} \ddot{\phi}_1. \end{aligned}$$

See Section A for details.

Now the virtual power of internal work is

$$P_{(i)}^* = \int_{\Omega} \overline{\overline{D}}^{*T} : \overline{\overline{\sigma}} d\Omega, \quad (8)$$

where $\overline{\overline{D}}^*$ is the virtual tensor of deformation and $\overline{\overline{\sigma}}$ is the tensor of the constraints.

Since

$$\overline{\overline{D}}^* = \begin{bmatrix} D^*_{11} & D^*_{12} & D^*_{13} \\ D^*_{21} & D^*_{22} & D^*_{23} \\ D^*_{31} & D^*_{32} & D^*_{33} \end{bmatrix}, \quad \overline{\overline{\sigma}} = \begin{bmatrix} \sigma_{11} & \sigma_{12} & \sigma_{13} \\ \sigma_{21} & \sigma_{22} & \sigma_{23} \\ \sigma_{31} & \sigma_{32} & \sigma_{33} \end{bmatrix},$$

in two dimensions

$$\overline{\overline{D}}^* : \overline{\overline{\sigma}} = D^*_{11} \sigma_{11} + 2D^*_{13} \sigma_{13}. \quad (9)$$

Resultant stresses $N_{\alpha\beta}$, $M_{\alpha\beta}$ and $P_{\alpha\beta}$ are defined as

$$\begin{aligned} N_{11} &= \int_{-h/2}^{h/2} \sigma_{11} dx_3, & M_{11} &= \int_{-h/2}^{h/2} x_3 \sigma_{11} dx_3, \\ P_{11} &= \int_{-h/2}^{h/2} h_1(x_3) \sigma_{11} dx_3, & P_{13} &= \int_{-h/2}^{h/2} h_{1,3}(x_3) \sigma_{13} dx_3, \end{aligned} \quad (10)$$

so Equation (8) becomes

$$P_{(i)}^* = \int_0^L (N_{11,1} u_1^{0*} + M_{11,1} w^* + (P_{11,1} - P_{13}) \phi_1^*) dx_1 - N_{11} u_1^{0*} - M_{11,1} w^* + M_{11} w^*_{,1} - P_{11} \phi_1^*. \quad (11)$$

See Section B for details.

Now the virtual power of external loading is

$$P_{(e)}^* = \int_{\Omega} U^{*T} \cdot \vec{f} d\Omega + \int_{\Gamma} U^{*T} \vec{F} d\Gamma. \quad (12)$$

Here

$$U^{*T} = [U_1^* \quad 0 \quad U_3^*], \quad \vec{f} = \begin{bmatrix} f_1 \\ f_2 \\ f_3 \end{bmatrix}, \quad \vec{F} = \begin{bmatrix} F_1 \\ F_2 \\ F_3 \end{bmatrix},$$

where \vec{f} and \vec{F} are the vector forces of volume and surface, respectively, with

$$\begin{aligned} U_1^* &= u_1^{0*} - x_3 w_{,1}^* + h_1(x_3)\phi_1^*, \\ U_2^* &= 0, \\ U_3^* &= w^*. \end{aligned}$$

We define

$$\begin{aligned} \bar{n}_i &= \int_{-h/2}^{h/2} f_i dx_3, & \bar{N}_i &= \int_{-h/2}^{h/2} F_i dx_3, \\ \bar{m}_i &= \int_{-h/2}^{h/2} x_3 f_i dx_3, & \bar{M}_i &= \int_{-h/2}^{h/2} x_3 F_i dx_3, \\ \bar{p}_i &= \int_{-h/2}^{h/2} h_1(x_3) f_i dx_3, & \bar{P}_i &= \int_{-h/2}^{h/2} h_1(x_3) F_i dx_3, \end{aligned} \tag{13}$$

so Equation (12) becomes

$$P_{(e)}^* = \int_0^L (\bar{n}_1 u_1^{0*} + (\bar{n}_3 + \bar{m}_{1,1})w^* + \bar{p}_1 \phi_1^*) dx_1 + \bar{N}_1 u_1^{0*} (\bar{N}_3 - \bar{m}_1)w^* - \bar{M}_1 w_{,1}^* + \bar{P}_1 \phi_1^*. \tag{14}$$

See Section C for details.

Now, by Equations (4), (7), (11) and (14), governing equations and natural boundary conditions for all u_1^{0*} , w^* , ϕ_1^* we have

$$\begin{aligned} \Gamma^{(u)} &= N_{11,1} + \bar{n}_1, \\ \Gamma^{(w)} &= M_{11,11} + (\bar{n}_3 + \bar{m}_{1,1}), \\ \Gamma^{(\phi)} &= P_{11,1} - P_{13} + \bar{p}_1. \end{aligned} \tag{15}$$

And natural boundary conditions for all u_1^{0*} , w^* , ϕ_1^* , $w_{,1}^*$ are

$$\bar{\Gamma}^{(w)} = -M_{11,1} + (\bar{N}_3 - \bar{m}_1), \quad 0 = -N_{11} + \bar{N}_1 = -P_{11} + \bar{P}_1 = M_{11} - \bar{M}_1. \tag{16}$$

The three-dimensional orthotropic constitutive law is

$$\left\{ \begin{matrix} \sigma_{11} \\ \sigma_{22} \\ \sigma_{33} \\ \sigma_{23} \\ \sigma_{13} \\ \sigma_{12} \end{matrix} \right\} = \left[\begin{matrix} C_{11} & C_{12} & C_{13} & 0 & 0 & 0 \\ C_{12} & C_{22} & C_{23} & 0 & 0 & 0 \\ C_{13} & C_{23} & C_{33} & 0 & 0 & 0 \\ 0 & 0 & 0 & C_{44} & 0 & 0 \\ 0 & 0 & 0 & 0 & C_{55} & 0 \\ 0 & 0 & 0 & 0 & 0 & C_{66} \end{matrix} \right] \left\{ \begin{matrix} \varepsilon_{11} \\ \varepsilon_{22} \\ \varepsilon_{33} \\ 2\varepsilon_{23} \\ 2\varepsilon_{13} \\ 2\varepsilon_{12} \end{matrix} \right\}. \tag{17}$$

The dimension according to x_2 is supposed to be equal to the unit and the effects of the σ_{33} are neglected, so orthotropic law (17) becomes

$$\left\{ \begin{matrix} \sigma_{11} \\ \sigma_{13} \end{matrix} \right\} = \left[\begin{matrix} C'_{11} & 0 \\ 0 & C_{55} \end{matrix} \right] \left\{ \begin{matrix} \varepsilon_{11} \\ 2\varepsilon_{13} \end{matrix} \right\}, \tag{18}$$

with $\varepsilon_{11} = U_{1,1} = u_{1,1}^{0*} - x_3 w_{,11} + h_1 \phi_{1,1}$, $2\varepsilon_{31} = h_{1,3} \phi_1$, and

$$C'_{11} = \frac{C_{11}C_{33} - C_{13}^2}{C_{33}}.$$

Now, the generalized constitutive law is

$$\begin{bmatrix} N_{11} \\ M_{11} \\ P_{11} \\ P_{13} \end{bmatrix} = \begin{bmatrix} A_{11} & B_{11} & \tilde{K} & 0 \\ B_{11} & D_{11} & \tilde{T} & 0 \\ \tilde{K} & \tilde{T} & \tilde{S} & 0 \\ 0 & 0 & 0 & \tilde{Y} \end{bmatrix} \begin{bmatrix} u_{1,1}^{0*} \\ -w_{,11} \\ \phi_{1,1} \\ \phi_1 \end{bmatrix}.$$

So, the governing equations (15) become

$$\begin{aligned} \Gamma^{(u)} &= A_{11}u_{1,1}^{0*} - B_{11}w_{,111} + \tilde{K}\phi_{1,11} + \bar{n}_1, \\ \Gamma^{(w)} &= B_{11}u_{1,111}^{0*} - D_{11}w_{,1111} + \tilde{T}\phi_{1,111} + \bar{n}_3 + \bar{m}_{1,1}, \\ \Gamma^{(\phi)} &= \tilde{K}u_{1,11}^{0*} - \tilde{T}w_{,111} + \tilde{S}\phi_{1,11} - \tilde{Y}\phi_1 + \bar{p}_1. \end{aligned} \tag{19}$$

Then the natural boundary conditions (16) become

$$\begin{aligned} 0 &= A_{11}u_{1,1}^{0*} - B_{11}w_{,11} - \tilde{K}\phi_{1,1} + \bar{N}_1, \\ \bar{\Gamma}^{(w)} &= -B_{11}u_{1,11}^{0*} + D_{11}w_{,111} - \tilde{T}\phi_{1,11} + \bar{N}_3 - \bar{m}_1, \\ 0 &= -\tilde{K}u_{1,1}^{0*} + \tilde{T}w_{,11} - \tilde{S}\phi_{1,1} + \bar{P}_1, \\ 0 &= -B_{11}u_{1,1}^{0*} - D_{11}w_{,11} + \tilde{T}\phi_{1,1} - \bar{M}_1. \end{aligned} \tag{20}$$

2.1. Continuity coefficients (λ). To find out the value of the continuity coefficients, the conditions of the continuity of the transverse shear stress between each layer interface were used (see Figure 1):

$$\sigma_{13}^{(m)}(x_3 = x_3^{(m)}) = \sigma_{13}^{(m+1)}(x_3 = x_3^{(m)}).$$

Interface of layer 1 and layer 2 also gives

$$\sigma_{13}^{(1)}(x_3 = x_3^{(1)}) = \sigma_{13}^{(2)}(x_3 = x_3^{(1)}),$$

and

$$\begin{aligned} Q_{55}^1 \phi(x_1) &\left[g'(x_3^{(1)}) + \frac{1}{2}(\lambda_1^{(1)} + \lambda_1^{(2)} + \lambda_1^{(3)})(-1 + f'(x_3^{(1)})) \right] \\ &= Q_{55}^2 \phi(x_1) \left[g'(x_3^{(1)}) + \frac{1}{2}(\lambda_1^{(1)} + \lambda_1^{(2)} + \lambda_1^{(3)})(-1 + f'(x_3^{(1)})) + \lambda_1^{(1)} \right]. \end{aligned} \tag{21}$$

Interface of layer 2 and layer 3 gives

$$\sigma_{13}^{(2)}(x_3 = x_3^{(2)}) = \sigma_{13}^{(3)}(x_3 = x_3^{(2)}).$$

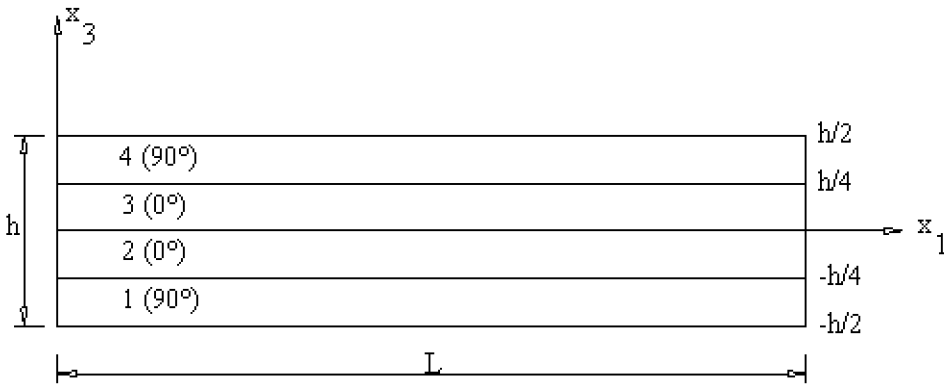


Figure 1. Side view of a laminated composite beam (90°/0°/0°/90°).

Since Q_{55} of the second and third layer are equal (Figure 1), we get

$$Q_{55}^2 \phi(x_1) \left[g'(x_3^{(2)}) + \frac{1}{2}(\lambda_1^{(1)} + \lambda_1^{(2)} + \lambda_1^{(3)})(-1 + f'(x_3^{(2)})) + \lambda_1^{(1)} \right] = Q_{55}^3 \phi(x_1) \left[g'(x_3^{(2)}) + \frac{1}{2}(\lambda_1^{(1)} + \lambda_1^{(2)} + \lambda_1^{(3)})(-1 + f'(x_3^{(2)})) + \lambda_1^{(1)} + \lambda_1^{(2)} \right]. \quad (22)$$

Now, by Equations (21) and (22),

$$\begin{aligned} \lambda_1^{(1)} &= \lambda_1^{(1)} + \lambda_1^{(2)}, \\ \lambda_1^{(2)} &= 0. \end{aligned} \quad (23)$$

This shows that if the mechanical characteristics of the two consecutive layers are the same (Figure 1), the coefficient of the continuity will be zero ($\lambda^{(2)} = 0$).

Interface of layer 3 and layer 4 gives

$$\sigma_{13}^{(3)}(x_3 = x_3^{(3)}) = \sigma_{13}^{(4)}(x_3 = x_3^{(3)})$$

and

$$Q_{55}^3 \phi(x_1) \left[g'(x_3^{(3)}) + \frac{1}{2}(\lambda_1^{(1)} + \lambda_1^{(2)} + \lambda_1^{(3)})(-1 + f'(x_3^{(3)})) + \lambda_1^{(1)} + \lambda_1^{(2)} \right] = Q_{55}^4 \phi(x_1) \left[g'(x_3^{(3)}) + \frac{1}{2}(\lambda_1^{(1)} + \lambda_1^{(2)} + \lambda_1^{(3)})(-1 + f'(x_3^{(3)})) + \lambda_1^{(1)} + \lambda_1^{(2)} + \lambda_1^{(3)} \right], \quad (24)$$

where

$$\begin{aligned} f'(x_3^{(1)}) &= -h/4 = f'(x_3^{(3)}) = h/4, \\ g'(x_3^{(1)}) &= -h/4 = g'(x_3^{(3)}) = h/4. \end{aligned}$$

So, using Equations (22)–(24), we obtain

$$Q_{55}^1 \phi(x_1) \left[g'(x_3^{(3)}) + \frac{1}{2}(\lambda_1^{(1)} + \lambda_1^{(2)} + \lambda_1^{(3)})(-1 + f'(x_3^{(3)})) \right] \\ = Q_{55}^4 \phi(x_1) \left[g'(x_3^{(3)}) + \frac{1}{2}(\lambda_1^{(1)} + \lambda_1^{(2)} + \lambda_1^{(3)})(-1 + f'(x_3^{(3)})) + \lambda_1^{(1)} + \lambda_1^{(3)} \right] \quad (25)$$

and

$$0 = \lambda_1^{(1)} + \lambda_1^{(3)} \quad \longrightarrow \quad \lambda_1^{(1)} = -\lambda_1^{(3)}. \quad (26)$$

So, by Equations (23) and (25), Equation (21) becomes

$$Q_{55}^1(g'(x_3^{(1)})) = Q_{55}^2(g'(x_3^{(1)}) + \lambda_1^{(1)}), \quad \lambda_1^{(1)} = \frac{(Q_{55}^1 - Q_{55}^2)g'(x_3^{(1)})}{Q_{55}^2}, \quad (27) \\ \lambda_1^{(3)} = \frac{(Q_{55}^2 - Q_{55}^1)g'(x_3^{(1)})}{Q_{55}^2}.$$

2.2. Finite element analysis. Since no exact three-dimensional solution exists for the considered case study, ABAQUS (finite element analysis software) is used to show the efficiency of the present model. In this paper, finite element results are taken as a reference for the comparison of different models of laminated composite structures, done by Karama et al. [1998]. The three-dimensional approximation of the behavior is carried out by element type “CPS8” (quadrilateral element of eight nodes, 16 dof per element). To validate the finite element results, it is first necessary to find out the convergence of laminate meshing. So, for the given problem, in static and dynamic, the convergence is obtained with 1680 elements, including 24 elements of thickness.

3. Some evaluations of the present model

3.1. Bending analysis. The static bending analysis is studied, so the virtual power of acceleration quantities is canceled. Three different bending analyses have been developed for three different specific boundary conditions. For the simply supported conditions, the unknown variables are deduced directly by the equation of motions. For clamped conditions, kinematical boundary conditions are used and, finally, in a free edge case, natural boundary conditions are employed.

The beam studied has a length of $L = 6.35$ m, a unitary width, and a thickness $h = 2.794$ m in the thick case and $h = 0.2794$ m in the thin case. The beam possesses four layers of the same thickness at $90^\circ/0^\circ/0^\circ/90^\circ$. The material used for the four layers is boron epoxy. The mechanical properties of the 0° layer are as follows [Widera and Logan 1980]:

$$E_{11} = 241.5 \text{ GPa}, \quad E_{22} = E_{33} = 18.89 \text{ GPa}, \quad G_{12} = G_{13} = 5.18 \text{ GPa}, \quad \rho = 2015 \text{ kg/m}^3, \\ G_{23} = 3.45 \text{ GPa}, \quad \nu_{23} = 0.25, \quad \nu_{12} = \nu_{13} = 0.24,$$

The continuity coefficients from Equations (23), (26)–(27) are evaluated as

$$\lambda_1^{(1)} = -\lambda_1^{(3)} = 0.2210501411, \quad \lambda_1^{(2)} = 0.$$

3.2. Bending of a simply supported beam under distributed sinusoidal load. The surface and volume force components are canceled except for

$$\bar{n}_3 = \int_0^h f_3 dx_3 = q = q_o \sin\left(\frac{\pi x_1}{L}\right).$$

For the simply supported boundary conditions, the Levy solution is used, which is defined as

$$u_1^o = u_o \cos\left(\frac{\pi x_1}{L}\right), \quad w = w_o \sin\left(\frac{\pi x_1}{L}\right), \quad \phi_1 = \phi_o \cos\left(\frac{\pi x_1}{L}\right).$$

Now, the governing equations (19) with $P_{(a)}^* = 0$ become

$$\begin{aligned} 0 &= A_{11}u_{1,11}^{0*} - B_{11}w_{,111} + \tilde{K}\phi_{1,11}, \\ 0 &= B_{11}u_{1,111}^{0*} - D_{11}w_{,1111} + \tilde{T}\phi_{1,111} + q_o \sin\left(\frac{\pi x_1}{L}\right), \\ 0 &= \tilde{K}u_{1,11}^{0*} - \tilde{T}w_{,111} + \tilde{S}\phi_{1,11} - \tilde{Y}\phi_1. \end{aligned}$$

For the Levy solution, the governing equations become

$$\begin{aligned} 0 &= -A_{11}\alpha^2 u_o \cos \alpha x_1 + B_{11}\alpha^3 w_o \cos \alpha x_1 - \tilde{K}\alpha^2 \phi_o \cos \alpha x_1, \\ 0 &= B_{11}\alpha^3 u_o \sin \alpha x_1 - D_{11}\alpha^4 w_o \sin \alpha x_1 + \tilde{T}\alpha^3 \phi_o \sin \alpha x_1 + q_o \sin \alpha x_1, \\ 0 &= -\tilde{K}\alpha^2 u_o \cos \alpha x_1 + \tilde{T}\alpha^3 w_o \cos \alpha x_1 - \tilde{S}\alpha^2 \phi_o \cos \alpha x_1 - \tilde{Y}\phi_o \cos \alpha x_1, \end{aligned}$$

with $\alpha = \pi/L$. In matrix form,

$$\begin{bmatrix} -\alpha^2 A_{11} & \alpha^3 B_{11} & -\alpha^2 \tilde{K} \\ \alpha^3 B_{11} & -\alpha^4 D_{11} & \alpha^3 \tilde{T} \\ -\alpha^2 \tilde{K} & \alpha^3 \tilde{T} & -\alpha^2 \tilde{S} - \tilde{Y} \end{bmatrix} \begin{pmatrix} u_o \\ w_o \\ \phi_o \end{pmatrix} = \begin{pmatrix} 0 \\ -q_o \\ 0 \end{pmatrix}.$$

Also, the displacement (1), becomes

$$\begin{aligned} U_1(x_1, x_3) &= (u_o - x_3 w_o \alpha + h_1(x_3) \phi_o) \cos(\alpha x_1), \\ U_2 &= 0, \\ U_3 &= w_o \sin(\alpha x_1), \end{aligned}$$

and by relation (18), the stresses are

$$\begin{aligned} \sigma_{11}(x_1, x_3) &= -\alpha C'_{11}(u_o - \alpha x_3 w_o + h_1 \phi_o) \sin(\alpha x_1), \\ \sigma_{13}(x_1, x_3) &= C_{55} h_{1,3} \phi_o \cos(\alpha x_1). \end{aligned}$$

Integration of the equilibrium equation $\sigma_{13,1} + \sigma_{33,3} = 0$ enables us to calculate the analytical value of σ_{33} , giving

$$\sigma_{33} = \alpha C_{55} h_1(x_3) \phi_o \sin(\alpha x_1).$$

The numerical results obtained ($q_o = -10^6$ Pa) using the present model are compared with those obtained by the finite element analysis [Karama et al. 1998] and the sine model [Touratier 1991] in Table 1. For this problem, the present model predicts mechanical behavior more accurately than the sine

Model	$U_3(L/2)$ [m]	$U_1(h/2)$ [m]	$\sigma_{13}(L/4, 0)$ (Interface) [Pa]	$\sigma_{11}(L/2, -h/4)$ (Interface) [Pa]	$\sigma_{33}(L/2, h/2)$ [Pa]
Present (error)	6.3701×10^{-4} (4.4%)	2.1196×10^{-4} (8.3%)	- 940098.0 (6.6%)	8112840.0 (3.5%)	-1039990.0 (3.9%)
Sine (error)	-6.2794×10^{-4} (2.9%)	2.0180×10^{-4} (12.7%)	- 896865.0 (10.8%)	8158932.0 (4.1%)	-1047274.0 (4.6%)
Abaqus	-6.1006×10^{-4}	2.3125×10^{-4}	-1006000.0	7835200.0	-1000900.0

Table 1. Bending of the simply supported thick beam under distributed sinusoidal load.

model when compared to the finite element analysis results, except for the transverse deflection (U_3). Percentage error reduction is more significant in the case of transverse shear stress (σ_{13}) at the interfaces between layers.

The efficiency of this model is shown in Figures 2–5; different stresses and displacements plotted according to the length and thickness of the beam show that, at every point on the beam, the present model is closer to the finite element results than are those of the sine model. Here we can also see the continuity of displacement and transverse shear stress between layer interfaces of the present model.

3.3. Bending of a clamped free beam under distributed uniform load. In this case the value of \bar{n}_3 is:

$$\bar{n}_3 = \int_{-h/2}^{h/2} f_3 dx_3 = q.$$

Now, the governing equations from the system of Equations (19) takes the form

$$\begin{aligned} 0 &= A_{11}u_{1,11}^{0*} - B_{11}w_{,111} + \tilde{K}\phi_{1,11}, \\ 0 &= B_{11}u_{1,111}^{0*} - D_{11}w_{,1111} + \tilde{T}\phi_{1,111} + q, \\ 0 &= \tilde{K}u_{1,11}^{0*} - \tilde{T}w_{,111} + \tilde{S}\phi_{1,11} - \tilde{Y}\phi_1. \end{aligned}$$

Integrating and simultaneously solving the above equations, gives

$$\begin{aligned} \phi_1(x_1) &= C_1 e^{-Px_1} + C_2 e^{Px_1} - (qx_1 + C_3) \frac{\tilde{T}}{\tilde{Y}D_{11}}, \\ u_1^o(x_1) &= -\frac{\tilde{K}}{A_{11}}\phi_1(x_1) + C_7 x_1 + C_8, \\ w(x_1) &= \frac{\tilde{T}}{PD_{11}} \left[C_1 e^{-Px_1} + C_2 e^{Px_1} - \left(\frac{1}{2}qx_1^2 + C_3 x_1 \right) \frac{P}{\tilde{Y}} \right] + \frac{1}{D_{11}} \left(\frac{1}{24}qx_1^4 + \frac{1}{6}C_3 x_1^3 \right) + \frac{1}{2}C_4 x_1^2 + C_5 x + C_6, \end{aligned}$$

where

$$P = \sqrt{\frac{-\tilde{Y}A_{11}D_{11}}{\tilde{K}^2 D_{11} + \tilde{T}^2 A_{11} - \tilde{S}A_{11}D_{11}}},$$

and $B_{11} = 0$ due to the symmetry at mid-surface. The eight constants C_i are determined by the four natural boundary conditions at the free edge deduced from (20) with $P_{(a)}^* = 0$:

$$\begin{aligned} 0 &= A_{11}u_{1,1}^{0*}(L) - \tilde{K}\phi_{1,1}(L), & 0 &= D_{11}w_{,111}(L) - \tilde{T}\phi_{1,11}(L), \\ 0 &= -\tilde{K}u_{1,1}^{0*}(L) + \tilde{T}w_{,11}(L) - \tilde{S}\phi_{1,1}(L), & 0 &= -D_{11}w_{,11}(L) + \tilde{T}\phi_{1,1}(L). \end{aligned}$$

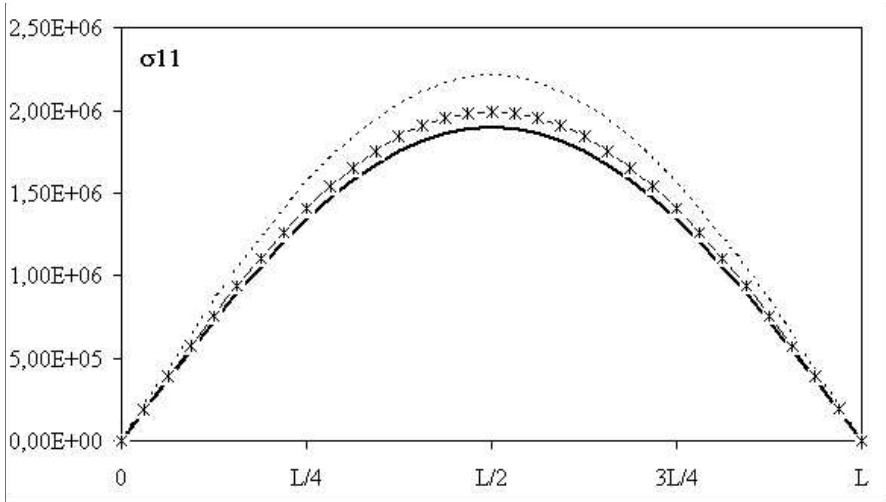


Figure 2. Variation of the stress σ_{11} along the direction x_1 for $x_3 = -\frac{h}{2}$ for Section 3.2. Abaqus (dashed line plot), Sine (solid line), and Present (dashes and crosses).

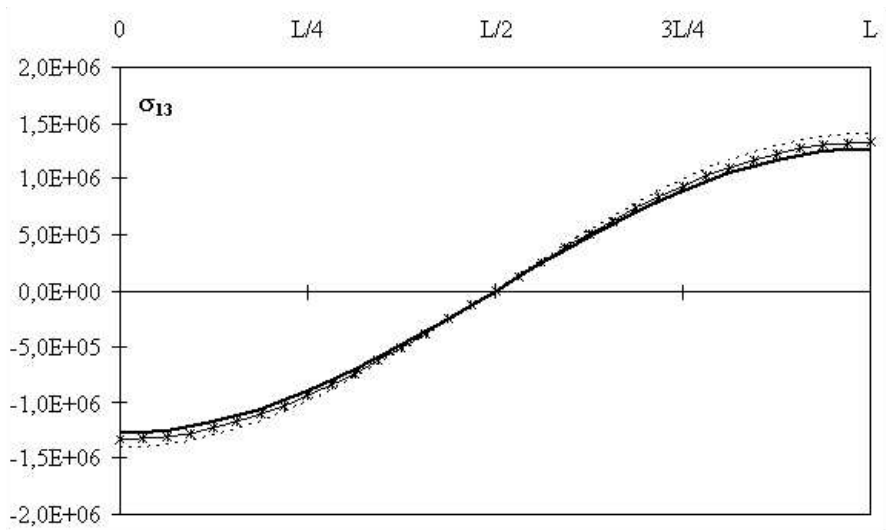


Figure 3. Variation of the transverse shear σ_{13} through the thickness for $x_3 = 0$ (Interface) for Section 3.2. Abaqus (dashed line plot), Sine (solid line), and Present (dashes and crosses).

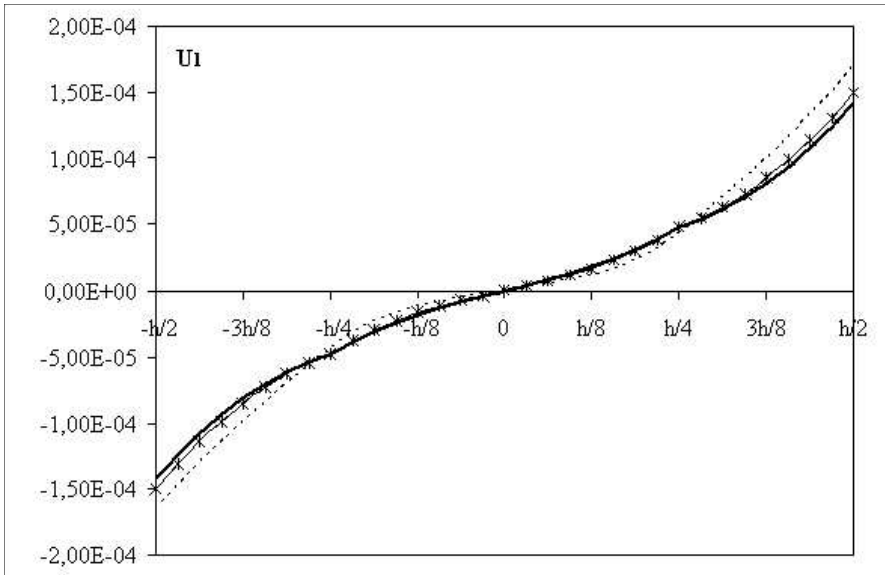


Figure 4. Variation of the displacement U_1 through the thickness for $x_1 = L/4$ for Section 3.2. Abaqus (dashed line plot), Sine (solid line), and Present (dashes and crosses).

The four kinematic boundary conditions at the clamped edge are:

$$\begin{aligned} u_1^0(0) &= 0, & w(0) &= 0, \\ w_{,1}(0) &= 0, & \phi_1(0) &= 0. \end{aligned}$$

Model	$U_3(L)$ [m]	$U_1(L/2, h/2)$ [m]	$\sigma_{13}(L/4, 0)$ (Interface) [Pa]	$\sigma_{11}(L/2, -h/4)$ (Interface) [Pa]	$\sigma_{33}(L/2, h/2)$ [Pa]
Present (error)	-4.40057×10^{-6} (2.6%)	7.36497×10^{-7} (9.8%)	-3181.03 (-2.3%)	-9986.18 (7.9%)	-1067.10 (-4.3%)
Sine (error)	-4.37885×10^{-6} (3.1%)	7.19163×10^{-7} (11.9%)	-3031.42 (2.5%)	-9939.30 (8.3%)	-1066.64 (-4.3%)
Abaqus	-4.51810×10^{-6}	8.16300×10^{-7}	-3110.00	-10842.00	-1023.00

Table 2. Bending of a clamped/free thick beam under uniformly distributed load.

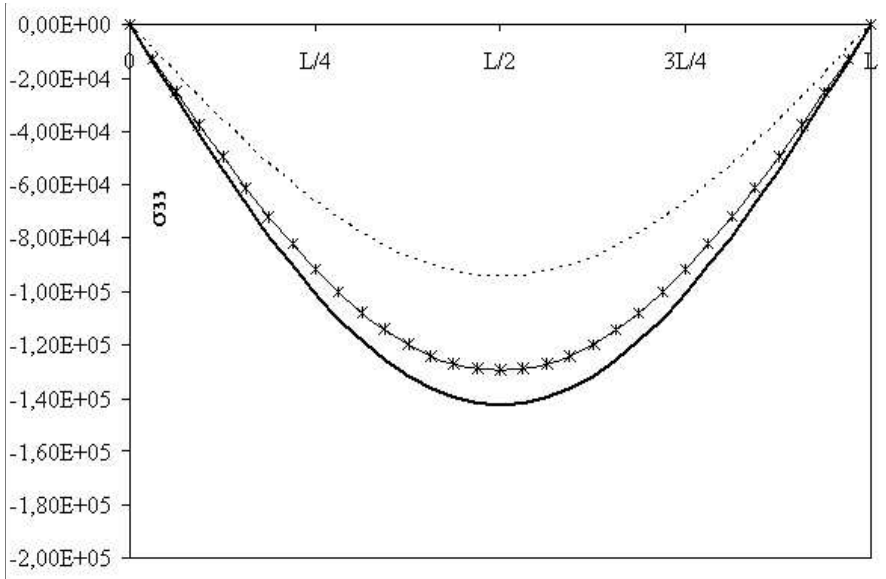


Figure 5. Variation of the stress σ_{33} along the direction x_1 for $x_3 = h/4$ (Interface), for Section 3.2. Abaqus (dashed line plot), Sine (solid line), and Present (dashes and crosses).

The numerical results for Table 2 are obtained for a load $q = -1000$ N/m for the same beam as in Section 3.2, except for the load now being uniformly distributed instead of *sinusoidal*, show that the present model still has less percentage of error compared to the sine model. In Figures 6–9, different stresses and displacements are plotted according to the length and thickness of the beam, showing the difference between the present model and sine model as regards the finite element. The present model is in close agreement with the results of Karama et al. [1998].

3.4. Bending of a clamped free beam under concentrated load. The load is applied at the free end; in this case the value of \bar{N}_3 is:

$$\bar{N}_3 = \int_{-h/2}^{h/2} F_3 dx_3 = q.$$

Now, the governing equation from the system of Equations (19),

$$\begin{aligned} 0 &= A_{11}u_{1,11}^{0*} - B_{11}w_{,111} + \tilde{K}\phi_{1,11}, \\ 0 &= B_{11}u_{1,111}^{0*} - D_{11}w_{,1111} + \tilde{T}\phi_{1,111}, \\ 0 &= \tilde{K}u_{1,11}^{0*} - \tilde{T}w_{,111} + \tilde{S}\phi_{1,11} - \tilde{Y}\phi_1, \end{aligned}$$

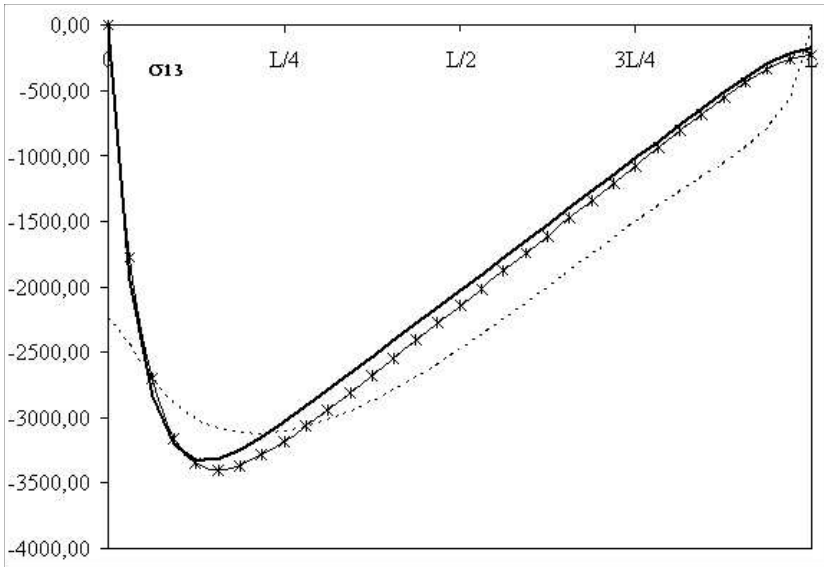


Figure 6. Variation of the stress σ_{13} along the direction x_1 for $x_3 = 0$ (Interface) for Section 3.3. Abaqus (dashed line plot), Sine (solid line), and Present (dashes and crosses).

by integration and simultaneous solving of the above equations, gives

$$\begin{aligned} \phi_1(x_1) &= C_1 e^{-Px_1} + C_2 e^{Px_1} - C_3 \frac{\tilde{T}}{\tilde{Y} D_{11}}, \\ u_1^o(x_1) &= -\frac{\tilde{K}}{A_{11}} \phi_1(x_1) + C_7 x_1 + C_8, \\ w(x_1) &= \frac{\tilde{T}}{P D_{11}} \left[C_1 e^{-Px_1} + C_2 e^{Px_1} - C_3 x_1 \frac{P}{\tilde{Y}} \right] + \frac{C_3}{6 D_{11}} x_1^3 + \frac{1}{2} C_4 x_1^2 + C_5 x + C_6, \end{aligned}$$

where

$$P = \sqrt{\frac{-\tilde{Y} A_{11} D_{11}}{\tilde{K}^2 D_{11} + \tilde{T}^2 A_{11} - \tilde{S} A_{11} D_{11}}},$$

and $B_{11} = 0$ due to the symmetry at mid-surface. The eight constants C_i are determined by the four natural boundary conditions at the free edge deduced from Equation (20) with $P_{(a)}^* = 0$, namely,

$$\begin{aligned} 0 &= A_{11} u_{1,1}^{0*}(L) - \tilde{K} \phi_{1,1}(L), & 0 &= -D_{11} w_{,111}(L) + \tilde{T} \phi_{1,11}(L) - q, \\ 0 &= -D_{11} w_{,11}(L) + \tilde{T} \phi_{1,1}(L), & 0 &= -\tilde{K} u_{1,1}^{0*}(L) + \tilde{T} w_{,11}(L) - \tilde{S} \phi_{1,1}(L), \end{aligned}$$

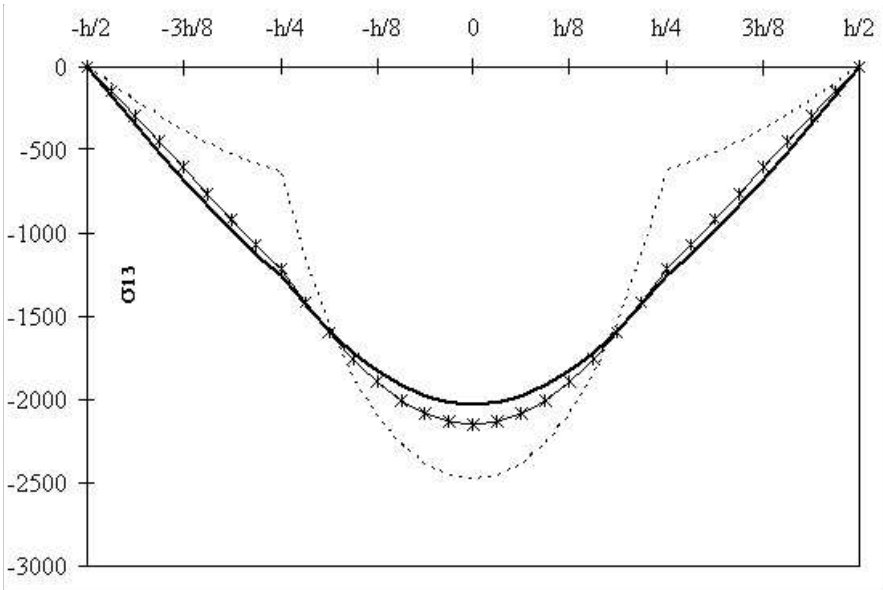


Figure 7. Variation of the stress σ_{13} through the thickness for $x_1 = L/2$ at $x_3 = 0$ for Section 3.3. Abaqus (dashed line plot), Sine (solid line), and Present (dashes and crosses).

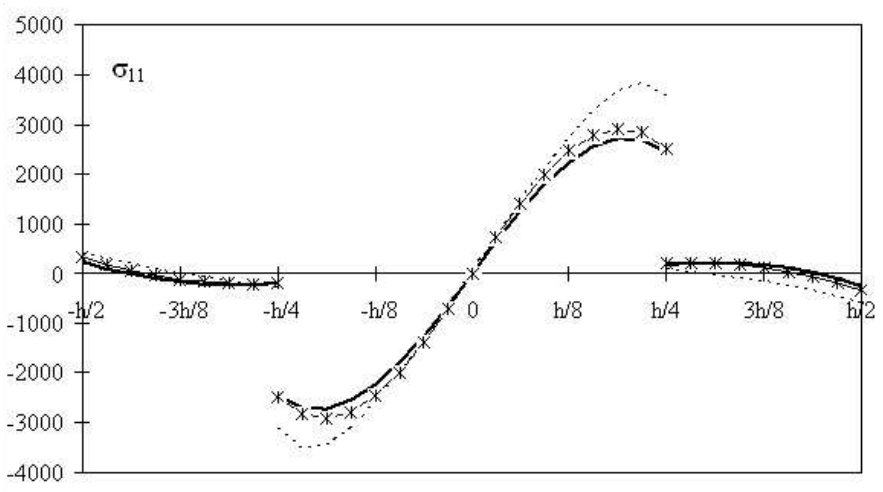


Figure 8. Variation of the stress σ_{11} through the thickness for $x_1 = 3L/4$ for Section 3.3. Abaqus (dashed line plot), Sine (solid line), and Present (dashes and crosses).

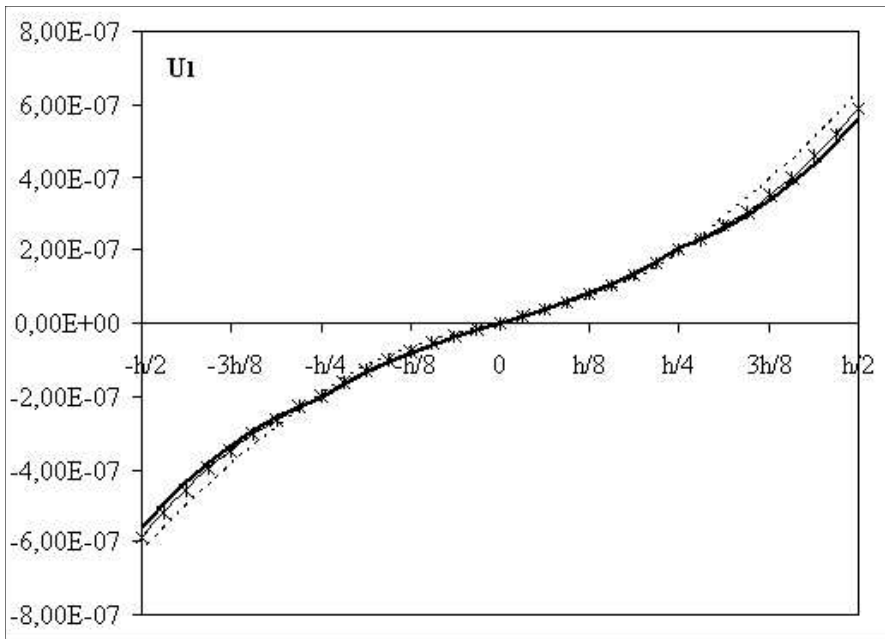


Figure 9. Variation of the displacement U_1 through the thickness for $x_1 = L/4$ for Section 3.3. Abaqus (dashed line plot), Sine (solid line), and Present (dashes and crosses).

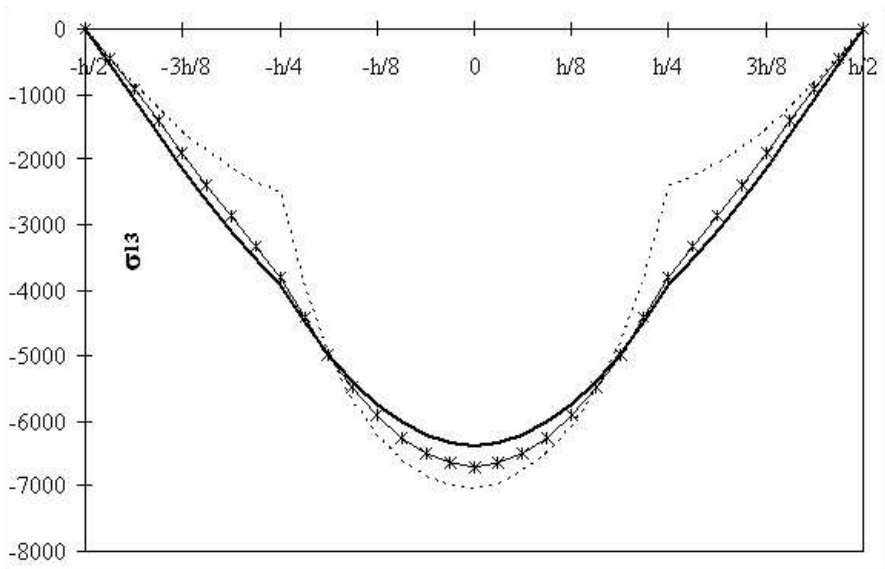


Figure 10. Variation of the stress σ_{13} through the thickness for $x_1 = L/4$ for Section 3.4. Abaqus (dashed line plot), Sine (solid line), and Present (dashes and crosses).

Model	$U_3(L)$ [m]	$U_1(L/2, h/2)$ [m]	$\sigma_{13}(L/4, 0)$ (Interface) [Pa]	$\sigma_{11}(L/2, -h/4)$ (Interface) [Pa]
Present (error)	-1.67021×10^{-5} (0.1%)	2.87160×10^{-6} (8.8%)	-6699.43 (4.7%)	-62969.5 (-1.4%)
Sine (error)	-1.65722×10^{-5} (0.8%)	2.81698×10^{-6} (10.5%)	-6372.07 (9.3%)	-62969.5 (-1.4%)
Abaqus	-1.67110×10^{-5}	3.14800×10^{-6}	-7027.00	-62091.0

Table 3. Bending of a clamped/free thick beam under concentrated load.

along with the four kinematic boundary conditions at the clamped edge:

$$\begin{aligned}
 u_1^0(0) &= 0, \\
 w(0) &= 0, \\
 w_{,1}(0) &= 0, \\
 \phi_1(0) &= 0.
 \end{aligned}$$

The numerical results presented in Table 3 obtained $q = -10000$ N using the present model for the same beam as in Section 3.3 except that loading is now concentrated at the free end of the beam, our reference still being the Karama et al. [1998] results, show that the present model still has very good results compared to the sine model except with regard to membrane stress (σ_{11}) where no difference was found.

4. Conclusion

Continuity of displacement and transverse shear stresses at layer interfaces and the boundary conditions for a laminated composite are fully satisfied by this present new multilayered structure exponential with the help of the Heaviside step function (Figures 2–10). For the new proposed model the results are compared to the existing model (like the sine model by Touratier [1991]) and by the finite element method by Abaqus [Karama et al. 1998]. Results show that the new proposed exponential model presents a better approximation than the sine [Karama et al. 1998] model when compared to results obtained using finite element analyses, with certain exceptions (Tables 1–3). Specifically results are very favorable at layer interfaces.

The new model is also simple in so far as no correction factor is used, contrary to the other higher order models.

In the case of static analysis the numerical results for the bending deformation under different types of loading and boundary conditions on a thick beam (Figures 2–10) showed that the present model is always closer to the finite element analysis by Abaqus [Karama et al. 1998].

On the whole, we can conclude that the present exponential model is more accurate than other existing analytical models for multilayered structures when compared to finite element analysis.

Appendix A. Virtual power of the acceleration quantities

We have

$$\begin{aligned} \dot{U}_1 &= \ddot{u}_1^o - x_3 \ddot{w}_{,1} + h_1 \ddot{\phi}_1, & \dot{U}_3 &= \ddot{w}, \\ U_1^* &= u_1^{0*} - x_3 w_{,1}^* + h_1 \phi_1^*, & U_3^* &= w^*. \end{aligned}$$

So Equation (5) becomes

$$\begin{aligned} P_{(a)}^* &= \int_{\Omega} \rho(U_1^* \dot{U}_1 + U_3^* \dot{U}_3) d\Omega \\ &= \int_{\Omega} \rho[u_1^{0*} \ddot{u}_1 + (\ddot{u}_3 + x_3 \ddot{u}_{1,1}) w^* + h_1(x_3) \phi_1^* \ddot{u}_1] d\Omega - \int_{\Gamma} \rho x_3 w^* \ddot{u}_1 d\Gamma \\ &= \int_{\Omega} \rho \left[(\ddot{u}_1^o - x_3 \ddot{w}_{,1} + h_1(x_3) \ddot{\phi}_1) u_1^{0*} + (\ddot{w} + x_3 (\ddot{u}_{1,1}^o - x_3 \ddot{w}_{,11} + h_1(x_3) \ddot{\phi}_{1,1})) w^* \right. \\ &\quad \left. + h_1(x_3) (\ddot{u}_1^o - x_3 \ddot{w}_{,1} + h_1(x_3) \ddot{\phi}_1) \phi_1^* \right] d\Omega \\ &\quad - \int_{\Gamma} \rho x_3 (\ddot{u}_1^o - x_3 \ddot{w}_{,1} + h_1(x_3) \ddot{\phi}_1) w^* d\Gamma, \end{aligned}$$

where in the second line we integrated by parts.

Then,

$$\begin{aligned} P_{(a)}^* &= \int_0^L \left[u_1^{0*} \int_{-h/2}^{h/2} (\rho \ddot{u}_1^o - \rho x_3 \ddot{w}_{,1} + \rho h_1(x_3) \ddot{\phi}_1) dx_3 \right. \\ &\quad \left. + w^* \int_{-h/2}^{h/2} (\rho \ddot{w} + \rho x_3 \ddot{u}_{1,1}^o + \rho x_3^2 \ddot{w}_{,11} + \rho x_3 h_1(x_3) \ddot{\phi}_{1,1}) dx_3 \right. \\ &\quad \left. + \phi_1^* \int_{-h/2}^{h/2} (\rho h_1(x_3) \ddot{u}_1^o - \rho x_3 h_1(x_3) \ddot{w}_{,1} + \rho h_1^2(x_3) \ddot{\phi}_1) dx_3 \right] dx_1 \\ &\quad + w^* \int_{-h/2}^{h/2} (-\rho x_3 \ddot{u}_1^o + \rho x_3^2 \ddot{w}_{,1} - \rho x_3 h_1(x_3) \ddot{\phi}_{1,1}) dx_3 \\ &= \int_0^L (\Gamma^{(u)} u_1^{0*} + \Gamma^{(w)} w^* + \Gamma^{(\phi)} \phi_1^*) dx_1 + \bar{\Gamma}^{(w)} w^*, \end{aligned}$$

where the last line comes from using the relations (6).

Appendix B. Virtual power of the internal work

By relation (9), virtual power of the internal work (8) becomes

$$\begin{aligned}
 P_{(i)}^* &= - \int_{\Omega} \left[(u_{1,1}^{0*} - x_3 w_{,11}^* + h_1(x_3) \phi_{1,1}^*) \sigma_{11} + 2 \left(\frac{1}{2} h_{1,3}(x_3) \phi_1^* \right) \sigma_{13} \right] d\Omega \\
 &= - \int_{\Omega} \left[-\sigma_{11,1} u_1^{0*} - x_3 \sigma_{11,11} w^* - h_1(x_3) \sigma_{11,1} \phi_1^* + h_{1,3}(x_3) \sigma_{13} \phi_1^* \right] d\Omega \\
 &\quad - \int_{\Gamma} \left[\sigma_{11} u_1^{0*} - x_3 \sigma_{11} w_{,1}^* + x_3 \sigma_{11,1} w^* + h_1(x_3) \sigma_{11} \phi_1^* \right] d\Gamma \\
 &= \int_0^L \left[u_1^{0*} \int_{-h/2}^{h/2} \sigma_{11,1} dx_3 + w^* \int_{-h/2}^{h/2} x_3 \sigma_{11,11} dx_3 + \phi_1^* \int_{-h/2}^{h/2} \left(h_1(x_3) \sigma_{11,1} - h_{1,3}(x_3) \sigma_{13} \right) dx_3 \right] dx_1 \\
 &\quad - u_1^{0*} \int_{-h/2}^{h/2} \sigma_{11} dx_3 + w_{,1}^* \int_{-h/2}^{h/2} x_3 \sigma_{11} dx_3 - w^* \int_{-h/2}^{h/2} x_3 \sigma_{11,1} dx_3 - \phi_1^* \int_{-h/2}^{h/2} h_1(x_3) \sigma_{11} dx_3,
 \end{aligned}$$

where in the second line we integrated by parts.

Using relations (10), we obtain

$$P_{(i)}^* = \int_0^L (N_{11,1} u_1^{0*} + M_{11,11} w^* + (P_{11,1} - P_{13}) \phi_1^*) dx_1 - N_{11} u_1^{0*} - M_{11,1} w^* + M_{11} w_{,1}^* - P_{11} \phi_1^*.$$

Appendix C. Virtual power of the external loading

By relations (13), virtual power of external loading (12) becomes

$$\begin{aligned}
 P_{(e)}^* &= \int_{\Omega} [U_1^* \ 0 \ U_3^*] \cdot \begin{bmatrix} f_1 \\ f_2 \\ f_3 \end{bmatrix} d\Omega + \int_{\Gamma} [U_1^* \ 0 \ U_3^*] \cdot \begin{bmatrix} F_1 \\ F_2 \\ F_3 \end{bmatrix} d\Gamma \\
 &= \int_{\Omega} (f_1 U_1^* + f_3 U_3^*) d\Omega + \int_{\Gamma} (F_1 U_1^* + F_3 U_3^*) d\Gamma \\
 &= \int_{\Omega} (f_1 u_1^{0*} - f_1 x_3 w_{,1}^* + h_1(x_3) f_1 \phi_1^* + f_3 w^*) d\Omega + \int_{\Gamma} (F_1 u_1^{0*} - F_1 x_3 w_{,1}^* + h_1(x_3) F_1 \phi_1^* + F_3 w^*) d\Gamma \\
 &= \int_0^L \left[u_1^{0*} \int_{-h/2}^{h/2} f_1 dx_3 + w^* \int_{-h/2}^{h/2} (f_3 + x_3 f_{1,1}) dx_3 + \phi_1^* \int_{-h/2}^{h/2} h_1(x_3) f_1 dx_3 \right] dx_1 \\
 &\quad + u_1^{0*} \int_{-h/2}^{h/2} F_1 dx_3 + w^* \int_{-h/2}^{h/2} (F_3 - x_3 f_1) dx_3 + \phi_1^* \int_{-h/2}^{h/2} h_1(x_3) F_1 dx_3 - w_{,1}^* \int_{-h/2}^{h/2} x_3 F_1 dx_3 \\
 &= \int_0^L (\bar{n}_1 u_1^{0*} + (\bar{n}_3 + \bar{m}_{1,1}) w^* + \bar{p}_1 \phi_1^*) dx_1 + \bar{N}_1 u_1^{0*} (\bar{N}_3 - \bar{m}_1) w^* - \bar{M}_1 w_{,1}^* + \bar{P}_1 \phi_1^*,
 \end{aligned}$$

where the last line utilizes relation (13).

References

- [Ambartsumian 1958] S. A. Ambartsumian, "On theory of bending plates", *Izv. Otd. Tech. Nauk. AN SSSR* **5** (1958), 69–77.
- [Beakou 1991] A. Beakou, *Homogénéisation et modélisation des coques composites multicouches*, PhD Thesis, ENSAM, Paris, 1991.
- [Di Sciuva 1987] M. Di Sciuva, "An improved shear deformation theory for moderately thick multi-layered anisotropic shells and plates", *J. Appl. Mech. (Trans. ASME)* **54** (1987), 589–596.
- [Di Sciuva 1993] M. Di Sciuva, "A general quadrilateral multilayered plate element with continuous interlaminar stresses", *Comput. Struct.* **47**:1 (1993), 91–105.
- [He 1994] L. H. He, "A linear theory of laminated shells accounting for continuity of displacements and transverse shear stresses at layer interfaces", *Int. J. Solids Struct.* **31**:5 (1994), 613–627.
- [Idlbi 1995] A. Idlbi, *Comparaison de théories de plaque et estimation de la qualité des solution dans la zone bord*, PhD Thesis, ENSAM, Paris, 1995.
- [Kaczkowski 1968] Z. Kaczkowski, *Plates-statistical calculations*, Arkady, Warsaw, 1968.
- [Karama et al. 1998] M. Karama, B. Abouharb, S. Mistou, and S. Caperaa, "Bending, buckling and free vibration of laminated composite with a transverse shear stress continuity model", *Compos. B:Eng.* **29**:3 (1998), 223–234.
- [Kirchhoff 1850] G. J. Kirchhoff, "Über das Gleichgewicht und die Bewegung einer elastischen Schreibe", *Reine Angew Math* **40** (1850), 51–58.
- [Levinson 1980] M. Levinson, "An accurate simple theory of the statics and dynamics of elastic plates", *Mech. Res. Commun.* **7**:6 (1980), 343–350.
- [Love 1934] A. E. H. Love, *A treatise on the mathematical theory of elasticity*, 4 ed., Cambridge University Press, 1934.
- [Mindlin 1951] R. D. Mindlin, "Influence of rotary inertia and shear on flexural motions of isotropic elastic plates", *J. Appl. Mech. (Trans. ASME)* **18** (1951), 31–38.
- [Murthy 1981] M. V. V. Murthy, "An improved transverse shear deformation theory for laminated anisotropic plates", NASA Technical Paper, 1981, Available at http://ntrs.nasa.gov/archive/nasa/casi.ntrs.nasa.gov/19820003615_1982003615%20.pdf.
- [Ossadzow et al. 1995] C. Ossadzow, P. Muller, and M. Touratier, *Une théorie générale des coques composites multicouches*, vol. 1, Deuxième Colloque National en Calcul des Structures, Hermes, 1995.
- [Pagano 1970] N. J. Pagano, "Exact solution for rectangular bi-directional composites and sandwich plates", *J. Compos. Mater.* **4** (1970), 20–34.
- [Panc 1975] V. Panc, *Theories of elastic plates*, Academia, Prague, 1975.
- [Reddy 1984] J. N. Reddy, "A simple high-order theory of laminated composite plate", *J. App. Mech. (Trans. ASME)* **51** (1984), 745–752.
- [Reissner 1945] E. Reissner, "Reflection on the theory of elastic plates", *J. Appl. Mech. (Trans. ASME)* **38** (1945), 1453–1464.
- [Reissner 1975] E. Reissner, "On transverse bending of plates, including the effect of transverse shear deformation", *Int. J. Solids Struct.* **11**:5 (1975), 569–573.
- [Touratier 1991] M. Touratier, "An efficient standard plate theory", *Int. J. Eng. Sci.* **29**:8 (1991), 901–916.
- [Touratier 1992] M. Touratier, "A generalization of shear deformation theories for axisymmetric multilayered shells", *Int. J. Solids Struct.* **29**:11 (1992), 1379–1399.
- [Widera and Logan 1980] G. E. O. Widera and D. L. Logan, "Refined theories for non-homogeneous anisotropic cylindrical shells, I and II", *J. Eng. Mech. Div. ASCE* **EM6** (1980), 1053–1090.

Received 4 Dec 2005.

M. KARAMA: moussa@enit.fr

École Nationale d'Ingénieurs de Tarbes, 47 av. Azereix BP1629, 65016 Tarbes, France

K. S. AFAQ: kamran@enit.fr

École Nationale d'Ingénieurs de Tarbes, 47 av. Azereix BP1629, 65016 Tarbes, France

S. MISTOU: mistou@enit.fr

École Nationale d'Ingénieurs de Tarbes, 47 av. Azereix BP1629, 65016 Tarbes, France

A MACROSCOPIC MODEL FOR KINK BANDING INSTABILITIES IN FIBER COMPOSITES

SHILADITYA BASU, ANTHONY M. WAAS AND DAMODAR R. AMBUR

In this paper, a mechanism-based lamina level modeling approach is used as the basis for developing a macroscopic (lamina level) model to capture the mechanisms of kink banding. Laminae are modeled as inelastic degrading *homogenized* layers in a state of plane stress according to Schapery Theory (ST). However, the principal orthotropic material axes are allowed to rotate as a function of deformation. In ST, each lamina degrades as characterized through laboratory scale experiments. In the fiber direction, elastic behavior prevails; however, in this work, the phenomenon of fiber microbuckling leading to kink banding, which is responsible for the sudden degradation of the axial lamina properties under compression, is explicitly accounted for by allowing the fiber rotation at a material point to be a variable in the problem. These features are built into a user-defined material subroutine that is implemented through the commercial finite element (FE) software ABAQUS. Thus, in this model we eschew the notion of a fixed compressive strength of a lamina and instead use the mechanics of the failure process to provide the in situ compression strength of a material point in a lamina, the latter being dictated strongly by the current local stress state, the current state of the lamina transverse material properties, and the local fiber rotation. The inputs to this model are laboratory scale, coupon level test data (at the lamina level) that provide information on the lamina transverse property degradation (that is, appropriate, measured, strain-stress relations of the lamina transverse properties), the elastic lamina orthotropic properties and the geometry of the lamina. The validity of the approach advocated is demonstrated through numerical simulations of unidirectional lamina with initial fiber imperfections. The predictions of the simulations reported in this paper are compared against previously reported results from micromechanical analyses. Good agreement between the present macroscopic modeling approach and the previous micromechanical observations are reported.

1. Introduction

Development of computational methodologies for the prediction of damage accumulation and growth in continuous fiber composite laminates is an active area of research. There exists a large body of literature devoted to progressive failure analysis (PFA) of composite laminated structures. Many of the PFA schemes available today rely on the phenomenological approach of defining strength criteria for a single lamina when subjected to different single component stress states. These methods define the onset of failure through specific indices that are expressed as functions of the current stress state. When any of these indices exceeds a predefined critical value, the material at that point is said to have failed [Hashin 1980; Chang and Lessard 1991]. When a material point has failed, for subsequent loading, it is assumed to have a reduced stiffness that is predetermined in an empirical manner. Depending on the type of failure (for instance, fiber breaking and/or matrix cracking due to tension along the fibers, fiber kink-banding due

Keywords: fiber kinking, fiber rotation, matrix damage, progressive failure analysis, compressive response.

to compression along the fibers, fiber/matrix debonding due to in-plane shear), different elastic moduli are set to zero. In addition, linear elastic material behavior is assumed throughout the analysis.

In a laminated composite plate, the stiffness at a material point is determined by the current local stress state and the local 'state' of the material. The local stress state, in general, is multiaxial and a material point at the current state may have accumulated damage, dictated by the loading history. Thus, 'strength' at a material point is influenced to a great extent by the current stress and strain state and is predicated on the mechanism of failure. PFA methodologies that abruptly change material properties based on strength 'indices' and rely on a linear elastic analysis may be unable to realistically account for features associated with the mechanisms of failure. Furthermore, these approaches lack an appropriate definition of the material state beyond first failure. For progressive failure modeling, a framework that accounts for the continued degradation of the material is needed.

Schapery [1990] introduced a thermodynamically based theory (referred to as ST) that uses internal state variables (ISVs) to analyze damage evolution in composite laminates. These ISVs are related to mechanical aspects of damage mechanisms. The ISVs are related to the energy required for the evolution of the damaged states. Different damage mechanisms can have distinct ISVs to track the damage evolution. For instance, matrix microcracking can be expressed via one ISV, while transverse cracking can be represented by another ISV [Schapery and Sicking 1995]. The evolution of these ISVs with global loading is determined at each material point as functions of load history, by means of a thermodynamic criterion (an evolution equation) throughout the loading history. Therefore, the 'state' of the material is continually updated according to the stress and strain history that a material point experiences throughout the loading history.

Various experimental [Vogler and Kyriakides 1999; Lee and Waas 1999; Oguni et al. 2000] and analytical [Basu et al. 2006a] studies show that the maximum load sustained by a lamina in the axial direction (σ_{11}^{cr}) in compression depends greatly on the presence of other in-plane stress components such as σ_{22} and τ_{12} . Experimental, analytical and micromechanical studies show that the main physical event occurring during kink banding is the rotation of fibers in a band within a degrading matrix. The rotation of fibers gives rise to high localized shear strains that drive the shear degradation of the local matrix. The shear degradation in turn drives the rotation of the fibers creating a positive feedback loop. These simultaneous phenomena result in a limit load situation for a lamina under axial compression. This limit load, which is dictated by the local stress state and the state of the transverse lamina properties, can be relieved (increased) by the presence of other stress components or, in certain cases, can be elevated (reduced). The present approach captures these two phenomena in a macroscopic numerical setting and is able to reproduce the fine scale micromechanical observations seen in experiments and in associated numerical models [Vogler and Kyriakides 1997; Lee and Waas 1999; Yerramalli and Waas 2004; Basu 2005; Basu et al. 2006b]. It is to be noted that Merodio and Pence [2001] have presented a comprehensive analysis of the formation of kinks, defined as surfaces across which the deformation gradient and hydrostatic pressure suffer jumps, in directionally reinforced neo-Hookean materials. Their results, which are carried out for purely elastic materials, bear some resemblance to the results reported in the literature for fiber reinforced materials with a polymer matrix [Vogler and Kyriakides 1997; Lee and Waas 1999; Oguni et al. 2000]. This work has recently been further extended by Fu and Zhang [2006], who have considered the rotation of the kink band with continued loading.

2. Modeling of a damaging matrix using Schapery Theory (ST)

2.1. Elements of the PFA approach.

2.1.1. Non-linear constitutive formulation. Schapery [1989] developed nonlinear elastic constitutive relations for an orthotropic lamina using a work potential approach which accounted for the effect of microdamage. The lamina stress-strain relations are

$$\sigma_{11} = Q_{11}\epsilon_{11} + Q_{12}\epsilon_{22}, \quad \sigma_{22} = Q_{12}\epsilon_{11} + Q_{22}\epsilon_{22}, \quad \tau_{12} = Q_{66}\gamma_{12}, \quad (1)$$

where

$$\begin{aligned} Q_{11} &= \frac{E_{11}}{1 - \nu_{12}\nu_{21}}, & Q_{22} &= \frac{E_{22}}{1 - \nu_{12}\nu_{21}}, \\ Q_{12} &= \nu_{12}Q_{22}, & Q_{66} &= G_{12}, \\ \nu_{21} &= \frac{\nu_{12}E_{22}}{E_{11}} \end{aligned}$$

In the existing literature on damage mechanics as applied to continuous fiber laminated composite materials, the effect of damage is incorporated through the change in transverse Young's modulus E_{22} and in plane shear modulus G_{12} . For instance, Sun and Chen [1989] proposed a one parameter plastic potential in conjunction with orthotropic incremental plasticity theory to study the evolution of E_{22} and G_{12} in tension. Schapery and Sicking [1995] used ST to study the evolution of E_{22} and G_{12} . These studies were not concerned with the state of the lamina beyond first failure in the fiber direction. Yet it is recognized [Dávila et al. 2000] that such damage is dominant for compression loaded composite structures. Lamina level coupon tests in tension have shown that fiber direction modulus E_{11} and Poisson's ratio ν_{12} can be assumed to be independent of microdamage that influences E_{22} and G_{12} [Schapery 1995]. This is also true for compression until the onset of kinking (the axial compression load reaches a maximum limit load at the point in which a kink band starts to form, for example, as shown in [Lee and Waas 1999]). During kink band formation and propagation, it is likely that microdamage mechanisms do influence E_{11} , ν_{12} , E_{22} and G_{12} . Subsequent to kink banding, other failure mechanisms such as delamination can occur. These mechanisms are not accounted for here, but have received attention recently in the context of PFA [Goyal et al. 2002].

2.1.2. Elements of Schapery Theory. Schapery [1990] introduced a general thermodynamic framework to study materials that undergo damage. In [Schapery and Sicking 1995], ISVs are used to incorporate *inelastic* behavior in the material response. In these developments in a mechanical process the total work done, W_T , is composed of the inelastic work, W_s and the work of deformation W : $W_T = W + W_s$. The irrecoverable portion of total energy (W_s) can be determined from the material stress-strain response as shown in Figure 1. ISVs are described through S_i 's. Each S_i is associated with a particular damage mechanism. To satisfy the path independence of total work, these ISVs have to satisfy the following relation,

$$f_i = \frac{\partial W_s}{\partial S_i}. \quad (2)$$

The left-hand side of Equation (2) is called the *thermodynamic force* related to the i^{th} ISV. If the i^{th} *driving force*, which is the available thermodynamic force, given by Equation (3), exceeds $\partial W_s/\partial S_i$,

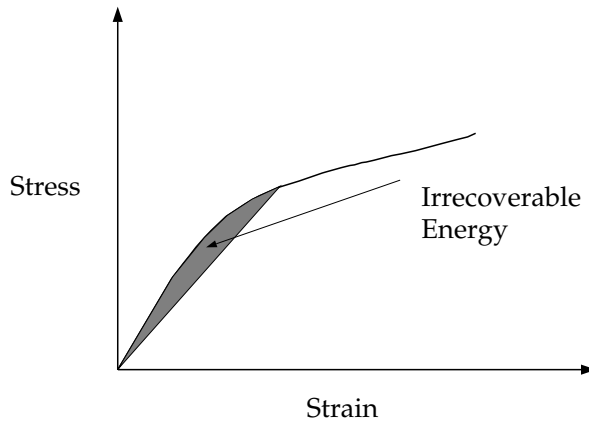


Figure 1. Definition of irrecoverable energy using a generic stress-strain curve.

then the material undergoes a structural change associated with S_i :

$$f_i \equiv -\frac{\partial W}{\partial S_i}. \tag{3}$$

Stated another way, $\dot{S}_i > 0$. However, as Schapery [1990] pointed out, if the available thermodynamic force ($-\partial W/\partial S_i$) is less than the required thermodynamic force ($\partial W_s/\partial S_i$), then $\dot{S}_i = 0$. Furthermore, S_i need not change continuously with the loading.

Schapery considered two ISVs. They were the energies associated with matrix microcracks (S) and of the transverse intra-ply cracks (S_c), respectively. Inelastic work is described as $W_s = S + S_c$. In the present work, the effect of only one ISV is considered; it is denoted by S and represents the irrecoverable energy content due to the accumulation of microcracks.

The ISV affects the moduli E_{22} and G_{12} through Equation (4):

$$E_{22} = E_{22_0}e_s(S), \quad G_{12} = G_{12_0}g_s(S). \tag{4}$$

Here, E_{22_0} and G_{12_0} are transverse and shear moduli of the virgin material, that is, at zero strain and zero damage; $e_s(S)$ and $g_s(S)$ are functions relating these two moduli to microcracking ISV, S . The functions e_s and g_s are expressed as polynomial relations in the ISV, S [Schapery and Sicking 1995].

The strain energy density (or work of deformation) can be written as

$$W = \frac{1}{2}(Q_{11}\epsilon_{11}^2 + Q_{22}\epsilon_{22}^2) + Q_{12}\epsilon_{11}\epsilon_{22} + \frac{1}{2}Q_{66}\gamma_{12}^2. \tag{5}$$

To incorporate geometric nonlinearities, Green’s strains and the second Piola Kirchoff stresses need to be used in the expression for W . For small strains, Equation (5) would contain only the first order terms in the strain-displacement relations. Schapery and Sicking [1995] have shown that material nonlinearities as incorporated in Equation (5) are still significant for fiber reinforced composites even when inclusion of geometric nonlinearities are not called for [Schapery 2002]. Using Equations (1)–(3), the evolution

equation for S is as follows,

$$\frac{\epsilon_{11}^2}{2} \frac{\partial Q_{11}}{\partial S} + \frac{\epsilon_{22}^2}{2} \frac{\partial Q_{22}}{\partial S} + \epsilon_{11}\epsilon_{22} \frac{\partial Q_{12}}{\partial S} + \frac{\gamma_{12}^2}{2} \frac{\partial G_{12}}{\partial S} = -1. \quad (6)$$

For most materials, $\nu_{12}\nu_{21} \ll 1$, which implies that the Q_{ij} 's can be replaced by E_{ij} 's. In this work, it is assumed that the fiber direction stiffnesses are unaffected by S . Thus, the term containing Q_{11} in Equation (6) can be neglected. It is also assumed that ν_{12} changes with S such that $\nu_{12}E_{22}$ remains constant during loading. The implications of this assumption are twofold. Firstly, it allows for a change in ν_{12} with damage accumulation in the lamina. Secondly, it makes it possible to uncouple ϵ_{11} from the microcracking damage accumulation. If ϵ_{11} is present in the evolution equation (Equation (6)), then microcracking damage becomes a direct function of the longitudinal strain, which is an improper representation of the underlying mechanism. Equation (6) can be reduced to

$$\frac{\epsilon_{22}^2}{2} \frac{\partial E_{22}}{\partial S} + \frac{\gamma_{12}^2}{2} \frac{\partial G_{12}}{\partial S} = -1.$$

For an inelastic process, the entropy production rate is nonnegative. Hence,

$$\dot{S} \geq 0. \quad (7)$$

The overdot represents temporal derivative. Physically, \dot{S} is nonnegative because healing (or reversible damage) is not allowed for in the damage mechanism considered.

From experiments [Schapery and Sicking 1995], it has been observed that for small strains, S behaves as ϵ^3 . This is based on the fact that the moduli are constant for small strains. Thus to express the moduli E_{22} and G_{12} in terms of a polynomial of S , a reduced variable S_r can be used, namely, $S_r \equiv S^{1/3}$. The evolution equation for S_r now becomes

$$\frac{\epsilon_{22}^2}{2} \frac{\partial E_{22}}{\partial S_r} + \frac{\gamma_{12}^2}{2} \frac{\partial G_{12}}{\partial S_r} = -3S_r^2. \quad (8)$$

It should be noted that it is possible to include other softening damage mechanisms such as local fiber-matrix debonding and shear banding through S as has been discussed by Schapery [1990].

During laboratory experiments, the density of microcracks in a lamina reaches a saturation limit and the specimen fails in a catastrophic manner. The corresponding value of S_r , obtained from the resultant stress-strain plot, is denoted by S_r^* . The constitutive model described thus far holds true for $S_r \leq S_r^*$. For $S_r > S_r^*$, any constitutive modeling idea is somewhat hypothetical as no material physically exists anymore. For the purpose of extending the analyses beyond S_r^* , it is imperative for the design of a PFA to ensure a stable procedure to degrade the material beyond this point.

2.1.3. Fiber rotation under axial compression. Imperfect fiber systems are prone to rotation under axial compression. That is, the fibers within a lamina that are subjected to axial compression have the propensity to *change* their alignment. This change is dictated by the local multiaxial stress state and the local shear stiffness of the matrix. As the local shear strains increase, the matrix shear stiffness decreases, which indicates that the resistance to fiber rotation diminishes and gradually the fiber rotation begins to build up, which in turn creates more local imperfection and local shear strain. Thus, a positive feedback loop is established between these two competing events. A point is reached when the in situ shear stiffness

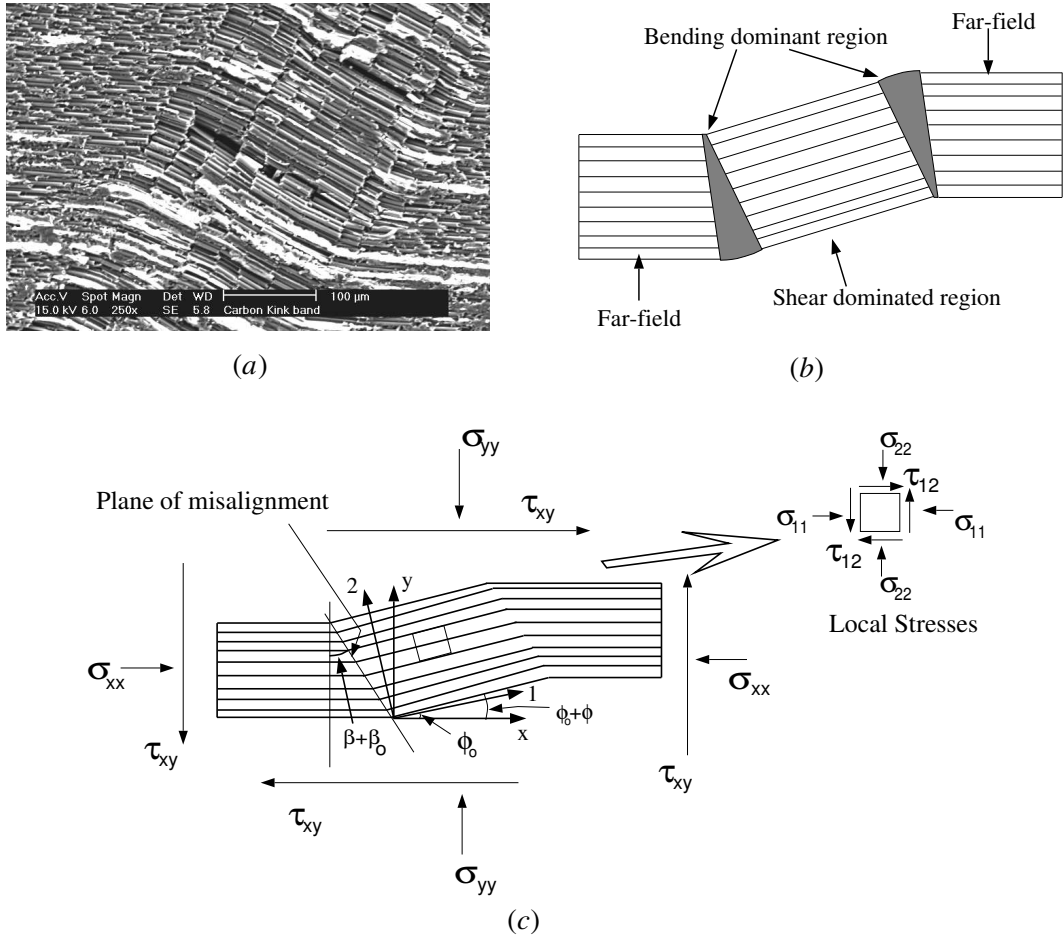


Figure 2. (a) The developing kink band in Carbon composites [Yerramalli 2003]; (b) the schematic representation of such within a lamina; and (c) a unidirectional lamina with a band of misaligned fibers in equilibrium under a multiaxial stress state. Inset shows the stress state inside the misaligned band.

is *not* sufficient to prevent additional fiber rotation. This point usually coincides with the peak load in an axial material response curve. Beyond this point, the matrix offers diminishing resistance to fiber rotation and the fibers rotate and break along boundaries within localized deformed bands, commonly described as ‘kink bands’ [Evans and Adler 1978].

Consider a fiber reinforced lamina under a generalized load state as indicated in Figure 2. A reference frame x – y can be defined such that the x -direction is parallel to the nominal fiber direction in the lamina and the y -direction is normal to it. In subsequent discussions, the x – y reference frame will be termed as the ‘global’ frame. The misaligned band of fibers, in the current configuration, is defined through two angles, $\hat{\phi} = \phi + \phi_0$ and $\hat{\beta} = \beta + \beta_0$. The angles ϕ_0 and β_0 are constants, and the angles ϕ and β are variables that may change as a function of current far-field stress state. The reference frame 1–2 is defined in the unstressed initial configuration of the misaligned lamina. Fibers inside the misaligned band

are parallel to the ‘1’ direction in the initial state. A current reference frame 1’–2’ is defined where ‘1’ is always parallel to the current fiber direction inside the band, so that the 1-axis rotates to 1’-axis during loading. The ‘2’ and ‘2’ directions are always orthogonal to the ‘1’ and ‘1’ directions respectively. The 1–2 frame will be defined as the ‘local’ frame and the 1’–2’ system will be termed the instantaneous frame. Initially, when the matrix retains most of its in situ shear stiffness, the 1–2 and 1’–2’ axes systems will be nearly coincident. As the matrix loses its in situ shear stiffness, the local shear strain, γ_{12} , will start to rise rapidly. As shown in Basu et al. [2006a], the angle between the 1-axis and the 1’-axis, given by ϕ and γ_{12} , for small strains, is related by $\gamma_{12} = \gamma_{12}^{\infty} + \phi - \beta$. Here, γ_{12}^{∞} is the contribution from the externally applied shear loading, if any. For a uniaxial compression loading and assuming $\beta = \beta_0 = 0$, we arrive at

$$\gamma_{12} \approx \phi. \quad (9)$$

2.1.4. Fiber rotation under axial compression-finite deformation. In Equation (9) the angle ϕ is computed with a small strain assumption and without contribution from the fiber axial strain. In situ fiber orientation can also be computed using the deformation gradient in the following manner [Fung and Tong 2001]. If the unit vector of a line element in the undeformed configuration is given by e_{f_0} , and F is the deformation gradient tensor, then the stretch ratio of that line element due to deformation can be computed as

$$\lambda = \sqrt{e_{f_0} \cdot F^T \cdot F \cdot e_{f_0}}.$$

Consequently, the new unit vector of that line element after deformation will be

$$e_f = \frac{1}{\lambda} F \cdot e_{f_0}. \quad (10)$$

Equation (10) can be used to obtain the instantaneous fiber orientation in the 1–2 plane.

$$\phi = \arctan \frac{e_f(2)}{e_f(1)}. \quad (11)$$

This expression of ϕ is not subject to simplifications associated with the smallness of quantities.

2.2. Numerical implementation using the finite element (FE) method. The material behavior outlined in the previous subsection is modeled in the numerical domain using the commercially available FE package ABAQUS. ABAQUS has the capability of integrating user-defined material behavior with its existing element library through user-defined material subroutines, UMAT [ABAQUS 2003]. This subroutine is called at each material point for which the constitutive law is defined through the user-defined option. A UMAT receives, from the solver in ABAQUS, the stresses and strains from the previous loading step, the increment of strain in the current loading step and various other parameters. After calculations, the UMAT returns to the solver the updated stresses and internal state variables, if any, and the incremental tangent stiffness matrix, $\partial\sigma_{ij}/\partial\epsilon_{ij}$. Here it is pertinent to relate the three reference frames described in the previous subsection to the finite element solver reference systems. The x – y reference frame is the ‘global’ or ‘laminate’ frame. The master geometry of the numerical domain is defined in this system. We will also use this frame to define external loading. The 1–2 reference frame coincides with the ‘local’ lamina orientation, without any loss in its significance. The solver in ABAQUS passes variables to a

UMAT in this coordinate frame. The 1'–2' reference frame is the ‘instantaneous’ frame, with the 1' direction coincident with the current fiber direction, and is used for computations within the UMAT.

In the n^{th} loading increment, the solver sends in the stresses σ_{ij}^{n-1} in the 1–2 coordinate frame which are related to the stresses in the x – y frame via the plane-stress transformation relation:

$$\begin{aligned} \sigma_{11}^{n-1} &= \cos^2(\phi^{n-1})\sigma_{xx}^{n-1} + \sin^2(\phi^{n-1})\sigma_{yy}^{n-1} + 2 \cos(\phi^{n-1}) \sin(\phi^{n-1})\tau_{xy}^{n-1}, \\ \sigma_{22}^{n-1} &= \sin^2(\phi^{n-1})\sigma_{xx}^{n-1} + \cos^2(\phi^{n-1})\sigma_{yy}^{n-1} - 2 \cos(\phi^{n-1}) \sin(\phi^{n-1})\tau_{xy}^{n-1}, \\ \tau_{12}^{n-1} &= \cos(\phi^{n-1}) \sin(\phi^{n-1})(\sigma_{xx}^{n-1} - \sigma_{yy}^{n-1}) + (\cos^2(\phi^{n-1}) - \sin^2(\phi^{n-1}))\tau_{xy}^{n-1}. \end{aligned}$$

The strains ϵ_{ij}^{n-1} and strain increments $d\epsilon_{ij}^n$ in the local 1–2 coordinate system are also passed in from the solver. Within the UMAT, these local strain increments ($d\epsilon_{ij}^n$) are added to the total strains, ϵ_{ij}^{n-1} , to obtain the total strains ϵ_{ij}^n . The strains, ϵ_{ij}^n , are then transformed to the 1'–2' system using the angle between the local and the instantaneous frames, ϕ^{n-1} , to obtain total strains in the instantaneous direction, $\epsilon_{i'j'}^n$. If the stored value of S_r (solution from the previous load increment) is greater than S_r^* , all material parameters are degraded in a pre-determined fashion such that a zero secant stiffness state is reached asymptotically. If $S_r < S_r^*$, then these strains $\epsilon_{i'j'}^n$ are used in Equation (8) to solve for the thermodynamic damage variable S_r . If the S_r value thus obtained satisfies Equation (7), then the material point accumulates damage and the lamina in situ moduli E_{22} and G_{12} are degraded according to the input data provided. If S_r does not satisfy Equation (7), then the in situ moduli are not changed from their previous values. This ensures that a material point accumulates damage without reversibility and the moduli always degrade monotonically. Subsequently, the material secant constitutive matrix $Q_{i'j'}^n$ is computed using the in situ moduli, E_{11} , ν_{12} , E_{22} and G_{12} . According to the present modeling scheme, E_{11} is not affected by S_r . Thus it remains constant at the undamaged state value until S_r becomes greater than S_r^* during the analysis. Next, the stresses $\sigma_{i'j'}^n$ are updated and the material incremental constitutive matrix $\partial\sigma_{i'j'}^n/\partial\epsilon_{i'j'}^n$ is computed:

$$J = \begin{pmatrix} E_{110} & \nu_{12}E_{22} & 0 \\ \nu_{12}E_{22} & E_{22} + \frac{\partial E_{22}}{\partial \epsilon_{22}}\epsilon_{22} & \frac{\partial E_{22}}{\partial \gamma_{12}}\epsilon_{22} \\ 0 & \frac{\partial G_{12}}{\partial \epsilon_{22}}\gamma_{12} & G_{12} + \frac{\partial G_{12}}{\partial \gamma_{12}}\gamma_{12} \end{pmatrix}$$

When the increment of shear strain is small, the instantaneous fiber rotation can be equated to the change in shear strain $d\gamma_{1'2'}^n$ [Schapery 1995]. From the constitutive relation one can also write

$$\gamma_{1'2'}^n = S_{66}^n \tau_{1'2'}^n, \tag{12}$$

where $S_{66} = 1/G_{12}$. Taking differentials on both sides of Equation (12),

$$d\gamma_{1'2'}^n = S_{66}^n d\tau_{1'2'}^n + dS_{66}^n \tau_{1'2'}^n. \tag{13}$$

Equation (13) provides an expression for the change in angle $d\phi^n$. This change is added to the fiber angle value of the previous step to obtain the current fiber angle ϕ^n :

$$\phi^n = \phi^{n-1} + d\phi^n. \tag{14}$$

	Length (mm)	Width (mm)	Aspect Ratio
Mesh A	1.00	1.00	1.0
Mesh B	3.00	1.00	3.0
Mesh C	3.00	1.00	3.0

Table 1. Dimensions of the three meshes used in the present analyses.

This angle is used in the current increment, to transform the stresses and the material incremental constitutive matrix computed in the $1'-2'$ frame to the $1-2$ frame, to return to the solver in ABAQUS. In the absence of damage (or when the damage is small) the angle ϕ^n will be small. But with the accumulation of damage, ϕ^n starts to increase leading to local fiber direction instability. It should be noted that the definition of fiber rotation via Equation (13) allows the possibility of elastic rotation recovery that is instrumental in deformation localization during kink banding.

The steps outlined in this section are repeated at each loading increment until the analyses are completed.

3. Numerical simulations

We assess the capabilities of the present lamina level modeling scheme by simulating the micromechanical analyses performed earlier on unidirectional axially loaded composite lamina [Basu 2005]. This earlier study considered the composite lamina to consist of discretely layered fiber and matrix phases. Fiber elements were assigned linear elastic properties and the matrix elements were modeled as elastic-plastic materials obeying a J2 incremental flow theory of plasticity with a Mises yield criterion and isotropic hardening. Similar FE studies that were performed earlier [Kyriakides et al. 1995; Vogler and Kyriakides 1997; Lee and Waas 1999; Yerramalli and Waas 2004] considered nonuniform fiber spacing effects, 3D effects (variation in fiber packing) and in a limited manner, multiaxial loading. These studies established that a 2D representation of the composite with uniform packing sufficed to capture the important aspects of kink banding, provided that the fiber volume fraction was in excess of 50%.

For this study, the laminae are assumed to be degrading homogenized orthotropic media, with fiber volume fraction of $v_f = 50\%$. Two lamina geometries with aspect ratio $AR = 1$ (1 mm \times 1 mm dimension) and $AR = 3$ (1 mm \times 3 mm dimension) are considered (data in Table 1). These laminae are discretized

	Mesh A	Mesh B	Mesh C
Elements	1	3	3600
Nodes	8	18	11041
Degrees of Freedom	16	36	22082

Table 2. Summary of the element and nodal data for mesh A, mesh B and mesh C.

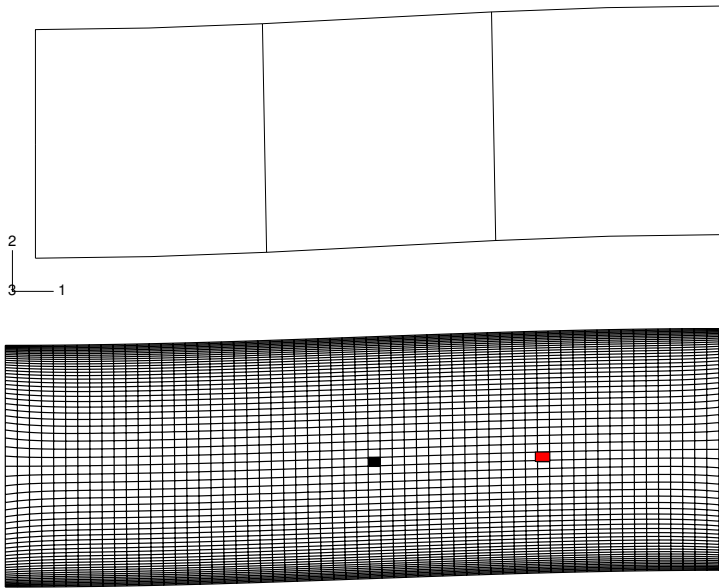


Figure 3. Finite element meshes used in the present analyses for the AR3 lamina. The element darkened at the center is element number 330 and the element shaded in red is element 316. Quantities extracted from these two elements are presented later.

using quadratic plane stress continuum elements CPS8 available in the commercial finite element software package ABAQUS. The AR1 lamina is discretized using a single CPS8 element. The AR3 lamina is meshed using two different finite element discretization schemes which are shown in Figure 3. A summary of the nodal and elemental data are presented in Table 2. In generating these meshes (AR3 mesh) a gradation of element sizes is used, with a finer discretization near the free boundaries. This was done to preclude any artificial stiffening that can be introduced due to edge effects if a uniform mesh is used in conjunction with slight misalignment of the principal material axis with respect to the loading direction. For both ARs, static analyses are performed using displacement control loading. Linear eigenvalue buckling analyses are also performed to generate perturbations in the form of the linear eigen modes to be used in subsequent response analyses. Geometric nonlinearity is included in the response analysis through the RIKS [Riks 1972] option available in ABAQUS.

Elastic material properties for the AS4/3501-6 [Soden et al. 1998] material system are described in Table 3, which are consistent with the lamina properties derived from the fiber and matrix properties described in [Basu 2005]. The nonlinear behavior in shear and in the transverse direction are provided as input, as normalized moduli variation against S_r as shown in Figure 4. A material point is denoted as ‘damaged’ when S_r at that location reaches S_r^* (or the end of the input stress-strain curve). For this analysis, this refers to a 55% degradation in the in situ secant shear modulus, G_{12} . The complete material constitutive behavior is modeled via the user material subroutine option of ABAQUS. Unit thickness in the z -direction of the lamina is assumed for the plane stress element section definition.

	AS4/3501-6 (GPa)
E_{11}	116.00
E_{22}	12.74
G_{12}	4.78
ν	0.27

Table 3. Elastic constants of the material used in the present study.

Boundary conditions for the laminae are applied at nodal positions and are similar to the micromechanical analyses performed earlier as indicated in Figure 5. The edge AB of the mesh is constrained from moving in the axial or X -direction, but allowed to ‘breath’ in the transverse or Y -direction. The center point of this edge is prevented from moving at all, eliminating any possible rigid body motion. Edge CD is used to provide the displacement control loading simulating an axial compressive load. Edges AD and BC are allowed to deform as per the equilibrium requirements of the boundary value problem, that is, on these edges $\sigma_{yy} = 0$ and $\tau_{xy} = 0$.

Geometric and material perturbations are both used in the present analyses. Geometric perturbation is provided using the lowest linear eigenvalue buckling mode such that the perturbed centerline of the mesh creates an angle of 2° with the horizontal at the center of the mesh. In addition, a 2° initial

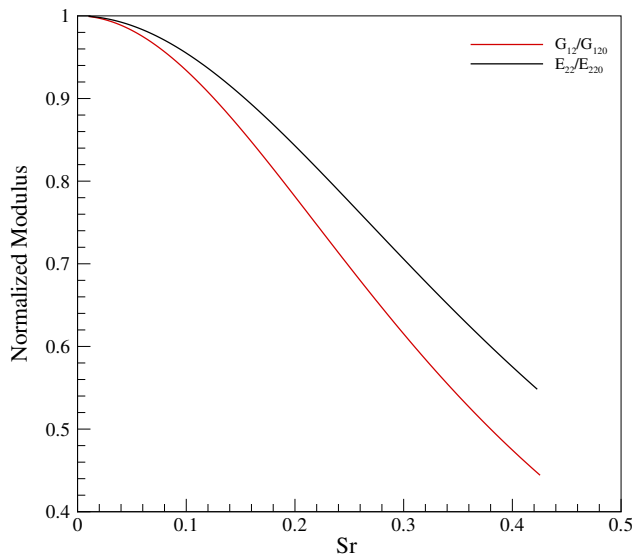


Figure 4. Normalized moduli plotted against the damage parameter S_r .



Figure 5. Boundary conditions and loading used in the present analyses.

fiber angle value (Equation (14)) is used as an initial misalignment. These imperfection magnitudes are similar to the ones used in Basu [2005] and are commonly observed as typical misalignment angles for pre-preg based laminates [Budiansky and Fleck 1993].

4. Results and discussion

Results from the FE study outlined in the previous section are presented here. For each mesh, the load-end shortening data are normalized as described in Equation (15):

$$\sigma = \frac{P}{A}, \quad \epsilon = \frac{\Delta}{L}. \tag{15}$$

Here, A and L denote the initial cross-sectional area and the initial axial length respectively. Deformed shapes of the finite element mesh at various load levels are presented. Contour plots showing the evolution of the instantaneous fiber rotation angle ϕ and deformation magnitude are also presented.

4.1. AR1 lamina results. The normalized load-end shortening response ($\bar{\sigma}$ - $\bar{\epsilon}$) for the AR1 lamina is shown in Figure 6 with the corresponding result from the micromechanical study [Basu 2005] presented for comparison. The macrolevel response for this aspect ratio matches quite well with the micromechanical prediction. As the mesh A has only 16 degrees of freedom compared to the nearly 128,000 for the micromechanical analysis, it behaves more stiffly than the micromechanical analysis mesh. This is observable in the slight deviation near the peak of the $\bar{\sigma}$ - $\bar{\epsilon}$ response of mesh A. On the other hand, such a low resolution of the current mesh does not allow it to capture the gradients of stresses, strains or the deformation field accurately. This actually magnifies the effect of the material imperfection used in the present analysis and we obtain a lower peak load for the AR1 lamina compared to the corresponding micromechanical analysis. The post-peak response from the micromechanical analysis shows a ‘snapback’ where the stress and the strain both decrease. Subsequently, the response shows a softening behavior where the stress continues to drop with increasing strain. The current analysis follows the peak load with a steep snapback and the stress reaches nearly zero before a softening regime appears in the global response. As mentioned before, the present approach degrades both E_{22} and G_{12} , when $S_r > S_r^*$. This occurs after the global response passes through a peak. As the moduli are degraded, the stresses carried by the system degrade as well. Thus the residual strength and the residual stiffness of the system are both reduced. In the micromechanical analysis, the stresses computed for the matrix elements

remain constant (as the material is modeled as an isotropic hardening material followed by a perfectly plastic regime) which implies a reduction in the effective stiffness. For a lamina, the transverse direction response and the shear response are matrix dominated. Hence the micromechanical analysis produces constant stresses for an equivalent lamina, rather than a degradation in the load carried by it. Thus a softening branch with significant load carrying capacity is observed for the micromechanical analysis which is an artifact of the assumed material model rather than an experimentally observed one. In an experiment, the lamina fails at the peak point rather catastrophically, and the load drops in a near vertical fashion [Oguni et al. 2000].

A sensitivity study is performed to ascertain the effect of the E_{11} degradation beyond $S_r > S_r^*$ on the global response. Figure 7 presents the data from this study and shows the dependence of the post-peak equilibrium path on the rate of degradation of E_{11} . When E_{11} is not degraded, the unstable post-peak equilibrium follows a path nearly parallel to the initial loading path. On the other hand, when E_{11} is degraded by 10% per load increment, the snapback vanishes and the post-peak response assumes a softening behavior. This indicates that there is a rate of E_{11} degradation at which the post-peak response transitions from a snapback to a softening behavior. For this study this rate is nearly 8.5% per load increment and the global response closely resembles observations from laboratory tests [Lee and Waas 1999; Oguni et al. 2000; Yerramalli 2003]. It should be kept in mind that the rate at which the E_{11} degrades is a numerical consideration (to produce a stable algorithm) and does not affect the overall load or the overall behavior. The rates of E_{22} and G_{12} degradations, beyond S_r^* , are fixed at 10% per increment during this study.

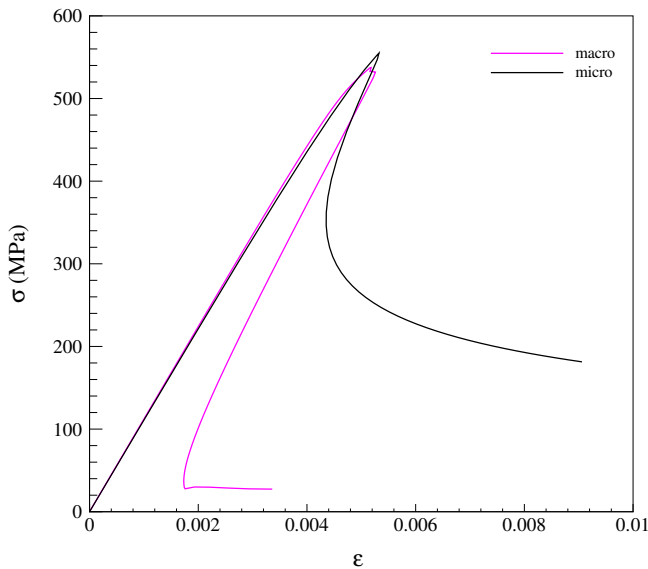


Figure 6. Normalized stress-strain response for AR1 lamina.

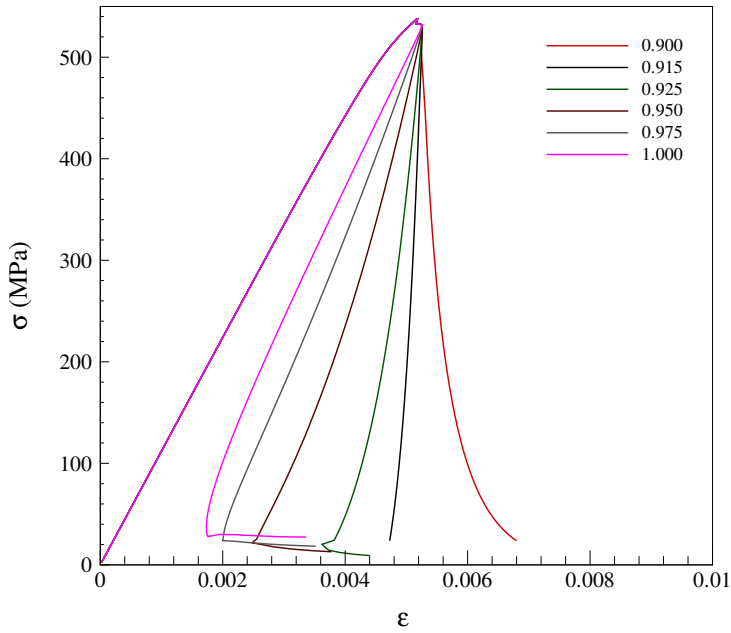


Figure 7. Normalized axial stress-strain response as a function of axial stiffness degradation.

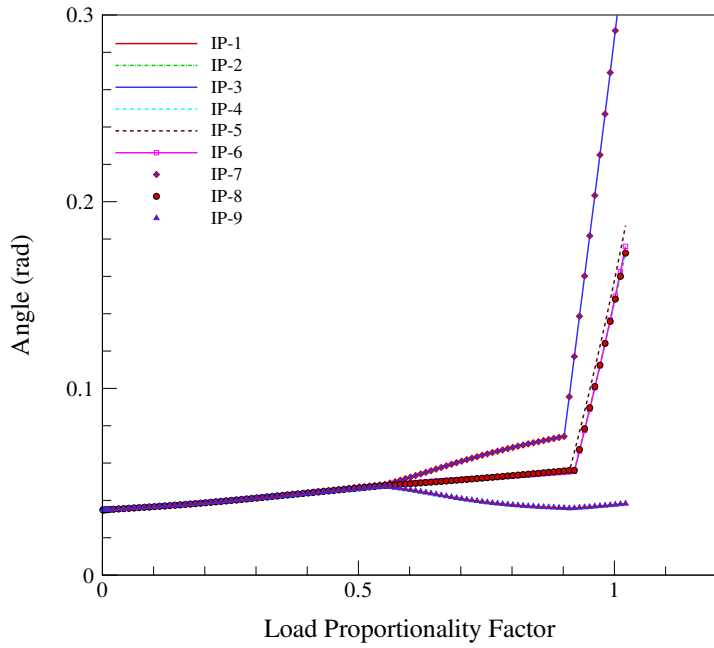


Figure 8. Evolution of instantaneous fiber angle for AR1 lamina.

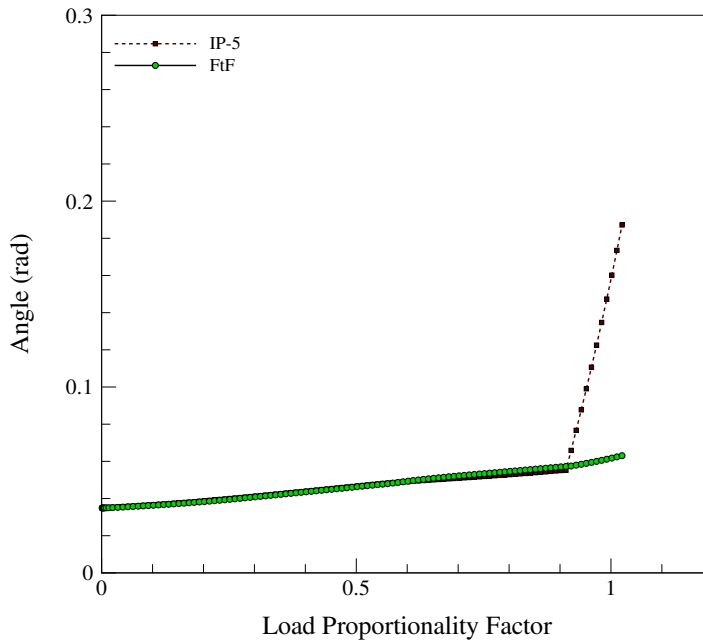


Figure 9. Comparison of instantaneous fiber angle for AR1 geometry computed using two different methods.

Analysis output such as the in situ fiber rotation are also reported for a general E_{11} degradation (5% degradation per load increment) to illustrate the similarities between the present macro-level modeling and the micromechanical analysis. It is understood that this discussion uses the values of different variables sampled at the Gauss points of the CPS8 element in ABAQUS. In situ fiber rotation, ϕ , is plotted in Figure 8. In the prepeak stage, the complete geometry undergoes uniform straining as is evident from the near uniform rotation angle at all locations. Near the peak, the strain distribution becomes nonuniform. While some locations begin to strain faster, some begin to rotate slower than the rest. This phenomenon is similar to the strain redistribution observed during the micromechanical analysis and allows the deformation field to localize and eventually form a kink band. It shall also be noted that, when E_{11} begins to drop in the $S_r > S_r^*$ region, the in situ fiber rotation accelerates, leading to a very large rotation within a small change in loading, precipitating a catastrophic failure event. The results, plotted in Figure 9, show the instantaneous fiber orientation ($1'$ -direction) computed using Equation (11) and Equation (14). It can be seen that these two different approaches are nearly identical, which validates the approximations made during derivation of the fiber rotation angle.

4.2. AR3 lamina results. The normalized load-end shortening response ($\bar{\sigma}-\bar{\epsilon}$) of the AR3 lamina are presented in Figure 10. Both mesh B and mesh C capture the overall global behavior though they use widely different finite element discretization. It can be seen that the macro-level responses are stiffer than the micromechanical response, which is because both these meshes have significantly fewer degrees of freedom compared to the micromechanical mesh (less than 10%). Mesh B has the lowest possible

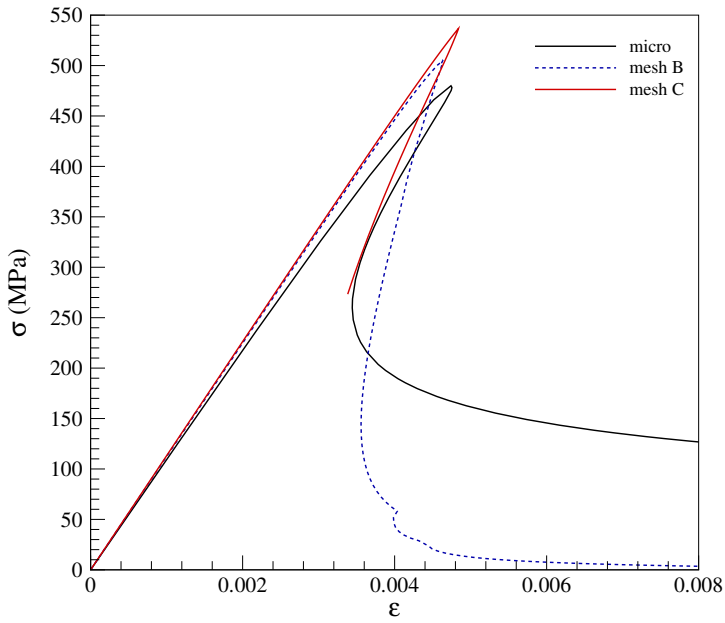


Figure 10. $\bar{\sigma} - \bar{\epsilon}$ response for AR3 lamina.

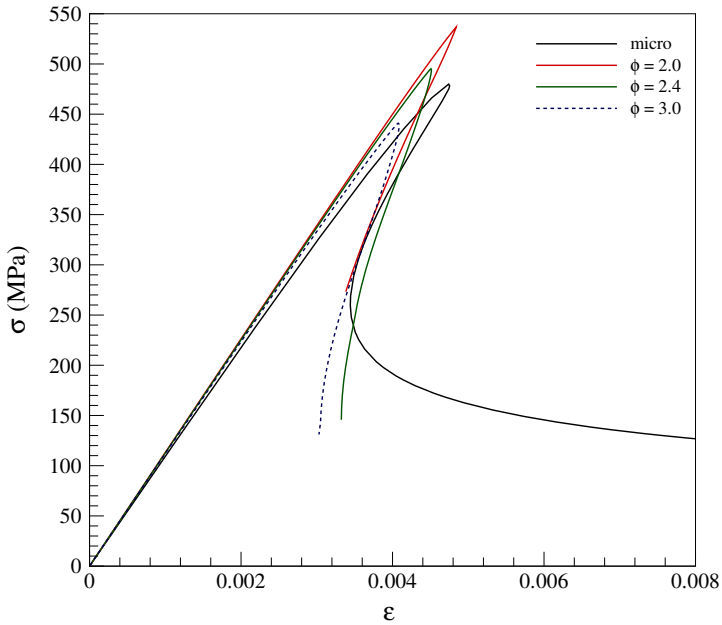


Figure 11. Variation of mesh C response with initial imperfection.

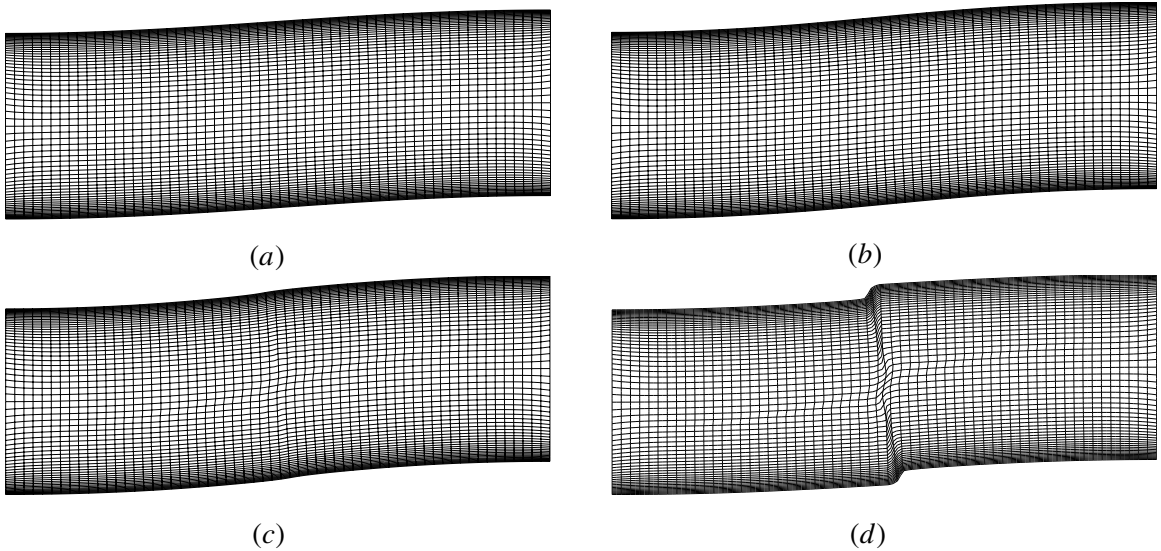


Figure 12. Plots of deformed shape for mesh C at different load levels: (a) 411 MPa, (b) 495 MPa, (c) 420 MPa, (d) 146 MPa.

resolution for this lamina and hence behaves similarly to mesh A. For mesh C, the material imperfection is provided by normalizing the shear strain distribution. Thus an imperfection magnitude of 2° is effectively lower than a uniform 2° imperfection, which appears for mesh B. This is apparent from the peak load predictions of mesh B and mesh C. When the imperfection magnitude of mesh C is increased (effectively bringing the imperfection magnitude closer to the imperfection magnitude of the micromechanical mesh) the peak load matches more closely with the micromechanical prediction as shown in Figure 11.

Plots showing the deformation shapes at various load levels are shown in Figure 12. From these plots it can be observed that a band of elements (four element length wide) at the center of the lamina undergoes severe deformation during the global compression. Using this band as the kink band, the ratio of the kinked and unkinked volumes for this homogenized (or smeared) system is 7% percent compared to the corresponding ratio of 8% percent obtained from the micromechanical analysis.

Colored contour plots showing the distribution of local fiber rotation magnitudes are presented in Figure 14. In the pre-peak region, the complete geometry deforms. As the loading progresses, the fibers rotate locally based on the initial imperfection present in the system. This allows some areas to rotate faster than the rest of the lamina. Locations where fiber rotation is lower store significant amounts of elastic energy. Beyond the peak load, this energy is released and redistributed in the lamina. This results in further rotation of the higher rotation locations leading to a deformation localization which is manifested as a kinked band of fibers. The in situ fiber rotation ϕ is plotted for two different locations on mesh C in Figure 13. This plot reveals that beyond the peak-load, some portion of the lamina continues straining monotonically whereas some portions release the elastic straining they have undergone. This shows that the elastic strain redistribution which is connected to the stored elastic

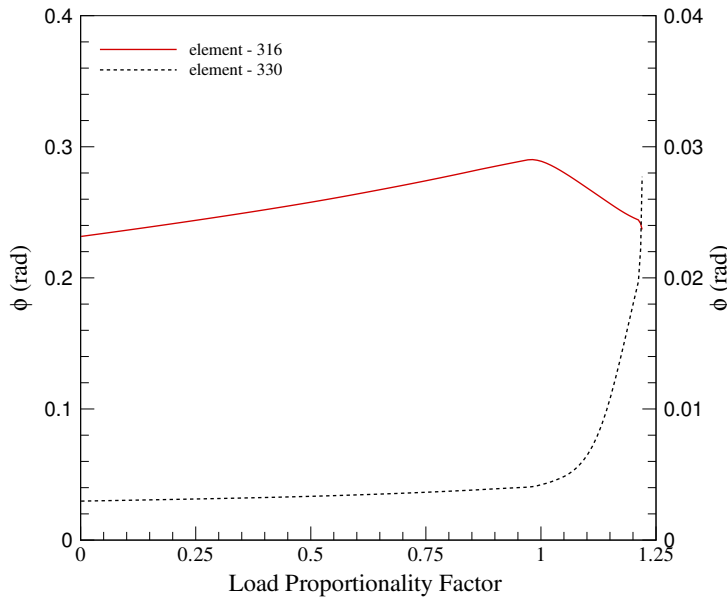


Figure 13. Plot of in situ fiber rotations from two different locations from the mesh C analysis. Element 316 result is plotted on the right-hand side vertical axis. Element 330 result is plotted on the left-hand side vertical axis.

energy causes deformation localization ultimately leading to kink banding. The mechanism of kink banding observed from this macro-level smeared approach is similar to the mechanisms observed in the micromechanical analyses, which validates the analysis approach used here. Thus, it appears that the smeared system, designed to capture the salient features associated with the kink band formation, performs as intended.

Contours of the damage variable S_r are also plotted in Figure 15 for mesh C, which shows the damage accumulation and localization during loading. The areas shaded in gray represent the most damaged regions. It is clear that these contour plots visually capture the region in which deformation is localized. It should be also noted that when the damaged region stretches across the specimen, the load carrying path between the end supports is broken, rendering the specimen unable to carry any more load. In Figure 11, the termination points of the individual responses correspond to this phenomenon.

5. Concluding remarks

In this paper, a mechanism based lamina level modeling approach is developed to study fiber kinking and validated against rigorous micromechanical analyses of unidirectional laminae. This modeling approach uses the complete nonlinear stress-strain relations for the lamina in shear and in transverse tension/compression as input, along with readily available lamina level elastic properties. Using only these (a minimum number) as inputs, compressive failure due to fiber kinking is modeled for unidirectional laminae of varying geometry and varying levels of finite element discretization. The present modeling approach is able to capture the pertinent features of the micromechanical analysis namely, the peak load,

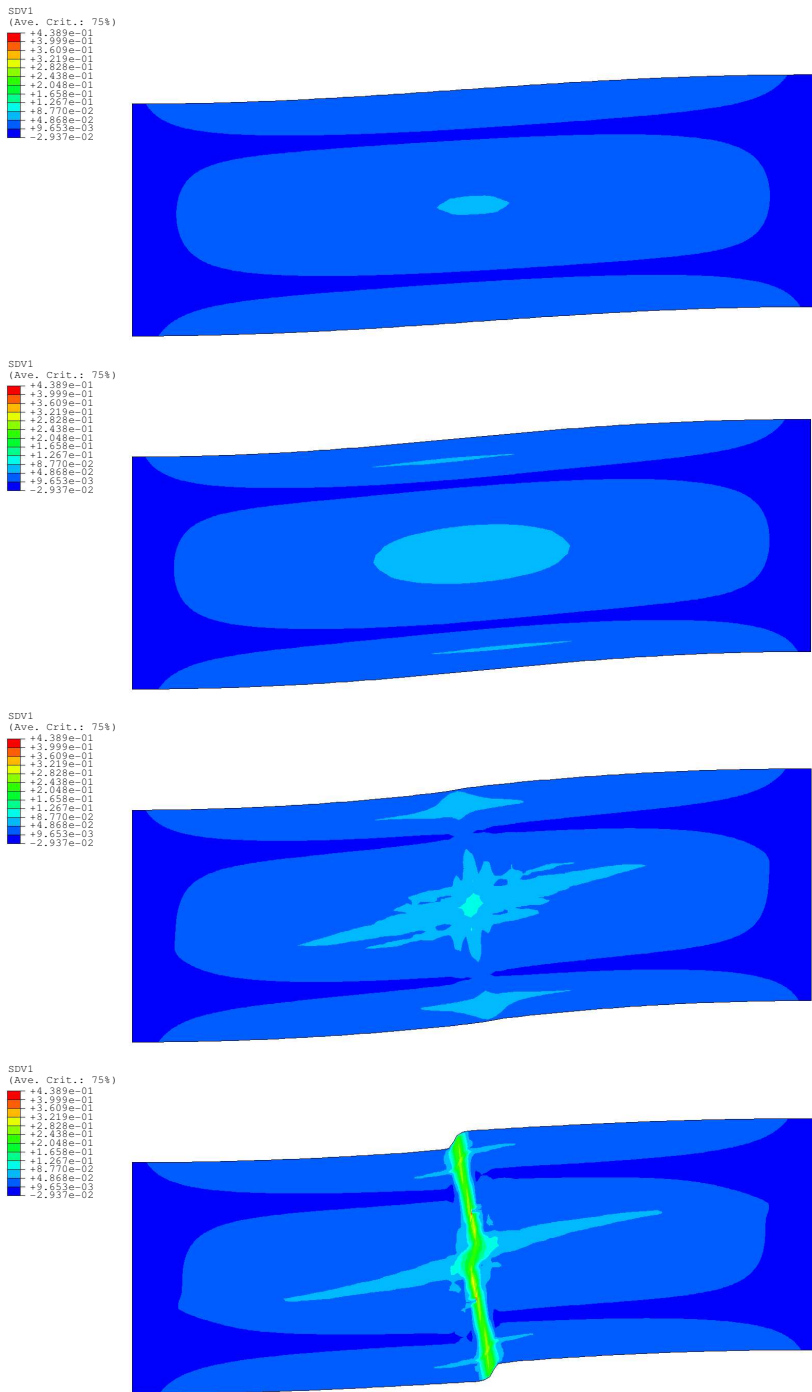


Figure 14. Contour plots showing the in situ fiber angle ϕ at various load levels for mesh C (from top to bottom): 411 MPa, 495 MPa, 420 MPa, 146 MPa.

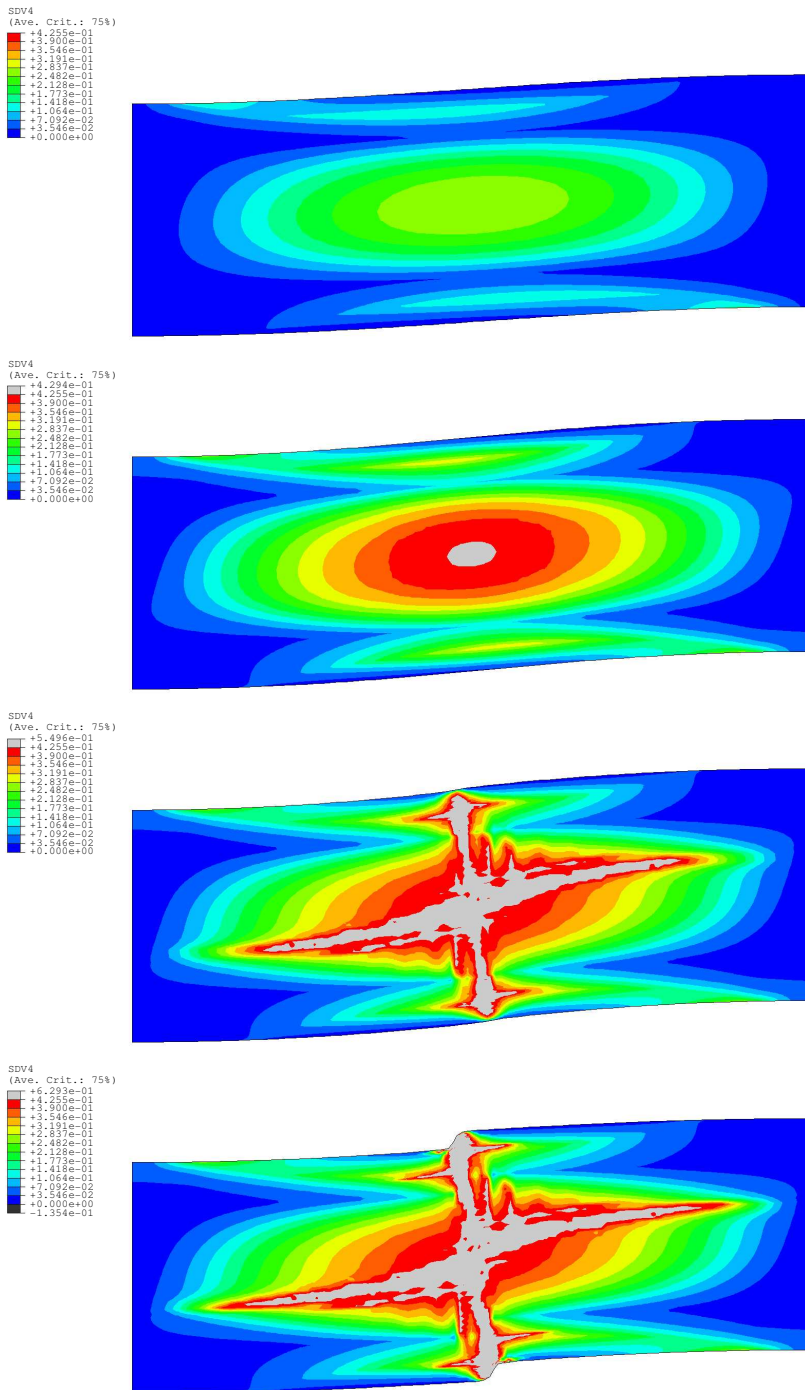


Figure 15. Contour plots showing the damage accumulation from mesh C analysis (from top to bottom): 411 MPa, 495 MPa, 420 MPa, 146 MPa.

the deformation localization and kink band width. Quantitatively the predictions of the present approach matches with the micromechanical analyses very well. The present approach has shown a drastic reduction in the computational costs in capturing a highly nonlinear and complex deformation localization phenomenon. The success of this approach is encouraging and points the way for extending this modeling approach to more complex structural configurations, with increased computational efficiency.

References

- [ABAQUS 2003] *ABAQUS user's manual*, Version 6.3-1, Hibbit and Karlsson and Sorensen Inc., Pawtucket, RI, 2003.
- [Basu 2005] S. Basu, *Computational modeling of progressive failure and damage in composite laminates*, Ph.D. thesis, Aerospace Engineering Department, University of Michigan, Ann Arbor, 2005.
- [Basu et al. 2006a] S. Basu, A. M. Waas, and D. R. Ambur, "Compressive failure of fiber composites under multiaxial loading", *J. Mech. Phys. Solids* **54**:3 (March 2006), 611–634.
- [Basu et al. 2006b] S. Basu, A. M. Waas, and D. R. Ambur, "Prediction of progressive failure in multidirectional composite laminated panels", *Int. J. Solids Struct.* (2006). Available online 18 August 2006.
- [Budiansky and Fleck 1993] B. Budiansky and N. A. Fleck, "Compressive failure of fibre composites", *J. Mech. Phys. Solids* **41**:1 (1993), 183–211.
- [Chang and Lessard 1991] F.-K. Chang and L. B. Lessard, "Damage tolerance of laminated composites containing an open hole and subjected to compressive loadings: part I—analysis", *J. Compos. Mater.* **25** (January 1991), 2–43.
- [Dávila et al. 2000] C. G. Dávila, D. R. Ambur, and D. M. McGowan, "Analytical prediction of damage growth in notched composite panels loaded in compression", *J. Aircr.* **37**:5 (2000), 898–905.
- [Evans and Adler 1978] A. G. Evans and W. F. Adler, "Kinking as a mode of structural degradation in carbon fiber composites", *Acta Metall.* **26** (1978), 725–738.
- [Fu and Zhang 2006] Y. B. Fu and Y. T. Zhang, "Continuum-mechanical modelling of kink-band formation in fibre-reinforced composites", *Int. J. Solids Struct.* **43**:11–12 (2006), 3306–3323.
- [Fung and Tong 2001] Y. C. Fung and P. Tong, *Classical and computational solid mechanics*, World Scientific, Singapore, 2001.
- [Goyal et al. 2002] V. K. Goyal, N. Jaunky, E. R. Johnson, and D. Ambur, "Intralaminar and interlaminar progressive failure analysis of composite panels with circular cutouts", pp. 1–12 in *43rd SDM Conference (AIAA 2002-1745)* (Denver, 2002), AIAA, 2002.
- [Hashin 1980] Z. Hashin, "Failure criteria for unidirectional fiber composites", *J. Appl. Mech. (Trans. ASME)* **47** (June 1980), 329–334.
- [Kyriakides et al. 1995] S. Kyriakides, R. Arseculeratne, E. J. Perry, and K. M. Liechti, "On the compressive failure of fiber reinforced composites", *Int. J. Solids Struct.* **32**:6/7 (1995), 689–738.
- [Lee and Waas 1999] S. H. Lee and A. M. Waas, "Compressive response and failure of fiber reinforced unidirectional composites", *Int. J. Fract.* **100**:3 (1999), 275–306.
- [Merodio and Pence 2001] J. Merodio and T. J. Pence, "Kink surfaces in a directionally reinforced neo-Hookean material under plane deformation, II: Kink band stability and maximally dissipative band broadening", *J. Elasticity* **62**:2 (2001), 145–170.
- [Oguni et al. 2000] K. Oguni, C. Y. Tan, and G. Ravichandran, "Failure mode transition in unidirectional E-glass/vinylester composites under multiaxial compression", *J. Compos. Mater.* **34**:24 (2000), 2081–2097.
- [Riks 1972] E. Riks, "The application of Newton's method to the problem of elastic stability", *J. Appl. Mech. (Trans. ASME)* **39**:4 (1972), 1060–1065.
- [Schapery 1989] R. A. Schapery, "Mechanical characterization and analysis of inelastic composite laminates with growing damage", *Mech. Compos. Mater. Struct.* **AMD-100** (1989), 1–9.
- [Schapery 1990] R. A. Schapery, "A theory of mechanical behavior of elastic media with growing damage and other changes in structure", *J. Mech. Phys. Solids* **38**:2 (1990), 215–253.

- [Schapery 1995] R. A. Schapery, "Prediction of compressive strength and kink bands in composites using a work potential", *Int. J. Solids Struct.* **32**:6/7 (1995), 739–765.
- [Schapery 2002] R. A. Schapery, Private communication, 2002.
- [Schapery and Sicking 1995] R. A. Schapery and D. L. Sicking, "On nonlinear constitutive equations for elastic and viscoelastic composites with growing damage", pp. 45–76 in *Proceedings of the Seventh International Conference on Mechanical Behavior of Materials*, Society of Materials Science, Kyoto, 1995.
- [Soden et al. 1998] P. Soden, M. J. Hinton, and A. S. Kaddour, "Lamina properties, lay-up configurations and loading conditions for a range of fibre-reinforced composite laminates", *Compos. Sci. Technol.* **58**:7 (1998), 1011–1022.
- [Sun and Chen 1989] C. T. Sun and J. L. Chen, "A simple flow rule for characterizing nonlinear behavior of fiber composites", *J. Compos. Mater.* **23**:10 (October 1989), 1009–1020.
- [Vogler and Kyriakides 1997] T. J. Vogler and S. Kyriakides, "Initiation and axial propagation of kink bands in fiber composites", *Acta Mater.* **45**:6 (1997), 2443–2454.
- [Vogler and Kyriakides 1999] T. J. Vogler and S. Kyriakides, "On the axial propagation of kink bands in fiber composites: part I experiments", *Int. J. Solids Struct.* **36**:4 (1999), 557–574.
- [Yerramalli 2003] C. Yerramalli, *A mechanism based Modeling approach to failure in fiber reinforced composites*, Ph.D. thesis, Aerospace Engineering Department, University of Michigan, Ann Arbor, 2003.
- [Yerramalli and Waas 2004] C. S. Yerramalli and A. M. Waas, "The effect of fiber diameter on the compressive strength of composites; A 3D finite element based study", *Comput. Model. Eng. Sci.* **6**:1 (2004), 1–16.

Received 8 Dec 2005.

SHILADITYA BASU: basus@umich.edu

Technical Professional–Marine, Granherne Inc., 601 Jefferson Ave., Houston, TX 77054, United States

ANTHONY M. WAAS: dcw@umich.edu

Composite Structures Laboratory, Aerospace Engineering Department, University of Michigan, 1320 Beal Avenue, Ann Arbor, MI 48109, United States

DAMODAR R. AMBUR: damodar.r.ambur@nasa.gov

Structures Division, NASA Glenn Research Center, Cleveland, OH 44135, United States

STUDY OF VISCOELASTIC AND FRICTION DAMPER CONFIGURATIONS IN THE SEISMIC MITIGATION OF MEDIUM-RISE STRUCTURES

JULIUS MARKO, DAVID THAMBIRATNAM AND NIMAL PERERA

This paper presents a comprehensive study of the seismic mitigation of medium rise frame-shear wall structures using embedded dampers. Two building structures with embedded viscoelastic and friction dampers in different configurations and placed in various locations throughout the structure are subjected to five different earthquake loadings. Finite element techniques are used to model the dampers and the structures and to obtain the dynamic responses. Influence of damper type and properties, configuration, and location are investigated using time history responses. Results for tip deflection and acceleration are evaluated for a number of cases and demonstrate the feasibility of the technique for seismic mitigation of these structures for a range of excitations, even when the dominant seismic frequencies match the natural frequency of the structure. Results also provide information which can be used for optimal damper placement for seismic mitigation.

1. Introduction

Under earthquake activity buildings have known to suffer extensive damage and even total collapse. In order to achieve satisfactory earthquake response of a structure, three methods can be identified as being practical and efficient: *structural isolation*, energy absorption at *plastic hinges*, and use of *mechanical devices* to provide structural control.

In recent times, there has been interest in the use of mechanical energy absorbing devices located within a structure. These mechanical energy absorbers have been found to be quite promising and they form the focus of the present study. These devices absorb energy from an earthquake, reducing harmful effects on the critical components of the structure. After the earthquake, these absorbers, which do not themselves support the normal loads of the structure, can be replaced leaving the building undamaged.

There are two types of structural control provided by the addition of mechanical devices: *active* and *passive* control. Active control requires a power supply to activate the dampers and hence are undependable during seismic events where the power supply is disrupted. For this reason, dampers with active control have been tested on tall buildings subjected to wind induced loading rather than the more unpredictable cyclic loading caused by earthquakes.

On the other hand, *passive energy dissipation systems* have emerged as special devices that are incorporated within a structure to absorb a portion of the input seismic energy. As a result, the energy dissipation demand on primary structural members is often considerably reduced, along with the potential for structural damage.

The idea of utilizing separate *passive energy dissipating dampers* within a structure to absorb a large portion of the seismic energy began with the conceptual and experimental work of [Kelly et al. 1972].

Keywords: dampers, multistory buildings, seismic mitigation, finite element techniques.

Today there are various types of manufactured passive dampers available that use a variety of materials to obtain different levels of stiffness and damping. These dampers have been reviewed by [Constantinou et al. 1998], and [Sadek et al. 1996]. Some of these include viscoelastic, viscous fluid, friction, and metallic yield dampers. These dampers have different dynamic characteristics and so will affect the seismic response of structures differently.

The characteristics of *viscoelastic (VE)* and *viscous dampers* are that they dissipate energy at all levels of deformation and over a broad range of excitation frequencies. *Friction dampers*, on the other hand, dissipate energy only when the slip force is reached and exceeded. A combination of these dampers can be used within the structural system to effectively damp out the high and low frequency contents of earthquakes [Hisano et al. 2000; Shao and Miyamoto 1999]. This is commonly referred to as a *hybrid system*.

There have been several studies undertaken to develop a method which optimizes the use of energy dissipating dampers in vibration control of buildings under earthquake loads [Abdullah 1999; Aiken et al. 1990; Ashour and Hanson 1987; Constantinou and Tadjbakhsh 1983; Hahn and Sathivageeswaran 1992; Hanson 1993; Hanson et al. 1993; Madsen 2001; Natke 1993; Ray et al. 1974; Ribakov and Gluck 1999; Zhang and Soong 1992]. However the basic theories behind these methods vary widely, and in certain respects are downright contradictory. Moreover, there are numerous types of dampers available commercially as well as numerous types of high-rise buildings which could be treated under seismic loads with different properties. This could produce a wide range of results as will be discussed later in this paper. In the light of this, there is still a great necessity for further development of methods to determine the optimal use of dampers in high rise buildings.

This comprehensive study investigates the mitigation of the seismic response of 18-story and 12-story frame-shear wall structures with embedded dampers. Three damping mechanisms were used: (i) displacement-dependent friction dampers, (ii) velocity-dependent VE dampers, and (iii) hybrid system, the latter being a combination of friction and VE dampers. Six different damping systems, arising from these three damping mechanisms in different configurations, were studied. These were friction and VE diagonal dampers, friction and VE chevron brace dampers, and hybrid friction-VE dampers and VE lower toggle dampers. The damping systems were embedded in six different locations (one at a time) within cut-outs of the shear wall in the structure. Damper properties such as stiffness, damping coefficient, location, configuration, and size were varied to obtain tip deflections and accelerations from time history analyses under five different earthquake records.

The results of this study will provide information for optimizing the use of embedded dampers in seismic mitigation of medium-rise building structures.

2. Model description

2.1. Damper properties. Finite Element (FE) methods were employed to model, analyze and investigate the effects of these three types of damping devices and their configurations on the seismic response of the structures. The program selected for the numerical analysis in this study was ABAQUS/Standard Version 6.3. In conjunction with this program, MSC/PATRAN 2003 was used as the pre-processor for generating the geometry, element mesh, boundary conditions and loading conditions of the model, and as the post-processor for viewing the results of the analysis.

A direct integration dynamic analysis was selected to obtain the response of the structure under seismic loading. This analysis assembles the mass, stiffness and damping matrices and solves the equations of dynamic equilibrium at each point in time. The response of the structure is obtained for selected time steps of the input earthquake accelerogram. The dynamic procedure in ABAQUS/Standard uses implicit time integration. To study the effectiveness of the damping system in mitigating the seismic response of the buildings in this study, the maximum displacements and accelerations at the tip of the structure are obtained from the results of the analysis, and compared with those of the undamped building structure.

The first class of damping mechanisms used in this study were the *friction dampers*. The initial focus of this research was on the development of a model which would represent the real behavior of friction dampers. This was achieved by modeling the frictional contact between two tubes with one sliding inside the other.

The extended version of the classical isotropic Coulomb friction model is provided in the computer program ABAQUS (the program available to the authors) for use with all contact analyses. In the basic form of the Coulomb friction model, two contacting surfaces can carry shear stresses up to a certain magnitude across their interface before they start sliding relative to one another.

In two-dimensional contact problems, the direction of frictional slip must lie in the plane, and hence there are only two options: slip to the right or left. The contact problem is therefore in the linear range, since all the states are governed by linear equations and nonlinearity is introduced only through the inequalities that trigger changes of state.

The second class of damping mechanisms used in this study were *VE dampers*. A VE damper was modeled as a linear spring and dashpot in parallel (known as the Kelvin model) where the spring represents stiffness and the dashpot represents damping. Abbas and Kelly [1993] define the stiffness and damping coefficients as follows:

$$k_d = \frac{G' A}{t}, \quad (1)$$

$$C_d = \frac{G'' A}{f t}, \quad (2)$$

where A is the shear area of the VE material, t is the thickness of the VE material, f is the loading frequency of the VE damper, G' is the shear storage modulus, G'' is the shear loss modulus, and T is temperature in °C. The following expressions were used to obtain the moduli of the VE material as defined by [Abbas and Kelly 1993]:

$$G' = 16.0 f^{0.51} \gamma^{-0.23} e^{(72.46/T)}, \quad (3)$$

$$G'' = 18.5 f^{0.51} \gamma^{-0.20} e^{(73.89/T)}, \quad (4)$$

where γ is the shear strain. Temperature variations will have an effect on damper properties as evident from equations (3) and (4), and, hence, on the results. We have not considered temperature effects in this paper. This model approximates the true behavior of a VE damper under vibratory loading to within 10%, which was considered sufficiently accurate for the purposes of this study. In order to create a computer model, appropriate values of the frequency of loading applied to the damper, the shear strain and the temperature of the VE material have to be selected. In this investigation, the ambient temperature of the VE material was assumed to be 21° C; the shear strain, γ , was assumed to remain constant at 100%.

(It has been shown that a large decrease in the stiffness occurs in the 0–50% strain range, whereas in the 50–200% strain range the stiffness remains approximately constant.) For the loading frequency, f , the first mode of vibration of the structures was used because it was assumed that the structure vibrate predominantly in this mode.

The third class of damping mechanisms used in this study were *hybrid friction-VE damper* consisting of friction and VE damper models in series.

Different configurations consisting of diagonal, chevron brace, hybrid diagonal-chevron brace, and lower toggle configuration of each of these damping mechanisms at different location in the structure were considered to investigate their influence on seismic mitigation.

2.2. Description of structure — damper models. The structural models treated in this paper are represented by two types of frame-shear wall structures. The first set of models shows two-dimensional medium-rise 18-story structures. The shear walls of these models were constructed using shell elements of designation S4R5, having 4 nodes per element and five degrees of freedom at each node. The dimensions of the shear walls were 6 m wide and 0.4 m thick. The columns and beams were located on either side of the wall, as seen in Figure 1. The column and beams had cross-sectional dimensions of 0.75×0.75 m and 0.75×0.45 m, respectively; the beam spans were 6.0 m. The height between stories was set at 4.0 m, which made the overall height of the structures 72.0 m.

The second set of models (Figure 2) represents 12-story structures, each with a shear wall of the same parameters as in the previous models; columns and beams had cross-sectional dimensions of 0.6×0.6 m and 0.6×0.45 m respectively. The spans of the beams were 6.0 m and the height between stories was 4.0 m, which made the overall height 48.0 m.

The natural frequency of the 18-story undamped structure was 0.614 Hz and in the range 0.570–0.650 Hz when fitted with dampers, while the natural frequency of the 12-story undamped structure was 1.050 Hz and in range 0.951–1.100 Hz when fitted with dampers. These values are within the range of dominant frequencies of all the earthquakes chosen in this investigation (varying from 0.58 Hz to 1.07 Hz, as will be seen later) and hence this study treats the structural response under a range of seismic excitations including a resonant range.

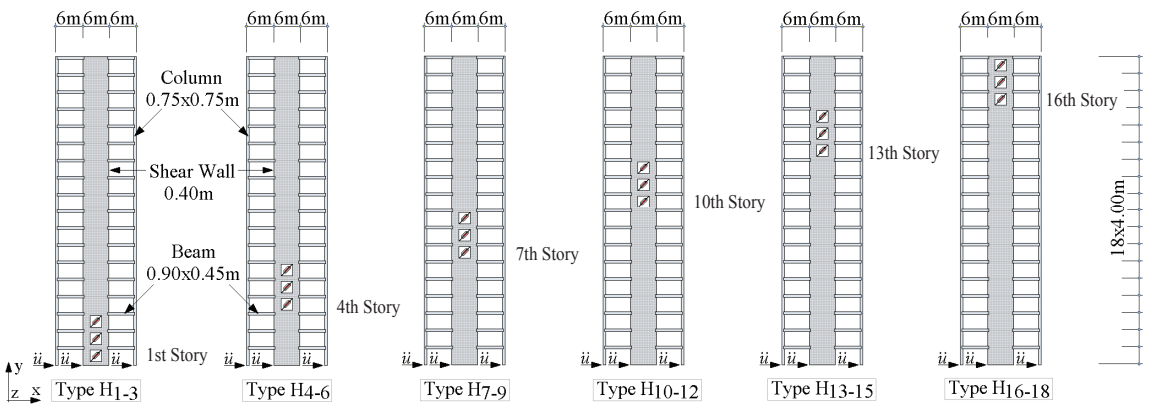


Figure 1. Placement of dampers within 18-story frame-shear wall structures.

A total of six different damping systems were considered. Seismic analyses were carried out with one type of damping system at a time. Four different configurations of the VE and friction dampers were considered- diagonal, chevron brace, lower toggle and a hybrid configuration with the friction damper oriented horizontally and the VE damper mounted diagonally. Furthermore, six different damper placements as shown in Figures 1 and 2 were used in each structural model to study the influence of location on their seismic response. The undamped structures were also analyzed in order to compare results.

Concrete material properties were chosen since many high-rise buildings are constructed by using reinforced concrete. The concrete had a compressive strength, f'_c of 32 MPa, Young's modulus, E_c of 30,000 MPa, which assumes predominantly elastic response with little wall cracking, Poisson's ratio, ν of 0.2, and density, ρ of 2500 kg/m³. No internal damping for the concrete was taken into consideration as it was assumed to be small in relation to the damping added by the devices. Structural steel was used to model friction dampers and hybrid dampers with Poisson's ratio ν of 0.3 and density, ρ of 7700 kg/m³. The coefficient of friction was 0.25 for the friction dampers.

2.2.1. Models with friction dampers — diagonal configuration. After preliminary convergence study, the concrete shear walls were modeled with 2016 S4R5 shell elements for 18-story and 1344 S4R5 shell elements for 12-story structures, respectively.

Details of the damper located within shear wall of the frame-shear wall model can be seen in Figure 3, where a 3.5 m wide by 3.5 m high wall section has been cut out and replaced by a diagonal friction damper. In creating a frictional damper, there were a few options in the computer program Abaqus, available to the authors. The best results were achieved with the particular model described below. The validity of results, however, is restricted to the nominal damper properties assumed.

The damper was modeled as a pair of diagonal tubes each with a thickness of 50 mm, and with one tube placed within the other.

- (1) The outer tube having an inner diameter of 200 mm and length 3.75 m was modeled using 264 S4R5 shell elements.
- (2) The inner tube having an outer diameter of 198 mm and length 3.75 m was modeled using 252 S4R5 shell elements.

The radial clearance between the tubes was 1 mm and the contact area in the unloaded state was 3.71 m². The connection between each tube and the shear wall was modeled using a MPC (Multipoint

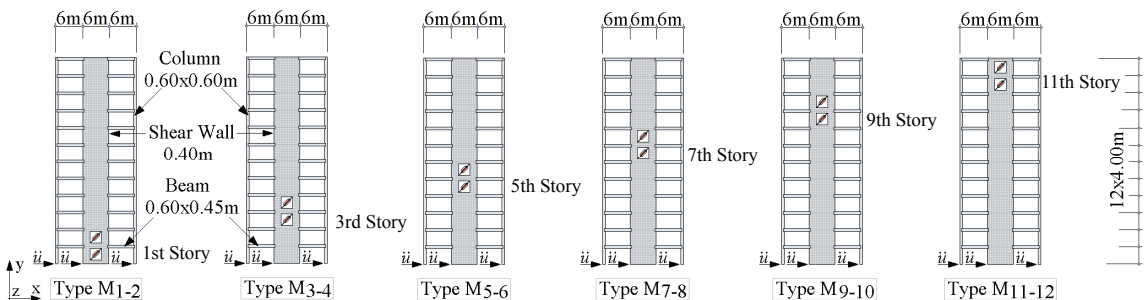


Figure 2. Placement of dampers within 12-story frame-shear wall structures.

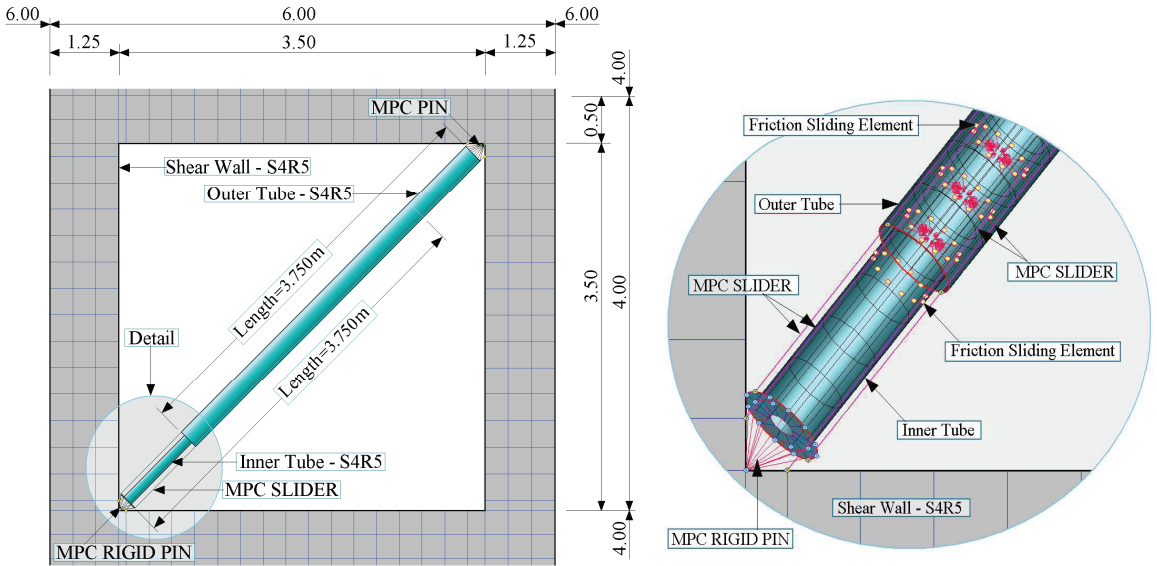


Figure 3. Details of diagonal friction damper.

Constraint) pin-type connecting element, which provides a pinned joint between two nodes. This MPC makes the displacement of the two nodes equal but allows differential rotations, if these exist, independent of each other. A MPC Slider type connecting element was chosen to ensure frictional sliding between the tubes in a determined direction. This MPC keeps a node on a straight line defined by two other nodes such that the node can move along the line, and the line can also change length. Figure 3 also shows the details of the MPC connection between the damper and shear wall in the computer model. The efficiency of these dampers as well as that of the other damping systems described below, were analyzed under the five earthquake excitations.

2.2.2. Models with VE dampers — diagonal configuration. The concrete frame-shear wall structure was modeled using the same FE mesh, material properties and dimensions as described above. Details of the diagonal VE damper located within the cut out of the shear wall can be seen in Figure 4. The properties of the damper for 18-story models were first calculated as $k_d = 10 \times 10^6$ N/m and $C_d = 63 \times 10^6$ Ns/m based on double layer damper in parallel with dimensions of 1,850 mm by 300 mm by 10 mm and the values $G' = 900,000$ Pa and $G'' = 350,000$ Pa. These moduli were calculated using the loading frequency $f = 0.614$ Hz, which corresponded to the fundamental frequency of this structure model. In a similar manner, damping properties of VE dampers located in the 12-story models (with $f = 1.05$ Hz), were calculated. The values for this structure had $k_d = 10 \times 10^6$ N/m and $C_d = 38 \times 10^6$ Ns/m with dimensions of 1,670 mm by 300 mm by 10 mm and the values $G' = 950,000$ Pa and $G'' = 450,000$ Pa. The results for both structure were evaluated and in order to facilitate comparisons, approximate average values of $k_d = 10 \times 10^6$ N/m and $C_d = 50 \times 10^6$ Ns/m, were used in all the subsequent analyses.

2.2.3. Models with hybrid friction-VE dampers. The hybrid friction-VE damper was created to represent 50% of the damping force of the diagonal VE damper, and 66.6% of the damping force of the chevron brace friction dampers. It was anticipated that results for structures fitted with a hybrid friction-VE

damper which contains the displacement-dependent friction part, and the velocity-dependent VE part, can provide more effective control of the structure response.

The concrete frame-shear wall structures were using the FE mesh, material properties and dimensions as before. The only difference was in the size of the cut out which was reduced to 3.5 m wide by 2.5 m high.

The friction component of the hybrid friction-VE damper was modeled as a pair of horizontal tubes, with one tube placed within the other.

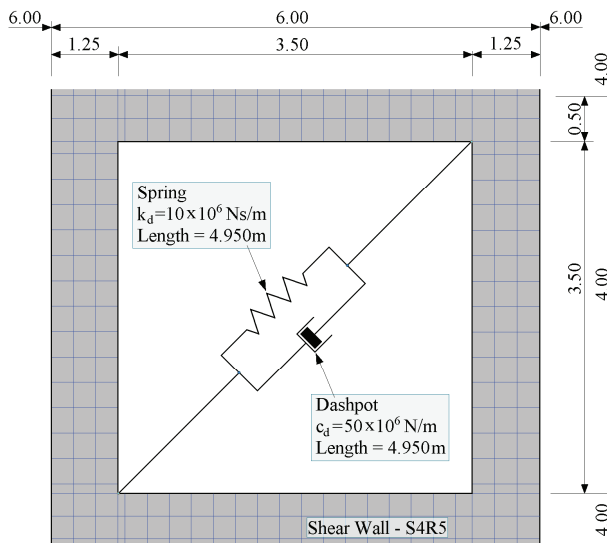


Figure 4. Details of diagonal VE damper.

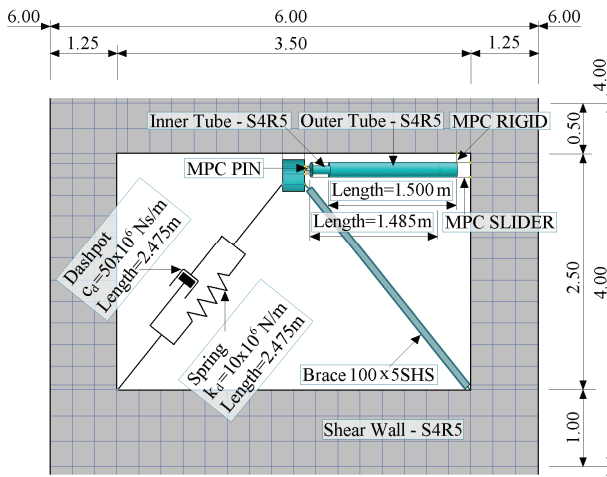


Figure 5. Details of hybrid friction-VE damper.

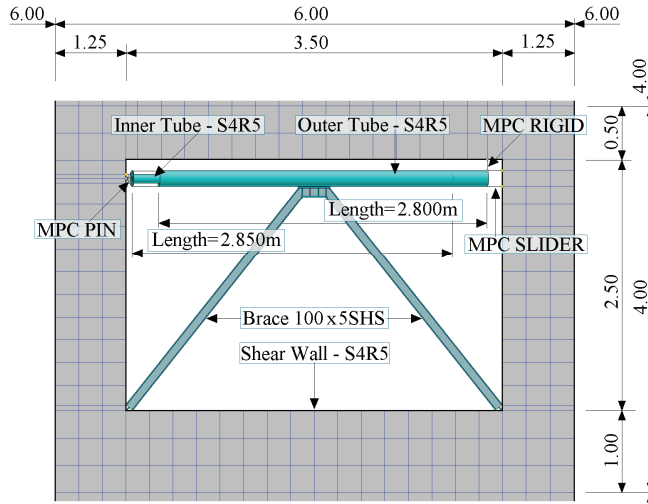


Figure 6. Details of chevron brace friction damper.

- (1) The outer tube was constructed from 384 S4R5 shell elements, the inner diameter of this tube was 200 mm and its length was 1.500 m.
- (2) The inner tube was constructed from 155 S4R5 shell elements, the outer diameter of this tube was 396 mm and its length was 1.4850 m.

The thickness of both tubes was 50 mm, the radial clearance between the tubes was 1 mm, the contact area in the unloaded state was 1.67 m^2 and the coefficient of friction between the tubes was 0.25. The direction of frictional sliding was determined by Slider and Pin type MPCs.

The VE part of the hybrid damper which represented both spring and dashpot elements was oriented with one end attached to a steel holder placed in the middle of the upper edge of the cut out, and the other end attached to the lower left-hand corner of the cut out, as shown in Figure 5. This oriented the damper at 45° to the horizontal while its length was 2.475 m. The values of damping and stiffness were kept the same as in the model with diagonal VE dampers.

The hybrid damper is expected to utilize the desirable features of both the VE and friction components. But, these dampers combining VE and friction components in series can cause a practical problem, if the 2 components are not properly isolated. As the VE material dissipates energy it heats and softens, while the frictional element does not and hence at a certain point the frictional element will not be pushed hard enough to slip.

2.2.4. Models with friction dampers — chevron brace configuration. The concrete frame-shear wall model was made using the same FE mesh, material properties and dimensions as the model incorporating hybrid dampers. Figure 6 shows the detail of frame-shear wall model with a friction damper of chevron brace configuration. The friction damper is modeled as a pair of horizontal tubes, where one tube is placed within the other.

- (1) The outer tube was constructed from 264 S4R5 shell elements, the inner diameter of this tube was 200 mm and its length was 2.565 m.

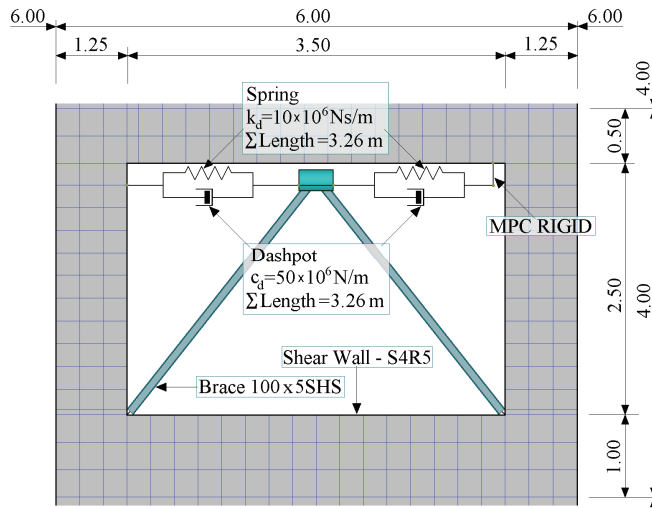


Figure 7. Details of chevron brace VE damper.

(2) The inner tube was constructed from 276 S4R5 shell elements, the outer diameter of this tube was 276 mm and its length was 2.565 m.

The thickness of both tubes was 50 mm, the radial clearance between the tubes was 1 mm, and the contact area in the unloaded state was 3.09 m². The connection between each tube and the shear wall was modeled using a MPC Pin type connecting element, and a MPC Slider type connecting element was chosen to ensure frictional sliding between the tubes in a determined direction. The details of the MPC connection between the damper and shear wall in the computer model are also shown in Figure 6.

2.2.5. Models with VE dampers — chevron brace configuration. The concrete frame-shear wall model was created as in the previous case. The damper placed within the shear wall, as shown in Figure 7, was oriented horizontally in the upper part of the cut out, attached at one end directly to the left side of the shear wall and attached at the other end to the upper edge of the shear wall via an MPC Rigid connection.

2.2.6. Models with VE dampers — lower toggle configuration. Quite recently several new configurations of passive energy dissipation devices have emerged [Constantinou and Sigaher 2000]. These configurations utilize innovative mechanisms to amplify displacement and hence lower input force demand in the energy dissipating devices. They have, however, not received attention comparable to the more traditional diagonal and chevron brace configurations, probably due to their complex nature. These new configurations include the upper, lower and reverse toggle systems. One of them, the lower toggle system was considered in this study.

The concrete frame-shear wall models were created using the FE mesh, material properties and dimensions as before. The only difference was in the size of the cut out which was enlarged to 3.5 m wide by 3.0 m high. Detail of the lower toggle VE damper located within the cut out of the frame-shear wall model can be seen in Figure 8. This damper oriented at 45° to the horizontal with its length of 2.262 m had one end attached to the lower arm of the steel holder and the other end attached to the lower right-hand corner of the cut out. In this configuration, the arms of the brace assembly were created from

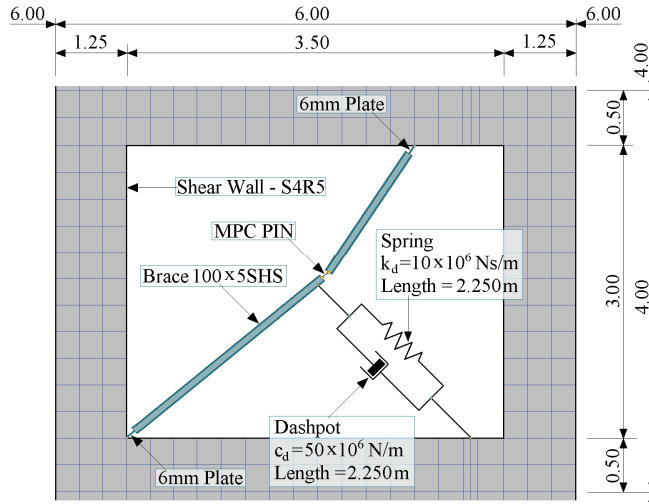


Figure 8. Details of lower toggle VE damper.

100 × 5 SHS and these arms were connected to each other by 6 mm pre-bent plate and the connection to the shear wall was by MPC Pin.

These structural models have natural frequencies which match those of typical medium rise buildings and hence the results could have wider application.

3. Earthquake records

In general, all earthquake records possess different properties such as peak acceleration, duration of strong motion and ranges of dominant frequencies and therefore have different influences on the structure. In order to ensure that the chosen mitigation procedure is effective under different types of excitations, five, well-known earthquakes records were used in this study. These were all applied for the first 20 s of their duration. For more consistent comparison, all earthquake records were scaled to a peak acceleration of 0.15 g. Duration of the strong motion and range of dominant frequencies were kept unchanged and were evaluated by Welch's method [Welch 1967], based on Fast Fourier Transform Techniques, using the computer program MATLAB Version 6.5. The earthquake records [Comerio et al. 2002] which have been selected to investigate the dynamic response of the models are:

- (1) El Centro (1940) with strong motion during 1.5–5.5 secs and dominant frequencies in the range 0.39–6.39 Hz,
- (2) Hachinohe (1994) with strong motion during 3.5–7.5 secs and dominant frequencies in the range 0.19–2.19 Hz,
- (3) Kobe (1995) with strong motion during 7.5–12.5 secs and dominant frequencies in the range 0.29–1.12 Hz,

- (4) Northridge (1994) with strong motion during 3.5–8.0 secs and dominant frequencies in the range 0.14–1.07 Hz and
- (5) San Fernando (1971) with strong motion during 4.5–9.5 secs and dominant frequencies in the range 0.58–4.39 Hz.

Graphs of these earthquake records and their dominant frequencies are for convenience presented in Figures 9–13.

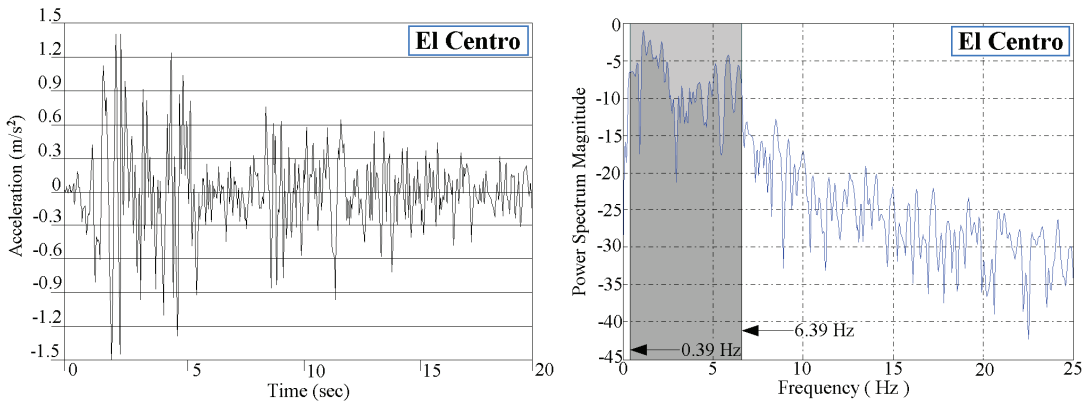


Figure 9. El Centro earthquake record and its dominant frequencies.

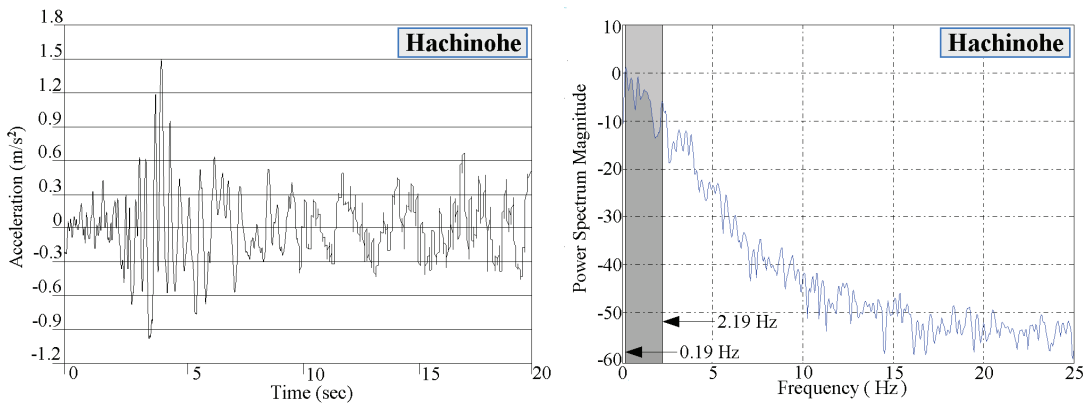


Figure 10. Hachinohe earthquake record and its dominant frequencies.

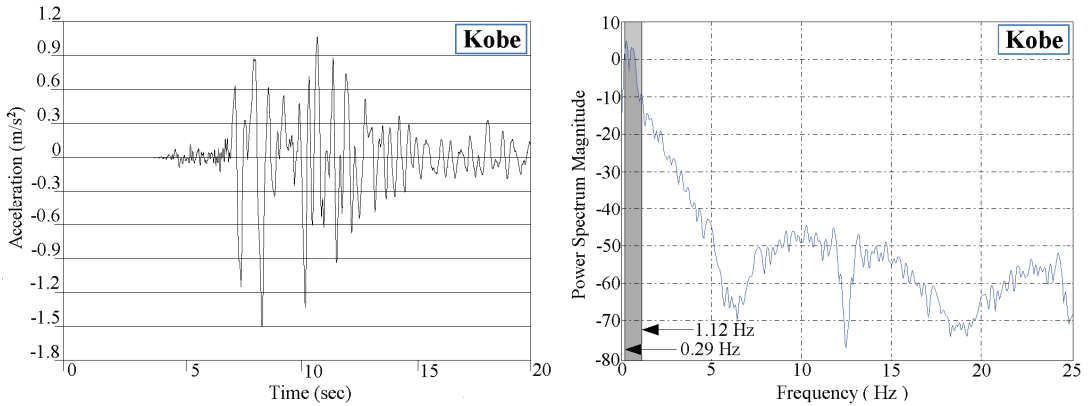


Figure 11. Kobe earthquake record and its dominant frequencies.

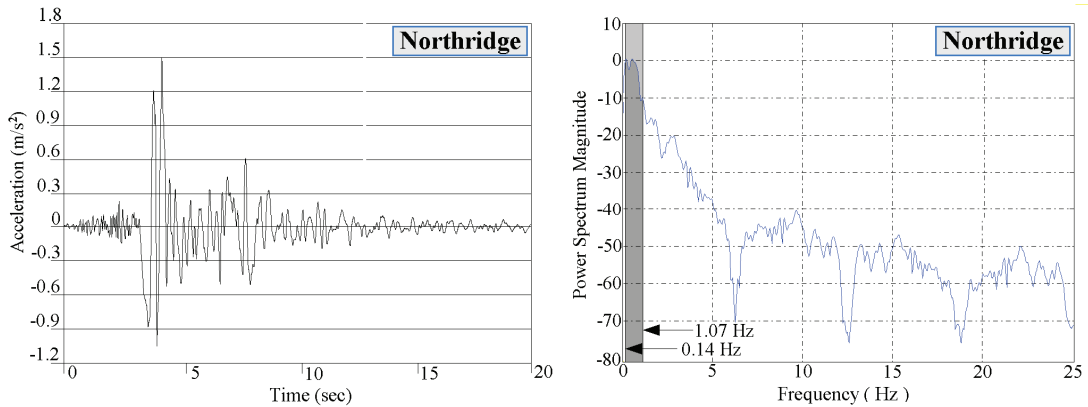


Figure 12. Northridge earthquake record and its dominant frequencies.

4. Results and discussion

4.1. 18-story models. The first type of the medium rise structure which was investigated in this paper was represented by the 18-story frame-shear wall model described in Section 2.2. The results for this structure under five earthquake excitations are presented below.

There are various ways of assessing seismic response, but computation of tip deflection is a reasonable measure of the overall effect of the earthquake. Working back from tip deflection to equivalent base shear and moment is one way of ‘averaging out’ the seismic effects of varying accelerations up the wall. Hence any reduction in tip deflection represents a worthwhile reduction in overall seismic design force. The results presented below show that this reduction is dependent on the complex characteristics of the time histories used for assessment and hence the benefits can only be legitimately assessed if the analysis is carried out for the suite of time histories.

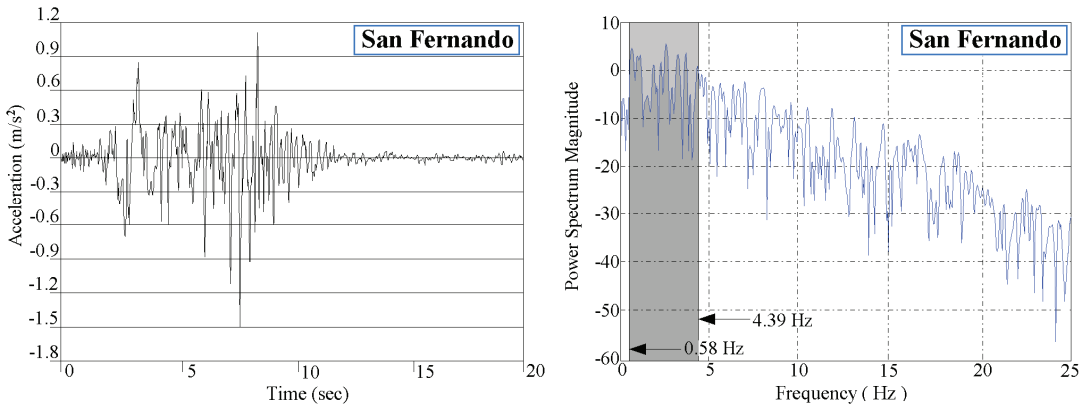


Figure 13. San Fernando earthquake record and its dominant frequencies.

Figures 14–18 illustrates the typical time history responses of the structure of designation H1-3 with the diagonal friction and VE dampers fitted in the lowest three stories. These graphs illustrate tip deflection and tip acceleration responses under five earthquake excitations compared with the responses of the undamped structure. From these graphs it is evident that the dampers embedded into the cut-outs of shear walls significantly reduced the tip deflection and acceleration throughout the duration of the earthquakes. However from these graphs, as well as from numerous other results obtained with dampers at different placements, it was also evident that the different damping properties of the friction and VE dampers resulted in different responses. The friction dampers in the vast majority of cases surpassed the VE dampers in their ability to reduce the intensity of the initial strong motion. In contrast, the advantage of the VE dampers was in gradually decreasing the tip deflection and tip acceleration of the structure.

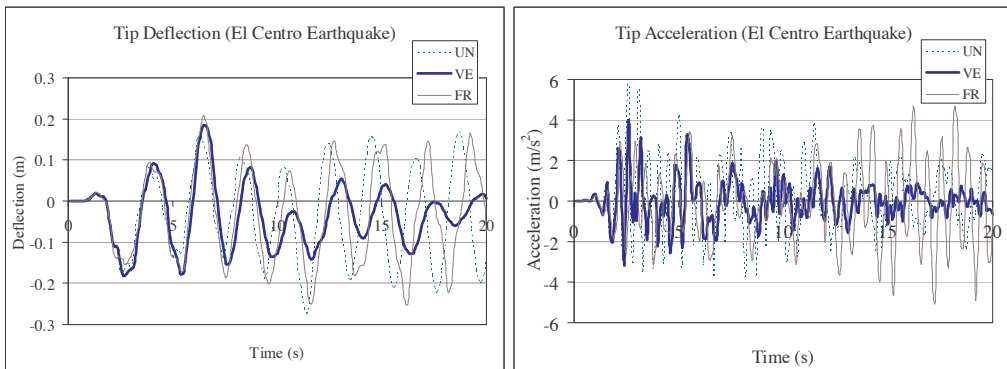


Figure 14. Tip deflection and acceleration responses of H 1-3 structure fitted with diagonal VE and friction dampers and undamped structure under the El Centro earthquake.

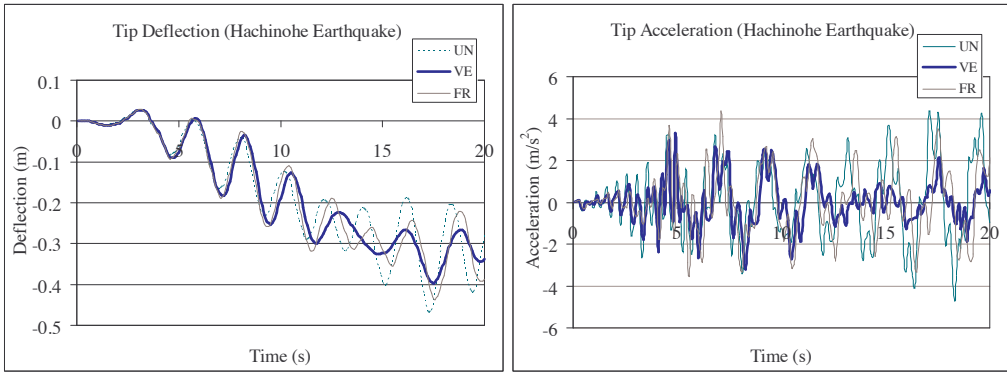


Figure 15. Tip deflection and acceleration response of H 1-3 structure fitted with diagonal VE and friction dampers and undamped structure under the Hachinohe earthquake.

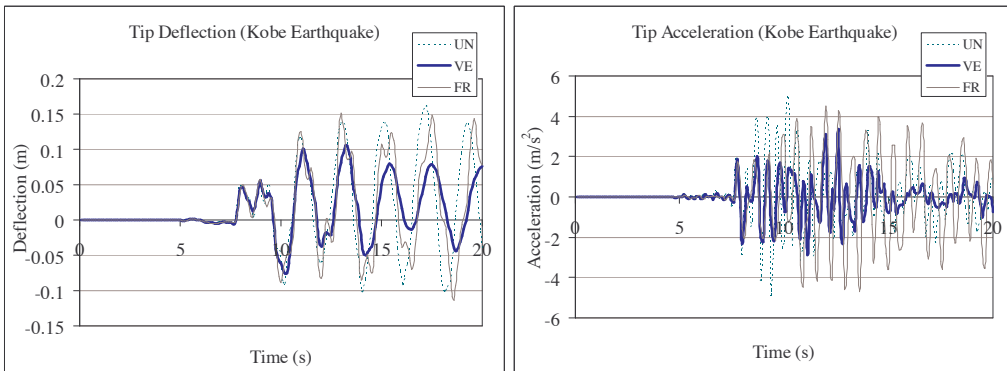


Figure 16. Tip deflection and acceleration response of H 1-3 structure fitted with diagonal VE and friction dampers and undamped structure under the Kobe earthquake.

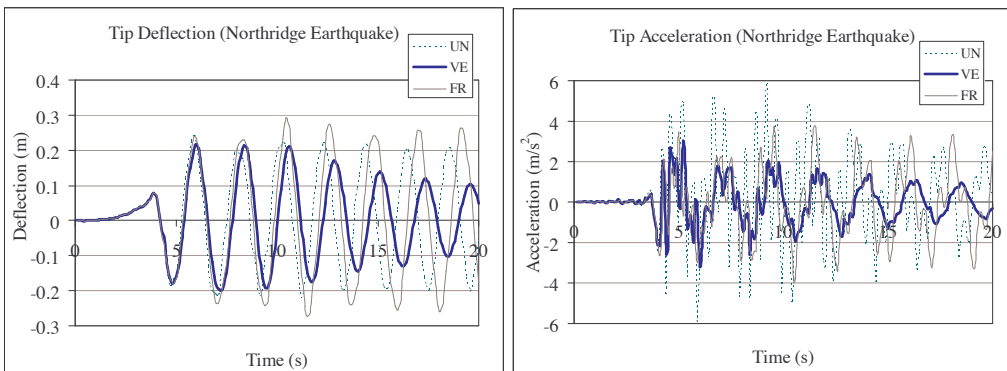


Figure 17. Tip deflection and acceleration response of H 1-3 structure fitted with diagonal VE and friction dampers and undamped structure under the Northridge earthquake.

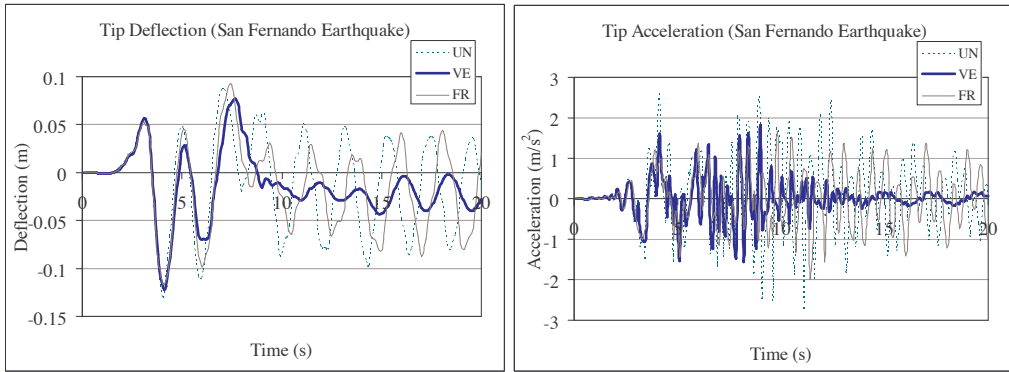


Figure 18. Tip deflection and acceleration response of H 1-3 structure fitted with diagonal VE and friction dampers and undamped structure under the San Fernando earthquake.

4.1.1. Undamped structural model. The undamped structural model was created in order to compare its results with the results of the structures fitted with the damping systems. The results of the tip deflection and tip acceleration of this structure experienced under five earthquake excitations are presented in Table 1.

	<i>El Centro</i>	<i>Hachinohe</i>	<i>Kobe</i>	<i>Northridge</i>	<i>S.Fernando</i>
Deflection(m)	0.275	0.464	0.163	0.245	0.130
Acceleration(m/s ²)	5.66	4.72	4.93	5.95	2.72

Table 1. Tip deflection and tip acceleration of the undamped 18-story structure.

4.1.2. Structural models with friction and VE dampers—diagonal configuration. Table 2 illustrates the results of the percentage reductions in the peak values of the tip deflection experienced by the structures fitted with the diagonal friction dampers. It is evident that the dampers display a wide range of efficiency, with significant reductions in most cases with an average reduction of 23.6% under the Hachinohe earthquake. In some cases, there are increases, especially under the San Fernando earthquake. This may be attributed to inadequate compensation for removed stiffness and/or partial resonance of the damped structure and insufficient push on the friction damper to make it fully operational.

In terms of damper placement, the highest average tip deflection reduction was achieved by the structure with dampers fitted in the top stories, while the lowest average reduction occurred for the structures with dampers placed in the stories 10 to 12. The results achieved under the El Centro, Hachinohe and Northridge earthquakes fully support Hanson’s theory [Hanson 1993], which recommends placement of friction dampers at levels of maximum interstory drift (Table 3). On the other hand, with the Kobe and San Fernando earthquakes, a high efficiency was displayed only with dampers fitted in the lowest stories.

Table 4 presents the percentage reduction in tip deflection of the structures incorporating the diagonal VE dampers. The overall performance of the models was significantly high; however the range of

<i>Model</i>	<i>El Centro</i>	<i>Hachinohe</i>	<i>Kobe</i>	<i>Northridge</i>	<i>S.Fernando</i>	<i>Average</i>
H 1-3	14.55	13.48	13.50	-11.02	8.40	7.78
H 4-6	13.09	19.15	-7.36	11.43	1.53	7.57
H 7-9	17.09	28.37	-6.75	16.73	-37.40	3.61
H 10-12	22.55	26.24	-6.13	6.94	-41.22	1.67
H 13-15	24.36	25.53	-4.29	16.33	-34.35	5.52
H 16-18	22.18	29.08	1.23	31.43	-22.90	12.20
Average	18.97	23.64	-1.64	11.97	-20.99	6.39
Optimal	H13/19.10	H13/21.84	H1/5.21	H1/18.44	H4/4.86	H13/ 9.10

Table 2. Percentage reductions in tip deflection of model with diagonal friction dampers.

<i>Drift</i>	<i>El Centro</i>	<i>Hachinohe</i>	<i>Kobe</i>	<i>Northridge</i>	<i>S.Fernando</i>
1 st largest	14-15	11-12	14-15	16-17	13-14
2 nd largest	15-16	10-11	15-16	15-16	14-15
3 rd largest	16-17	12-13	16-17	14-15	12-13

Table 3. Floors with largest interstory drift.

results remained wide. The average tip deflection reductions varied from 4.1% under the San Fernando earthquake, to 19.3% under the El Centro earthquake.

The best performance was achieved when the dampers were placed in the lowest stories, while moving them towards the top of the structure resulted in a gradual decrease in tip deflection under all earthquake excitations. According to a study conducted by [Ashour and Hanson 1987], the optimal placement of dampers should be one that maximizes the damping ratio of the fundamental mode, as this mode’s contribution to the structure’s overall response is always significant. Our results revealed that the best performance was achieved when dampers were placed in the lowest parts of each structure, while placing dampers towards the top of the structure decreased the damper efficiency. These results are in accordance with Ashour’s study.

Though tip deflection is more important in assessing overall seismic response, this study also investigated the reductions in the peak values of tip accelerations at the top of the structures.

<i>Model</i>	<i>El Centro</i>	<i>Hachinohe</i>	<i>Kobe</i>	<i>Northridge</i>	<i>S.Fernando</i>	<i>Average</i>
H 1-3	33.09	15.60	35.58	11.84	6.11	20.44
H 4-6	33.82	12.06	28.22	13.47	6.87	18.89
H 7-9	20.36	8.51	24.54	8.16	5.34	13.38
H 10-12	12.73	4.96	14.72	5.31	3.82	8.31
H 13-15	8.00	2.13	3.07	4.90	3.82	4.38
H 16-18	7.64	2.84	-10.43	3.67	-1.53	0.44
Average	19.27	7.68	15.95	7.89	4.07	10.97
Optimal	H1/7.64	H1/3.19	H4/9.82	H1/2.45	H7/2.29	H1/ 4.53

Table 4. Percentage reductions in tip deflection of model with diagonal VE dampers.

<i>Model</i>	<i>El Centro</i>	<i>Hachinohe</i>	<i>Kobe</i>	<i>Northridge</i>	<i>S.Fernando</i>	<i>Average</i>
H 1-3	16.25	14.38	7.30	37.27	33.70	21.78
H 4-6	18.90	-1.48	26.98	30.86	20.51	19.16
H 7-9	13.43	40.80	-4.87	7.42	-54.95	0.37
H 10-12	23.14	17.34	7.30	5.23	-35.16	3.57
H 13-15	35.16	50.53	25.15	17.54	-28.94	19.89
H 16-18	-2.30	-12.26	-25.56	-11.30	-35.53	-17.39
Average	17.43	18.22	6.05	14.50	-16.73	7.90
Optimal	H16/14.65	H10/22.26	H1/9.54	H13/2.28	H46.81	H4/ 4.07

Table 5. Percentage reductions in tip acceleration of model with diagonal friction dampers.

Table 5 shows the tip acceleration reductions of the structures fitted with the diagonal friction dampers, compared with results of the undamped structure. In terms of efficiency of these dampers under a variety of earthquake loadings, a similar trend as that of the tip deflection can be observed. The range of the results was once again very wide, varying from 16.7%, an average increase that occurred under the San Fernando earthquake, to 18.2%, an average reduction obtained under the Hachinohe earthquake.

The diagonal friction dampers achieved the highest acceleration reductions when placed in the lowest six stories and in the stories 13–15. On the other hand, when they were placed in the highest stories, a significant increase in tip acceleration was experienced. This tip acceleration increase was mainly due to the operating principle of the friction dampers, which caused transfer of acceleration to the ambient structural elements as well as decrease in stiffness of the top stories due to the cut-out in the shear wall.

The percentage reductions in the tip acceleration at the top of the structures for the structure embedded with the diagonal VE dampers are presented in Table 6. The highest average acceleration reduction of 22.4% was obtained for the Hachinohe earthquake. However, the acceleration reductions that occurred under the other earthquakes were also adequately high. The greatest tip acceleration reductions were obtained when the dampers were placed in the lowest stories. The tip acceleration reductions were still relatively high for dampers placed in the middle stories. On the other hand, when the dampers were placed in the top stories, an increase in tip acceleration was experienced.

4.1.3. Structural models with friction and VE dampers — chevron brace configuration. The percentage reductions in tip deflection experienced by structures fitted with the chevron brace friction dampers are illustrated in Table 7.

<i>Model</i>	<i>El Centro</i>	<i>Hachinohe</i>	<i>Kobe</i>	<i>Northridge</i>	<i>S.Fernando</i>	<i>Average</i>
H 1-3	30.21	31.92	33.67	46.71	40.29	36.56
H 4-6	22.44	36.58	38.74	36.42	18.32	30.50
H 7-9	8.66	31.08	10.75	18.38	3.66	14.51
H 10-12	3.18	25.16	1.22	5.56	-7.33	5.56
H 13-15	8.30	10.78	15.42	20.74	10.62	13.17
H 16-18	-5.65	-1.27	-6.29	2.53	-21.61	-6.46
Average	11.19	22.37	15.58	21.73	7.33	15.64
Optimal	H4/6.01	H1/20.72	H1/12.78	H4/18.72	H7/9.16	H4/ 11.37

Table 6. Percentage reductions in tip acceleration of model with diagonal VE dampers.

<i>Model</i>	<i>El Centro</i>	<i>Hachinohe</i>	<i>Kobe</i>	<i>Northridge</i>	<i>S.Fernando</i>	<i>Average</i>
H 1-3	4.71	-3.15	17.35	7.98	14.79	8.34
H 4-6	6.67	2.36	13.27	9.24	13.38	8.98
H 7-9	7.45	5.51	12.24	8.40	10.56	8.83
H 10-12	10.98	9.45	6.63	9.66	5.63	8.47
H 13-15	15.29	14.17	1.02	12.61	4.23	9.46
H 16-18	12.55	13.39	7.14	10.50	-0.70	8.58
Average	9.61	6.96	9.61	9.73	7.98	8.78
Optimal	H13/5.48	H16/6.73	H1/13.82	H16/4.79	H1/10.06	H13/ 5.95

Table 7. Percentage reductions in tip deflection of model with chevron braced friction dampers.

The performances of the dampers were within a very narrow range from 7.0%, under the Hachinohe earthquake, to 9.7%, under the Fernando earthquakes were mostly insufficient. The highest average acceleration reduction was achieved by the dampers placed in stories 4–6. The acceleration reductions of the dampers fitted in the other stories were considerably lower and also rather inconsistent.

Table 8 shows the reduction in tip acceleration for the chevron brace VE dampers. The highest average reduction of 10.9% was obtained under the El Centro earthquake. The results from the other excitations were obviously less significant. The highest acceleration reduction was achieved when dampers were placed in the lowest stories, with a decrease in their efficiency as they were moved toward the top of the structures.

Both types of chevron brace dampers were created to represent only 66.6% of the damping force of the diagonal dampers. Despite this fact, the overall reductions in tip deflection were equally high compared to those of the diagonal dampers. The reductions in tip displacement for both types of the chevron brace dampers revealed unexpectedly low sensitivity to the placement and, also, noticeably higher reliability than the diagonal dampers. On the other hand, while comparing the acceleration reductions, the chevron brace dampers were less effective and also less reliable than the diagonal dampers.

4.1.4. Structural models with hybrid friction-VE dampers. Table 9 illustrates the percentage reductions in the peak values of the tip deflection experienced by the structures fitted with the hybrid friction-VE dampers compared with results of the undamped structures. The dampers achieved satisfactory average reductions under the Kobe, Northridge and San Fernando earthquakes, whereas the reductions experienced under the El Centro and Hachinohe earthquakes were only moderate. In the case of the El

<i>Model</i>	<i>El Centro</i>	<i>Hachinohe</i>	<i>Kobe</i>	<i>Northridge</i>	<i>S.Fernando</i>	<i>Average</i>
H 1-3	9.33	9.44	18.79	-7.08	10.76	8.25
H 4-6	18.49	1.85	1.43	5.96	7.56	7.06
H 7-9	11.95	-0.74	-2.39	5.40	0.29	2.90
H 10-12	15.88	3.15	-1.59	-0.37	-8.14	1.78
H 13-15	13.42	-0.74	-1.91	2.98	-9.30	0.89
H 16-18	-3.44	7.78	1.27	-4.66	1.16	0.42
Average	10.94	3.46	2.60	0.37	0.39	3.55
Optimal	H4/10.82	H16/5.77	H16/3.89	H4/11.58	H4/11.97	H4/ 6.02

Table 8. Percentage reductions in tip acceleration of model with chevron braced VE dampers.

Centro, Hachinohe and Northridge earthquakes, the highest average deflection reductions were obtained when the dampers were placed in the stories 13 to 15 while in the case of the Kobe and San Fernando earthquakes, it was when the dampers were placed in the lowest stories.

The percentage reductions in the peak values of the tip acceleration experienced by the same structures are illustrated in Table 10. The range of the results was unexpectedly wide varying from an average reduction of 15.3% obtained under the El Centro earthquake to a poor 0.8% average reduction recorded under the Northridge earthquake. Clearly the highest reduction occurred in the structures with the dampers fitted in the stories 4 to 6. The tip acceleration reductions for the other damper placements were considerably lower and also less consistent.

The results presented in Tables 9 and 10 show that the expected high and reliable performance of the hybrid friction-VE dampers was achieved only partially. It is evident that the structures using the hybrid friction-VE dampers followed a similar trend to the structures fitted with the chevron brace friction dampers. This means that whereas the friction components of the hybrid dampers operated appropriately, the VE component remained essentially ineffective.

4.1.5. Structural models with VE dampers — lower toggle configuration. The percentage reductions in tip deflection for the lower toggle VE dampers are illustrated in Table 11. The highest average reduction of 18.8% was obtained under the Kobe earthquake, whereas the lowest average reduction of 7.9% occurred under the Hachinohe earthquake. In the cases of the El Centro and Hachinohe earthquakes, the highest average tip deflection reductions occurred when the dampers were placed in the uppermost stories, while a gradual decrease in efficiency was experienced as the dampers were moved towards the

Model	El Centro	Hachinohe	Kobe	Northridge	S.Fernando	Average
H 1-3	1.81	-4.68	19.69	6.45	16.70	7.99
H 4-6	7.47	-0.62	10.09	9.81	14.66	8.28
H 7-9	4.64	4.25	12.62	7.29	10.56	7.87
H 10-12	8.27	9.11	5.04	8.55	7.14	7.62
H 13-15	10.70	10.74	2.52	9.39	5.78	7.82
H 16-18	8.68	9.93	9.59	8.97	3.73	8.18
Average	6.93	4.79	9.92	8.41	9.76	7.96
Optimal	H7/9.19	H7/13.04	H10/9.61	H7/11.84	H1/8.37	H7/ 9.45

Table 9. Percentage reductions in tip deflection of model with hybrid friction-VE dampers.

Model	El Centro	Hachinohe	Kobe	Northridge	S.Fernando	Average
H 1-3	10.24	17.02	24.67	-9.37	-1.55	8.20
H 4-6	23.44	17.38	21.42	1.53	17.17	16.19
H 7-9	15.67	6.22	2.39	6.28	-0.13	6.08
H 10-12	16.55	6.76	1.46	2.76	0.43	5.59
H 13-15	20.80	0.82	-3.18	6.98	0.72	5.23
H 16-18	5.11	-0.08	7.19	-3.22	-1.27	1.54
Average	15.30	8.02	8.99	0.82	2.56	7.14
Optimal	H10/47.05	H7/20.03	H7/28.38	H4/6.70	H16/4.97	H7/ 14.09

Table 10. Percentage reductions in tip acceleration of model with hybrid friction-VE dampers.

<i>Model</i>	<i>El Centro</i>	<i>Hachinohe</i>	<i>Kobe</i>	<i>Northridge</i>	<i>S.Fernando</i>	<i>Average</i>
H 1-3	8.94	-0.18	30.22	9.99	23.74	14.54
H 4-6	4.58	1.41	19.33	17.39	23.07	13.16
H 7-9	8.15	3.80	21.81	13.28	21.06	13.62
H 10-12	10.52	10.16	20.32	13.69	17.05	14.35
H 13-15	13.29	14.93	11.91	17.80	11.03	13.79
H 16-18	15.67	17.31	8.94	17.39	-1.68	11.52
Average	10.19	7.90	18.75	14.92	15.71	13.50
Optimal	H13/7.35	H16/9.84	H1/17.35	H1/9.32	H1/13.79	H13/ 8.77

Table 11. Percentage reductions in tip deflection of model with lower toggle damping systems.

bottom of the structure. A reverse trend occurred under the Kobe and San Fernando earthquakes with the dampers being more effective in the lower stories and decreasing in efficiency as they were moved towards the top of the structure. In the case of the Northridge earthquake, the performance remained relatively consistent for all of the placements.

The results for the same damping systems in terms of reduction in tip acceleration are presented in Table 12. The highest average reduction of 21.2% was achieved under the El Centro earthquake, while the lowest average reduction of 11.2% occurred under the Northridge earthquake. The dampers displayed extraordinary performance when placed in the stories 1–6 and 13–15. By contrast, when fitted in the uppermost stories, an increase in average acceleration by 6.5% was experienced.

Despite the fact that the VE damper was created to represent only 42% of the damping force of the diagonal VE damper, its overall performance was noticeably higher and also more reliable. The results for the reduction in tip deflection followed a trend relatively close to the one for the structures fitted with the chevron brace friction dampers. With regard to reductions in tip acceleration, the results comply with a trend which was closest to that of the diagonal VE dampers.

To provide extra comparisons, structures embedded with the lower toggle friction dampers were also analyzed. The results revealed a noticeable level of similarity to those of the lower toggle VE dampers and for that reason are not presented in this paper. However, the time history graphs of both types of dampers make more obvious the fact that amplifying the force of the toggle brace assembly altered the damping response of friction (or VE) dampers so that they operated in a relatively similar way.

<i>Model</i>	<i>El Centro</i>	<i>Hachinohe</i>	<i>Kobe</i>	<i>Northridge</i>	<i>S.Fernando</i>	<i>Average</i>
H 1-3	10.19	-2.01	25.73	30.39	40.52	20.96
H 4-6	33.47	25.55	24.83	32.46	18.84	27.03
H 7-9	21.97	12.66	19.22	11.10	-0.89	12.81
H 10-12	18.66	4.97	9.67	5.24	9.67	9.64
H 13-15	35.91	30.56	29.07	15.23	16.06	25.37
H 16-18	6.88	-2.01	3.00	-26.98	-13.40	-6.50
Average	21.18	11.62	18.59	11.24	11.80	14.89
Optimal	H13/29.33	H1/7.75	H1/10.47	H7/12.26	H7/13.75	H4/ 11.39

Table 12. Percentage reductions in tip acceleration of model with lower toggle damping systems.

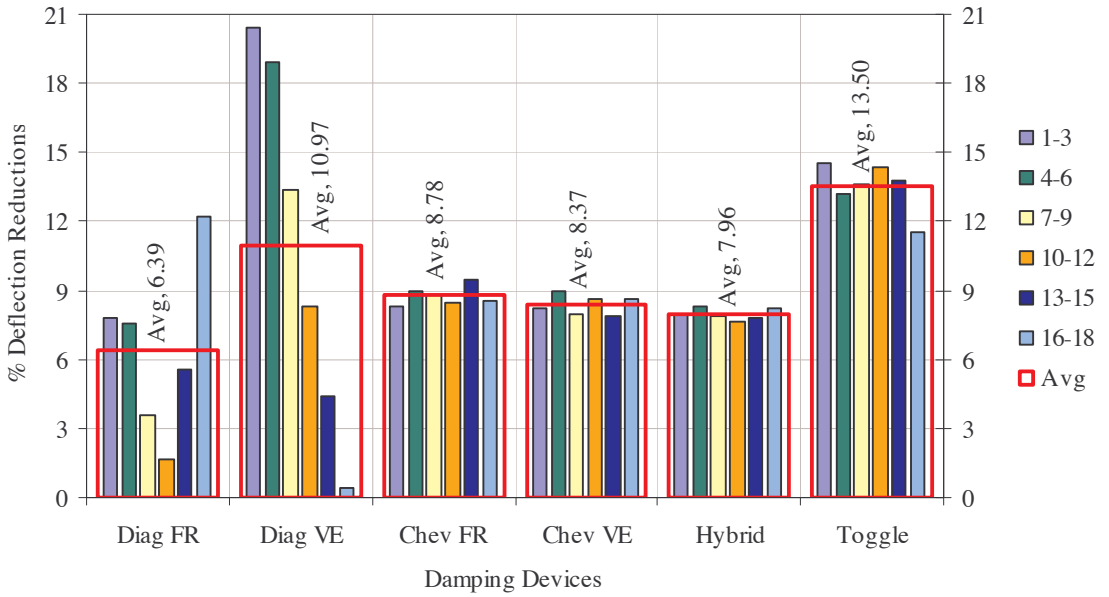


Figure 19. Average percentage deflection reductions for all damping systems in all placements in 18-story structure.

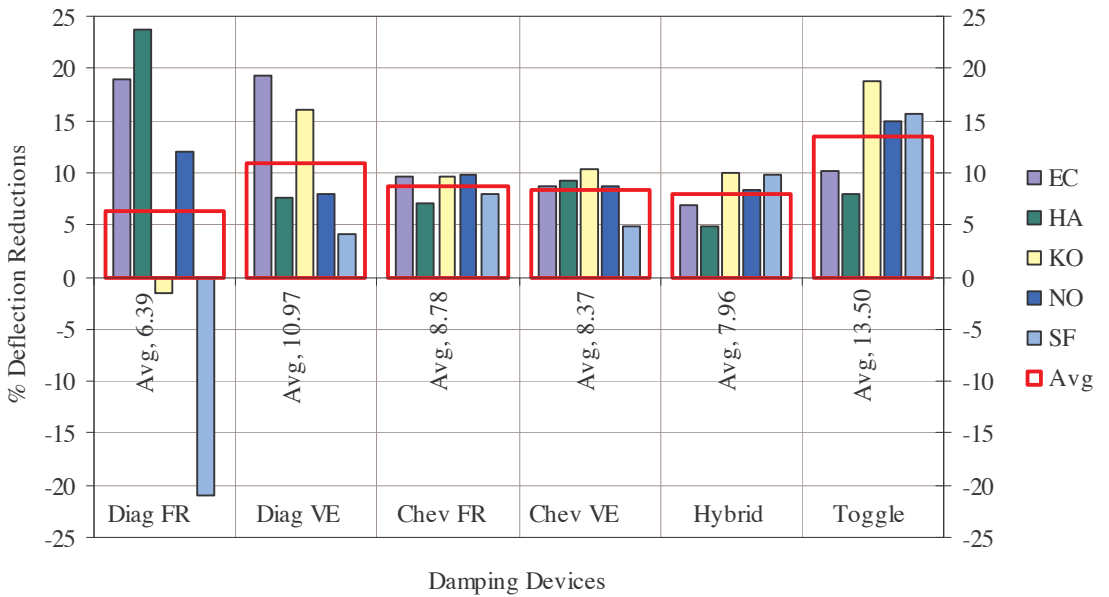


Figure 20. Average percentage deflection reductions of all damping systems under different earthquake excitations in 18-story structure.

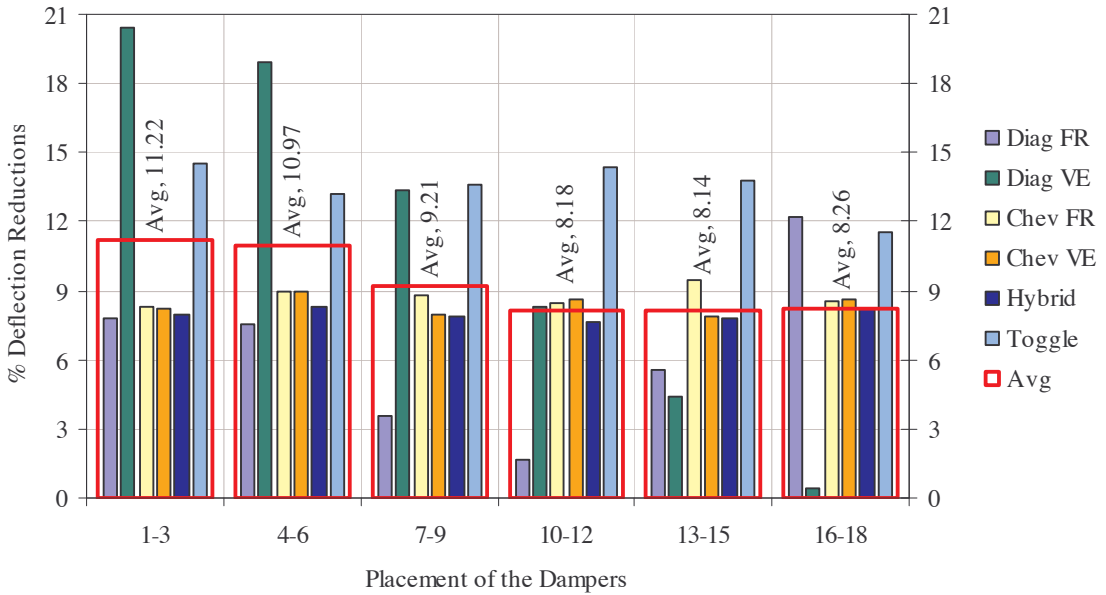


Figure 21. Average percentage deflection reductions of all damping systems in terms of damper placement in 18-story structure.

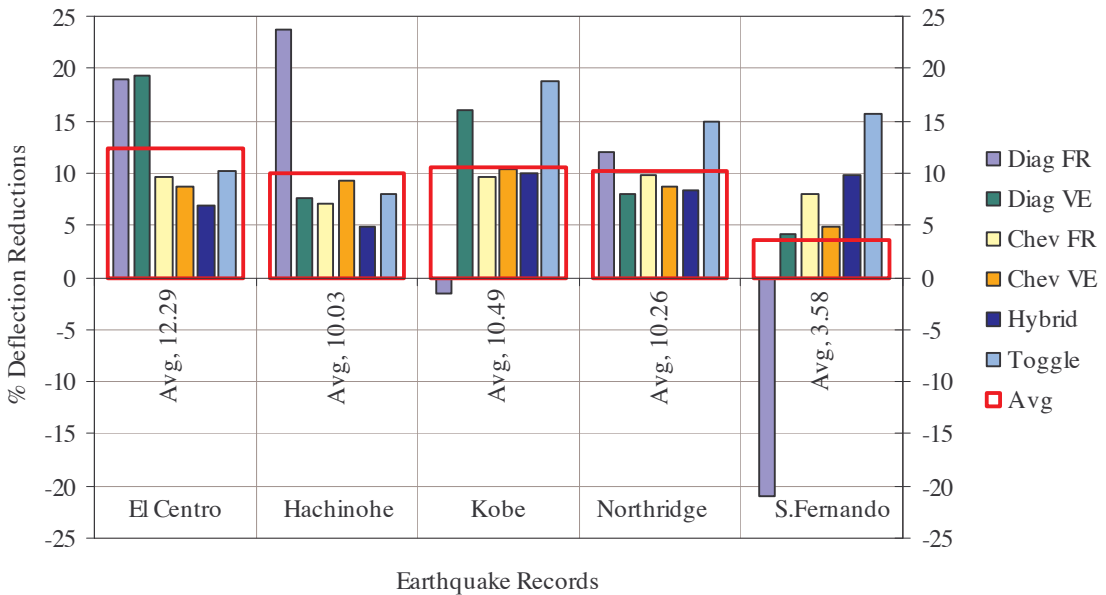


Figure 22. Average percentage deflection reductions of all damping systems under different earthquake excitations in 18-story structure.

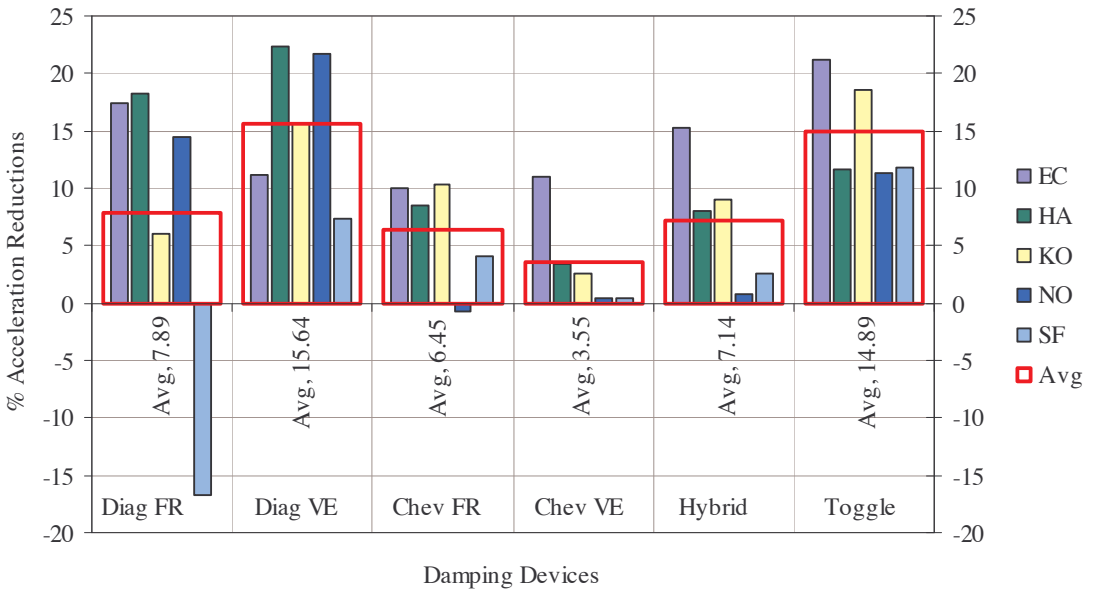


Figure 23. Average percentage acceleration reductions of all damping systems under different earthquake excitations in 18-story structure.

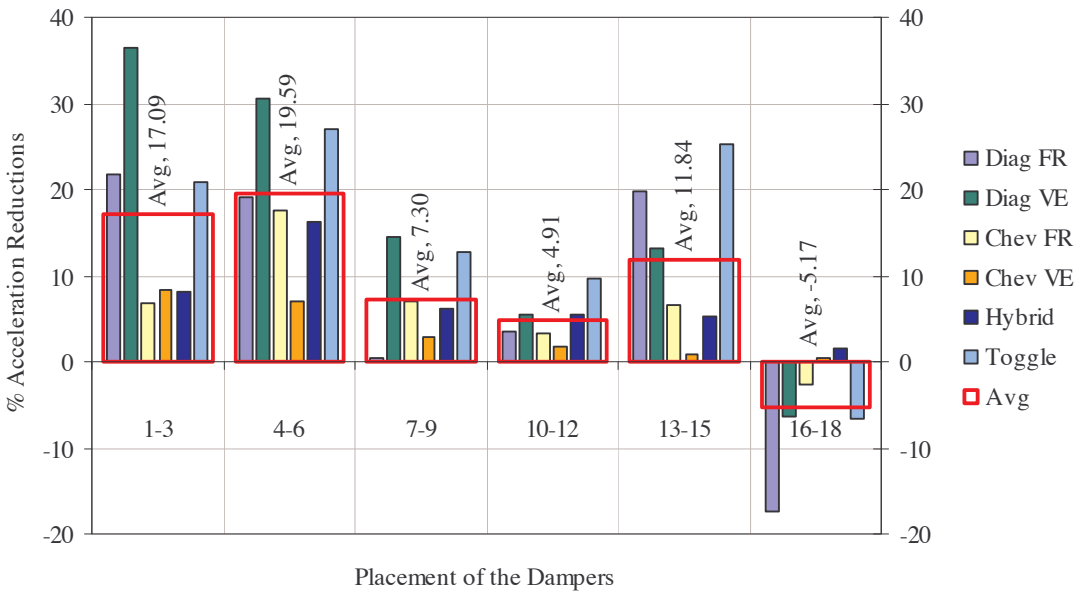


Figure 24. 18-story structure: Average percentage acceleration reductions of all damping systems in terms of damper placement.

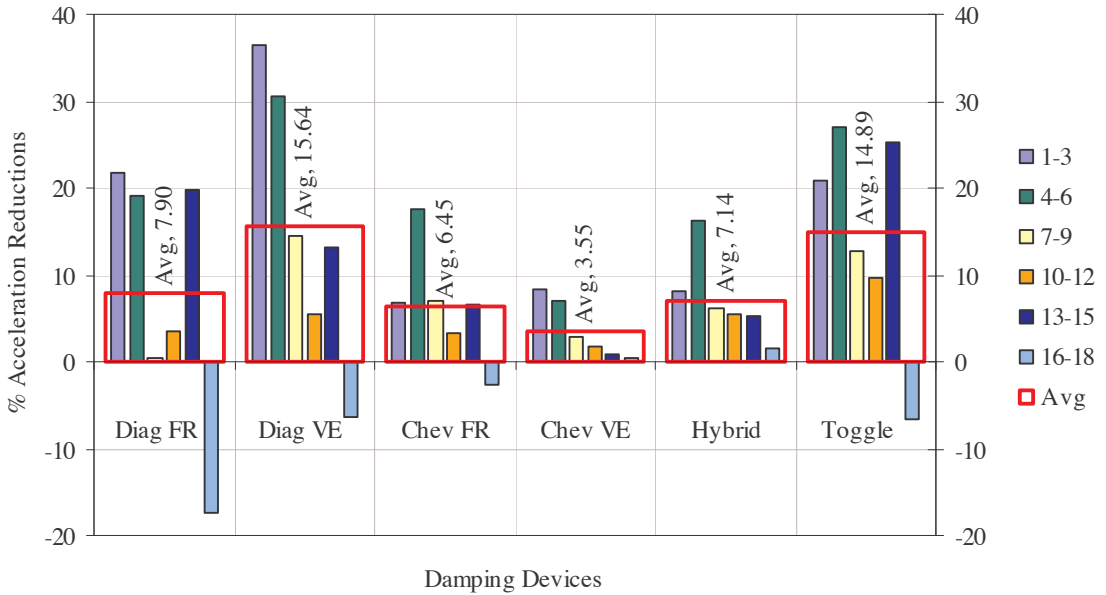


Figure 25. Average percentage acceleration reductions for all damping systems in all placements in 18-story structure.

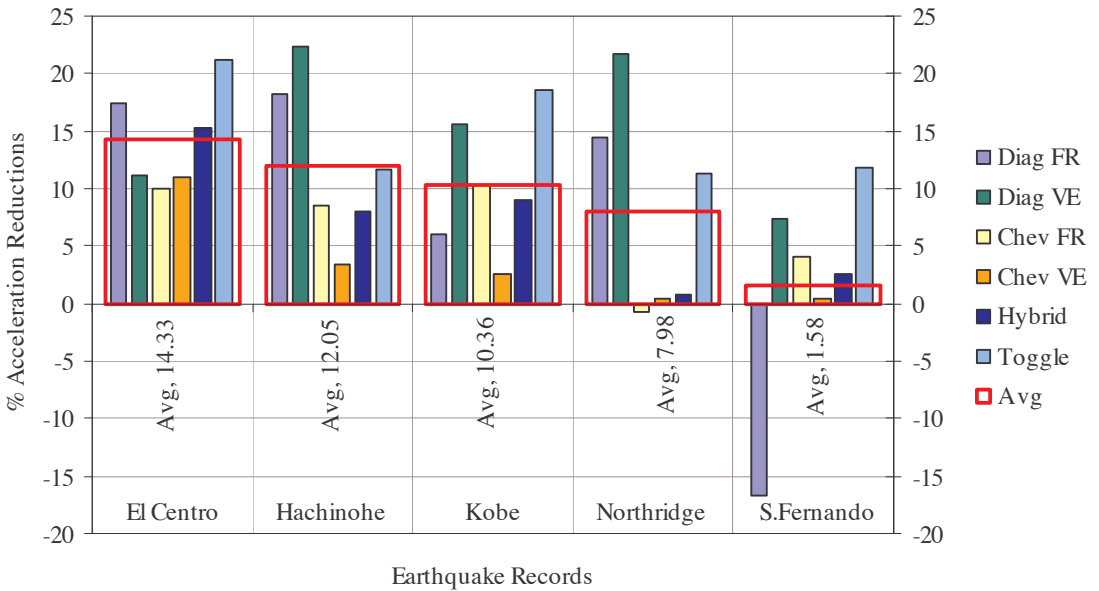


Figure 26. Average percentage acceleration reductions of all damping systems under different earthquake excitations in 18-story structure.

4.1.6. Summary of findings in the 18-story structural model. The overall results for an 18-story frame-shear wall structure in terms of reduction in the peak values of the tip deflection are illustrated in Figures 19–25. The highest reductions were recorded, as was expected, for the structure fitted with the lower toggle VE dampers. The results reveal a high level of reliability under all excitations and when fitted in all the placements. The reductions obtained by the diagonal VE dampers were even higher at lower stories; however their efficiency considerably decreases when moved towards the top of the structure. The most consistent performances in all placements and under all seismic excitations were revealed for both types of chevron brace dampers.

The hybrid friction-VE dampers acted in a similar way to the friction chevron brace dampers, which indicates that only the friction part of this damping system was working properly, while the VE part remained ineffective in most cases. Finally, the results of the diagonal friction dampers reveal the highest sensitivity to placement and also to variations in seismic excitations. These dampers achieved the highest reductions under the Hachinohe earthquake, which caused the highest structural deflections from all excitations. On the other hand, involvement of the diagonal friction dampers under the San Fernando earthquake excitation, which causes the lowest structural deflection, was rather unfavorable.

In the peak values of the tip acceleration for the same structure (Figures 25–26), the highest reductions were recorded for the structure fitted with the diagonal VE dampers. The tip acceleration reductions of these dampers were greatest when placed in the lower stories. The average reductions for lower toggle dampers were close to those of the diagonal VE dampers; however, their reductions for the lowest story placements were noticeably lower. The diagonal friction dampers displayed once again the highest sensitivity to variation of the dampers placement and seismic excitations. The slightly lower overall tip acceleration reduction was attributed to their ineffectiveness in the uppermost stories and particularly their poor effectiveness under the San Fernando earthquake excitation.

The hybrid friction-VE damper and the friction chevron brace dampers followed similar trends with rather inconsistent acceleration reductions under the El Centro, Hachinohe and Kobe earthquakes while the reductions under the Northridge and San Fernando earthquakes were quite small. The lowest tip acceleration reduction was displayed for the chevron brace VE dampers where satisfactory reductions were recorded only under the El Centro earthquake excitation.

As the results for the diagonal friction damper were inconsistent, a combined damping system consisting of the diagonal friction damper placed in the 16th story and the diagonal VE damper placed in the 1st story was also analyzed under all the earthquake excitation. The results are presented in Table 13 and it can be seen that there are significant reductions in both the investigated parameters under all 5 earthquake excitations. Furthermore, to emphasize the significance of these results, it should be pointed out that this combined damping system consisted of only two dampers.

	El Centro	Hachinohe	Kobe	Northridge	S.Fernando	Average
% Defl. Red.	26.16	19.18	7.36	25.31	6.92	16.99
% Accel. Red.	15.55	25.85	14.80	13.28	8.82	15.66

Table 13. Reductions in tip deflection and acceleration of model with combined damping system.

	<i>El Centro</i>	<i>Hachinohe</i>	<i>Kobe</i>	<i>Northridge</i>	<i>S.Fernando</i>
Deflection(m)	0.206	0.374	0.154	0.145	0.141
Acceleration(m/s ²)	5.69	6.61	6.93	5.76	3.51

Table 14. Tip deflection and tip acceleration of the undamped 12-story structure.

4.2. 12-story models. The second type of medium-rise structure investigated in this paper was represented by the 12-story frame-shear wall model (see Figure 2). The results of this structure under five earthquake excitations are presented below.

4.2.1. Undamped structural model. An undamped structural model was again considered in order to compare its results with the results of the structures fitted with the damping systems. The tip deflection and tip acceleration of this structure under five earthquake excitations can be seen in Table 14.

4.2.2. Structural models with friction and VE dampers — diagonal configuration. The percentage reductions in the peak values of the tip deflection experienced by the structures fitted with the diagonal friction dampers are presented in Table 15. The dampers display a very high level of efficiency in most cases. The highest average reduction of 27.9% was obtained under the El Centro earthquake and even the lowest overall reductions achieved under the Kobe earthquakes were reasonably high. The dampers placed in the lowest stories produced in the majority of cases, only minor tip deflection reductions; on the other hand, the deflection reductions were significantly higher when the dampers were placed in the stories with the higher interstory drifts (Table 16).

Percentage reductions in tip deflection for the same structure fitted with the diagonal VE dampers are illustrated in Table 17. Clearly the highest performance was achieved under the El Centro earthquake with an exceptional average reduction of 29.6%. The average deflection reduction that occurred under the Kobe earthquake was also reasonably high. However, the reductions under the San Fernando and Hachinohe earthquakes were only moderate and there were only minimal reductions under the Northridge earthquake. The results show very high average deflection reductions for the structure with the dampers located in the lower and middle stories, while moving the dampers towards the uppermost stories resulted in noticeably lower performance.

The results of tip acceleration reduction for the structures fitted with both damping systems are illustrated in Tables 18 and 19. The highest acceleration reductions can be observed when the dampers were

<i>Model</i>	<i>El Centro</i>	<i>Hachinohe</i>	<i>Kobe</i>	<i>Northridge</i>	<i>S.Fernando</i>	<i>Average</i>
M 1-2	28.99	4.46	-8.44	-2.07	0.68	4.72
M 3-4	19.32	9.82	1.30	10.34	8.16	9.79
M 5-6	18.36	3.57	20.13	17.93	14.97	14.99
M 7-8	35.75	4.46	13.64	24.14	21.09	19.82
M 9-10	30.92	9.82	-1.95	28.97	23.13	18.18
M 11-12	33.82	9.82	8.44	28.97	22.45	20.70
Average	27.86	6.99	5.52	18.05	15.08	14.70
Optimal	M11/23.87	M3/6.20	M7/20.41	M9/16.18	M11/14.52	M11/14.46

Table 15. Percentage reductions in tip deflection of model with diagonal friction dampers.

<i>Drift</i>	<i>El Centro</i>	<i>Hachinohe</i>	<i>Kobe</i>	<i>Northridge</i>	<i>S.Fernando</i>
1 st largest	9-10	9-10	10-11	6-7	10-11
2 nd largest	10-11	10-11	9-10	7-8	9-10
3 rd largest	8-9	8-9	8-9	8-9	8-9

Table 16. Floors with largest interstory drift.

<i>Model</i>	<i>El Centro</i>	<i>Hachinohe</i>	<i>Kobe</i>	<i>Northridge</i>	<i>S.Fernando</i>	<i>Average</i>
M 1-2	39.61	5.36	25.32	-5.52	6.80	14.32
M 3-4	41.06	5.36	15.58	-0.69	10.88	14.44
M 5-6	42.03	6.25	12.34	3.45	9.52	14.72
M 7-8	39.13	8.93	18.83	2.07	8.84	15.56
M 9-10	14.98	2.68	18.18	2.76	3.40	8.40
M 11-12	0.48	-4.46	14.29	2.76	1.36	2.88
Average	29.55	4.02	17.42	0.80	6.80	11.72
Optimal	M3/30.92	M5/5.36	M11/14.29	M7/6.21	M72.72	M7/7.87

Table 17. Percentage reductions in tip deflection of model with diagonal VE dampers.

placed in the lowest stories, while their repositioning towards the top of the structure caused a gradual decrease in acceleration reductions.

<i>Model</i>	<i>El Centro</i>	<i>Hachinohe</i>	<i>Kobe</i>	<i>Northridge</i>	<i>S.Fernando</i>	<i>Average</i>
M 1-2	27.24	23.87	8.65	9.53	-9.38	11.98
M 3-4	22.67	11.63	19.74	14.38	-2.27	13.23
M 5-6	15.99	-9.82	20.89	2.95	2.84	6.57
M 7-8	26.19	-4.68	-10.23	15.94	-8.24	3.80
M 9-10	13.18	-3.78	4.61	22.18	-21.31	2.98
M 11-12	-8.44	-11.33	-1.15	-1.91	-17.33	-8.03
Average	16.14	0.98	7.08	10.51	-9.28	5.09
Optimal	M1/27.41	M9/6.49	M11/23.27	M11/17.53	M3/4-4.76	M7/5.18

Table 18. Percentage reductions in tip acceleration of model with diagonal friction dampers.

<i>Model</i>	<i>El Centro</i>	<i>Hachinohe</i>	<i>Kobe</i>	<i>Northridge</i>	<i>S.Fernando</i>	<i>Average</i>
M 1-2	42.88	25.98	12.25	-3.64	8.24	17.14
M 3-4	28.82	18.13	19.74	0.69	13.92	16.26
M 5-6	16.17	8.46	4.18	0.35	18.75	9.58
M 7-8	12.83	6.34	5.33	-1.21	7.10	6.08
M 9-10	11.60	6.04	21.18	-2.43	1.70	7.62
M 11-12	-3.69	-0.76	17.29	-10.23	-10.80	-1.64
Average	18.10	10.70	13.33	-2.74	6.49	9.17
Optimal	M1/14.41	M3/6.95	M11/9.22	M5/2.60	M3/9.66	M3/5.25

Table 19. Percentage reductions in tip acceleration of model with diagonal VE dampers.

<i>Model</i>	<i>El Centro</i>	<i>Hachinohe</i>	<i>Kobe</i>	<i>Northridge</i>	<i>S.Fernando</i>	<i>Average</i>
M 1-2	0.48	1.79	18.18	6.90	4.08	6.29
M 3-4	5.31	3.57	18.83	11.03	12.24	10.20
M 5-6	24.15	2.68	15.58	15.17	13.61	14.24
M 7-8	32.85	3.57	16.23	18.62	18.37	17.93
M 9-10	33.33	2.68	11.04	20.00	20.41	17.49
M 11-12	32.85	1.79	15.58	17.24	17.01	16.89
Average	21.50	2.68	15.91	14.83	14.29	13.84
Optimal	M9/27.35	M3/0.68	M1/16.40	M9/14.05	M9/18.02	M9/14.26

Table 20. Percentage reductions in tip deflection of model with chevron brace friction dampers.

The presented results once again confirmed patterns indicating that tip deflection reductions for the structures fitted with the diagonal friction dampers gradually increased as the dampers were moved toward the top of the structure, whereas this trend was reversed for structures fitted with diagonal VE dampers. The highest tip acceleration reduction for both damping systems was achieved when the dampers were placed in the lowest stories and gradually decreased as they were moved toward the top of the structure.

4.2.3. Structural models with friction and VE dampers — chevron brace configuration. The percentage reductions in tip deflection for the structures fitted with chevron brace friction dampers are illustrated in Table 20. The best performance, with an average deflection reduction of 21.5%, was obtained under the El Centro earthquake; this was followed by still adequately high reductions occurring under the Kobe, Northridge and San Fernando earthquakes. Conversely, the reductions displayed under the Hachinohe earthquake were rather insignificant.

The highest average deflection reduction occurred when the dampers were placed in the stories 7 and 8. Consequent repositioning of these dampers towards the top of the structure caused slight decreases in efficiency, whereas the decrease in efficiency was much stronger as the dampers were repositioning towards the bottom of the structure.

Deflection reductions for the same structures fitted with the chevron brace VE dampers are displayed in Table 21. Clearly the best performance with an average reduction of 18.2% was obtained under the Kobe earthquake. The reductions occurring under the El Centro, Northridge and San Fernando earthquakes were still reasonably high, whereas the reductions experienced under the Hachinohe earthquake were yet

<i>Model</i>	<i>El Centro</i>	<i>Hachinohe</i>	<i>Kobe</i>	<i>Northridge</i>	<i>S.Fernando</i>	<i>Average</i>
M 1-2	-0.97	1.79	18.18	6.90	4.76	6.13
M 3-4	6.76	2.68	19.48	8.97	7.48	9.07
M 5-6	8.70	2.68	16.88	11.72	10.88	10.17
M 7-8	16.43	3.57	19.48	13.79	11.56	12.97
M 9-10	22.22	1.79	20.13	14.48	11.56	14.04
M 11-12	27.05	0.89	14.94	15.17	13.61	14.33
Average	13.37	2.23	18.18	11.84	9.98	11.12
Optimal	M11/16.41	M3/0.68	M3/16.40	M11/11.21	M11/9.61	M11/9.82

Table 21. Percentage reductions in tip deflection of model with chevron brace VE dampers.

<i>Model</i>	<i>El Centro</i>	<i>Hachinohe</i>	<i>Kobe</i>	<i>Northridge</i>	<i>S.Fernando</i>	<i>Average</i>
M 1-2	-14.41	-16.47	-8.79	-23.57	-20.17	-16.68
M 3-4	-12.30	-7.25	19.45	-8.15	-49.72	-11.59
M 5-6	-9.84	0.15	17.00	10.75	-49.15	-6.22
M 7-8	-22.50v	-9.06	12.54	-1.04	-66.19	-17.25
M 9-10	-27.94	-4.08	0.00	3.29	-52.84	-16.31
M 11-12	-44.82	-24.92	14.84	-17.33	-89.49	-32.34
Average	-21.97	-10.27	9.17	-6.01	-54.59	-16.73
Optimal	M3/-8.07	M3/-2.22	M9/25.64	M3/2.36	M3/-18.22	M3/-2.77

Table 22. Percentage reductions in tip acceleration of model with chevron brace friction dampers.

again insignificant. A gradual increase in tip deflection can be seen as the dampers were moved from the bottom to the top of the structures. The deflection increases that occurred under the El Centro, Northridge and San Fernando earthquakes were also accompanied by a noticeable level of regularity, whereas the reduction for the Hachinohe and Kobe earthquakes remained in a relatively narrow range throughout all placements.

Percentage reductions in tip acceleration for the chevron brace friction dampers are illustrated in Tables 22. The results revealed high acceleration reductions obtained under the Kobe earthquake, however the reductions occurred under the other earthquakes were noticeably poorer. Clearly, the worst results occurred under the San Fernando earthquake with increase in average tip acceleration by 54.6%.

The reduction in tip acceleration experienced by the structures fitted with the chevron brace VE dampers are presented in Table 23. The results followed a trend similar to that of the structure fitted with the chevron brace friction dampers. The average tip acceleration reduction occurring under the Kobe earthquake was very high. Nevertheless, the reductions that occurred under the other earthquake scenarios were clearly lower. The poorest results were recorded under the San Fernando earthquake, with an increase in the average acceleration of 36.6%.

In terms of damper placement, both types of dampers displayed some common features. The average tip acceleration reductions showed unfavorable increases for the all damper placements. However, the lowest increase for both types of dampers occurred when the dampers were placed in the stories 5 and 6, while the highest were experienced when the dampers were placed in the uppermost stories.

<i>Model</i>	<i>El Centro</i>	<i>Hachinohe</i>	<i>Kobe</i>	<i>Northridge</i>	<i>S.Fernando</i>	<i>Average</i>
M 1-2	-6.50	-9.52	2.31	-15.77	-13.35	-8.57
M 3-4	-2.64	-6.95	11.38	-9.71	-8.24	-3.23
M 5-6	-8.44	-1.81	13.54	11.79	-21.59	-1.30
M 7-8	4.39	-6.50	14.70	1.91	-43.75	-5.85
M 9-10	-28.65	-4.53	20.03	4.16	-54.55	-12.71
M 11-12	-42.88	-20.24	25.36	-17.33	-78.13	-26.64
Average	-14.12	-8.26	14.55	-4.16	-36.60	-9.72
Optimal	M3/-2.64	M5/2.91	M3/22.08	M5/-6.03	M3/-7.68	M3/0.02

Table 23. Percentage reductions in tip acceleration of model with chevron brace VE dampers.

Model	El Centro	Hachinohe	Kobe	Northridge	S.Fernando	Average
M 1-2	30.60	6.17	24.74	-0.72	1.82	12.52
M 3-4	27.03	11.33	14.32	3.58	0.18	11.29
M 5-6	23.96	12.19	9.68	7.89	7.55	12.25
M 7-8	14.27	9.61	6.79	7.89	9.18	9.55
M 9-10	10.19	7.89	7.95	9.61	11.64	9.45
M 11-12	4.06	9.61	12.00	10.47	14.09	10.05
Average	18.35	9.47	12.58	6.45	7.41	10.85
Optimal	M1/20.89	M3/8.64	M1/8.44	M7/8.64	M11/8.92	M3/7.54

Table 24. Percentage reductions in tip deflection of model with hybrid friction-VE dampers.

The overall reductions in tip deflection for the chevron brace dampers were equally high compared to those of the diagonal dampers. The reductions in tip displacement for both types of the chevron brace dampers revealed a lower level sensitivity to the placement and a higher consistency than the diagonal dampers. On the other hand in terms of acceleration reduction, both types of the chevron brace dampers were the least effective damping systems which in most cases created unfavorable results.

4.2.4. Structural models with hybrid friction-VE dampers. The percentage reductions in the peak values of the tip deflection experienced by the structures fitted with hybrid friction-VE dampers are illustrated in Table 24. The highest performance occurred under the El Centro earthquake with an average reduction of 18.4%. Damper performances obtained under the other earthquakes were noticeably lower and the lowest average reduction of 6.5% was recorded under the Northridge earthquake.

The dampers experienced a consistent performance in all of the placements. However, their effectiveness was slightly higher when fitted in the lower stories. In the case of the El Centro and Kobe earthquakes tip deflection reductions gradually increased as the dampers were moved from the top to the bottom of the structures, while under the Northridge and San Fernando earthquakes this trend was reversed. The reductions occurred under the Hachinohe earthquake were consistent over the all placements.

Model	El Centro	Hachinohe	Kobe	Northridge	S.Fernando	Average
M 1-2	22.87	20.78	1.24	8.07	-3.59	9.87
M 3-4	-2.89	29.79	19.20	11.03	4.44	12.31
M 5-6	-3.64	25.61	14.83	10.21	-1.68	9.07
M 7-8	-4.84	9.90	6.34	12.51	0.43	4.87
M 9-10	3.70	19.57	10.95	13.99	4.82	10.61
M 11-12	-4.09	12.10	6.70	4.95	-12.95	1.34
Average	1.85	19.62	9.88	10.13	-1.42	8.01
Optimal	M9/-0.04	M9/27.41	M11/7.86	M9/7.78	M11/0.78	M9/6.77

Table 25. Percentage reductions in tip acceleration of model with hybrid friction-VE dampers.

<i>Model</i>	<i>El Centro</i>	<i>Hachinohe</i>	<i>Kobe</i>	<i>Northridge</i>	<i>S.Fernando</i>	<i>Average</i>
M 1-2	26.50	9.75	28.53	4.69	3.80	14.65
M 3-4	35.00	12.28	30.23	6.37	8.61	18.50
M 5-6	30.50	15.65	18.32	12.28	7.81	16.91
M 7-8	21.00	14.81	11.51	13.12	16.63	15.41
M 9-10	10.50	13.97	14.35	15.65	23.04	15.50
M 11-12	7.50	16.50	9.24	19.03	22.24	14.90
Average	21.83	13.82	18.69	11.86	13.69	15.98
Optimal	M1/23.71	M1/12.17	M1/9.94	M11/9.57	M11/12.40	M5/10.71

Table 26. Percentage reductions in tip deflection of model with lower toggle VE dampers.

<i>Model</i>	<i>El Centro</i>	<i>Hachinohe</i>	<i>Kobe</i>	<i>Northridge</i>	<i>S.Fernando</i>	<i>Average</i>
M 1-2	4.61	19.90	29.39	1.71	-6.36	9.85
M 3-4	30.74	26.47	14.53	16.53	8.43	19.34
M 5-6	12.83	33.36	26.89	19.11	-6.55	17.13
M 7-8	6.38	33.68	23.68	16.37	3.19	16.66
M 9-10	14.45	26.90	20.71	24.91	18.17	21.03
M 11-12	-39.12	-9.60	-10.19	4.77	-37.45	-18.32
Average	4.98	21.79	17.50	13.90	-3.43	10.95
Optimal	M9/2.72	M9/31.30	M5/9.80	M9/12.46	M3/7.92	M9/11.35

Table 27. Percentage reductions in tip acceleration of model with lower toggle VE dampers.

Table 25 presents the percentage reduction in tip acceleration for the same structure. The highest average reduction of 19.6% occurred under the Hachinohe earthquake. The reductions experienced under the Northridge and Kobe earthquakes were noticeably lower, although still relatively high. The lowest reductions (including some increases in acceleration) occurred under the El Centro and San Fernando earthquakes. The highest tip acceleration reductions occurred when the dampers were fitted in the stories 3 and 4; by contrast, the least effective were in the top stories. In the case of the El Centro earthquake, the dampers were effective only in the lowest stories.

From the results it is clear that the structures fitted with the hybrid friction-VE dampers followed relatively closely the pattern of the structures fitted with the diagonal VE dampers. Based on these results, it seems that whereas the VE part of the hybrid damper operated appropriately, the friction part remain rather ineffective. The illustrated high efficiency of the diagonal VE part and the inefficiency of the chevron brace friction part of the hybrid damper were in direct contrast to the hybrid damper fitted in the 18-story structures (where only the chevron brace friction dampers operated effectively). The contrast in performances makes it obvious that creating a hybrid friction-VE damper is rather complex and so requires a more comprehensive study.

4.2.5. Structural models with VE dampers — lower toggle configuration. The percentage reduction in tip deflection for the structures fitted with the lower toggle VE dampers are presented in Table 26. The

	El Centro	Hachinohe	Kobe	Northridge	S.Fernando	Average
% Defl. Red.	26.70	12.30	27.26	20.69	17.73	20.93
% Accel. Red.	26.53	15.13	33.47	9.02	11.36	19.10

Table 28. Reduction tip deflection and tip acceleration of the model with combined damping system.

dampers show a high performance under the all earthquake excitations. The highest average reduction of 21.8% occurred under the El Centro earthquake. High average deflection reductions were also recorded under the other earthquakes and even the lowest average reduction recorded under the Northridge earthquake reached a value of 11.9%.

While considering the efficiency of the placements, the highest average deflection reduction was obtained by the structures with the dampers fitted in the stories 3 and 4. From Table 26 it can also be seen that under the Northridge and San Fernando earthquakes, damper efficiency increased from the bottom to the top of the structures, while under the El Centro earthquake, the reverse trend was experienced. In the case of the Kobe earthquake, the dampers performed significantly better in the lower stories while in the case of the Hachinohe earthquake, the results were rather complex and did not follow any obvious pattern.

The percentage reductions in tip acceleration for the same structures are presented in Table 27. Despite a convincing overall performance a wide range of results was experienced. The tip acceleration varied from a 3.4% average increase, experienced under the San Fernando earthquake, to 21.8% average reduction obtained under the Hachinohe earthquake. The highest average acceleration reduction occurred when the dampers were fitted in the stories 9 and 10 while in contrast a significant increase in acceleration occurred when the dampers were fitted in the uppermost stories.

4.2.6. Summary of finding in the 12-story structural model. The overall results of all damping systems for the 12-story structure in terms of reduction in the peak values of tip deflection (Figures 27–32) were significantly high, with an exceptionally narrow interval of overall performance. On the other hand, the range of particular reductions remained relatively wide.

The highest tip deflection reductions and also the most consistent performance were obtained, yet again, for the lower toggle dampers. The tip deflection reductions for the diagonal friction dampers were generally comparable to those of the lower toggle VE dampers; however, in a few cases, this remained rather ineffective. Slightly lower overall deflection reductions for both the chevron brace dampers as compared to the diagonal friction dampers were due to their poor performances under the Hachinohe earthquake. The widest range of results was displayed for diagonal VE dampers. However, their overall reduction also remained at an adequately high level. The reductions for the hybrid friction-VE dampers were comparable to those of the other damping systems. However, their results suggested that, whereas the VE part of damping system operated effectively, the friction part of this damping system remained rather ineffective.

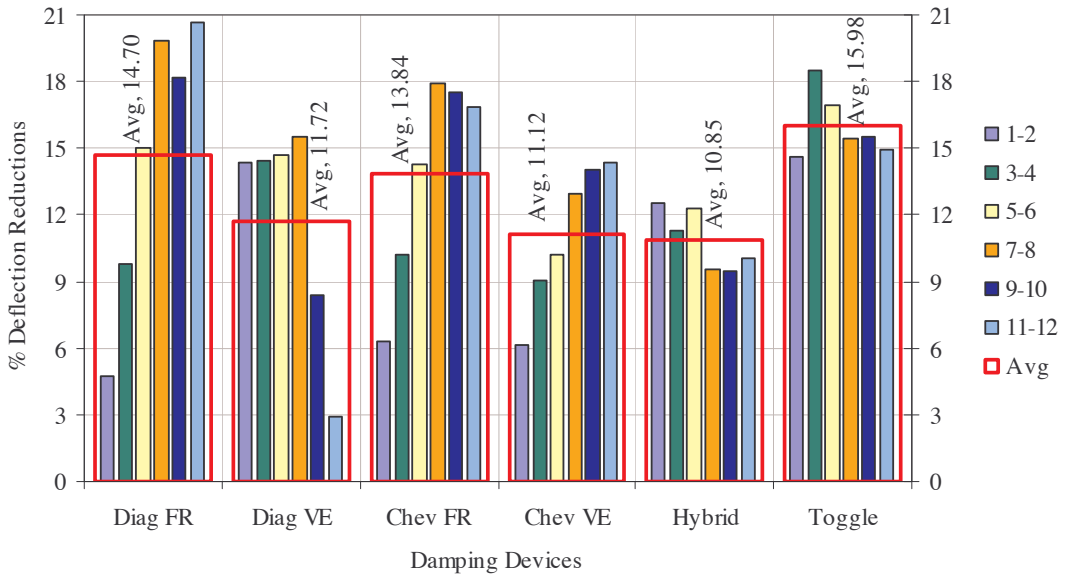


Figure 27. Average percentage deflection reductions for all damping systems in all placements in 12-story structure.

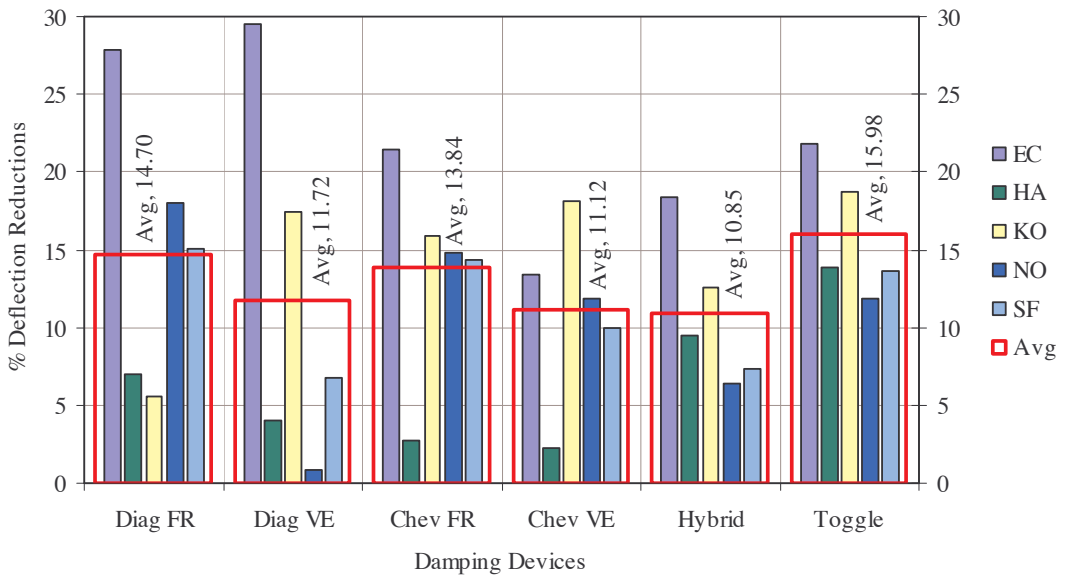


Figure 28. Average percentage deflection reductions of all damping systems under different earthquake excitations in 12-story structure.

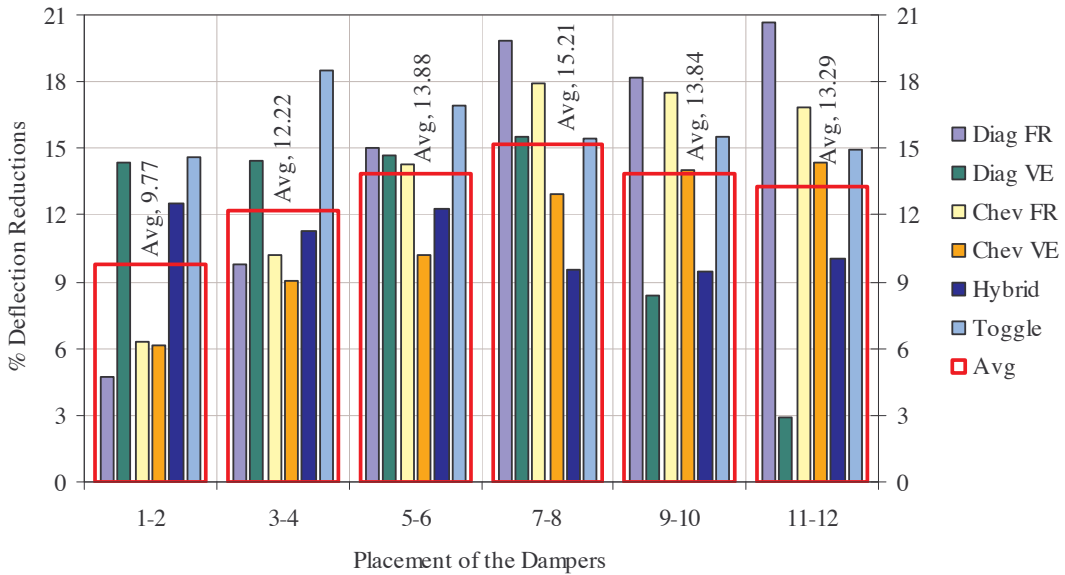


Figure 29. Average percentage deflection reductions of all damping systems in terms of damper placements in 12-story structure.

Whilst in terms of tip deflection reduction for the 12-story structure, all damping systems performed exceptionally well, the results in terms of the peak values of tip acceleration reduction were considerably poorer (Figures 31–34). The highest reductions were recorded for the lower toggle VE dampers. However, even these dampers remained unreliable under the San Fernando earthquake. The reductions for the diagonal VE dampers were rather inconsistent with an increase in tip accelerations under the Northridge earthquake. The reductions for the hybrid friction-VE damper were generally high except for the El Centro and San Fernando earthquakes where slight increases in acceleration were recorded. The tip acceleration reductions of the diagonal friction dampers were uneven and in many cases rather insufficient. Clearly the poorest results with strong increase in tip acceleration were recorded for the chevron brace VE dampers and chevron brace friction dampers which performed effectively only under the Kobe earthquake.

Similar to what was done in the case of the 18-story structure, a combined damping system, which consisted of the diagonal friction damper placed in the 11th story and the diagonal VE damper placed in the first story was also analyzed. The results presented in Table 28 demonstrate significant tip deflection and tip acceleration reduction under all earthquake excitations.

5. Discussion and conclusion

This comprehensive study has treated seismic mitigation by using six different damping systems, namely, friction and VE diagonal dampers, friction and VE chevron brace dampers, and hybrid friction-VE dampers and lower toggle VE dampers. These damping systems were embedded in six different placements (one at a time) within cut-outs of shear walls to mitigate the seismic response of medium-rise

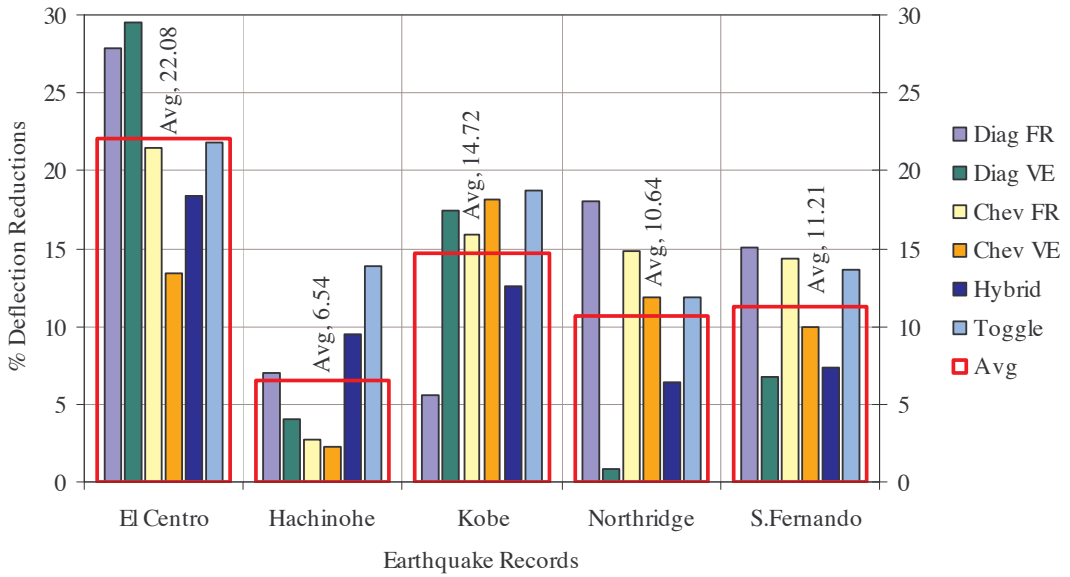


Figure 30. Average percentage deflection reductions of all damping systems under different earthquake excitations in 12-story structure.

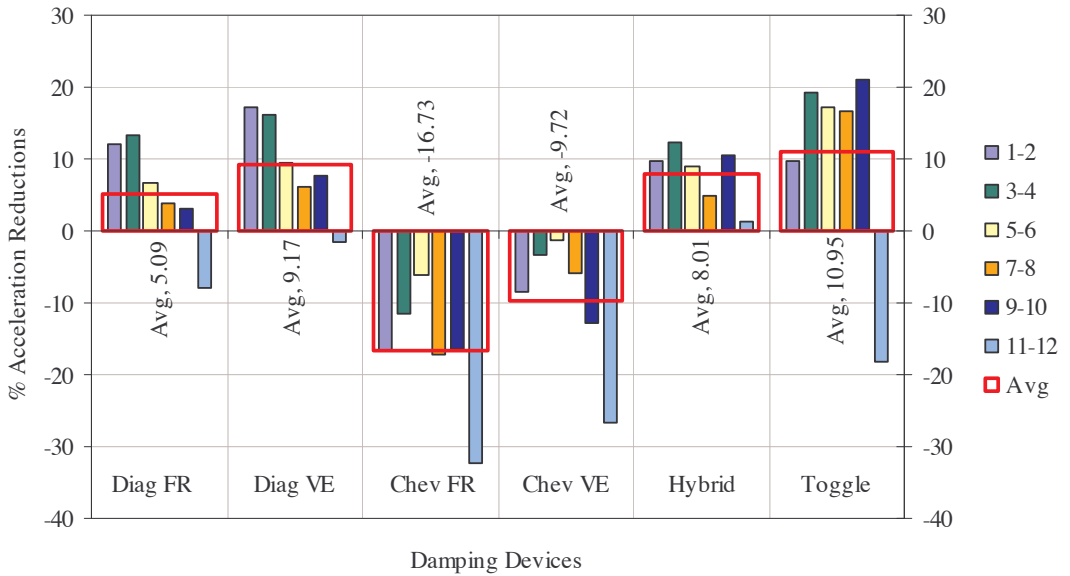


Figure 31. Average percentage acceleration reductions for all damping systems in all placements in 12-story structure.

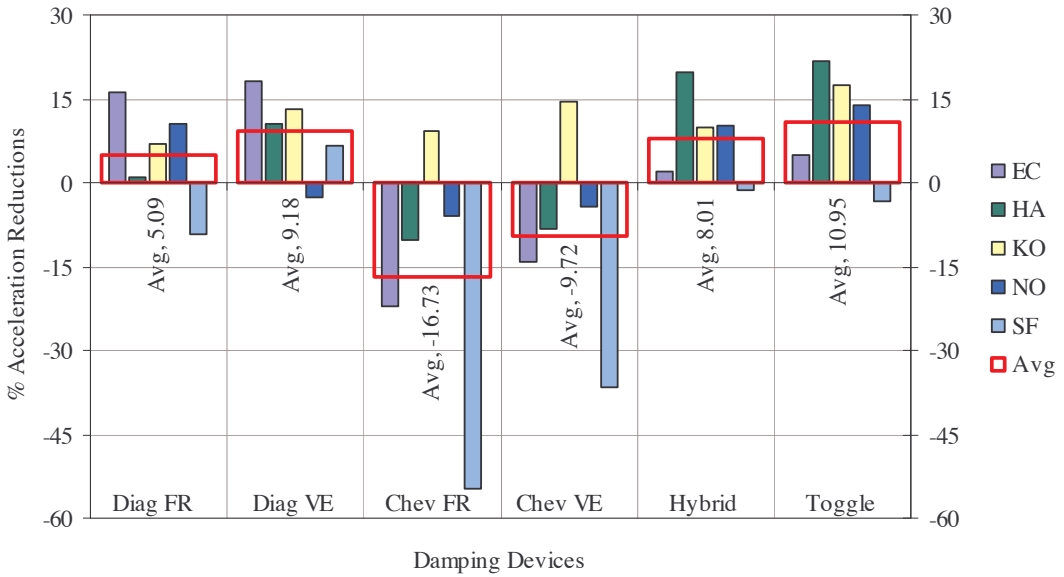


Figure 32. Average percentage acceleration reductions of all damping systems under different earthquake excitations in 12-story structure.

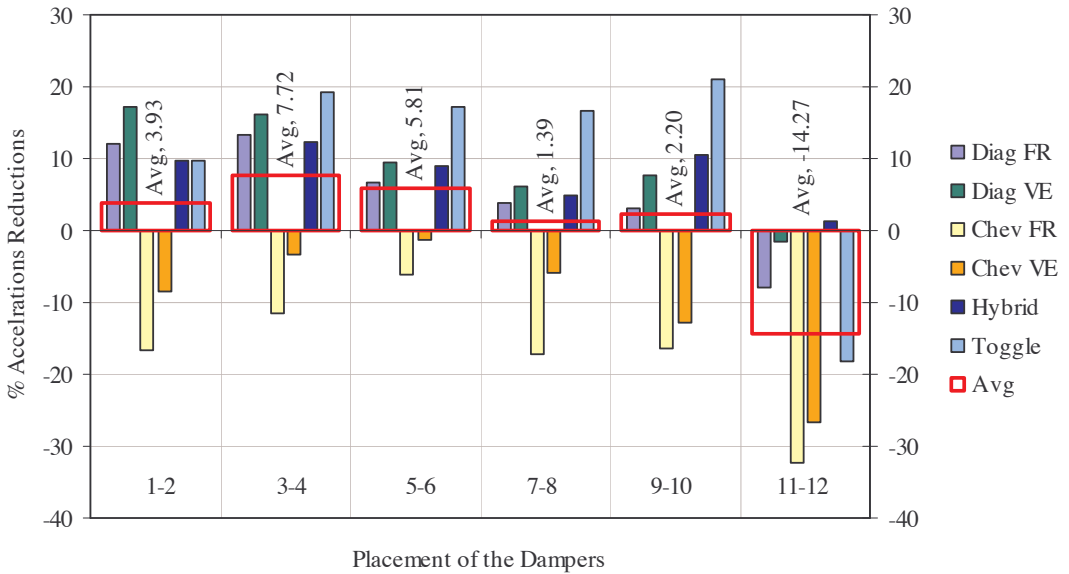


Figure 33. Average percentage acceleration reductions of all damping systems in terms of damper placements in 12-story structure.

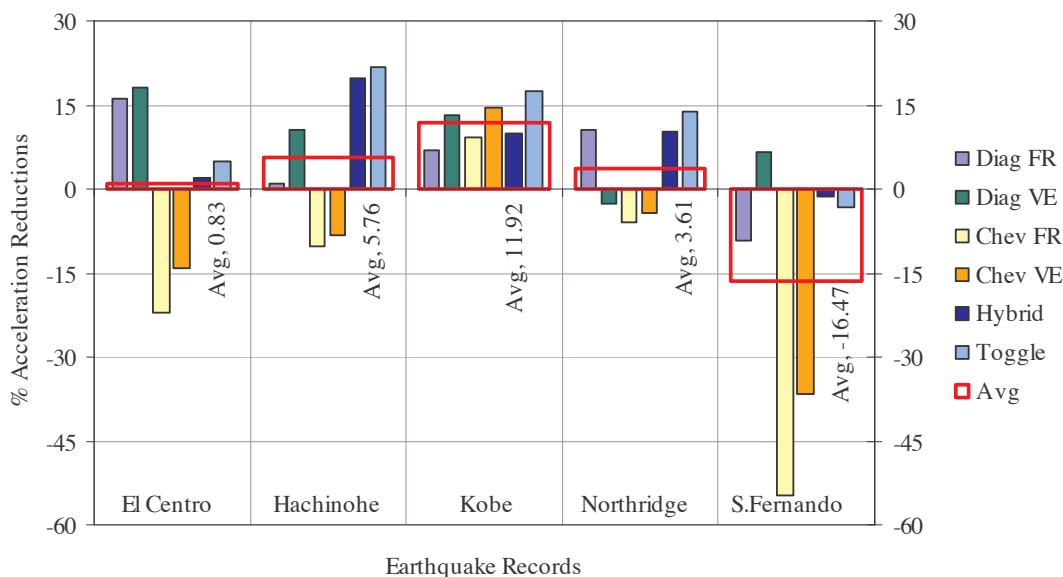


Figure 34. Average percentage acceleration reductions of all damping systems under different earthquake excitations in 12-story structure.

building structures. Finite element techniques were used to model the dampers and the structures to obtain the dynamic responses under five different earthquake excitations, using time history analyses. Damper properties such as stiffness, damping coefficient, location, configuration and size were varied and results for tip deflections and accelerations were obtained.

Despite the availability of sophisticated computer facilities, calculating the type of damping devices and their optimal placement and size still remains a highly iterative trial-and-error process. What makes the problem even more difficult is the uncertainty of seismic inputs as the forces of nature can vary tremendously. The range of the results presented in this paper illustrates the complexity of the problem of optimization in the use of damping devices. Nevertheless, the overall performances of all damping systems were satisfactory and some useful features can be observed.

In the 18-story structure reductions of up to 36% in the peak values of tip deflections and 47% in the peak values of the tip accelerations were obtained while in the 12-story structure the highest tip deflection reduction was 43% and the tip acceleration reduction 50%

With regards to performance of particular damping systems, the friction dampers in the huge majority of cases surpassed the VE dampers in their ability to reduce the intensity of the initial strong strikes. By contrast, the VE dampers gradually decreased the deflection and acceleration of the structure. The performance of the friction dampers increased with higher interstory drift, while the best performance of VE dampers was achieved when placed in the lowest stories. In addition, the diagonal friction dampers performed better under the earthquakes which produced higher deflections of the structure. By contrast, the performance of these dampers under earthquakes that caused a lower structural deflection was less favorable. The performance of the diagonal VE dampers was noticeably less sensitive to this aspect. With

regard to the reductions of the tip acceleration, both damping systems experienced the best performance in the lowest stories, while their performance gradually decreased as the dampers were moved towards the uppermost stories.

Despite the fact that both types of the chevron brace dampers were created to represent only 66.6% of the damping force of the diagonal dampers, their overall tip deflection reduction was comparatively high and even significantly more reliable than those of the diagonal dampers. On the other hand, both types of chevron brace dampers were clearly the least effective in terms of tip acceleration reduction. The hybrid friction-VE dampers performed in a more stable and reliable manner than the diagonal and chevron brace dampers; nevertheless their overall reductions were, in the majority of cases, slightly lower. The results of these dampers in an 18-story structure indicate that only the friction part of the hybrid damper was operating properly; on the other hand, in the 12-story structure it was only the VE parts that did so. The lower toggle VE damper displayed the highest performance and reliability from all damping systems. Despite the use of the VE damping mechanism, the trend in the tip deflection reductions of the lower toggle damper was similar to that of the chevron brace friction dampers.

A number of analyses of the two different structure types fitted with different damping systems and treated under different earthquake excitations were carried out to gain a better understanding of the effectiveness of the dampers and their placement. This study treated the structural response under a range of seismic excitations even when the dominant seismic frequencies matched the natural frequency of the structure.

A strategy for protecting buildings from earthquakes is to limit the tip deflection which provides an overall assessment of the seismic response of the structure. To this end, findings of the present study demonstrate that friction dampers are most effective when placed close to regions of the maximum interstory drift, whereas VE dampers are most effective when placed in the lowest stories. The combined damping system, which consists of the diagonal friction damper placed in the story with the highest interstory drift and the diagonal VE damper placed in the lowest story, is clearly more effective than the hybrid friction-VE dampers placed in the same cut-outs. The relatively new configuration of lower toggle VE damper seems to be the best choice for seismic mitigation. This study has shown that it is possible to have seismic mitigation, under all earthquakes, by using certain damper types appropriately located within the structure. The large amount and variety of information generated in this study can enable the optimum use of dampers to mitigate seismic response in medium-rise building structures.

References

- [Abbas and Kelly 1993] H. Abbas and J. M. Kelly, "A methodology for design of viscoelastic dampers in earthquake-resistant structures", Tech. report UCB/EERC-93/09, Earthquake Engineering Research Center, Univ. of California, Berkeley, 1993, Available at <http://nisee.berkeley.edu/elibrary/getdoc?id=238850>.
- [Abdullah 1999] M. Abdullah, "Optimal placement of DVFC controllers on buildings subjected to earthquake loading", *Earthq. Eng. Struct. Dyn.* **28**:2 (1999), 127–141.
- [Aiken et al. 1990] I. D. Aiken, J. M. Kelly, and P. Mahmoodi, "The application of VE dampers to seismically resistant structures", pp. 459–468 in *Proc. 4th U. S. National Conf. on Earthquake Engineering*, vol. 3, Palm Springs, California, 1990.
- [Ashour and Hanson 1987] S. A. Ashour and R. D. Hanson, "Elastic seismic response of buildings with supplemental damping", Tech. Report UMCE 87-1, Univ. of Michigan, Ann Arbor, MI, 1987.

- [Comerio et al. 2002] M. C. Comerio, J. C. Stallmeyer, W. T. Holmes, and P. Morris, “Nonstructural loss estimation: the UC Berkeley case study”, Tech. report PEER Report 2002/01, Pacific Earthquake Engineering Research Center, Univ. of California, Berkeley, Berkeley, 2002. Available at <http://nisee.berkeley.edu/elibrary/getdoc?id=1275992>.
- [Constantinou and Sigaher 2000] M. C. Constantinou and A. N. Sigaher, “Energy dissipation system configurations for improved performance”, in *Proc. of the 2000 Structures Congress and Exposition*, ASCE, Philadelphia, PA, May 8-10 2000.
- [Constantinou and Tadjbakhsh 1983] M. C. Constantinou and I. G. Tadjbakhsh, “Optimum design of a first story damping system”, *Comput. Struct.* **17**:2 (1983), 305–310.
- [Constantinou et al. 1998] M. C. Constantinou, T. T. Soong, and G. F. Dargush, “Passive energy dissipation systems for structural design and retrofit”, Monograph 1, Multidisciplinary Center for Earthquake Engineering Research, State Univ. of New York, Buffalo, N. Y., 1998, Available at <http://mceer.buffalo.edu/publications/monographs/98-MN01.asp>.
- [Hahn and Sathivageeswaran 1992] G. D. Hahn and K. R. Sathivageeswaran, “Effects of added-damper distribution on the seismic response of buildings”, *Comput. Struct.* **43**:5 (1992), 941–950.
- [Hanson 1993] R. Hanson, “Supplemental damping for improved seismic performance”, *Earthq. Spectra* **9**:3 (1993), 319–334.
- [Hanson et al. 1993] R. D. Hanson, I. Aiken, D. K. Nims, P. J. Richter, and R. Bachman, “State-of-the-art and state-of-the-practice in seismic energy dissipation”, pp. 449–471 in *ATC-17-1 seminar on seismic isolation, passive energy dissipation, and active control*, San Francisco, CA, 1993.
- [Hisano et al. 2000] K. Hisano, H. Kuribayashi, and K. Saitou, “The application example of the hybrid friction-VE damper combined the hysteretic damper with viscous damper to high-rise building”, pp. 451–456 in *5th Inter. Conf. on Motion and Vibration Control*, vol. 1, Sydney, Australia, 2000.
- [Kelly et al. 1972] J. M. Kelly, R. I. Skinner, and A. J. Heine, “Mechanism of Energy Absorption in Special Devices for Use in Earthquake Resistant Structures”, *Bull. New Zealand Soc. Earthq. Eng.* **5** (1972), 63–88.
- [Madsen 2001] L. P. B. Madsen, “Improving the seismic response of structures by the use of dampers in shear walls”, ME thesis, School of Civil Engineering, Queensland Univ. of Technology, Brisbane, Australia, 2001.
- [Natke 1993] H. G. Natke, “Topological structural optimization under dynamic loads”, pp. 67–78 in *Optimization of structural systems and applications*, edited by S. Hernandez and C. A. Brebbia, Comp. Mech. Publications, Southampton, 1993.
- [Ray et al. 1974] D. Ray, K. S. Pister, and A. K. Chopra, “Optimum design of earthquake resistant shear buildings”, Tech. Report UCB/EERC 74-3, Earthquake Engineering Research Center, Univ. of California at Berkeley, Berkeley, CA, 1974, Available at <http://nisee.berkeley.edu/elibrary/getdoc?id=41000961>.
- [Ribakov and Gluck 1999] Y. Ribakov and J. Gluck, “Optimal design of ADAS damped MDOF structures”, *Earthq. Spectra* **15**:2 (1999), 317–330.
- [Sadek et al. 1996] F. Sadek, B. Mohraz, A. W. Taylor, and R. M. Chung, “Passive energy dissipation devices for seismic applications”, Tech. report NISTIR 5923, Building and Fire Research Laboratory, National Institute of Standards and Technology, Gaithersburg, Maryland 20899, November 1996, Available at <http://www.fire.nist.gov/bfrlpubs/build97/art050.html>.
- [Shao and Miyamoto 1999] D. Shao and H. K. Miyamoto, “Viscous damper versus friction damper for retrofit of a non-ductile reinforced concrete building with unreinforced masonry infill”, SEAOC 1999 Convention, 1999, Available at http://www.vcdesign.com/msm/pdf_files/ViscousDampe3EE9C.pdf.
- [Welch 1967] P. D. Welch, “The use of fast Fourier transform for the estimation of power spectra: A method based on time averaging over short, modified periodograms”, *IEEE Trans. Audio Electroacoust.* **15**:2 (1967), 70–73.
- [Zhang and Soong 1992] R. H. Zhang and T. T. Soong, “Seismic design of viscoelastic dampers for structural applications”, *J. Struct. Eng.* **118**:5 (1992), 1375–1392.

Received 20 Dec 2005.

JULIUS MARKO: j2.marko@student.qut.edu.au

School of Urban Development, Queensland University of Technology, GPO Box 2434, Brisbane 4001, Australia

DAVID THAMBIRATNAM: d.thambiratnam@qut.edu.au

School of Urban Development, Queensland University of Technology, GPO Box 2434, Brisbane 4001, Australia

NIMAL PERERA: n2nperera@hotmail.com

Robert Bird & Partners, Warwick House, 25 Buckingham Palace Road, London SW1W 0PP, United Kingdom

THE EFFECT OF THIN FILM/SUBSTRATE RADII ON THE STONEY FORMULA FOR THIN FILM/SUBSTRATE SUBJECTED TO NONUNIFORM AXISYMMETRIC MISFIT STRAIN AND TEMPERATURE

XUE FENG, YONGGANG HUANG, HANQING JIANG, DUC NGO AND ARES J. ROSAKIS

Current methodologies used for the inference of thin film stress through curvature measurements are strictly restricted to stress and curvature states which are assumed to remain uniform over the entire film/substrate system. There are recent studies of film/substrate systems subjected to nonuniform but axisymmetric misfit strain and temperature changes. The film stresses were found to depend nonlocally on system curvatures (that is, depend on the full-field curvatures). A very simple stress-curvature relation was established, but it is limited to thin film and substrate of same radius. We extend the analysis to thin film and substrate of different radii. Remarkably the same simple stress-curvature relation still holds regardless of the film/substrate radii mismatch.

1. Introduction

Stoney used a plate system composed of a stress bearing thin film of thickness h_f , deposited on a relatively thick substrate, of thickness h_s , and derived a simple relation between the curvature κ of the system and the stress $\sigma^{(f)}$ of the film as follows:

$$\sigma^{(f)} = \frac{E_s h_s^2 \kappa}{6 h_f (1 - \nu_s)}. \quad (1)$$

In the above the subscripts “ f ” and “ s ” denote the thin film and substrate, respectively, and E and ν are the Young’s modulus and Poisson’s ratio. Equation (1) is called the Stoney formula, and it has been extensively used in the literature to infer film stress changes from experimental measurement of system curvature changes [Stoney 1909; Freund and Suresh 2004].

Stoney’s formula involves a number of assumptions given in the following:

- (i) both the film thickness h_f and the substrate thickness h_s are uniform, the film and substrate have the same radius R , and $h_f \ll h_s \ll R$;
- (ii) the strains and rotations of the plate system are infinitesimal;
- (iii) both the film and substrate are homogeneous, isotropic, and linearly elastic;
- (iv) the film stress states are in-plane isotropic or equi-biaxial (two equal stress components in any two, mutually orthogonal in-plane directions) while the out-of-plane direct stress and all shear stresses vanish;

Keywords: thin film radius, nonuniform misfit strain, nonuniform wafer curvatures, stress-curvature relations, nonlocal effects, interfacial shears.

- (v) the system's curvature components are equi-biaxial (two equal direct curvatures) while the twist curvature vanishes in all directions; and
- (vi) all surviving stress and curvature components are spatially constant over the plate system's surface, a situation which is often violated in practice.

Despite the explicitly stated assumptions, the Stoney formula is often arbitrarily applied to cases of practical interest where these assumptions are violated. This is typically done by applying Stoney's formula pointwise and thus extracting a local value of stress from a local measurement of the curvature of the system. This approach of inferring film stress clearly violates the uniformity assumptions of the analysis and, as such, its accuracy as an approximation is expected to deteriorate as the levels of curvature nonuniformity become more severe.

Following the initial formulation by Stoney, a number of extensions have been derived to relax some assumptions. Such extensions of the initial formulation include relaxation of the assumption of equi-biaxiality as well as the assumption of small deformations/deflections. A biaxial form of Stoney formula (with different direct stress values and nonzero in-plane shear stress) was derived by relaxing the assumption (v) of curvature equi-biaxiality [Freund and Suresh 2004]. Related analyses treating discontinuous films in the form of bare periodic lines [Wikstrom et al. 1999b] or composite films with periodic line structures (for example, bare or encapsulated periodic lines) have also been derived [Shen et al. 1996; Wikstrom et al. 1999a; Park and Suresh 2000]. These latter analyses have removed the assumptions (iv) and (v) of equi-biaxiality and have allowed the existence of three independent curvature and stress components in the form of two, nonequal, direct components and one shear or twist component. However, the uniformity assumption (vi) of all of these quantities over the entire plate system was retained. In addition to the above, single, multiple and graded films and substrates have been treated in various "large" deformation analyses [Masters and Salamon 1993; Salamon and Masters 1995; Finot et al. 1997; Freund 2000]. These analyses have removed both the restrictions of an equi-biaxial curvature state as well as the assumption (ii) of infinitesimal deformations. They have allowed for the prediction of kinematically nonlinear behavior and bifurcations in curvature states which have also been observed experimentally [Lee et al. 2001; Park et al. 2003; Fahnline et al. 1991]. These bifurcations are transformations from an initially equi-biaxial to a subsequently biaxial curvature state that may be induced by an increase in film stress beyond a critical level. This critical level is intimately related to the systems aspect ratio, that is, the ratio of in-plane to thickness dimension and the elastic stiffness. These analyses also retain the assumption (vi) of spatial curvature and stress uniformity across the system. However, they allow for deformations to evolve from an initially spherical shape to an energetically favored shape (for example, ellipsoidal, cylindrical or saddle shapes) which features three different, still spatially constant, curvature components [Lee et al. 2001; Park et al. 2003; Masters and Salamon 1993; Salamon and Masters 1995].

The above-discussed extensions of Stoney's methodology have not relaxed the most restrictive of Stoney's original assumption (vi) of spatial uniformity which does not allow film stress and curvature components to vary across the plate surface. This crucial assumption is often violated in practice since film stresses and the associated system curvatures are nonuniformly distributed over the plate area [Masters and Salamon 1994]. Recently Huang et al. [2005] and Huang and Rosakis [2005] relaxed the assumption (vi) (and also (iv) and (v)) to study the thin film/substrate system subject to nonuniform,

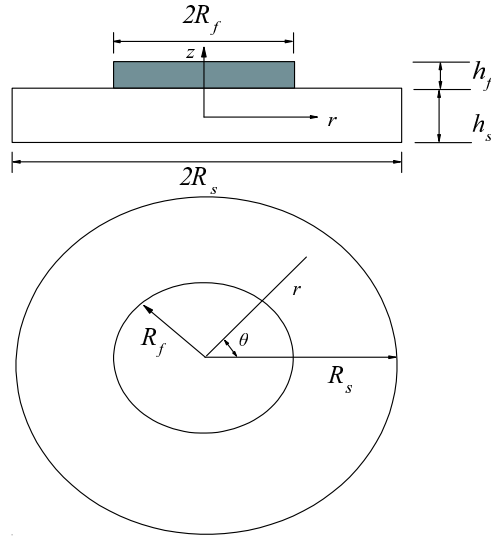


Figure 1. A schematic diagram of the thin film/substrate system with different film and substrate radii. The cylindrical coordinates (r, θ, z) are used.

axisymmetric misfit strain (in thin film) and temperature change (in both thin film and substrate), respectively. The axisymmetric variation in particular is often present in film/substrate systems due to the circular wafer geometry and the axisymmetric geometries of most processing equipment used to manufacture such wafers. Their most important result is that the film stresses depend *nonlocally* on the substrate curvatures, that is, they depend on curvatures of the entire substrate. Huang et al. [2005] and Huang and Rosakis [2005] established very simple relations between film stresses and substrate curvatures for arbitrarily nonuniform, axisymmetric misfit strain and temperature change, respectively, and such relations degenerate to Stoney's formula for uniform, equi-iaxial stresses and curvatures.

The main purpose of the present paper is to extend their work by relaxing the assumption (i) such that the thin film and substrate may have different radii. To do so we consider the case of a thin film and substrate with different radii subjected to arbitrary, radially symmetric misfit strain field $\varepsilon_m(r)$ in the thin film or temperature field $T(r)$ in the thin film and substrate. Our goal is to relate film stresses and system curvatures to the misfit strain (or temperature) distribution and to ultimately derive a relation between the film stresses and the system curvatures that would allow for the accurate experimental inference of film stress from full-field and real-time curvature measurements.

2. Nonuniform misfit strain

2.1. Governing equations. A circular thin film of radius R_f is deposited on a substrate of a larger radius $R_s > R_f$ (see Figure 1). The film thickness h_f is much less than the substrate thickness h_s , that is, $h_f \ll h_s$. The Young's modulus and Poisson's ratio of the film and substrate are denoted by E_f, ν_f, E_s and ν_s , respectively. The thin film is subjected to axisymmetric misfit strain distribution $\varepsilon_m(r)$, where r is the radial coordinate. The cylindrical coordinates (r, θ, z) are used (Figure 1) for this axisymmetric problem.

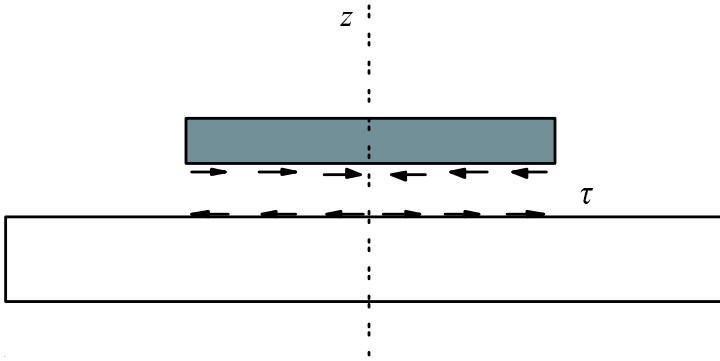


Figure 2. A schematic diagram of the nonuniform shear traction distribution at the interface between the film and the substrate.

The thin film and substrate are modeled as a membrane and a plate, respectively, since the film is very thin and has the negligible bending stiffness. Let u_f and u_s denote the radial displacements in the thin film and substrate (at the neutral axis). The strains are $\epsilon_{rr} = du/dr$ and $\epsilon_{\theta\theta} = u/r$, where u is u_f in the thin film and u_s in the substrate. The axial forces in the film and substrate can be obtained from the linear elastic constitutive model as

$$N_r = \frac{Eh}{1 - \nu^2} \left(\frac{du}{dr} + \nu \frac{u}{r} - (1 + \nu)\epsilon_{\text{misfit}} \right), \quad N_\theta = \frac{Eh}{1 - \nu^2} \left(\nu \frac{du}{dr} + \frac{u}{r} - (1 + \nu)\epsilon_{\text{misfit}} \right), \quad (2)$$

where E, ν, h and ϵ_{misfit} are E_f, ν_f, h_f and ϵ_m in the thin film and E_s, ν_s, h_s and 0 in the substrate.

The shear stress traction σ_{rz} at the film/substrate interface is denoted by $\tau(r)$ as shown in Figure 2. The normal stress traction σ_{zz} vanishes because the thin film cannot be subjected to bending. The equilibrium of forces requires

$$\frac{dN_r}{dr} + \frac{N_r - N_\theta}{r} \mp \tau = 0, \quad (3)$$

where $-\tau$ and $+\tau$ are for the thin film and substrate within the film portion ($r \leq R_f$), respectively, and τ vanishes for the substrate outside the film ($R_f < r \leq R_s$). The substitution of Equation (2) into Equation (3) yields the following governing equations for u_f, u_s and τ

$$\frac{d^2u_f}{dr^2} + \frac{1}{r} \frac{du_f}{dr} - \frac{u_f}{r^2} = \frac{1 - \nu_f^2}{E_f h_f} \tau + (1 + \nu_f) \frac{d\epsilon_m}{dr}, \quad \text{for } r \leq R_f, \quad (4)$$

$$\frac{d^2u_s}{dr^2} + \frac{1}{r} \frac{du_s}{dr} - \frac{u_s}{r^2} = \begin{cases} -\frac{1 - \nu_s^2}{E_s h_s} \tau, & \text{for } r \leq R_f, \\ 0, & \text{for } R_f < r \leq R_s. \end{cases} \quad (5)$$

Let w denote the lateral displacement of the substrate in the normal (z) direction. The bending moments in the substrate are given in terms of w by

$$M_r = \frac{E_s h_s^3}{12(1 - \nu_s^2)} \left(\frac{d^2w}{dr^2} + \frac{\nu_s}{r} \frac{dw}{dr} \right), \quad M_\theta = \frac{E_s h_s^3}{12(1 - \nu_s^2)} \left(\nu_s \frac{d^2w}{dr^2} + \frac{1}{r} \frac{dw}{dr} \right). \quad (6)$$

The out-of-plane force and moment equilibrium equations are

$$\frac{dM_r}{dr} + \frac{M_r - M_\theta}{r} + Q - \frac{h_s}{2}\tau = 0, \quad \frac{dQ}{dr} + \frac{Q}{r} = 0, \tag{7}$$

where Q is the shear force normal to the neutral axis, $h_s\tau/2$ is the contribution from the shear stress τ at the film/substrate interface within the film portion ($r \leq R_f$), and it vanishes for the substrate outside the film ($R_f < r \leq R_s$). The second equation in Equation (7) and the requirement of finite Q at the center $r = 0$ give $Q = 0$ in the entire substrate. The substitution of Equation (6) into the first equation in Equation (7) then gives the following governing equation for w and τ

$$\frac{d^3w}{dr^3} + \frac{1}{r} \frac{d^2w}{dr^2} - \frac{1}{r^2} \frac{dw}{dr} = \begin{cases} \frac{6(1-\nu_s^2)}{E_s h_s^2} \tau, & \text{for } r \leq R_f, \\ 0, & \text{for } R_f < r \leq R_s. \end{cases} \tag{8}$$

The continuity of displacement across the thin film/substrate interface requires

$$u_f = u_s - \frac{1}{2}h_s \frac{dw}{dr}, \quad \text{for } r \leq R_f. \tag{9}$$

Equations (4), (5), (8) and (9) constitute four ordinary differential equations for u_f , u_s , w and τ within the film portion ($r \leq R_f$). Outside the film ($R_f < r \leq R_s$) Equations (5) and (8) govern u_s and w .

The shear stress at the film/substrate interface can be obtained by eliminating u_f , u_s and w from these four equations as

$$\tau = -\frac{E_f h_f}{1 - \nu_f} \frac{d\varepsilon_m}{dr} \left(1 + \mathcal{O}\left(\frac{h_f}{h_s}\right) \right), \tag{10}$$

where the higher-order terms for $h_f/h_s \ll 1$ are neglected. That the interface shear stress is proportional to the gradient of misfit strain is a remarkable result. Equations (5) and (8) can then be solved analytically as

$$\frac{dw}{dr} = \begin{cases} -6 \frac{E_f h_f}{1 - \nu_f} \frac{1 - \nu_s^2}{E_s h_s^2} \frac{1}{r} \int_0^r \eta \varepsilon_m(\eta) d\eta + \frac{B_1}{2} r, & \text{for } r \leq R_f, \\ A_1 r + \frac{C_1}{r}, & \text{for } R_f < r \leq R_s, \end{cases} \tag{11}$$

$$u_s = \begin{cases} \frac{E_f h_f}{1 - \nu_f} \frac{1 - \nu_s^2}{E_s h_s^2} \frac{1}{r} \int_0^r \eta \varepsilon_m(\eta) d\eta + \frac{B_2}{2} r, & \text{for } r \leq R_f, \\ A_2 r + \frac{C_2}{r}, & \text{for } R_f < r \leq R_s, \end{cases} \tag{12}$$

where only the leading terms for $h_f/h_s \ll 1$ are shown, and B_1 , A_1 , C_1 , B_2 , A_2 and C_2 are constants to be determined by the continuity conditions across the edge of thin film ($r = R_f$) and boundary conditions at the edge of substrate ($r = R_s$) to be given in the next section. The displacement u_f in the thin film can be obtained from interface continuity condition in Equation (9).

2.2. Continuity conditions and boundary conditions. The displacement continuity conditions at the edge of thin film require

$$\left[\frac{dw}{dr} \right]_{r=R_f} = 0 \quad \text{and} \quad [u_s]_{r=R_f} = 0, \tag{13}$$

where $[\dots]$ stands for the jump. The jump of the axial force in substrate $[N_r^{(s)}]$ is related to the axial force in thin film $N_r^{(f)}$ by

$$N_r^{(f)}|_{r=R_f} - (N_r^{(s)})_{r=R_f} = 0,$$

such that the net external force vanishes. Similarly, the jump of the bending moment in substrate $[M_r]$ is related to the bending moment produced by the axial force in thin film with respect to the neutral axis of substrate by

$$-[M_r]_{r=R_f} - \frac{1}{2}(h_s + h_f)N_r^{(f)}|_{r=R_f} = 0$$

such that the net external moment vanishes.

The traction-free boundary conditions at the edge of substrate are

$$N_r^{(s)}|_{r=R_s} = 0 \quad \text{and} \quad M_r|_{r=R_s} = 0. \tag{14}$$

Equations (13)–(14) are 6 linear algebraic equations to determine B_1, A_1, C_1, B_2, A_2 and C_2 . The displacements in Equations (11), (12) and (9) are then given by

$$\frac{dw}{dr} = \begin{cases} -6 \frac{E_f h_f}{1-\nu_f} \frac{1-\nu_s^2}{E_s h_s^2} \left(\frac{1}{r} \int_0^r \eta \varepsilon_m(\eta) d\eta + \frac{1-\nu_s}{1+\nu_s} \frac{\bar{\varepsilon}_m}{2} r \right), & \text{for } r \leq R_f, \\ -6 \frac{E_f h_f}{1-\nu_f} \frac{1-\nu_s^2}{E_s h_s^2} \left(\frac{\bar{\varepsilon}_m}{2} \frac{R_s^2}{r} + \frac{1-\nu_s}{1+\nu_s} \frac{\bar{\varepsilon}_m}{2} r \right), & \text{for } R_f < r \leq R_s, \end{cases}$$

$$u_s = \begin{cases} \frac{E_f h_f}{1-\nu_f} \frac{1-\nu_s^2}{E_s h_s} \left(\frac{1}{r} \int_0^r \eta \varepsilon_m(\eta) d\eta + \frac{1-\nu_s}{1+\nu_s} \frac{\bar{\varepsilon}_m}{2} \cdot r \right), & \text{for } r \leq R_f, \\ \frac{E_f h_f}{1-\nu_f} \frac{1-\nu_s^2}{E_s h_s} \left(\frac{\bar{\varepsilon}_m}{2} \frac{R_s^2}{r} + \frac{1-\nu_s}{1+\nu_s} \frac{\bar{\varepsilon}_m}{2} r \right), & \text{for } R_f < r \leq R_s, \end{cases}$$

$$u_f = 4u_s, \quad \text{for } r \leq R_f,$$

where

$$\bar{\varepsilon}_m = \frac{2}{R_s^2} \int_0^{R_f} \eta \varepsilon_m(\eta) d\eta = \frac{1}{A_{\text{substrate}}} \int_{A_{\text{film}}} \varepsilon_m dA$$

is the average misfit strain, that is, the misfit strain of the thin film averaged over the entire substrate.

2.3. Thin film stresses and substrate curvatures. The substrate curvatures can be obtained from the displacement w as

$$\kappa_{rr} = \frac{d^2 w}{dr^2} = \begin{cases} -6 \frac{E_f h_f}{1-\nu_f} \frac{1-\nu_s^2}{E_s h_s^2} \left(\varepsilon_m - \frac{1}{r^2} \int_0^r \eta \varepsilon_m(\eta) d\eta + \frac{1-\nu_s}{1+\nu_s} \frac{\bar{\varepsilon}_m}{2} \right), & \text{for } r \leq R_f, \\ -6 \frac{E_f h_f}{1-\nu_f} \frac{1-\nu_s^2}{E_s h_s^2} \left(-\frac{\bar{\varepsilon}_m}{2} \frac{R_s^2}{r^2} + \frac{1-\nu_s}{1+\nu_s} \frac{\bar{\varepsilon}_m}{2} \right), & \text{for } R_f < r \leq R_s, \end{cases} \tag{15}$$

$$\kappa_{\theta\theta} = \frac{1}{r} \frac{dw}{dr} = \begin{cases} -6 \frac{E_f h_f}{1-\nu_f} \frac{1-\nu_s^2}{E_s h_s^2} \left(\frac{1}{r^2} \int_0^r \eta \varepsilon_m(\eta) d\eta + \frac{1-\nu_s}{1+\nu_s} \frac{\bar{\varepsilon}_m}{2} \right), & \text{for } r \leq R_f, \\ -6 \frac{E_f h_f}{1-\nu_f} \frac{1-\nu_s^2}{E_s h_s^2} \left(\frac{\bar{\varepsilon}_m}{2} \frac{R_s^2}{r^2} + \frac{1-\nu_s}{1+\nu_s} \frac{\bar{\varepsilon}_m}{2} \right), & \text{for } R_f < r \leq R_s. \end{cases} \tag{16}$$

The circumferential curvature $\kappa_{\theta\theta}$ is continuous across the edge of thin film ($r = R_f$), but the radial curvature has a jump. The sum of these two curvatures is

$$\kappa_{rr} + \kappa_{\theta\theta} = \begin{cases} -12 \frac{E_f h_f}{1-\nu_f} \frac{1-\nu_s}{E_s h_s^2} \left(\varepsilon_m - \frac{1-\nu_s}{2} (\varepsilon_m - \bar{\varepsilon}_m) \right), & \text{for } r \leq R_f, \\ -6 \frac{E_f h_f}{1-\nu_f} \frac{(1-\nu_s)^2}{E_s h_s^2} \bar{\varepsilon}_m, & \text{for } R_f < r \leq R_s, \end{cases}$$

where the first term on the right hand side of the first line corresponds to the local misfit strain ε_m , while the second term gives the deviation from the local misfit strain and is proportional to the difference between the local misfit strain and the average misfit strain $\varepsilon_m - \bar{\varepsilon}_m$. The difference between two curvatures in Equations (15)–(16) is

$$\kappa_{rr} - \kappa_{\theta\theta} = \begin{cases} -6 \frac{E_f h_f}{1-\nu_f} \frac{1-\nu_s^2}{E_s h_s^2} \left(\varepsilon_m - \frac{2}{r^2} \int_0^r \eta \varepsilon_m(\eta) d\eta \right), & \text{for } r \leq R_f, \\ 6 \frac{E_f h_f}{1-\nu_f} \frac{1-\nu_s^2}{E_s h_s^2} \frac{R_s^2}{r^2} \bar{\varepsilon}_m, & \text{for } R_f < r \leq R_s. \end{cases} \tag{17}$$

The stresses in the thin film are obtained from Equation (2) as

$$\sigma_{rr}^{(f)} = \frac{E_f}{1-\nu_f} \left\{ -\varepsilon_m + 4 \frac{E_f h_f}{1-\nu_f^2} \frac{1-\nu_s^2}{E_s h_s} \left(\varepsilon_m - (1-\nu_f) \frac{1}{r^2} \int_0^r \eta \varepsilon_m(\eta) d\eta + \frac{1+\nu_f}{2} \frac{1-\nu_s}{1+\nu_s} \bar{\varepsilon}_m \right) \right\},$$

$$\sigma_{\theta\theta}^{(f)} = \frac{E_f}{1-\nu_f} \left\{ -\varepsilon_m + 4 \frac{E_f h_f}{1-\nu_f^2} \frac{1-\nu_s^2}{E_s h_s} \left(\nu_f \varepsilon_m + (1-\nu_f) \frac{1}{r^2} \int_0^r \eta \varepsilon_m(\eta) d\eta + \frac{1+\nu_f}{2} \frac{1-\nu_s}{1+\nu_s} \bar{\varepsilon}_m \right) \right\}.$$

The sum and difference of these stresses have the following simple expressions

$$\sigma_{rr}^{(f)} + \sigma_{\theta\theta}^{(f)} = \frac{E_f}{1-\nu_f} (-2\varepsilon_m),$$

$$\sigma_{rr}^{(f)} - \sigma_{\theta\theta}^{(f)} = 4E_f \frac{E_f h_f}{1-\nu_f^2} \frac{1-\nu_s^2}{E_s h_s} \left(\varepsilon_m - \frac{2}{r^2} \int_0^r \eta \varepsilon_m(\eta) d\eta \right). \tag{18}$$

For uniform misfit strain $\varepsilon_m = \text{constant}$, the substrate curvatures from Equations (15)–(17) become

$$\kappa = \kappa_{rr} = \kappa_{\theta\theta} = -6 \frac{E_f h_f}{1-\nu_f} \frac{1-\nu_s}{E_s h_s^2} \left(1 - \frac{1-\nu_s}{2} \left(1 - \frac{R_f^2}{R_s^2} \right) \right) \varepsilon_m, \quad \text{for } r \leq R_f,$$

$$\kappa_{rr} = 3 \frac{E_f h_f}{1-\nu_f} \frac{1-\nu_s}{E_s h_s^2} \left((1+\nu_s) \frac{R_f^2}{r^2} - (1-\nu_s) \frac{R_f^2}{R_s^2} \right) \varepsilon_m, \quad \text{for } R_f < r \leq R_s,$$

$$\kappa_{\theta\theta} = -3 \frac{E_f h_f}{1-\nu_f} \frac{1-\nu_s}{E_s h_s^2} \left((1+\nu_s) \frac{R_f^2}{r^2} + (1-\nu_s) \frac{R_f^2}{R_s^2} \right) \varepsilon_m, \quad \text{for } R_f < r \leq R_s.$$

The curvature state is constant and equi-biaxial only within film portion $r \leq R_f$. It can be easily verified that the circumferential curvature is continuous across the edge of thin film, but the radial curvature has

a jump. The thin film stresses from (18) become

$$\sigma = \sigma_{rr}^{(f)} = \sigma_{\theta\theta}^{(f)} = \frac{E_f}{1 - \nu_f} (-\varepsilon_m).$$

For this special case only, the stress state becomes equi-biaxial. Elimination of misfit strain ε_m from the above two equations yields a simple relation

$$\sigma = \frac{E_s h_s^2}{6(1 - \nu_s) h_f \left(1 - \frac{1 - \nu_s}{2} \left(1 - \frac{R_f^2}{R_s^2} \right) \right)} \kappa,$$

where κ is the constant curvature within the film portion $r \leq R_f$. For the thin film and substrate of same radii, the above relation degenerates Stoney’s formula in Equation (1) which has been used to estimate the thin-film stress σ from the substrate curvature κ , if the misfit strain, stress and curvature are all constants, and if the plate system shape is spherical. For the thin film and substrate of different radii, the radius effect clearly comes into play. In the following, we establish a simple relation between film stress and substrate curvature for nonuniform misfit strain distribution.

2.4. Extension of Stoney formula for nonuniform misfit strain distribution. We extend the Stoney formula by establishing the direct relation between the thin-film stresses and substrate curvatures for the thin film and substrate of different radii subjected nonuniform misfit distribution. Both $\kappa_{rr} - \kappa_{\theta\theta}$ in Equation (17) and $\sigma_{rr}^{(f)} - \sigma_{\theta\theta}^{(f)}$ in Equation (18) are proportional to $\varepsilon_m(r) - \frac{2}{r^2} \int_0^r \eta \varepsilon_m(\eta) d\eta$. Therefore, elimination of misfit strain gives the difference $\sigma_{rr}^{(f)} - \sigma_{\theta\theta}^{(f)}$ in thin-film stresses directly proportional to the difference $\kappa_{rr} - \kappa_{\theta\theta}$ in substrate curvatures,

$$\sigma_{rr}^{(f)} - \sigma_{\theta\theta}^{(f)} = -\frac{2E_f h_s}{3(1 + \nu_f)} (\kappa_{rr} - \kappa_{\theta\theta}). \tag{19}$$

This relation is independent of the thin film and substrate radii, and is identical to its counterpart for the thin film and substrate with the same radii subjected to nonuniform misfit strain [Huang et al. 2005]. The above relation clearly shows that the radial and circumferential stress components will be equal only if the equivalent curvature components are also equal.

We now focus on the sum of thin-film stresses $\sigma_{rr}^{(f)} + \sigma_{\theta\theta}^{(f)}$ and sum of substrate curvatures $\kappa_{rr} + \kappa_{\theta\theta}$. We define the average substrate curvature $\overline{\kappa_{rr} + \kappa_{\theta\theta}}$ as

$$\overline{\kappa_{rr} + \kappa_{\theta\theta}} = \frac{1}{A_{\text{substrate}}} \iint_{A_{\text{substrate}}} (\kappa_{rr} + \kappa_{\theta\theta}) \eta d\eta d\theta = \frac{2}{R_s^2} \int_0^{R_s} \eta (\kappa_{rr} + \kappa_{\theta\theta}) d\eta,$$

where the integration is over the entire area $A_{\text{substrate}}$ of the substrate. The average substrate curvature can be related to the average misfit strain $\overline{\varepsilon_m}$ by averaging both sides of Equation (17), that is,

$$\overline{\kappa_{rr} + \kappa_{\theta\theta}} = 12 \frac{E_f h_f}{1 - \nu_f} \frac{1 - \nu_s}{E_s h_s^2} (-\overline{\varepsilon_m}).$$

Elimination of misfit strain ε_m and average misfit strain $\overline{\varepsilon_m}$ gives the sum of thin-film stresses in terms of curvatures as

$$\sigma_{rr} + \sigma_{\theta\theta} = \frac{E_s h_s^2}{6(1 - \nu_s) h_f} \left(\kappa_{rr} + \kappa_{\theta\theta} + \frac{1 - \nu_s}{1 + \nu_s} (\kappa_{rr} + \kappa_{\theta\theta} - \overline{\kappa_{rr} + \kappa_{\theta\theta}}) \right). \quad (20)$$

The above equation is once again independent of the thin film and substrate radii, and is identical to its counterpart for the thin film and substrate with the same radii subjected to nonuniform misfit strain [Huang et al. 2005]. Equations (19) and (20) provide direct relations between thin-film stresses and substrate curvatures. It is important to note that stresses at a point in the thin film depend not only on curvatures at the same point (local dependence), but also on the average curvature in the entire substrate (nonlocal dependence).

The interface stress $\tau(r)$ given in Equation (10) can also be directly related to substrate curvatures via

$$\tau = \frac{E_s h_s^2}{6(1 - \nu_s^2)} \frac{d}{dr} (\kappa_{rr} + \kappa_{\theta\theta}). \quad (21)$$

This provides a remarkably simple way to estimate the interface shear stress from the radial gradient of the sum of two substrate curvatures. Equation (21) is independent of the thin film and substrate radii, and is identical to its counterpart for the thin film and substrate with the same radii subjected to nonuniform misfit strain [Huang et al. 2005].

Since interfacial shear stresses are responsible for promoting system failures through delamination of the thin film from the substrate, Equation (21) has particular significance. It shows that such stresses are proportional to the radial gradient of $\kappa_{rr} + \kappa_{\theta\theta}$ and not to its magnitude as might have been expected of a local, Stoney-like formulation. The implementation value of Equation (21) is that it provides an easy way of inferring these special interfacial shear stresses once the full-field curvature information is available. As a result, the methodology also provides a way to evaluate the risk of and to mitigate such important forms of failure. It should be noted that for the special case of spatially constant curvatures, this interfacial shear stress τ vanishes as is the case for all Stoney-like formulations described in the introduction.

3. Nonuniform temperature

We now consider the thin film and substrate of radii R_f and $R_s > R_f$ subjected to nonuniform temperature change $T(r)$. The problem is still axisymmetric.

The linear elastic constitutive model given in Equation (2) still holds except that the misfit strain $\varepsilon_{\text{misfit}}$ is replaced by $\alpha_f T$ for the thin film and $\alpha_s T$ for the substrate, where α_f and α_s are the coefficients of thermal expansion. The equilibrium equations (3) and (7), moment-curvature relation (6), displacement continuity (9) across the thin film/substrate interface, and continuity and boundary conditions in Section 2.2 also hold.

The shear stress at the film/substrate interface is given by

$$\tau = \frac{E_f h_f}{1 - \nu_f^2} \left((1 + \nu_s) \alpha_s - (1 + \nu_f) \alpha_f \right) \frac{dT}{dr}.$$

This is a remarkable result that the interface shear stress is proportional to the gradient of temperature change. The displacements are given by

$$\frac{dw}{dr} = \begin{cases} \frac{6E_f h_f}{1-v_f^2} \frac{1-v_s^2}{E_s h_s^2} \left((1+v_s)\alpha_s - (1+v_f)\alpha_f \right) \frac{1}{r} \int_0^r \eta T(\eta) d\eta + \frac{B_1}{2} r, & \text{for } r \leq R_f, \\ \frac{3E_f h_f}{2(1-v_f)} \frac{1-v_s^2}{E_s h_s^2} \times \left\{ \left((1+v_s)\alpha_s - 2\alpha_f \right) \overline{T}_f + (1-v_s)\alpha_s \overline{T}_s \right\} \left(\frac{1-v_s}{1+v_s} \frac{R_f^2}{R_s^2} r + \frac{R_f^2}{r} \right), & \text{for } R_f < r \leq R_s, \end{cases}$$

$$u_s = (1+v_s)\alpha_s \frac{1}{r} \int_0^r \eta T(\eta) d\eta + \frac{1}{2}(1-v_s)\alpha_s \overline{T}_s, \quad \text{for } r \leq R_s,$$

$$u_f = u_s, \quad \text{for } r \leq R_f,$$

where

$$\overline{T}_f = \frac{1}{A_{\text{film}}} \iint_{A_{\text{film}}} T \eta d\eta d\theta = \frac{2}{R_f^2} \int_0^{R_f} \eta T d\eta \quad \text{and} \quad \overline{T}_s = \frac{1}{A_{\text{substrate}}} \iint_{A_{\text{substrate}}} T \eta d\eta d\theta = \frac{2}{R_s^2} \int_0^{R_s} \eta T d\eta$$

are the average temperatures in the film and substrate, respectively, and

$$\frac{B_1}{2} = \frac{3E_f h_f}{1-v_f^2} \frac{1-v_s^2}{E_s h_s^2} \times \left\{ \frac{1+v_f}{2} \left(\frac{1-v_s}{1+v_s} \frac{R_f^2}{R_s^2} + 1 \right) \left\{ \left((1+v_s)\alpha_s - 2\alpha_f \right) \overline{T}_f + (1-v_s)\alpha_s \overline{T}_s \right\} - \left((1+v_s)\alpha_s - (1+v_f)\alpha_f \right) \overline{T}_f \right\}.$$

The sum of two substrate curvatures is

$$\kappa_{rr} + \kappa_{\theta\theta} = \begin{cases} \frac{6E_f h_f}{1-v_f^2} \frac{1-v_s^2}{E_s h_s^2} \left((1+v_s)\alpha_s - (1+v_f)\alpha_f \right) T + B_1, & \text{for } r \leq R_f, \\ \frac{3E_f h_f}{1-v_f} \frac{(1-v_s)^2}{E_s h_s^2} \frac{R_f^2}{R_s^2} \left\{ \left((1+v_s)\alpha_s - 2\alpha_f \right) \overline{T}_f + (1-v_s)\alpha_s \overline{T}_s \right\}, & \text{for } R_f < r \leq R_s, \end{cases}$$

and the difference between two substrate curvatures is

$$\kappa_{rr} - \kappa_{\theta\theta} = \begin{cases} \frac{6E_f h_f}{1-v_f^2} \frac{1-v_s^2}{E_s h_s^2} \times \left((1+v_s)\alpha_s - (1+v_f)\alpha_f \right) \left(T - \frac{1}{r^2} \int_0^r \eta T(\eta) d\eta \right), & \text{for } r \leq R_f, \\ -\frac{3E_f h_f}{1-v_f} \frac{1-v_s^2}{E_s h_s^2} \times \left\{ \left((1+v_s)\alpha_s - 2\alpha_f \right) \overline{T}_f + (1-v_s)\alpha_s \overline{T}_s \right\} \frac{R_f^2}{r^2}, & \text{for } R_f < r \leq R_s. \end{cases}$$

Similarly, the sum and difference of thin-film stresses are given by

$$\begin{aligned} \sigma_{rr}^{(f)} + \sigma_{\theta\theta}^{(f)} &= \frac{E_f}{1-v_f} \left\{ \left((1+v_s)\alpha_s - 2\alpha_f \right) T + (1-v_s)\alpha_s \overline{T}_s \right\}, \\ \sigma_{rr}^{(f)} - \sigma_{\theta\theta}^{(f)} &= \frac{E_f}{1+v_f} (1+v_s)\alpha_s \left(T - \frac{2}{r^2} \int_0^r \eta T(\eta) d\eta \right). \end{aligned}$$

Elimination of temperature change gives the difference $\sigma_{rr}^{(f)} - \sigma_{\theta\theta}^{(f)}$ in thin-film stresses directly proportional to the difference $\kappa_{rr} - \kappa_{\theta\theta}$ in substrate curvatures,

$$\sigma_{rr}^{(f)} - \sigma_{\theta\theta}^{(f)} = \frac{E_s h_s^2}{6(1 - \nu_s)h_f} \frac{(1 - \nu_f)\alpha_s}{(1 + \nu_s)\alpha_s - (1 + \nu_f)\alpha_f} (\kappa_{rr} - \kappa_{\theta\theta}). \tag{22}$$

This relation is independent of the thin film and substrate radii, and is identical to its counterpart for the thin film and substrate with the same radii subjected to nonuniform temperature change [Huang and Rosakis 2005]. The sum of thin-film stresses $\sigma_{rr}^{(f)} + \sigma_{\theta\theta}^{(f)}$ is related to the sum of substrate curvatures $\kappa_{rr} + \kappa_{\theta\theta}$ by

$$\begin{aligned} \sigma_{rr}^{(f)} + \sigma_{\theta\theta}^{(f)} &= \frac{E_s h_s^2}{6(1 - \nu_s)h_f} \\ &\times \left\{ \kappa_{rr} + \kappa_{\theta\theta} + \left(\frac{1 - \nu_s}{1 + \nu_s} - \frac{(1 - \nu_f)\alpha_s}{(1 + \nu_s)\alpha_s - (1 + \nu_f)\alpha_f} \right) \right. \\ &\times \left. \left(\kappa_{rr} + \kappa_{\theta\theta} - \overline{\kappa_{rr} + \kappa_{\theta\theta}} \right) - \frac{1 + \nu_s}{2} \frac{(1 - \nu_f)\alpha_s}{(1 + \nu_s)\alpha_s - (1 + \nu_f)\alpha_f} \left(1 - \frac{R_f^2}{R_s^2} \right) \overline{\kappa_{rr} + \kappa_{\theta\theta}} \right\}, \end{aligned} \tag{23}$$

where

$$\overline{\kappa_{rr} + \kappa_{\theta\theta}} = \frac{1}{A_{\text{substrate}}} \iint_{A_{\text{substrate}}} (\kappa_{rr} + \kappa_{\theta\theta}) \eta \, d\eta \, d\theta$$

is the average substrate curvature. The above equation depends on the thin film and substrate radii, and is different from its counterpart for the thin film and substrate with the same radii subjected to nonuniform temperature change [Huang and Rosakis 2005].

The interface stress $\tau(r)$ can be directly related to substrate curvatures via

$$\tau = \frac{E_s h_s^2}{6(1 - \nu_s^2)} \frac{d}{dr} (\kappa_{rr} + \kappa_{\theta\theta}).$$

This once again provides a remarkably simple way to estimate the interface shear stress from the radial gradient of the sum of two substrate curvatures. Equation (23) is independent of the thin film and substrate radii, and is identical to its counterpart for the thin film and substrate with the same radii subjected to temperature change [Huang and Rosakis 2005].

4. Discussion and conclusions

The recent work of [Huang et al. 2005] and [Huang and Rosakis 2005] shows that, unlike Stoney’s formula in Equation (1), the thin film stresses depend on the substrate curvatures *nonlocally*—that is, the stress components at a point on the film depend on both the local value of the curvature components (at the same point) and on the value of curvatures of all other points on the plate system (nonlocal dependence). This demonstrates that analytical methods based on Stoney’s approach and its various extensions cannot handle the nonlocality of the stress/curvature dependence and may result in substantial stress prediction errors if such analyses are applied locally. The presence of nonlocal contributions, and the stress dependence on all curvature components, necessitates the use of full-field curvature measurement (over the entire surface of the plate system) in order to determine the film stresses. Furthermore, the

shear stress along the film/substrate interface is proportional to the radial derivative of the first curvature invariant $\kappa_{rr} + \kappa_{\theta\theta}$. This provides a means to determine the interface shear stress that is responsible for the delamination of thin film/substrate systems.

The results of [Huang et al. 2005] and [Huang and Rosakis 2005], however, are limited to thin film and substrate of the same radius. They are extended to thin film and substrate of different radii in the present paper. The most remarkable result is that, for thin film subjected to nonuniform, axisymmetric misfit strain, the film and substrate radii have no effect on the relation between thin film stresses and substrate curvatures, i.e., the stress-curvature relation is identical to that for thin film and substrate of the same radius. This conclusion is particularly useful to the determination of thin film stresses from substrate curvatures since one only needs to know the local and average curvatures of the substrate, and not the thin film and substrate radii.

For thin film and substrate subjected to nonuniform, axisymmetric temperature change, the film and substrate radii still do not affect the difference in film stresses $\sigma_{rr}^{(f)} - \sigma_{\theta\theta}^{(f)}$, but they influence the sum of film stresses $\sigma_{rr}^{(f)} + \sigma_{\theta\theta}^{(f)}$. The reason for this difference between misfit strain and temperature change is the former occurs only in the film, while the latter occurs in both the thin film and substrate, and the nonuniform temperature change in the substrate leads to stresses and curvatures that depend on the radii.

For both axisymmetric misfit strain and temperature change, the interface shear stress is always proportional to the radial gradient of curvature sum, and is independent of the thin film and substrate radii.

References

- [Fahnline et al. 1991] D. E. Fahnline, C. B. Masters, and N. J. Salamon, "Thin film stresses from nonspherical substrate bending measurements", *J. Vac. Sci. Technol. A* **9**:4 (1991), 2483–2487.
- [Finot et al. 1997] M. Finot, I. Blech, S. S., and H. Fijimoto, "Large deformation and geometric instability of substrates with thin-film deposits", *J. Appl. Phys.* **81**:8 (1997), 3457–3464.
- [Freund 2000] L. B. Freund, "Substrate curvature due to thin film mismatch strain in the nonlinear deformation range", *J. Mech. Phys. Solids* **48**:6-7 (2000), 1159–1174. MR 2001c:74029
- [Freund and Suresh 2004] L. B. Freund and S. Suresh, *Thin film materials; Stress, defect formation and surface evolution*, Cambridge University Press, New York, 2004.
- [Huang and Rosakis 2005] Y. Huang and A. J. Rosakis, "Extension of Stoney's formula to non-uniform temperature distributions in thin film/substrate systems: The case of radial symmetry", *J. Mech. Phys. Solids* **53**:11 (2005), 2483–2500.
- [Huang et al. 2005] Y. Huang, D. Ngo, and A. J. Rosakis, "Non-uniform, axisymmetric misfit strain: in thin films bonded on plate substrates/substrate systems: the relation between non-uniform film stresses and system curvatures", *Acta. Mech. Sinica* **21**:4 (2005), 362–370.
- [Lee et al. 2001] H. Lee, A. J. Rosakis, and L. B. Freund, "Full field optical measurement of curvatures in ultra-thin film/substrate systems in the range of geometrically nonlinear deformations", *J. Appl. Phys.* **89**:11 (2001), 6116–6129.
- [Masters and Salamon 1993] C. B. Masters and N. J. Salamon, "Geometrically nonlinear stress–deflection relations for thin film/substrate systems", *Int. J. Engrg. Sci.* **31**:6 (1993), 915–925.
- [Masters and Salamon 1994] C. B. Masters and N. J. Salamon, "Geometrically nonlinear stress-deflection relations for thin film/substrate systems with a finite element comparison", *J. Appl. Mech. (ASME)* **61** (1994), 872–878.
- [Park and Suresh 2000] T. S. Park and S. Suresh, "Effects of line and passivation geometry on curvature evolution during processing and thermal cycling in copper interconnect lines", *Acta Mater.* **48**:12 (2000), 3169–3175.
- [Park et al. 2003] T. S. Park, S. Suresh, A. J. Rosakis, and J. Ryu, "Measurement of full field curvature and geometrical instability of thin film-substrate systems through CGS interferometry", *J. Mech. Phys. Solids* **51**:11-12 (2003), 2191–2211.

- [Salamon and Masters 1995] N. J. Salamon and C. B. Masters, “Bifurcation in isotropic thin film/substrate plates”, *Int. J. Solids Struct.* **32**:3-4 (1995), 473–481.
- [Shen et al. 1996] Y. L. Shen, S. Suresh, and I. A. Blech, “Stresses, curvatures, and shape changes arising from patterned lines on silicon wafers”, *J. Appl. Phys.* **80**:3 (1996), 1388–1398.
- [Stoney 1909] G. G. Stoney, “The tension of metallic films deposited by electrolysis”, *Proc. R. Soc. Lond.* **82**:553 (1909), 172–175.
- [Wikstrom et al. 1999a] A. Wikstrom, P. Gudmundson, and S. Suresh, “Analysis of average thermal stresses in passivated metal interconnects”, *J. Appl. Phys.* **86**:11 (1999), 6088–6095.
- [Wikstrom et al. 1999b] A. Wikstrom, P. Gudmundson, and S. Suresh, “Thermoelastic analysis of periodic thin lines deposited on a substrate”, *J. Mech. Phys. Solids* **47**:5 (1999), 1113–1130.

Received 27 Dec 2005.

XUE FENG: xuefeng@uiuc.edu

Department of Mechanical and Industrial Engineering, University of Illinois, Urbana, IL 61801, United States

YONGGANG HUANG: huang9@uiuc.edu

Department of Mechanical and Industrial Engineering, University of Illinois, Urbana, IL 61801, United States

HANQING JIANG: hqjiang@uiuc.edu

Department of Mechanical and Aerospace Engineering, Arizona State University, Tempe, AZ 85287, United States

DUC NGO: ducngo2@uiuc.edu

Department of Mechanical and Industrial Engineering, University of Illinois, Urbana, IL 61801, United States

ARES J. ROSAKIS: rosakis@aero.caltech.edu

Graduate Aeronautical Laboratory, California Institute of Technology, Pasadena, CA 91125, United States

YIELD OF RANDOM ELASTOPLASTIC MATERIALS

WEI LI AND MARTIN OSTOJA-STARZEWSKI

When separation of scales in random media does not hold, the representative volume element (RVE) of deterministic continuum mechanics does not exist in the conventional sense, and new concepts and approaches are needed. This subject is discussed here in the context of microstructures of two types – planar random chessboards, and planar random inclusion-matrix composites – with microscale behavior of the elastic-plastic-hardening (power-law) variety. The microstructures are assumed to be spatially homogeneous and ergodic. Principal issues under consideration are yield and incipient plastic flow of statistical volume elements (SVE) on mesoscales, and the scaling trend of SVE to the RVE response on the macroscale. Indeed, the SVE responses under uniform displacement (or traction) boundary conditions bound from above (or below, respectively) the RVE response. We show through extensive simulations of plane stress that the larger the mesoscale, the tighter are both bounds. However, mesoscale flows under both kinds of loading do not generally display normality. Also, within the limitations of currently available computational resources, we do not recover normality (or even a trend towards it) when studying the largest possible SVE domains.

1. Introduction

For over a century, plasticity of materials has principally been studied from a homogeneous continuum perspective, where the deterministic response of a Representative Volume Element (RVE) was assumed a priori. The past two decades have seen an increasing focus on determination of effective plastic response from micromechanical considerations, albeit without much consideration of the finite-size-scaling to the RVE, for example, [Castaneda and Suquet 1997]. However, if one considers such a scaling, one must look at one or both of the following: stochastic responses below the RVE level, and the solution of plasticity problems where the random field is of finite extent. In the first case, one has to work with a Statistical Volume Element (SVE) defined over an ensemble of specimens not large enough to be the RVE, while in the second case one has to revisit various boundary value problems of plasticity (such as a punch on a half-space) in a random field setting. The RVE is set up on a macroscale, while the SVE is set up on a mesoscale. Reviews of all these issues have recently been presented by [Ostoja-Starzewski 2005; 2006].

Note that most micromechanics studies aim at determining the effective constitutive properties at the RVE level without clearly specifying the RVE size. Many studies obviate the entire problem by simply postulating a fictitious periodic microstructure, and directly identifying the periodic cell as the RVE. To introduce scale effects, consider Figure 1, which shows two different types of model random media, both much smaller than the RVE. It is convenient here to use a dimensionless scale parameter $\delta (= L/d)$ to characterize the mesoscale. Here d is the heterogeneity size, that is, an inclusion's diameter, and L is the

Keywords: random media, scale effects, plasticity, RVE, homogenization.

mesoscale size. As we pass from the mesoscale (δ finite) to macroscale (δ infinite), the RVE is obtained, and the question is: at what δ does RVE apply? Clearly, $\delta = \infty$ is impractical, but perhaps a response close to RVE can be attained on a relatively small mesoscale.

In this study we focus on the passage from SVE to RVE. If that passage—effectively, a scale dependence of constitutive response—displays a clear trend in a specified sense, we say that the RVE can be approximated within a certain error on a specific length scale. Our approach follows the first study in [Jiang et al. 2001], and is a particular case of a general methodology to assess RVE size [Huet 1990; Sab 1992] in elasticity and inelasticity in the sense of [Hill 1963], and to set up micromechanically-based random fields of continuum properties [Ostoja-Starzewski and Wang 1989; Ostoja-Starzewski 1994]. This approach has primarily been used in linear elasticity [Hazanov and Huet 1994; Cluni and Gusella 2004; Kanit et al. 2003; Ostoja-Starzewski 1999; 2000], and in new inroads in viscoelasticity [Huet 1995; 1999], elastoplasticity [Jiang et al. 2001; Ostoja-Starzewski 2005], plasticity with damage [Clayton and McDowell 2004], thermomechanics with internal variables [Ostoja-Starzewski 2002], and finite (thermo)elasticity [Khisaeva and Ostoja-Starzewski 2006]. Related studies in linear thermoelasticity and Stokesian flow in porous media are currently underway [Du and Ostoja-Starzewski 2006a; 2006b]. For elastic-perfectly plastic materials, similar results have been obtained by [He 2001] using a mathematically more rigorous analysis involving gauge functions.

Using this approach, it has already been shown that the effective plastic response of a random material with a statistically homogeneous and ergodic microstructure can be bounded from above and below by responses obtained under uniform kinematic and traction boundary conditions, respectively, applied to finite size domains. This procedure leads to scale-dependent hierarchies of upper and lower bounds, which converge, as the scale tends to infinity, towards the RVE. In particular, we present a computational mechanics study of yield and incipient plastic flow of SVE, and the aforementioned trend to the RVE, for two kinds of model planar random materials in plane stress: a random two-phase chessboard (Figure 1 (a, b)), and a matrix-inclusion composite (Figure 1 (c, d)). We also examine scale dependence of the flow rule, to determine whether normality holds. We find that even though each phase alone possesses normality, the mesoscale flow rule, in general, does not.

2. Model Formulation

2.1. Random material. The formulation of deterministic continuum mechanics involves a tacit assumption—the so-called *separation of scales*:

$$d < L \ll L_{\text{macro}}, \quad (2-1)$$

where d is the microscale (e.g., typical grain size), L is the size of RVE, and L_{macro} is the macro size which usually is assumed to be much larger than the RVE. The size of RVE, L , relative to d is not known a priori. That is why, to be on the safe side, the left inequality in Equation (2-1) is often replaced with \ll . Thus, the establishment of L/d for which the RVE may actually be adopted with a certain accuracy (of, say, 10%), is of key interest. Consistent with the methodology of our previous studies, we use a dimensionless number

$$\delta = L/d \geq 1$$

to denote the mesoscale.

In two dimensions, we work with square-shaped mesoscale domains, with sides of length L , containing the microstructure of characteristic microscale d (inclusion diameter); see Figure 1. Following [Huet 1990], we sometimes call the mesoscale properties *apparent*, and reserve the term *effective* for the RVE level.

Specimens $B_\delta(\omega)$ are drawn from the ensemble $\mathbf{B} = \{B_\delta(\omega); \omega \in \Omega\}$, where Ω is a sample space. For any sample $B_\delta(\omega)$ of size δ taken from Ω , its properties are deterministic but different from each other due to the random nature of the medium. All samples $B_\delta(\omega)$ constitute the *ensemble* $\mathbf{B} = \{B_\delta(\omega); \omega \in \Omega\}$.

The ergodic property (or hypothesis) of the random field of a specific material property \mathbf{F} , such as the stiffness tensor \mathbf{C} , can be described as

$$\overline{\mathbf{F}(\omega)} \equiv \lim_{L \rightarrow \infty} \frac{1}{L} \int_0^L \mathbf{F}(\omega, x) dx = \int_{\Omega} \mathbf{F}(\omega, x) dP(\omega) \equiv \langle \mathbf{F}(x) \rangle.$$

Here the overbar indicates the volume average, while $\langle \rangle$ stands for the ensemble average, whereby $P(\omega)$ is the probability measure assigned to the ensemble $\{\mathbf{F}(\omega, x); \omega \in \Omega, x \in \mathbf{X}\}$. In practice, we use

$$\overline{\mathbf{F}(\omega)} \equiv \frac{1}{M} \sum_{m=1}^M \mathbf{F}(\omega, x_m) = \frac{1}{N} \sum_{n=1}^N \mathbf{F}(\omega_n, x) \equiv \langle \mathbf{F}(x) \rangle,$$

where M denotes the finite number of sampling points over one realization ω , and N denotes the finite number of realizations ω_n at one sampling point.

For materials with statistically homogeneous and ergodic properties, the mesoscale properties should be obtained by taking the ensemble average over \mathbf{B} . Usually, the smaller the sample size δ , the larger the number of samples which should be taken. When the window size δ approaches ∞ , the mesoscale properties of any specimen $B_\delta(\omega)$ in \mathbf{B} should be identical and same as effective properties.

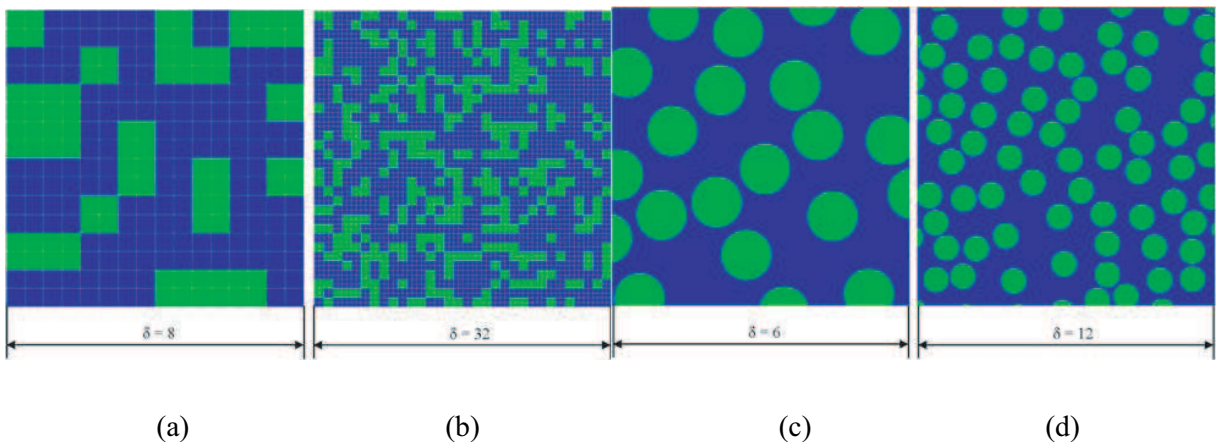


Figure 1. Realizations of random chessboard and matrix-inclusion materials on two mesoscales at a nominal volume fraction 35%. Blue pertains to a hard phase, and green to a soft one. (a) $\delta = 8$, chessboard; (b) $\delta = 32$, chessboard; (c) $\delta = 6$, matrix-inclusion; (d) $\delta = 12$, matrix-inclusion.

2.2. Boundary conditions. For linear elastic heterogeneous materials, the necessary and sufficient condition of the equivalence between energetically and mechanically defined effective properties is contained in the well-known Hill condition [Hill 1963]

$$\overline{\boldsymbol{\sigma} : \boldsymbol{\varepsilon}} = \bar{\boldsymbol{\sigma}} : \bar{\boldsymbol{\varepsilon}}. \tag{2-2}$$

[Hazanov 1998] generalized Equation (2-2) to nonlinear heterogeneous materials as

$$\overline{\int \boldsymbol{\sigma} : d\boldsymbol{\varepsilon}} = \int \bar{\boldsymbol{\sigma}} : d\bar{\boldsymbol{\varepsilon}}.$$

For materials with perfect interfaces and no body forces, Equation (2-2) becomes

$$\int_{\partial B_\delta} (\mathbf{t} - \bar{\boldsymbol{\sigma}} \cdot \mathbf{n}) \cdot (\mathbf{u} - \bar{\boldsymbol{\varepsilon}} \cdot \mathbf{x}) dS = 0.$$

where \mathbf{t} is the traction vector, \mathbf{u} is the displacement vector on the specimen boundary ∂B_δ , \mathbf{n} is the exterior unit normal vector, and \mathbf{x} is the coordinate vector. The above equation clearly shows that among the solutions of the Hill condition one can identify three important types of boundary conditions:

(1) *uniform kinematic* boundary condition (UKBC, also known as *displacement, essential* or *Dirichlet*)

$$\mathbf{u}(\mathbf{x}) = \boldsymbol{\varepsilon}^0 \cdot \mathbf{x}, \quad \text{for all } \mathbf{x} \in \partial B_\delta, \tag{2-3}$$

(2) *uniform static* boundary condition (USBC, also known as *traction, natural* or *Neumann*)

$$\mathbf{t}(\mathbf{x}) = \boldsymbol{\sigma}^0 \cdot \mathbf{n}, \quad \text{for all } \mathbf{x} \in \partial B_\delta, \tag{2-4}$$

(3) *uniform mixed-orthogonal* boundary condition (UMBC)

$$(\mathbf{t}(\mathbf{x}) - \boldsymbol{\sigma}^0 \cdot \mathbf{n}) \cdot (\mathbf{u}(\mathbf{x}) - \boldsymbol{\varepsilon}^0 \cdot \mathbf{x}) = 0, \quad \text{for all } \mathbf{x} \in \partial B_\delta. \tag{2-5}$$

In studies of scale effects thus far, most research has been done in terms of the first two cases since these provide, respectively, upper bounds and lower bounds for the effective properties. In common engineering practice, however, the UKBC and USBC loadings can be very difficult to realize. Interestingly, most laboratory and industrial testing is done under loadings closer to the mixed-orthogonal boundary condition in Equation (2-5).

2.3. Constitutive laws for elastic-plastic-hardening materials. For elastic-plastic-hardening materials, the constitutive responses of both phases $p (= 1, 2)$ are taken in the form [Hill 1950]

$$\begin{aligned} d\varepsilon'_{ij} &= \frac{d\sigma'_{ij}}{2G_p} + h \cdot df_p \cdot \frac{\partial f_p}{\partial \sigma_{ij}} && \text{when } f_p = c_p \text{ and } df_p \geq 0, \\ d\varepsilon'_{ij} &= d\sigma'_{ij}/2G_p && \text{when } f_p < c_p, \\ d\varepsilon &= d\sigma \cdot \frac{(1 - 2\nu_p)}{2G_p(1 + \nu_p)} && \text{where } \left(d\varepsilon = \frac{d\varepsilon_{ii}}{3}, d\sigma = \frac{d\sigma_{ii}}{3} \right), \end{aligned} \tag{2-6}$$

where primes indicate deviatoric tensor components. In Equation (2-6) G_p is a shear modulus, ν_p is a Poisson's ratio, f_p is a yield function, and c_p is a material constant. For von Mises–Huber materials

with associated flow rule and isotropic hardening, the yield surface is defined as

$$f_p = \sqrt{\frac{3}{2}\sigma'_{ij}\sigma'_{ij}} = c_p.$$

As is well known, the von Mises–Huber yield surface in the π -plane is that of a circle, and in the $\sigma_1\sigma_2$ -plane, is an ellipse. The flow rule (that is, the plastic strain direction) is described as

$$d\varepsilon_{ij}^p = d\lambda \cdot C \cdot \frac{\partial f}{\partial \sigma_{ij}} = d\lambda \cdot \frac{3}{2} \frac{\sigma'_{ij}}{\sqrt{\frac{3}{2}\sigma'_{kl}\sigma'_{kl}}}. \tag{2-7}$$

Since $f(\sigma_{ij}) = \text{constant}$ on the yield surface, $\frac{\partial f}{\partial \sigma_{ij}}$ must be normal to that surface; therefore, the plastic strain vector is normal to the yield locus.

2.4. Hierarchy of mesoscale bounds of stress/strain response for elastoplastic random materials. Under monotonically increasing loading, the elastoplastic hardening composites can be treated as physically nonlinear elastic materials. Using the variational principles, one can obtain

$$\begin{aligned} \langle w(\varepsilon^0, \infty) \rangle &\leq \langle w(\varepsilon^0, \delta) \rangle \leq \langle w(\varepsilon^0, \delta') \rangle \leq \langle w(\varepsilon^0, 1) \rangle \equiv w^V, \quad 1 < \delta' < \delta < \infty \\ \langle w^*(\sigma^0, \infty) \rangle &\leq \langle w^*(\sigma^0, \delta) \rangle \leq \langle w^*(\sigma^0, \delta') \rangle \leq \langle w^*(\sigma^0, 1) \rangle \equiv w^{*R}, \quad 1 < \delta' < \delta < \infty \end{aligned}$$

here $w(\varepsilon^0, \delta)$ and $w^*(\sigma^0, \delta)$ — obtained by Equations (2–3) and (2–4), respectively — represent the volume average strain energy and complementary energy densities of an arbitrary window of size δ that may be placed anywhere in the material domain of any random sample. w^V and w^{*R} are the Voigt and Reuss bounds respectively.

Since the stiffness and compliance tensors are no longer constant any more, we now consider the tangent stiffness and compliance moduli (C_δ^{Td} or S_δ^{Tt}), which are defined as

$$\overline{d\sigma} = C_\delta^{Td} : \overline{d\varepsilon} = C_\delta^{Td} : d\varepsilon^0; \quad \overline{d\varepsilon} = S_\delta^{Tt} : \overline{d\sigma} = S_\delta^{Tt} : d\sigma^0,$$

where superscript d (or t) indicates that the response is obtained under the displacement (or traction) boundary condition. Finally, there is a hierarchy of bounds on the effective tangent modulus for a linear comparison solid: [Jiang et al. 2001; Ostoja-Starzewski 2005]

$$\begin{aligned} \langle S_1^{TS} \rangle^{-1} &\equiv \langle S_1^{Tt} \rangle^{-1} \leq \dots \leq \langle S_{\delta'}^{Tt} \rangle^{-1} \leq \langle S_\delta^{Tt} \rangle^{-1} \leq \dots \leq \langle S_\infty^T \rangle^{-1} \\ &\equiv C_\infty^T \leq \dots \leq \langle C_\delta^{Td} \rangle \leq \langle C_{\delta'}^{Td} \rangle \leq \dots \leq \langle C_1^{Td} \rangle \\ &\equiv \langle C_1^{TT} \rangle, \quad \text{for all } \delta' < \delta \leq \infty, \end{aligned} \tag{2-8}$$

where $\langle s_1^{TS} \rangle^{-1}$ and $\langle c_1^{TT} \rangle$ are the Sachs and Taylor bounds, respectively.

2.5. Hierarchy of mesoscale yield surface bounds for elastoplastic random materials. To study the mesoscale yield surface, one must first define the mesoscale yield condition for a specimen. Due to the heterogeneity of the material, stress distribution is nonuniform under uniform loading, which leads the local stress to reach the yield stress level somewhere in the material domain, even though the volume average stress is far lower than the yield stress of the material. Obviously, it would not be reasonable

Material parameters	ε_0	σ_0 (MPa)	N	E (GPa)	ν
Soft phase	1.036e-3	75	0.25	72.4	0.33
Hard phase	1.425e-3	295	0.15	207	0.32

Table 1. Material parameters.

to define the yield condition of a sample as the stress level when the first yield occurs in the specimen. [Dvorak and Bahei-El-Din 1987] proposed a bimodal plasticity theory for heterogeneous composites where both the fiber and the matrix participate in carrying the applied load. According to this theory, the overall yield of a sample indicates magnitudes of the overall stress which causes local volume average stress to satisfy the yield condition in any phase.

For von Mises–Huber materials, the mesoscale yield condition of the composite in the overall stress space Σ is defined as

$$F_\delta(\Sigma) = \inf \left\{ \Sigma \in \mathbf{R}^{3 \times 3} \mid \exists \sigma(x) \text{ with } \bar{\sigma} = \Sigma, f_p(\mathbf{K}_p \Sigma) = c_p, \text{ for all } x \in B_\delta, p = 1, 2 \right\}, \quad (2-9)$$

where \mathbf{K}_p is the mechanical stress concentration factor, with (6×6) matrices, and Σ is treated as a (6×1) vector.

For a rigid-perfectly-plastic material, the hierarchy of inclusions for mesoscale yield surfaces is given in [Ostoja-Starzewski 2005] as

$$D_1^d \supseteq \dots \supseteq D_{\delta'}^d \supseteq D_\delta^d \supseteq \dots \supseteq D_\infty^d \equiv D_\infty^t \supseteq \dots \supseteq D_\delta^t \supseteq D_{\delta'}^t \supseteq \dots \supseteq D_1^t, \quad \text{for all } \delta' = \delta/2, \quad (2-10)$$

where D_δ denotes a domain in stress space bounded by an ensemble average yield surface $\langle F_\delta \rangle$. Without proof, we now conjecture that in an elastoplastic problem, the same type of hierarchy holds based on the definition (2–9). We confirm this conjecture through computations in Section 3.5.

2.6. The flow rule for elastoplastic random materials. The flow rule in Equation (2–7) pertains to homogeneous materials. However for heterogeneous materials, it is not at all clear that the normality rule (that is, the associated flow rule) still holds on mesoscales. In fact, it is still an open issue whether the normality rule is recovered computationally at the RVE level, that is, whether

$$d\varepsilon_{ij}^p = d\lambda \cdot C \cdot \frac{\partial f}{\partial \sigma_{ij}} \quad \text{or} \quad d\varepsilon_{ij}^p \neq d\lambda \cdot C \cdot \frac{\partial f}{\partial \sigma_{ij}}. \quad (2-11)$$

3. Computational mechanics of two random materials

3.1. Models of two random materials. We investigated two model two-phase composite materials. The first is a planar random chessboard, Figure 1 (a-b); the second one is a porous medium generated by placing circular disks whose centers come from a planar hard-core Poisson point field, Figure 1 (c-d). In both cases, the volume fraction of hard phases is 0.35. The *hard core* condition means that no two disks may touch. In fact, in order to avoid narrow-neck effects in the fluid field, the minimum distance between disk centers is set at 1.1 times the diameter of the disk.

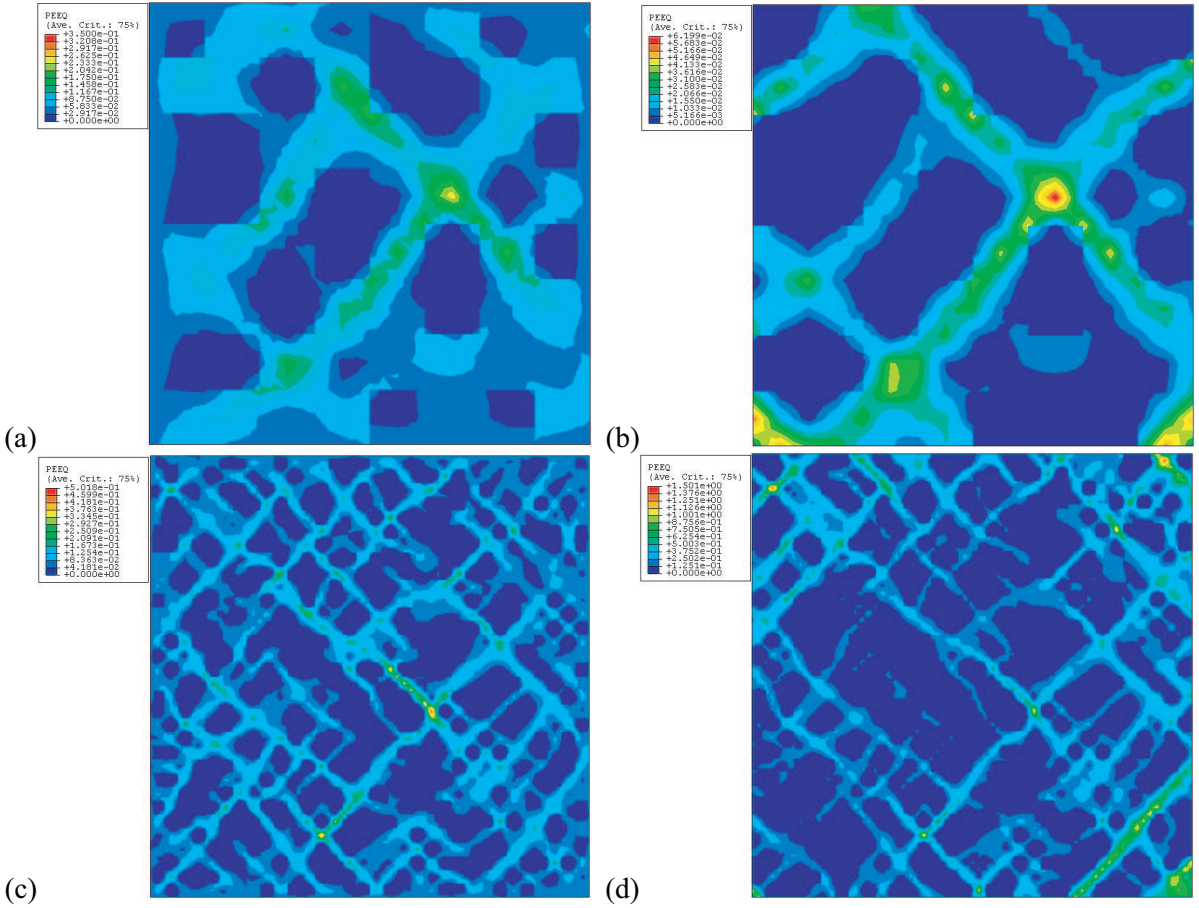


Figure 2. Contour plots of equivalent plastic strain for windows shown in Figure 1 (a, b) under different boundary conditions: (a, c) displacement; (b, d) traction.

A numerical analysis of composite materials shown in Figure 1, in plane stress, is carried out using ABAQUS. The interface between two phases is assumed to be perfect bonding, i.e. there is no phase-separation and no slip at interphase boundary. The stress-strain response is characterized by a piece-wise power law [Dowling 1993]

$$i\sigma/\sigma_0 = \begin{cases} \varepsilon/\varepsilon_0, & \text{if } \varepsilon \leq \varepsilon_0, \\ (\varepsilon/\varepsilon_0)^N, & \text{else.} \end{cases}$$

The material parameters are given in Table 1. The von Mises–Huber yield criterion, with associated flow rule, is assumed for each phase. Shear loading is applied through one of two types of uniform boundary conditions:

$$\text{UKBC: } \varepsilon_{11}^0 = -\varepsilon_{22}^0 = \varepsilon, \varepsilon_{12}^0 = 0 \quad \text{or} \quad \text{USBC: } \sigma_{11}^0 = -\sigma_{22}^0 = \sigma, \sigma_{12}^0 = 0. \quad (3-1)$$

Here the prescribed stress and strain are ~ 0.04 and $\sim 1.75e8$ Pa, respectively. The UMBC is not being used.

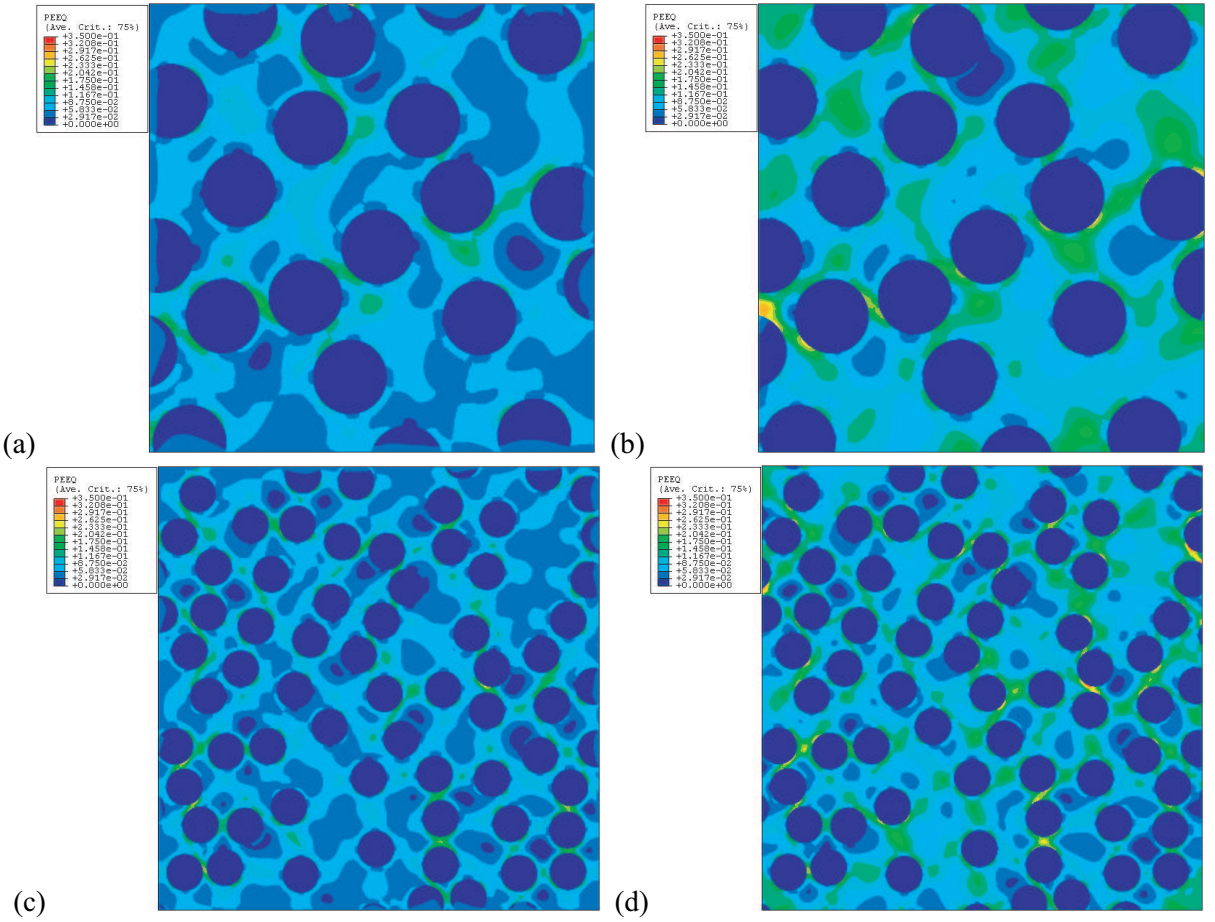


Figure 3. Contour plots of equivalent plastic strain for window shown in Figure 1 (c, d) under different boundary conditions: (a, c) displacement; (b, d) traction.

The mesoscale yield detection condition follows Equation (2–9) and involves an equality between the average stress of the soft phase and the yield stress of that phase within a 3.5% error.

3.2. Patterns of shear bands. The equivalent plastic strain (PEEQ) contours for differing window sizes of δ under differing boundary conditions are shown in Figure 2 for chessboard material, and in Figure 3 for the matrix-inclusion composite. Although the shear bands differ somewhat for the two types of material, clearly, we can see the following common characteristics:

- The shear bands are irregular, but conform to the actual spatial distribution of the material microstructure.
- The shear bands are roughly 45° from the principal axes of tensile loading.
- For a small window size of, say, $\delta = 8$, some shear bands can cross the entire window, but for a large window size, $\delta = 32$, almost no shear band can do so.

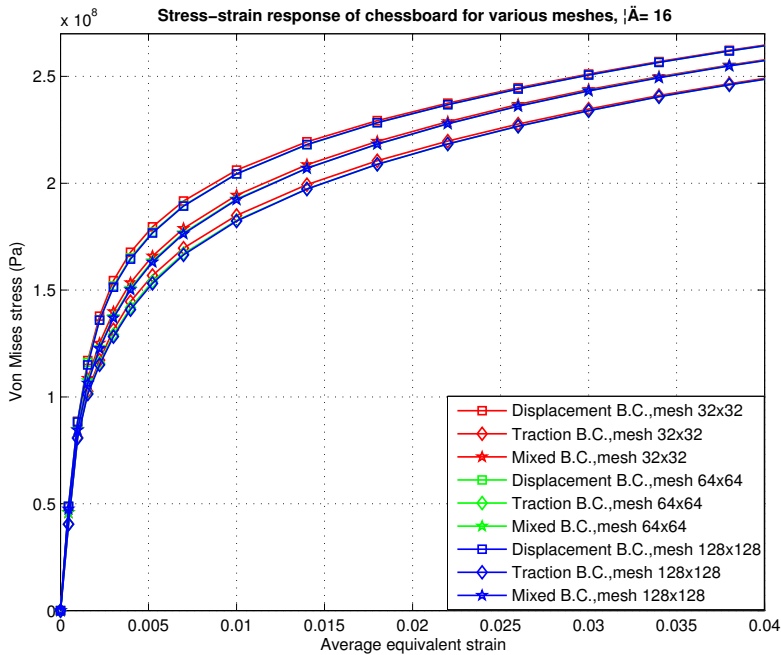
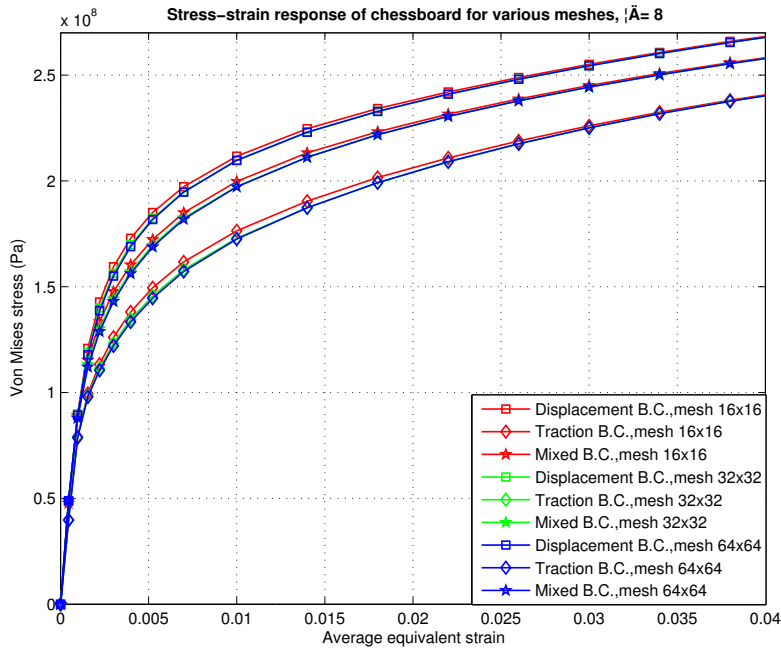


Figure 4. Comparison of ensemble average stress-strain responses of chessboard composites for various meshes: (a) $\delta = 8$; (b) $\delta = 16$.

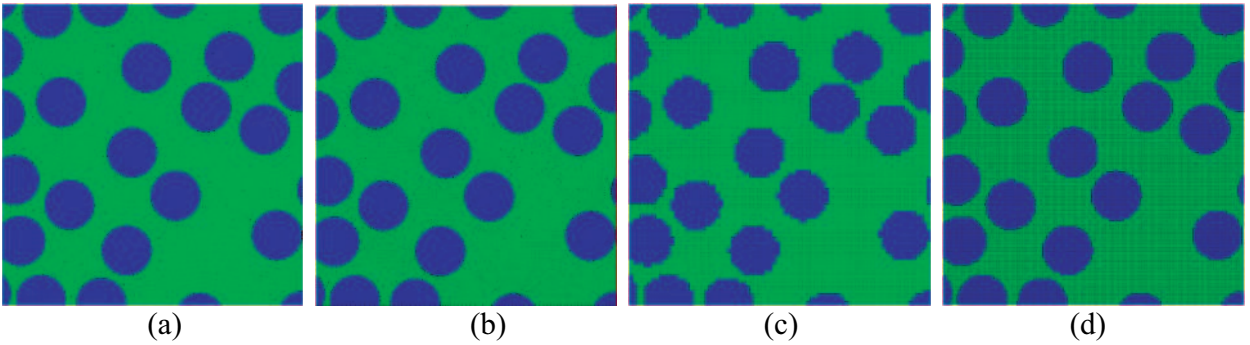


Figure 5. Comparison of different meshes for matrix-inclusion composites at $\delta = 6$: (a) coarse mesh, global mesh size = 1.0; (b) fine mesh, global mesh size = 0.5; (c) uniform grid, mesh 80×80 ; (d) uniform grid, mesh 160×160 .

- The shear band patterns are different under different boundary conditions, and seem to rank in the following order for stress concentration factors: displacement and traction.

3.3. Effects of mesh refinement.

3.3.1. Chessboard model. Figure 4 shows that all the stress-strain curves shift down with the increasing refinement of mesh, because introducing more finite elements furnishes more degrees of freedom. In particular, we notice that the shift when the mesh changes from 4×4 to 8×8 for each inclusion is much smaller than when the mesh changes from 2×2 to 4×4 , which means that the effect of mesh refinement tends to vanish at 8×8 .

3.3.2. Matrix-inclusion model. There are two types of mesh in the FE method: uniform and nonuniform. For uniform mesh, to approximate the complex geometry, a very large number of elements is needed, which requires more computational resources. Figure 5 (c) and (d) demonstrates grid refinements leading to improvement in the accuracy of a numerical simulation. The disadvantage of using uniform meshes is that the number of elements may become so large that, beyond a given window size δ , the computation becomes impractical.

The advantage of nonuniform mesh is that the mesh density can be adjusted according to a change of geometry, so it can greatly reduce the number of nodes while maintaining the same solution accuracy. Comparing the case of 6,400 (80×80) elements with that of 25,600 (160×160) elements in the uniform mesh—as shown in Figure 5 (c) and (d)—there are only 3,291 elements of the coarse mesh and 8,564 elements of the fine mesh, (see Figure 5 (a) and (b)). In addition, the nonuniform mesh geometry is more accurate than the uniform one.

Unlike to the chessboard composites, all the curves shift up with the increased mesh, but the shift is small and the curves almost overlap; see Figure 6. Since the area of the polygon inscribed into the circle is always smaller than that of the circle, the volume fraction of inclusions is always a little smaller than the real one, and this leads to very minor underestimates of material stiffness.

3.4. Ensemble average stress-strain responses. Figures 7 and 8 clearly show that with the increase in the mesoscale δ , the elastoplastic bounds obtained under kinematic and static boundary conditions

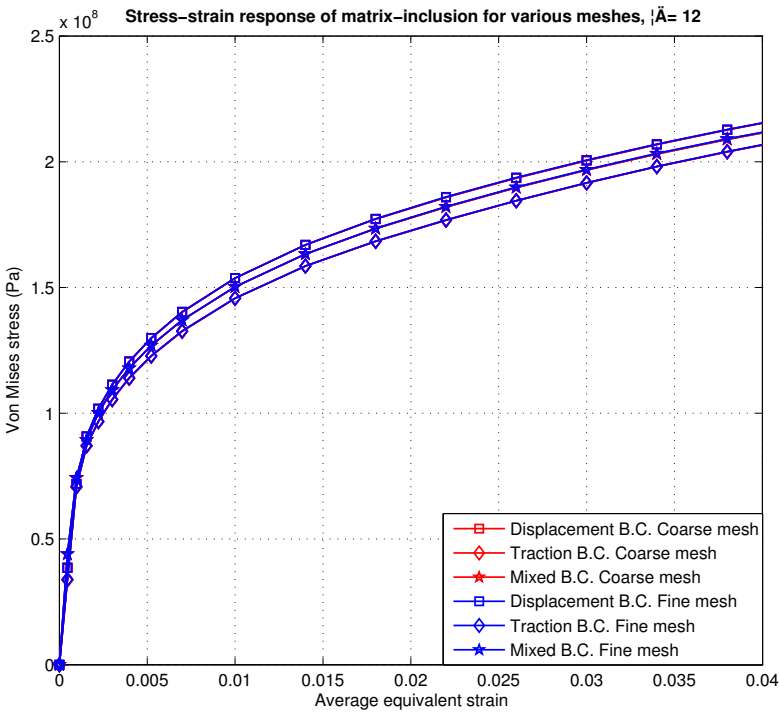
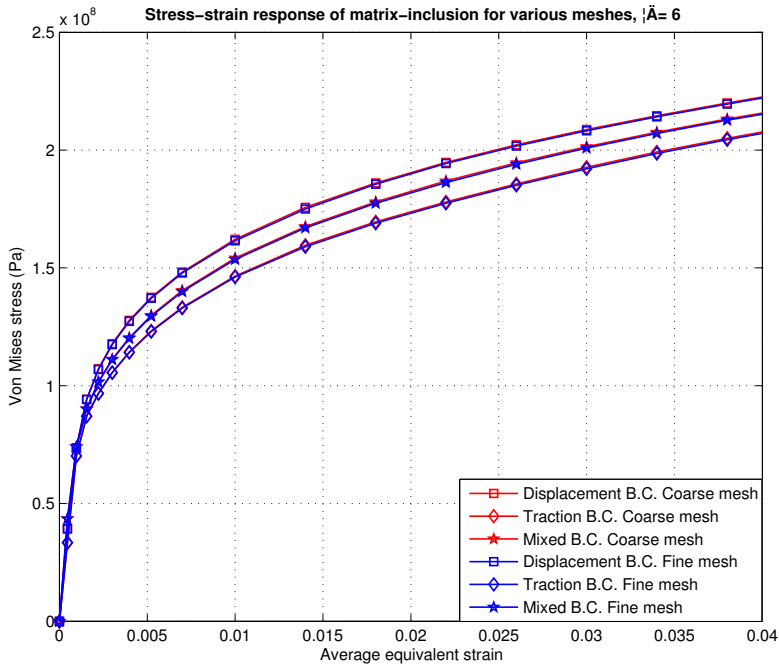


Figure 6. Comparison of ensemble average stress-strain responses of matrix-inclusion composites for differing meshes: (a) $\delta = 6$; (b) $\delta = 12$.

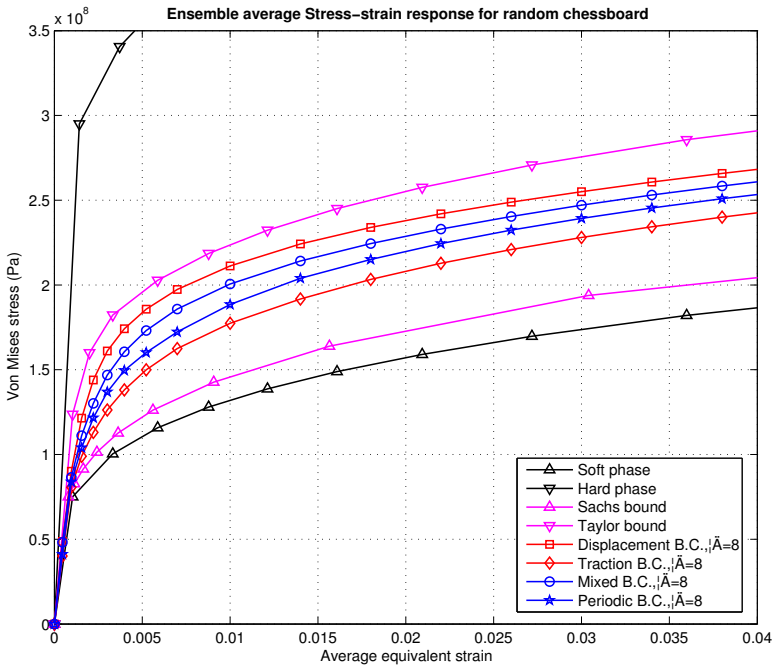


Figure 7. Ensemble average stress-strain responses for different mesoscales δ under various boundary conditions for the random chessboard. Responses of both constituent phases and the Sachs and Taylor bounds are also shown.

become tighter, while the slopes of curves, that is, the tangent moduli satisfy the relation described in Equation (2–8). For matrix-inclusion composites, one phenomenon we must consider is that the stress-strain curve can fall outside the Sachs bound, which is impossible for purely elastic materials. We can explain this by observing that, for the elastoplastic material, the stress concentration causes some local area or spot to yield which, in turn, softens the material. This is the result of the definition of yield (Equation (2–9)) employed here.

3.5. Yield surfaces and flow rules. To study the yield surface and the flow rule on mesoscales, we first introduce two different loading programs: displacement increment control and traction increment control. For the traction increment control

$$\Delta T = \Delta \Sigma \cdot n,$$

where ΔT is the increment of traction, and $\Delta \Sigma$ is the increment of volume average stress.

For the displacement increment control

$$\Delta U = \Delta E \cdot X,$$

where ΔU is the increment of displacement, ΔE is the increment of volume average strain.

For a specific load

$$E_1/E_2 = \text{const} \quad \text{or} \quad \Sigma_1/\Sigma_2 = \text{const}.$$

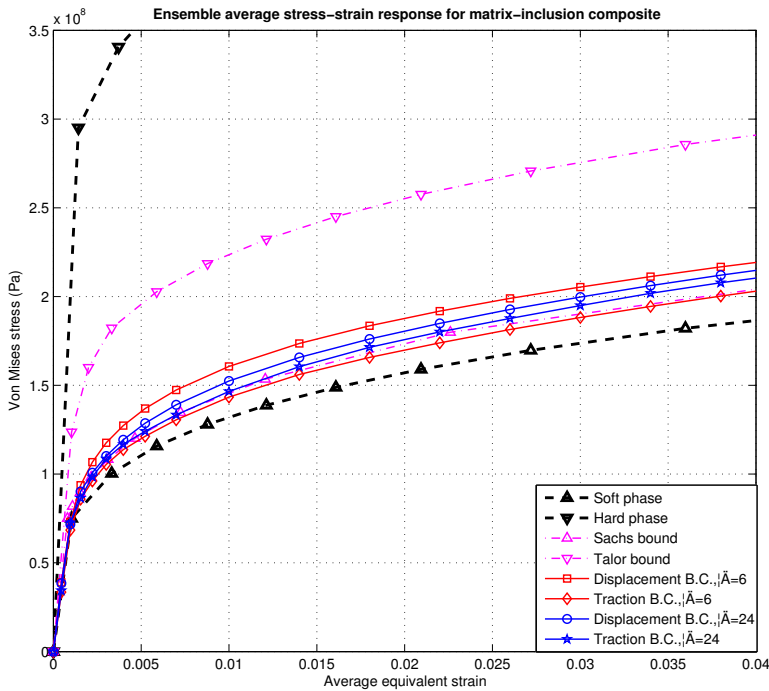


Figure 8. Ensemble average stress-strain responses for different mesoscales δ under various boundary conditions for the random matrix-inclusion composite. Also shown are the responses of both constituent phases as well as the Sachs and Taylor bounds.

In both loading programs, we fix the ratio of increment ($\Delta E_1/\Delta E_2 = \text{const}$ or $\Delta \Sigma_1/\Delta \Sigma_2 = \text{const}$) and continue to increase it until the volume average stress Σ satisfies Equation (2–9). We then get one specific yield point.

The loading paths are shown in Figure 9. For each sample we applied 17 different loading paths corresponding to 17 different ratios of loading to obtain 17 yield points whose ratios (Σ_1/Σ_2) vary from -1 to 1 (but only approximately so for displacement control). These 17 points cover quite densely one quarter of the yield surface, which, by symmetry arguments, is representative of the entire stress plane.

The loading paths are always linear for the traction increment control. However, for the displacement increment control, the loading paths are not linear since there are some areas or spots within the specimen yield due to local stress concentrations, even when the volume average stress is still lower than the yield stress; see Figure 9. For the chessboard composite, this phenomenon is even stronger than for the matrix-inclusion composite. Also, we can clearly see that the plastic strain rate is not always normal to the yield surface and the shape of yield surface is not perfectly elliptical.

Figure 10 depicts the scatter of yield locus of chessboard and matrix-inclusion composite materials for different window sizes of δ under traction and displacement boundary conditions. Obviously, the

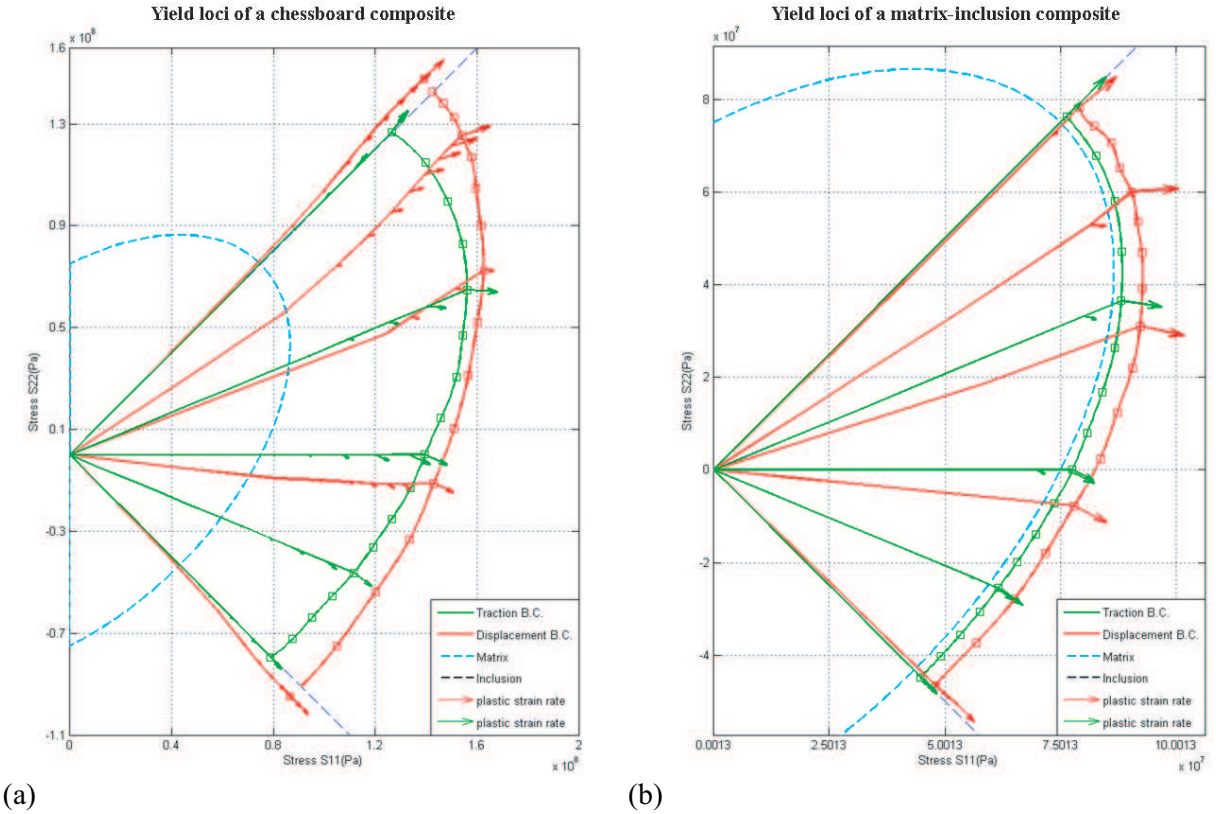


Figure 9. Yield surfaces and loading paths for one sample of (a) chessboard composite, $\delta = 8$, and (b) matrix-inclusion composite, $\delta = 6$.

smaller the window size, the higher the scatter; also the shape of the yield locus is more similar to an ellipse as the window size of δ increases.

Figure 11 shows the ensemble average yield surface on different mesoscales under two different loading controls. It shows that the mesoscale yield surfaces satisfy the hierarchy of inclusions conjectured in (2–10). Also with the increasing mesoscale δ , the yield surface bounds become tighter under displacement and traction boundary conditions.

Figure 12 shows the departure from normality of the plastic flow rate vector at mesoscale yield surfaces. We can infer that about 60% of yield surface is characterized by normality of plastic flow. Departure from normality occurs when the stress ratio Σ_{22}/Σ_{11} is around $0.3 \sim 0.9$, and is greater for the chessboard than for the matrix-inclusion composite.

3.6. Why the loss of normality? We base our understanding of normality in plasticity on the thermo-mechanics argument of Ziegler [1983], who points out the much more fundamental role played by the thermodynamic orthogonality in the space of velocities (that is, plastic strain rates). Only when the dissipation function Φ depends on velocities alone in its arguments will normality carry over to the space of dissipative stresses. When Φ depends also on other quantities, such as stresses or internal variables, normality is violated. For a disordered heterogeneous material, Φ is also a function of the

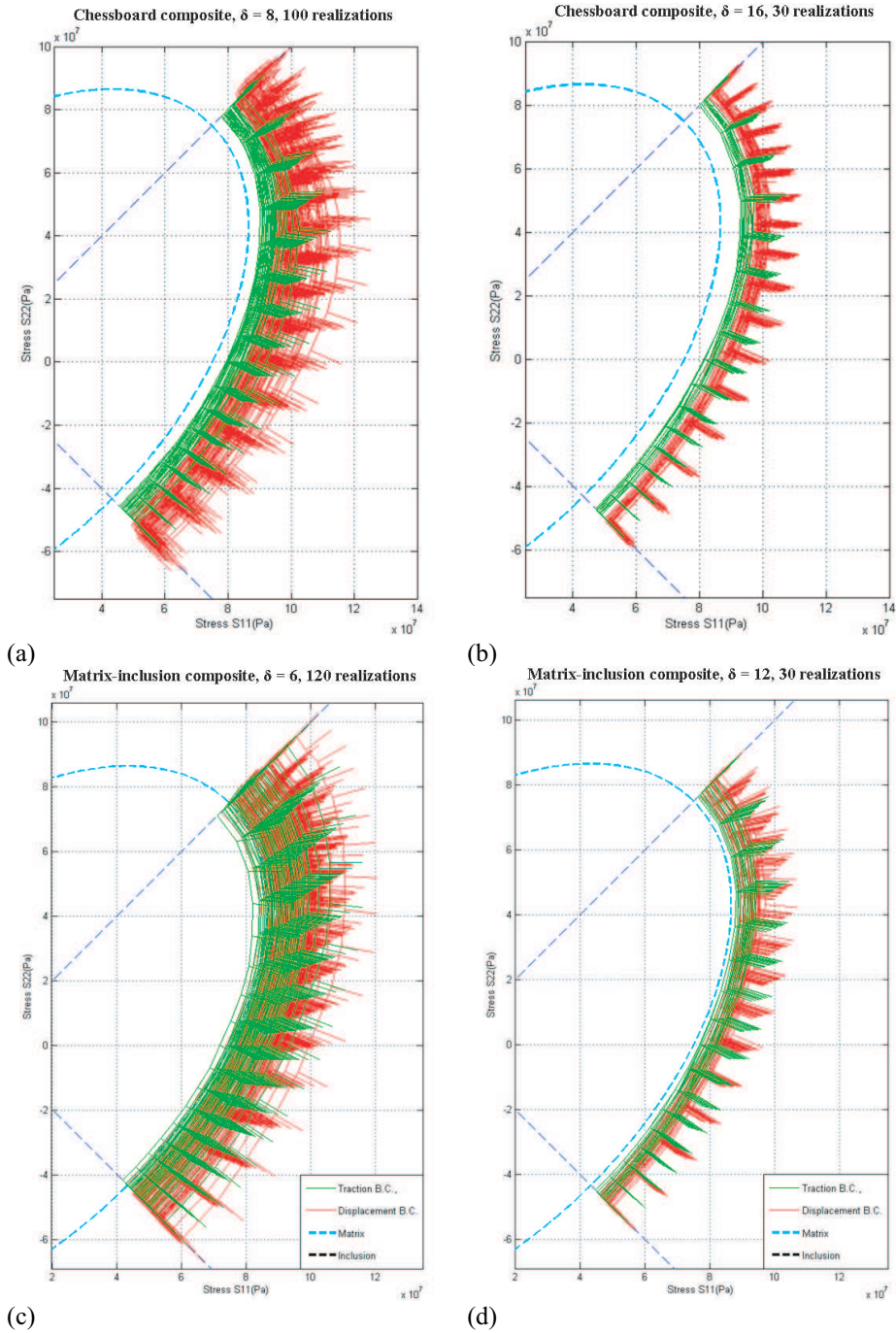


Figure 10. Scatter of yield locus under different boundary conditions for random materials: (a) chessboard composite at $\delta = 8$, 100 samples; (b) chessboard composite at $\delta = 16$, 30 samples; (c) matrix-inclusion composite at $\delta = 6$, 120 samples; (d) matrix-inclusion composite at $\delta = 12$, 30 samples.

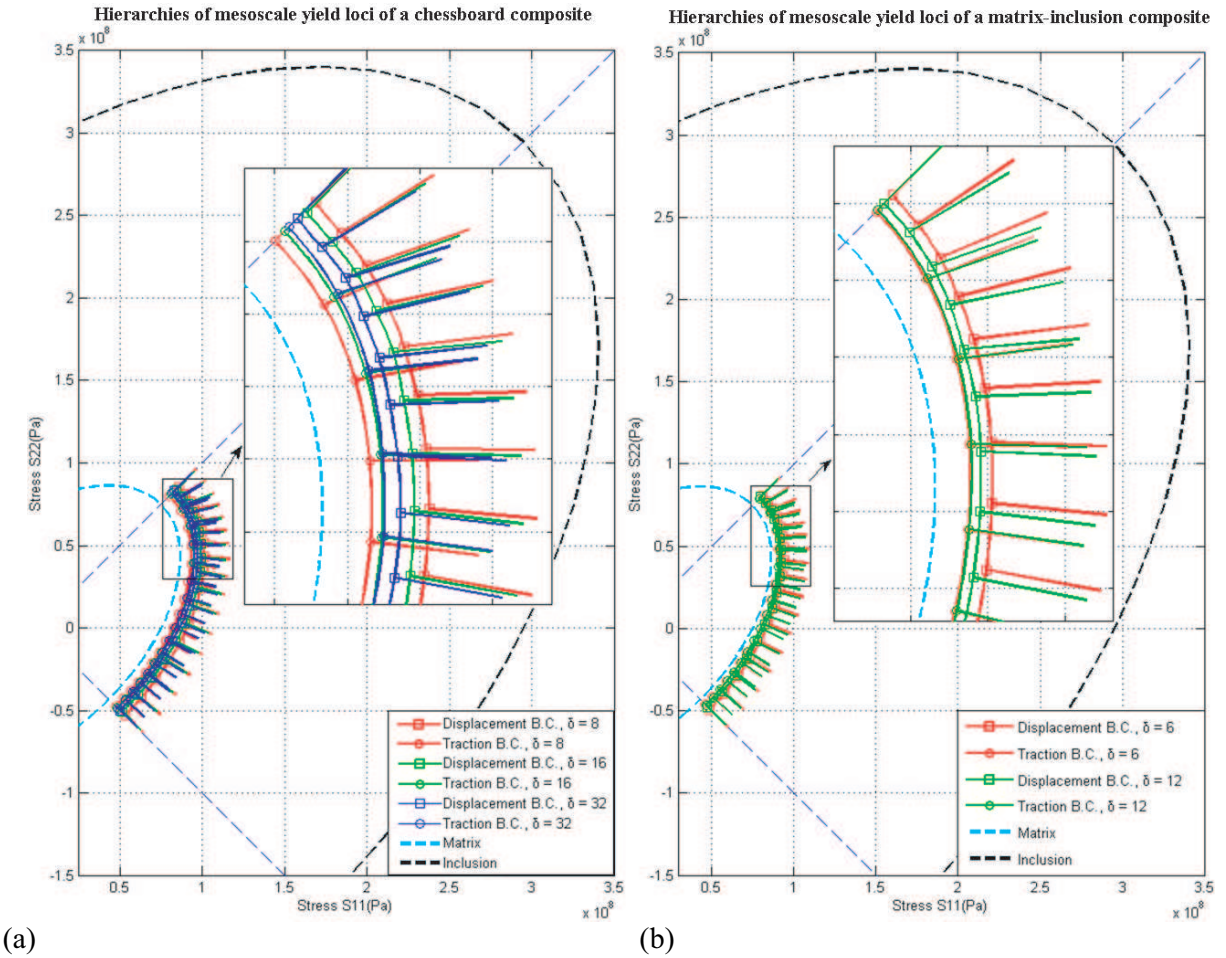


Figure 11. Hierarchy of (ensemble averaged) mesoscale bounds on RVE yield locus for (a) chessboard composite, and (b) matrix-inclusion composite.

specific microstructure, which may be represented by an internal variable α . This α must be chosen so that, for homogeneous material, it becomes null and the dependence of Φ on α vanishes. Thus, the simplest candidate for α may be the ratio of yield limits σ_0 of both phases. Other candidates are possible [Maugin 1998].

Another viewpoint refers to the classical result of nonlinear homogenization where the existence of a plasticity potential at the microlevel implies the existence of a macro-potential from which the effective constitutive equations are derived. The macro-potential is the mean value of the local potentials [Suquet 1997], so that the normality is preserved by a scale transition. In our study, according to Equation (2–9), macroyielding takes place as soon as local plastic flow begins for the first time at some point in the heterogeneous material. Such a macroyield criterion is not very useful in practical applications, but even for a more realistic (tolerant) yield criterion, the loss of normality would also persist under scale transition.

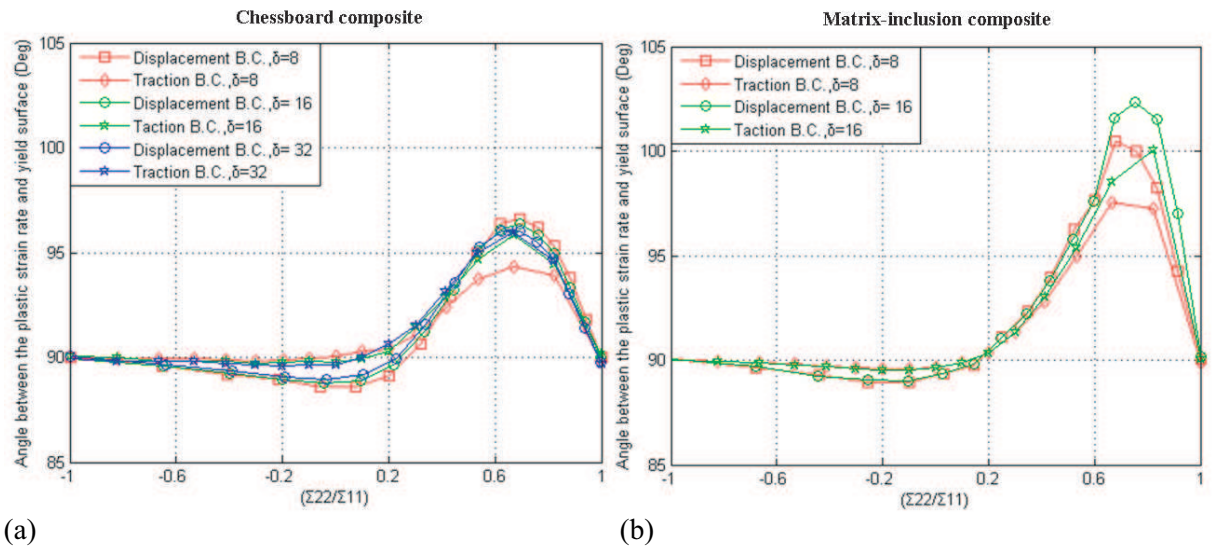


Figure 12. Departure from normality in mesoscale plastic flow under various boundary conditions on SVE for (a) chessboard composite and (b) matrix-inclusion composite.

4. Conclusions

We summarize the results of this study as follows:

- 1) We compute and verify the hierarchy of mesoscale stress-strain responses and the hierarchy of mesoscale yield surfaces for two models of elastoplastic-hardening random materials. The yield is studied employing the definition of yield point of [Dvorak and Bahei-El-Din 1987]. With this definition, mesoscale stress-strain responses under uniform traction boundary conditions may fall below the Sachs bound, although this occurs over a very small range of loading.
- 2) We find that mesoscale flow rule departs from normality under both uniform kinematic and traction boundary conditions. That departure is strongest when the ratio of two in-plane ensemble averaged principal stresses ranges from 0.3 to 0.9. Given the limitations of available computers, we cannot establish the expected trend to recover normality as the mesoscale domain (that is, SVE) grows and tends to the macroscale (RVE).
- 3) While we focus here on plane stress, very similar results have been found in plane strain.

Although our model materials have distinct and isotropic phases, our approach is also suited to analyze materials with piecewise-constant domains of anisotropic phases (polycrystals), and smoothly inhomogeneous media where no specific phase(s) can be distinguished. Fiber-structured paper is one example in the latter category [Ostoja-Starzewski and Castro 2003]. An extension to 3D problems is a matter of a far more extensive computational work.

Acknowledgements

The constructive comments of two anonymous reviewers are appreciated. This work has been supported by the Canada Research Chairs program and the NSERC.

References

- [Castaneda and Suquet 1997] P. P. Castaneda and P. Suquet, “Nonlinear composites”, *Adv. Appl. Mech.* **34** (1997), 171–302.
- [Clayton and McDowell 2004] J. D. Clayton and D. L. McDowell, “Homogenized finite elastoplasticity and damage: theory and computations”, *Mech. Mater.* **36**:9 (2004), 799–824.
- [Cluni and Gusella 2004] F. Cluni and V. Gusella, “Homogenization of non-periodic masonry structures”, *Int. J. Solids Struct.* **41**:7 (2004), 1911–1923.
- [Dowling 1993] N. E. Dowling, *Mechanical behavior of materials: engineering methods for deformation, fracture, and fatigue*, Prentice-Hall, Englewood Cliffs, NJ, 1993.
- [Du and Ostoja-Starzewski 2006a] X. Du and M. Ostoja-Starzewski, “On the scaling from statistical to representative volume element in thermoelasticity of random materials”, *Networks and Heterogeneous Media* **1**:2 (2006), 259–274.
- [Du and Ostoja-Starzewski 2006b] X. Du and M. Ostoja-Starzewski, “On the size of representative volume element for Darcy law in random media”, 2006. P. Roy. Soc. Lond. A Mat.
- [Dvorak and Bahei-El-Din 1987] G. J. Dvorak and Y. A. Bahei-El-Din, “A bimodal plasticity theory of fibrous composite materials”, *Acta Mech.* **69**:1-4 (1987), 219–241.
- [Hazanov 1998] S. Hazanov, “Hill condition and overall properties of composites”, *Arch. Appl. Mech.* **68**:6 (1998), 385–394.
- [Hazanov and Huet 1994] S. Hazanov and C. Huet, “Order relationships for boundary-conditions effect in heterogeneous bodies smaller than the representative volume”, *J. Mech. Phys. Solids* **42**:12 (1994), 1995–2011.
- [He 2001] Q. C. He, “Effects of size and boundary conditions on the yield strength of heterogeneous materials”, *J. Mech. Phys. Solids* **49**:11 (2001), 2557–2575.
- [Hill 1950] R. Hill, *The mathematical theory of plasticity*, Clarendon Press, Oxford, 1950.
- [Hill 1963] R. Hill, “Elastic properties of reinforced solids: some theoretical principles”, *J. Mech. Phys. Solids* **11**:5 (1963), 357–372.
- [Huet 1990] C. Huet, “Application of variational concepts to size effects in elastic heterogeneous bodies”, *J. Mech. Phys. Solids* **38**:6 (1990), 813–841.
- [Huet 1995] C. Huet, “Bounds and hierarchies for the overall properties of viscoelastic heterogeneous and composite materials”, *Arch. Mech.* **47**:6 (1995), 1125–1155.
- [Huet 1999] C. Huet, “Coupled size and boundary-condition effects in viscoelastic heterogeneous and composite bodies”, *Mech. Mater.* **31**:12 (1999), 787–829.
- [Jiang et al. 2001] M. Jiang, M. Ostoja-Starzewski, and I. Jasiuk, “Scale-dependent bounds on effective elastoplastic response of random composites”, *J. Mech. Phys. Solids* **49**:3 (2001), 655–673.
- [Kanit et al. 2003] T. Kanit, S. Forest, I. Galliet, V. Monoury, and D. Jeulin, “Determination of the size of the representative volume element for random composites: statistical and numerical approach”, *Int. J. Solids Struct.* **40**:13-14 (2003), 3647–3679.
- [Khisaeva and Ostoja-Starzewski 2006] Z. Khisaeva and M. Ostoja-Starzewski, “Mesoscale bounds in finite elasticity and thermoelasticity of random composites”, *P. Roy. Soc. Lond. A Mat.* **462**:2068 (2006), 1167–1180.
- [Maugin 1998] G. A. Maugin, *The thermomechanics of nonlinear irreversible behaviours: an introduction*, World Scientific, 1998.
- [Ostoja-Starzewski 1994] M. Ostoja-Starzewski, “Micromechanics as a basis of continuum random fields”, *Appl. Mech. Rev.* **47**:1, Pt. 2 (1994), S221–230.
- [Ostoja-Starzewski 1999] M. Ostoja-Starzewski, “Scale effects in materials with random distributions of needles and cracks”, *Mech. Mater.* **31**:12 (1999), 883–893.

- [Ostoja-Starzewski 2000] M. Ostoja-Starzewski, “Universal material property in conductivity of planar random microstructures”, *Phys. Rev. B* **62**:5 (2000), 2980–2982.
- [Ostoja-Starzewski 2002] M. Ostoja-Starzewski, “Towards stochastic continuum thermodynamics”, *J. Non-Equil. Thermodyn.* **27**:4 (2002), 335–348.
- [Ostoja-Starzewski 2005] M. Ostoja-Starzewski, “Scale effects in plasticity of random media: status and challenges”, *Int. J. Plast.* **21**:6 (2005), 1119–1160.
- [Ostoja-Starzewski 2006] M. Ostoja-Starzewski, “Material spatial randomness: from statistical to representative volume element”, *Probab. Eng. Mech.* **21**:2 (2006), 112–132.
- [Ostoja-Starzewski and Castro 2003] M. Ostoja-Starzewski and J. Castro, “Random formation, inelastic response, and scale effects in paper”, *Philos. T. Roy. Soc. A* **361**:1806 (2003), 965–985.
- [Ostoja-Starzewski and Wang 1989] M. Ostoja-Starzewski and C. Wang, “Linear elasticity of planar Delaunay networks: random field characterization of effective moduli”, *Acta Mech.* **80**:1-2 (1989), 61–80.
- [Sab 1992] K. Sab, “On the homogenization and the simulation of random materials”, *Eur. J. Mech. A:Solids* **11** (1992), 585–607.
- [Suquet 1997] P. Suquet, *Continuum micromechanics*, CISM Courses and Lectures **377**, Springer, Vienna, 1997.
- [Ziegler 1983] H. Ziegler, *An Introduction to thermomechanics*, North-Holland, Amsterdam, 1983.

Received 27 Dec 2005.

WEI LI: email_liwei@yahoo.com

Department of Mechanical Engineering, McGill University, Montréal, QC, H3A 2K6, Canada

MARTIN OSTOJA-STARZEWSKI: martinos@uiuc.edu

Mechanical Science and Engineering, University of Illinois at Urbana-Champaign, Urbana, IL 61801, United States

<http://www.mie.uiuc.edu/research/martinos>

EFFECTS OF IN-PLANE ELECTRIC FIELDS ON THE TOUGHENING BEHAVIOR OF FERROELECTRIC CERAMICS

JIANXIN WANG AND CHAD M. LANDIS

Mode-I steady state crack growth in poled ferroelectric ceramics subjected to simultaneous electrical and mechanical loading is analyzed to investigate the effect of in-plane electric fields and polarization on the toughening behavior. A multiaxial, incremental constitutive law for domain switching is implemented within the finite element method to obtain the electromechanical crack tip fields. Simulation results are presented for the cases of initial remanent polarization states and applied electric fields perpendicular to the crack plane and parallel to the crack growth direction. Specific results from the calculations include the shapes and sizes of switching zones, and the toughening effects due to domain switching near the crack tip.

1. Introduction

Ferroelectric ceramics have been widely used in smart structure applications due to their large electromechanical coupling effects. Since ferroelectric devices often operate under strong mechanical and electrical loading conditions, the brittle ferroelectric ceramic material is susceptible to fracture. Therefore, an understanding of ferroelectric fracture is a key issue for the efficient and reliable design of these devices. This paper is concerned with the study of the Mode-I fracture behavior of ferroelectric ceramics under combined in-plane electrical and mechanical loading.

The scenario investigated here is illustrated in Figure 1. A ferroelectric material is initially poled by an electric field either perpendicular or parallel to the direction of crack growth. After the initial poling, an electric field is applied along (positive electric field) or opposite (negative electric field) to the initial poling direction. Finally, mechanical loading is applied and crack growth occurs. Experimental observations of the fracture properties of ferroelectrics under such conditions have been obtained on several materials from indentation tests and compact tension specimens. Using indentation tests on a PZT-8 material composition, Tobin and Pak [1993] showed that for cracks perpendicular to the poling direction, the apparent fracture toughness decreases with positive electric field and increases with a negative field. For cracks parallel to the poling direction, their results indicated that both positive and negative electric fields have little influence on the toughening. Tobin and Pak [1993] also observed that with no applied electric field the fracture toughness was greater for cracks parallel to the poling direction than for cracks perpendicular to the poling direction. Park and Sun [1995] investigated electric field effects on crack growth in a PZT-4 ceramic by using conventional compact tension fracture tests. Their results agree with those of Tobin and Pak [1993] for the case of electric field applied perpendicular to the crack surface. However, the Vickers indentation tests of Wang and Singh [1997] showed that if the applied electric fields are perpendicular to the crack in a PZT EC-65 ceramic, then a positive electric field impedes

Keywords: fracture toughness, finite elements, ferroelectrics, piezoelectrics, domain switching.

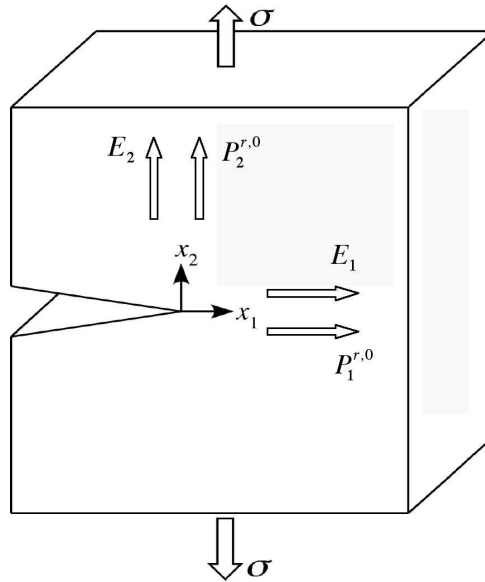


Figure 1. A schematic of the in-plane electrical and in-plane mechanical configuration to be modeled in this work. For any given sample, the electric field and remanent polarization are aligned in x_1 or x_2 direction. The in-plane mechanical loading is simply indicative of the Mode I symmetry to be modeled in this work and should not be interpreted literally.

crack propagation, whereas a negative electric field promotes crack propagation. For the electric field parallel to the crack, their results indicated that a negative field has little effect on the crack propagation while a positive field impedes crack propagation. Schneider and Heyer [1999] studied the effect of a static electric field on the fracture behavior of ferroelectric barium titanate using indentation tests. Their results indicate that the measured crack length versus the applied electric field shows hysteresis similar to the strain hysteresis. The more recent compact tension tests and indentation fracture tests on a PZT-841 ceramic, Fu and Zhang [2000], observed the reduction in the fracture toughness for a positive electric field as well as for a negative electric field if the electric field is applied perpendicular to the crack surface. Lucato et al. [2002] and Hackemann and Pfeiffer [2003] performed steady crack growth experiments and recorded R -curve behavior for a variety of electrical polarization conditions. It is the existence of this R -curve behavior that indicates that the toughness variations are at least influenced by an irreversible constitutive process occurring around the crack.

Several theoretical models have been proposed in an attempt to evaluate the effect of electric field on fracture toughness of ferroelectric ceramics. It is widely accepted that the nonlinear and hysteretic constitutive behavior of ferroelectrics plays a significant role in the fracture toughness behavior. Yang and Zhu [1998] and Beom and Atluri [2003] applied transformation toughening concepts to study the effects of electric field and domain switching on the fracture toughness. Zeng and Rajapakse [2001] considered the anisotropic material properties and electromechanical coupling effect of ferroelectric ceramics and showed that a positive electric field impedes the propagation of a crack perpendicular to the poling

direction while a negative field enhances it. In contrast to these approximate analytical models, this study applies an established constitutive model for the ferroelectric constitutive behavior within finite element computations to accurately determine the enhancement of the fracture toughness due to domain switching near a growing crack. More comprehensive reviews of the recent experimental and modeling efforts on ferroelectric fracture can be found in [Zhang et al. 2001] and [Chen and Lu 2002].

The purpose of this study is to investigate the effect of electric fields on fracture behavior of ferroelectric ceramics subjected to combined electrical and mechanical loading. The nonlinear phenomenological constitutive model for coupled electromechanical domain switching is presented in Section 2. In Section 3, the fracture model and the finite element formulation which implements the constitutive model for steady crack growth will be described. The results are presented and analyzed in Section 4. A discussion of the results and comparisons to experimental observations are included in Section 5.

2. The phenomenological constitutive model

The goal of any phenomenological constitutive theory is to provide a relatively simple framework within which the laws of thermodynamics are satisfied and a wide range of material behaviors can be represented. A summary of the recent developments on microelectromechanical and phenomenological constitutive modeling of ferroelectrics can be found in review articles by Kamlah [2001] and Landis [2004c]. The phenomenological constitutive model presented below is based on the work of Landis [2002a; 2003b; 2004]. This constitutive model has been verified against experimental observations and microelectromechanical self-consistent simulations based on the model of Huber et al. [1999]. A formulation of the model required to investigate the toughening behavior of the poled ferroelectric ceramics under different poling directions with in-plane mechanical loading only is presented here.

In this work, it is assumed that the mechanical loading is applied in the $x_1 - x_2$ -plane and electric field is applied either in the x_1 or in x_2 direction as illustrated in Figure 1. Due to the constraint of plane-strain, axial stresses in the x_3 direction are allowed to develop as well. In a polycrystal, the linear elastic, dielectric and piezoelectric properties are dependent on the remanent strain and remanent polarization history at each material point. For a material poled by a uniaxial electric field these properties will be homogeneous and transversely isotropic about the poling direction. In comparison to the piezoelectric properties, which must change sign as the direction of the remanent polarization reverses, the elastic and dielectric properties have a much weaker dependence on the remanent state. Hence, for simplicity it will be assumed that elastic compliance at constant electric field, s_{ijkl}^E , and the dielectric permittivity at constant stress, κ_{ij}^σ , are not affected by changes in the remanent polarization of the material. The piezoelectric properties are assumed to be linearly dependent on the remanent polarization and transversely isotropic about the remanent polarization direction. Given these assumptions the s_{ijkl}^E and κ_{ij}^σ tensors will take on their isotropic forms. However, due to the presence of piezoelectricity and its dependence on the remanent polarization, other elastic and dielectric tensors such as the elastic stiffness at constant electric displacement, c_{ijkl}^D , and the inverse dielectric permittivity at constant strain, β_{ij}^ϵ , will have transversely isotropic symmetry about the remanent polarization direction. With these assumptions the constitutive

relationships can then be expressed as

$$\varepsilon_{ij} - \varepsilon_{ij}^r = \frac{1 + \nu}{E} \sigma_{ij} - \frac{\nu}{E} \sigma_{kk} \delta_{ij} + d_{kij} E_k, \tag{2-1}$$

$$D_i - P_i^r = d_{ikl} \sigma_{kl} + \kappa E_i, \tag{2-2}$$

where

$$d_{kij} = \frac{d_{33}}{4} \frac{P^r}{P_0} (3n_i \delta_{jk} + 3n_j \delta_{ik} - 2n_k \delta_{ij}), \quad P^r = \sqrt{P_i^r P_i^r}$$

$$n_i = P_i^r / P^r.$$

Here, ε_{ij} , ε_{ij}^r , D_i and P_i^r are the Cartesian components of the strain, remanent strain, electric displacement and remanent polarization, respectively, and are referenced from a thermally depolarized state. The components of the stress and electric field are σ_{ij} and E_i . The isotropic elastic properties are the Poisson’s ratio ν and the Young’s modulus E , and δ_{ij} is the Kronecker delta. The dielectric permittivity is κ . Finally, d_{33} is the piezoelectric coefficient when P^r reaches the maximum attainable remanent polarization P_0 , and n_i is a unit vector in the direction of the remanent polarization. Note that this form for the piezoelectric coefficients has $d_{31} = -d_{33}/2$ and $d_{15} = 3d_{33}/2$. This is a reasonable assumption based on measured values in polycrystals, and this assumption can be relaxed at the added expense of complexity within the theory.

The purpose of the nonlinear constitutive law is to provide the evolution of the stress, electric displacement, remanent strain and remanent polarization histories given the total strain and electric field histories. Domain switching occurs when a specific switching condition is met. This switching criterion can be used to define a surface in stress and electric field space and will be referred to as the switching surface. The specific form of the switching surface implemented here is that proposed by Landis [2002a]

$$\Phi = \frac{3\hat{\sigma}_{ij}\hat{\sigma}_{ij}}{2\sigma_0^2} + \frac{\hat{E}_i\hat{E}_i}{E_0^2} + \frac{\beta\hat{E}_iP_j^r\hat{\sigma}_{ij}}{E_0P_0\sigma_0} - 1 = 0, \tag{2-3}$$

where

$$\hat{\sigma}_{ij} = \sigma_{ij} - \sigma_{ij}^B, \quad \text{with } \hat{\sigma}_{ij} = \hat{\sigma}_{ij} - \frac{1}{3}\sigma_{kk}\delta_{ij}$$

$$\hat{E}_i = E_i - E_i^B + \frac{\partial d_{jkl}}{\partial P_i^r} E_j \sigma_{kl}. \tag{2-4}$$

Here σ_{ij}^B is the back stress tensor, E_i^B is the back electric field, σ_0 is the initial switching strength of the material in uniaxial tension or compression, E_0 is the coercive field, and β is a positive scalar parameter. The postulate of maximum dissipation is satisfied if the switching surface is convex and the increments of remanent strain and polarization are normal to the surface. The switching surface defined in Equation (2-3) is convex if $\beta < 3$. Normality requires the remanent increments to be given as

$$\dot{\varepsilon}_{ij}^r = \lambda \frac{\partial \Phi}{\partial \hat{\sigma}_{ij}} \quad \text{and} \quad \dot{P}_i^r = \lambda \frac{\partial \Phi}{\partial \hat{E}_i}, \tag{2-5}$$

where λ is the switching multiplier. To determine the back stress and back electric field, it is assumed that the remanent strain and remanent polarization can be applied as internal variables that fully characterize the thermodynamic state of the material. This assumption leads to the identification of a remanent potential, $\Psi^r(\varepsilon_{ij}^r, P_i^r)$, such that the back stress and back electric field components can be derived from the potential in the following manner:

$$\sigma_{ij}^B = \frac{\partial \Psi^r}{\partial \varepsilon_{ij}^r}, \quad E_i^B = \frac{\partial \Psi^r}{\partial P_i^r}. \quad (2-6)$$

Finally, the form of Ψ^r must be specified to complete the constitutive theory. For the results to be presented Ψ^r is split into a mechanical part Ψ^σ that enforces the strain saturation conditions, and an electrical part Ψ^E that enforces the polarization saturation conditions,

$$\Psi^r = \Psi^\sigma + \Psi^E \quad (2-7)$$

$$\Psi^\sigma = \frac{1}{2} H_0^\sigma \varepsilon_c \left[\frac{J_2^e}{\varepsilon_c} \exp\left(\frac{m}{1 - \bar{\varepsilon}/\varepsilon_c}\right) \right]^2, \quad (2-8)$$

where H_0^σ is a characteristic level of back stress that primarily affects the initial slope of uniaxial stress versus remanent strain curve, m is another hardening parameter that controls how abruptly the strain saturation conditions can be approached. The multiaxial remanent strain saturation conditions are enforced by causing Ψ^σ to approach infinity as the strain-like variable $\bar{\varepsilon}$ approaches the saturation level of remanent strain in uniaxial compression ε_c . The effective saturation remanent strain quantity $\bar{\varepsilon}$ is defined as

$$\bar{\varepsilon} = J_2^e f(J_3^e/J_2^e), \quad (2-9)$$

where

$$f\left(\frac{J_3^e}{J_2^e}\right) = -0.0965 \left(\frac{J_3^e}{J_2^e}\right)^3 + 0.01 \left(\frac{J_3^e}{J_2^e}\right)^6 + 0.8935, \quad \text{for } \left(\frac{J_3^e}{J_2^e}\right) < 0 \quad (2-10)$$

and

$$f\left(\frac{J_3^e}{J_2^e}\right) = -0.1075 \left(\frac{J_3^e}{J_2^e}\right)^3 - 0.027 \left(\frac{J_3^e}{J_2^e}\right)^6 - 0.028 \left(\frac{J_3^e}{J_2^e}\right)^{21} + 0.8935, \quad \text{for } \left(\frac{J_3^e}{J_2^e}\right) \geq 0. \quad (2-11)$$

Here, f is a functional fit to the numerical results obtained from the micromechanical computations described in [Huber et al. 1999]. The following remanent strain invariants are used to describe the multiaxial remanent strain state

$$J_2^e = \left(\frac{2}{3} e_{ij}^r e_{ij}^r\right)^{1/2} \quad \text{and} \quad J_3^e = \left(\frac{4}{3} e_{ij}^r e_{jk}^r e_{ki}^r\right)^{1/3}, \quad (2-12)$$

where e_{ij}^r is the remanent strain deviator, $e_{ij}^r = \varepsilon_{ij}^r - \delta_{ij} \varepsilon_{kk}^r/3$.

Next, the electrical part of Ψ^r has the form of

$$\Psi^E = H_0^E P_0 \left[\ln\left(\frac{1}{1 - P^r/P_{sat}}\right) - \frac{P^r}{P_{sat}} \right], \quad (2-13)$$

where

$$P_{sat} = \frac{3P_0}{4(\varepsilon_t + \varepsilon_c)} (\varepsilon_{ij}^r n_i n_j + \varepsilon_c) + \frac{P_0}{4}. \quad (2-14)$$

Here ε_t is the remanent saturation strain in uniaxial tension and, according to Equations (2-8)–(2-11), is equal to $1.368\varepsilon_c$. The maximum attainable remanent polarization P_0 has been defined previously. Note that the level where the remanent polarization saturates P_{sat} is a function of the remanent strain and the maximum of P_0 can only be attained if $\varepsilon_{ij}^r n_i n_j = \varepsilon_t$. If $\varepsilon_{ij}^r n_i n_j = -\varepsilon_c$ then the maximum level for P^r is only $P_0/4$. This result and the linear approximation to the functional form for P_{sat} given in Equation (2-14) are taken directly from the microelectromechanical computations described in [Landis et al. 2004]. A more detailed description of the model can be found in references [Landis 2002a; Landis 2003b; Landis et al. 2004]. For the numerical implementation of the constitutive model into the finite element model, a backward Euler integration routine was developed to solve the constitutive equations. The scheme is similar to that described in [Landis 2003a].

3. The fracture model and finite element formulation

3.1. The loading process. Note that the straight lines within the loops in Figures 2a and 2b represent linear unloading during the removal of the applied electric field, and those in 2c and 2d depict the initial behavior during depolarization by compressive stress from different *partially* poled states. After the initial poling step or lack of it, the electromechanical loading history for the specimen is as follows. Electric field is applied in the x_α direction, again in the absence of mechanical stress. If the applied electric field is of sufficient magnitude then poling of initially unpoled samples or a reversal of poling in initially poled samples may result. In any case, this step in the electrical loading procedure induces new states of strain and electric displacement, which will be called the initial strain ε_{ij}^0 and initial electric displacement D_i^0 . The final step in the loading process is to apply the in-plane mechanical loads while keeping the applied electric field fixed at the level attained in the previous step. Under plane-strain conditions, the out-of-plane axial strain ε_{33} is assumed to remain unchanged from its state after the electrical loading step, that is, $\varepsilon_{33} = \varepsilon_{33}^0$. Steady crack growth then occurs while the in-plane mechanical loads are applied.

3.2. Boundary conditions. In the study of electromechanical fracture, determination of the crack face boundary conditions remains an unresolved question. Thorough reviews of the literature can be found in [McMeeking 1999], [Zhang et al. 2001] and [Chen and Lu 2002]. A point of contention among differing modeling approaches is the crack face boundary condition for the so-called “insulating” crack problem. Herein, three approaches have received considerable attention: the impermeable crack model, the permeable, or “closed”, crack model, and the “exact” boundary conditions. In this paper, the permeable boundary condition will be used. Landis [2004a] has shown that the permeable crack boundary conditions are a reasonable approximation when the electrical discharge strength of the medium within the crack is small (the permeable conditions are exact when the discharge strength is zero).

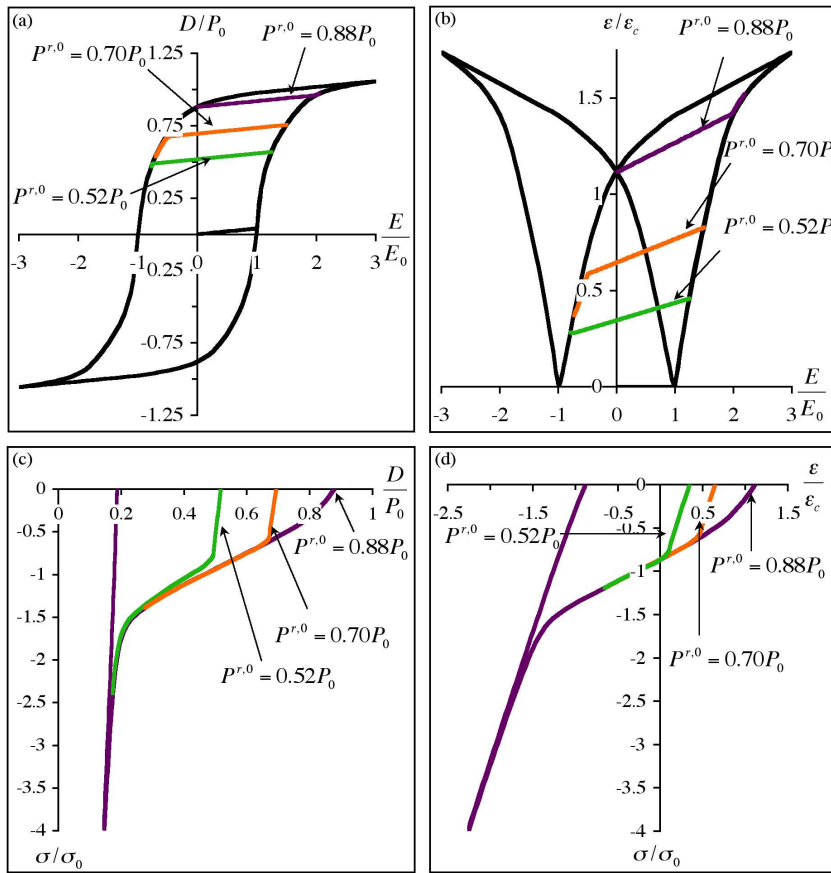


Figure 2. The uniaxial electromechanical behavior of the model material with three levels of the poling field, leading to different partially poled states: (a) the electric field versus electrical displacement hysteresis loops; (b) the electric field versus strain butterfly loop; (c) the stress versus electrical displacement depolarization loop; (d) the stress versus strain loop during depolarization. Notice that the intermediate lines in (a) and (b) represent the response during the unloading of electric field, and those in (c) and (d) represent the depolarization behavior from a partially poled state.

The electrically permeable and traction free crack face boundary conditions used in the present paper are stated as

$$D_2(r, \theta = \pi) = D_2(r, \theta = -\pi), \quad \phi(r, \theta = \pi) = \phi(r, \theta = -\pi),$$

$$\sigma_{i2}(r, \theta = \pm\pi) = 0, \quad (3-1)$$

where ϕ is the electric potential, r and θ represent a polar coordinate system centered on the crack tip, and θ measures the angle between the radial direction and the x_1 -axis. With a procedure similar to that outlined in [Landis 2004b], the asymptotic Mode I fields for the stresses and electric potential are

determined for the piezoelectric body and applied as far-field boundary conditions. The applied energy release rate for the far field is also determined from this solution. All of these quantities are not only dependent on K_I but also dependent on the piezoelectric coefficients, Young’s modulus, Poisson’s ratio, and initial remanent polarization $P_i^{r,0}$. Since the derivation is given in [Landis 2004b] and the results for the stresses involve relatively long formulas, only the applied energy release rate, G , is given here for brevity,

$$G = \begin{cases} -\frac{k_\varepsilon}{4D_D} \left(\frac{9D_E}{1+\nu} + 8(2-3\alpha_\varepsilon) \right) \frac{1-\nu^2}{E} K_I^2, & \text{poled parallel to the crack plane} \\ \frac{2k_\varepsilon\alpha_\varepsilon}{D_E} \frac{1-\nu^2}{E} K_I^2, & \text{poled perpendicular to the crack plane} \end{cases} \quad (3-2)$$

where

$$\begin{aligned} k_\varepsilon &= 2E(d_{31}P^{r,0})^2/P_0^2\kappa(1-\nu), \\ \alpha_\varepsilon &= \sqrt{1/(1-k_\varepsilon)}, \\ D_D &= k_\varepsilon(1-\nu) + 2(\alpha_\varepsilon - 1)(1+\nu), \\ D_E &= \kappa_\varepsilon\alpha_\varepsilon(1-\nu) + 2(\alpha_\varepsilon - 1)(1+\nu). \end{aligned}$$

3.3. Small scale switching. During crack growth, small scale switching will be assumed, such that the representative height of the nonlinear switching zone near the crack tip is much smaller than any other characteristic specimen dimension such as crack length, specimen width or ligament width. Furthermore, under plane-strain conditions it is assumed that the specimen thickness is much greater than the switching zone size as well. The assumption of small scale switching will not be valid when the switching occurs over the entire sample. However, it is assumed here that the in-plane applied mechanical loads can still be characterized by the applied energy release rate given by Equation (3-2). A characteristic length R_s can be identified as

$$R_s = \frac{1}{3\pi} \frac{GE'}{\sigma_0^2}. \quad (3-3)$$

Here E' is the plane strain Young’s modulus and R_s is a reasonable measure of the half-height of the switching zone in an unpoled, mechanically loaded material.

The remaining nonlinear analysis presented in this paper will focus only on the toughening due to domain switching during the steady crack growth. Under steady growth conditions, all increments of field quantities can be related to derivatives with respect to the x_1 coordinate direction by

$$\dot{\chi} = -\dot{a} \frac{\partial \chi}{\partial x_1}. \quad (3-4)$$

Here, χ is any scalar field quantity such as a Cartesian component of remanent strain or remanent polarization. Since the constitutive model used in this study is rate independent, \dot{a} represents the *increment* of crack advance in the x_1 direction. If rate dependent material behavior were considered then \dot{a} would represent the crack growth *rate*, [Landis et al. 2000]. In either case, if inertial effects are neglected, the determination of the energy flux to the crack tip given by Equation (3-5) and the finite element

formulation to solve for the electromechanical fields derived from Equations (3–7) and (3–8) are the same. Only the integration of the constitutive law would change with the additional feature of rate dependence.

Within this model, crack propagation will be assumed to occur when the crack tip energy release rate G_{tip} reaches a critical value. In order to compute the relationship between the applied steady state energy release rate G_{ss} and G_{tip} , a steady state finite element formulation is implemented to determine the electromechanical fields. Then, under steady-state conditions, G_{tip} can be calculated using the electromechanical form of [Hutchingson 1974] I -integral as

$$G_{tip} = I \equiv \int_S (W n_1 - \sigma_{ij} n_j u_{i,1} + D_i n_i E_1) dS, \quad (3-5)$$

where S is a surface enclosing the crack tip, n_i are the components of the unit normal directed outward from the surface, u_i are the components of the displacement vector, D_i are the components of the electric displacement vector, E_1 is the electric field in x_1 direction, and W is the history dependent electric enthalpy density at a material point defined by

$$W = \int_0^{\varepsilon_{ij}, E_i} \sigma_{ij} d\varepsilon_{ij} - D_i dE_i \quad (3-6)$$

The calculation of G_{tip} is carried out after the finite element solution is obtained.

3.4. Finite element formulation. To compute the electromechanical fields numerically, the following finite element formulation is applied. If we assume that the free charge density in the volume is equal to zero, the vector potential formulation proposed by Landis [2002b] can be used. The finite element formulation required to solve the steady crack growth boundary value problem is based on the variational statement

$$\int_V \sigma_{ij} \delta \varepsilon_{ij} + E_i \delta D_i dV = \int_S t_i \delta u_i + \phi \delta \omega dS. \quad (3-7)$$

After the implementation of the constitutive law, Equation (3–7) becomes

$$\begin{aligned} & \int_V \left((c_{ijkl}^{D,0} \Delta \varepsilon_{kl}^{n+1} - h_{kij}^0 \Delta D_k^{n+1}) \delta \Delta \varepsilon_{ij} + (-h_{ikl}^0 \Delta \varepsilon_{kl}^{n+1} + \beta_{ij}^{\varepsilon,0} \Delta D_j^{n+1}) \delta \Delta D_i \right) dV \\ & = \int_S (T_i \delta \Delta u_i + \phi \delta \Delta \omega) dS \\ & - \int_V \left((\Delta c_{ijkl}^D \Delta \varepsilon_{kl}^n - \Delta h_{kij} \Delta D_k^n) \delta \Delta \varepsilon_{ij} + (-\Delta h_{ikl} \Delta \varepsilon_{kl}^n + \Delta \beta_{ij}^{\varepsilon} \Delta D_j^n) \delta \Delta D_i \right) dV \\ & + \int_V \left\{ \left((c_{ijkl}^{D,0} + \Delta c_{ijkl}^D) (\varepsilon_{kl}^{r,0} + \Delta \varepsilon_{kl}^{r,n} - \varepsilon_{kl}^0) - (h_{kij}^0 + \Delta h_{kil}) (P_k^{r,0} + \Delta P_k^{r,n} - D_k^0) \right) \delta \Delta \varepsilon_{ij} \right. \\ & \left. + \left(-(h_{ikl}^0 + \Delta h_{ikl}) (\varepsilon_{kl}^{r,0} + \Delta \varepsilon_{kl}^{r,n} - \varepsilon_{kl}^0) + (\beta_{ij}^{\varepsilon,0} + \Delta \beta_{ij}^{\varepsilon}) (P_k^{r,0} + \Delta P_k^{r,n} - D_k^0) \right) \delta \Delta D_i \right\} dV, \end{aligned} \quad (3-8)$$

where S is the boundary of the volume V , $\Delta \omega$ is the change of surface charge, $c_{ijkl}^{D,0}$, Δc_{ijkl}^D are the Cartesian components of the elastic stiffness tensor and its change due to the evolution of remanency, h_{kij}^0 and Δh_{kij} are the third rank tensor of piezoelectricity and its change, and $\beta_{ij}^{\varepsilon,0}$ and $\Delta \beta_{ij}^{\varepsilon}$ are the second rank dielectric tensor and its change. $c_{ijkl}^{D,0}$, h_{kij}^0 and $\beta_{ij}^{\varepsilon,0}$ are the material properties at the initial remanent

state and are functions of $P_i^{r,0}$, while Δc_{ijkl}^D , Δh_{kij} , and $\Delta \beta_{ij}^\varepsilon$ are the changes of the material properties due to the change of remanent polarization. The tractions acting on the boundary S are given as $t_i = \sigma_{ji} n_j$. These tractions and the electric potential on the outer boundary are determined with a procedure similar to [Landis 2004b] and the electrically permeable boundary conditions are applied as stated in Equation (3–1). Returning to the finite element formulation, after the application of the appropriate finite element interpolations and the cancellation of the appropriate variational terms, the left-hand side of Equation (3–8) represents the stiffness matrix dotted with the vector of unknown nodal displacements at the $n + 1$ th iteration. Note that this stiffness matrix depends on initial remanent polarization and this matrix remains constant for all iterations. The first integral on the right-hand side represents the vector of known applied nodal “forces” arising from the tractions due to the mechanical loading and electrical potential due to electrical loading, which correspond to a specified level of the far field applied energy release rate. Note that these applied “forces” do not change from iteration to iteration. The second term on the right-hand side is an integrated body force due to the changes in the material properties. Finally, the third term on the right-hand side can be viewed as the body force due to the distributions of remanent polarization and remanent strain in the material from the n th iteration. As alluded to in this discussion, the finite element Equation (3–8) is solved with an iterative technique. To begin, uniform remanent strain and polarization distributions are assumed, integrated on the right hand side of Equation (3–8), and added to the applied traction boundary conditions. Next, the system of finite element equations is solved to obtain a new but approximate solution for the nodal unknowns. A new approximate strain and electric displacement distribution is derived from these nodal unknowns. Then, the incremental constitutive model described in Section 2 is integrated along streamlines of constant height above the crack plane from $x = +\infty$ to $x = -\infty$ to obtain updated approximations for the stress, electric field, remanent strain, and remanent polarization distributions. The new remanent strain and remanent polarization distributions are then integrated on the right hand side of Equation (3–8) and the matrix solution/streamline integration procedure is repeated until a suitable level of convergence is achieved. Additional descriptions of the steady state crack growth finite element formulation can be found in [Landis 2003a]. Once convergence is obtained, the crack tip energy release rate is computed from Equation (3–5) using an electromechanical generalization of the domain integral technique of [Li et al. 1985].

4. Results

The goal of this paper is to investigate the influence of the electric field on the fracture behavior of ferroelectric materials when the electric field or the poling direction is applied parallel or perpendicular to the crack surface in the plane of crack growth. As outlined in Section 3.1, two cases of electrical loading will be considered here, the initially unpoled and initially poled cases. After electrical loading of either case, the electric field E_α , ($\alpha = 1, 2$), is kept constant and the initial state ε_{ij}^0 , $\varepsilon_{ij}^{r,0}$, D_i^0 and $P_i^{r,0}$ is attained for the fracture simulation, after which the mechanical load is applied. In order to identify important parameters that affect the toughness of ferroelectric materials a dimensional analysis is performed on the constitutive equations (2–1)–(2–14), and the fundamental differential field equations. Such analysis identifies the following normalized field variables, σ_{ij}/σ_0 , $\varepsilon_{ij}/\varepsilon_c$, $\varepsilon_{ij}^r/\varepsilon_c$, D_i/P_0 , P_i^r/P_0 and E_i/E_0 . Each of these normalized field variables is a function of the normalized spatial coordinates x_1/R_s and x_2/R_s , and also depends on the initial remanent polarization $P_i^{r,0}/P_0$, the applied electric field

E_i^A/E_0 , and normalized material parameters $E\varepsilon_c/\sigma_0$, $d_{33}E_0/\varepsilon_c$, $\kappa E_0/P_0$, $\sigma_0\varepsilon_c/E_0P_0$, H_0^σ/σ_0 , H_0^E/E_0 , ν , β and m . Finally, the normalized steady state toughness of the material G_{ss}/G_0 is not a spatially varying field and hence will only depend on the normalized material parameters. It would be a sizeable task to parametrically investigate the effects of all ten dimensionless material quantities identified here. Instead, this work will focus on the effects of the initial remanent polarization $P_i^{r,0}/P_0$ on the toughening for a specific set of material properties. These material properties and constitutive parameters are characteristic of a soft PLZT material as measured by Lynch [1996], and are specifically given as:

$$\begin{aligned}\sigma_0 &= 27.5 \text{ MPa}, & E_0 &= 0.35 \text{ MV/m}, \\ P_0 &= 0.26 \text{ C/m}^2, & \varepsilon_c &= 0.12\%, \\ \beta &= 2.95, & \kappa &= 6 \times 10^{-8} \text{ C/m} \cdot \text{V}, \\ E &= 70 \text{ GPa}, & \nu &= 0.4, \\ d_{33} &= 3 \times 10^{-10} \text{ m/V}, & d_{31} &= -d_{33}/2, \\ m &= 0.01, & H_0^\sigma &= 0.5\sigma_0, \\ & & H_0^E &= 0.05E_0.\end{aligned}$$

It should be noted here that simply changing the parameters listed above does not always result in a model material that produces reasonable constitutive response like that displayed in Figure 2. Hence, if another material composition is to be modeled, it is likely that in addition to changing the constitutive parameters listed above, the functional forms of the remanent potentials of Equations (2–7), (2–8) and (2–13) must be changed as well.

4.1. Switching zones. As mentioned previously, the primary result of interest from each steady crack growth calculation is the ratio of the far field applied energy release rate, G_{ss} , to the crack tip energy release rate G_{tip} . However, prior to presenting results for the relative level of toughening, some features of the switching zones near the crack tip will be given first. Figure 3 illustrates the sizes and shapes of the switching zones around steadily growing cracks in initially unpoled material (a), and initially poled material (b, c, d, e). The specific electrical loading parameters used to generate these results are: (a) unpoled $P_\alpha^{r,0}/P_0 = 0$, $E_\alpha^A/E_0 = 0$, ($\alpha = 1, 2$); (b) poled parallel to the crack $P_1^{r,0}/P_0 = 0.75$ with no applied field $E_1^A/E_0 = 0$; (c) poled perpendicular to the crack $P_2^{r,0}/P_0 = 0.75$ with no applied field $E_2^A/E_0 = 0$; (d) poled parallel to the crack $P_1^{r,0}/P_0 = 0.47$ with negative applied field $E_1^A/E_0 = -0.2$; and (e) poled perpendicular to the crack $P_2^{r,0}/P_0 = 0.47$ with negative applied field $E_2^A/E_0 = -0.2$. Note that the spatial coordinates have been normalized by the length scale $R_0 = G_0E'/3\pi\sigma_0^2$, which can be interpreted as the size of the switching zone in a mechanically loaded unpoled material when the applied energy release rate is equal to G_0 . This normalization is used instead of R_s in order to make the scales on each plot in Figure 3 comparable.

In Figures 3a–e, the outer solid black line delineates the boundary between material that is undergoing changes in remanency due to the in-plane mechanical loading and material that is not. The inner solid red contour delineates the location inside the switching zone where the change in remanent strain reaches the characteristic elastic level of $\Delta\bar{\varepsilon}^r = \sigma_0/E$, and the inner solid blue contour is where the remanent polarization change achieves the characteristic linear dielectric level $|\Delta P^r| = \kappa E_0$. It is worth noting

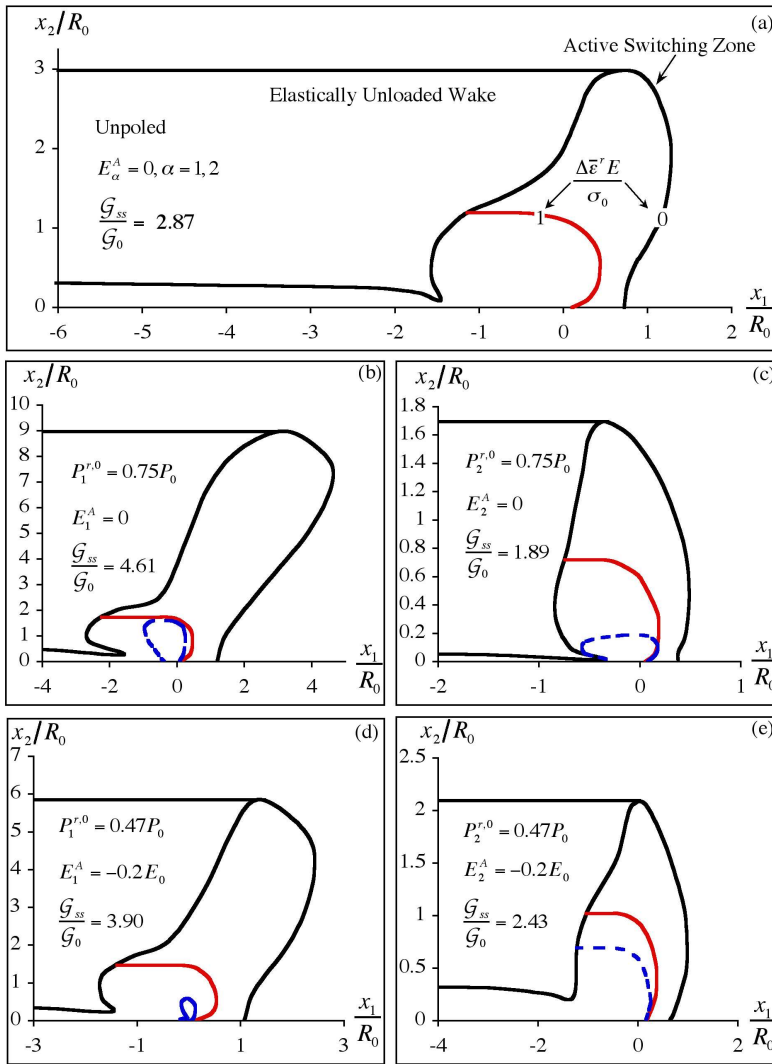


Figure 3. Switching zone sizes and shapes for initially unpoled (a) and initially poled (b)–(e) cases. The outermost curved contours on these plots delineate the location of the active switching boundary. The inner solid contours give the location within the active switching zones where the effective remanent strain change achieves the characteristic elastic level of $\Delta\bar{\varepsilon}^r \equiv \sqrt{2\Delta\varepsilon_{ij}^r\Delta\varepsilon_{ij}^r}/3 = \sigma_0/E$. The inner dashed contours give the location within the active switching zones where the change of remanent polarization achieves the characteristic linear dielectric level $|\Delta P^r| = \kappa E_0$. Notice that the spatial coordinates are normalized by R_0 , which is the characteristic switching zone size when the applied energy release rate reaches G_0 , specifically, $R_0 = G_0 E' / 3\pi\sigma_0^2$. Therefore, if G_0 is the same for all cases, then the spatial coordinate normalizations for each plot are identical.

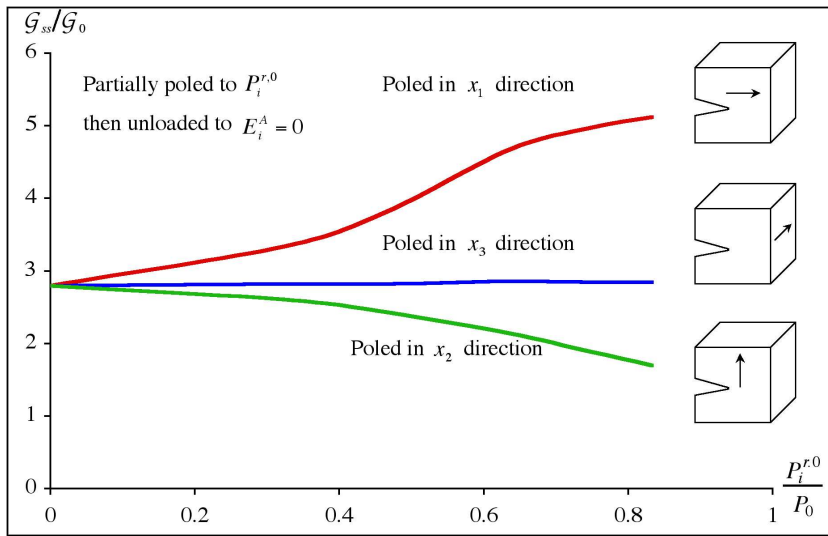


Figure 4. A comparison of the effects of poling direction on the toughening enhancement of partially poled materials. The normalized toughness enhancement G_{ss}/G_0 is plotted versus the initial remanent polarization state $P_i^{r,0}/P_0$, $i = 1, 2, 3$.

that in most cases the sizes of these inner switching zone contours where the effective remanent strain and polarization changes are equal to their characteristic linear values is significantly smaller than the outer switching zone boundary. This illustrates the fact that intense switching is confined to a region very close to the crack tip. Furthermore, note that the shapes of the switching zones depicted in these figures are that of the active switching zone. In other words, in the active switching zone, neighboring points at the same height above the crack plane have different remanent strain and polarization states. Whereas, in the linearly unloaded wake, neighboring points at the same height above the crack plane have identical remanent states. Lastly, material points outside of the active switching zone or the unloaded wake have a remanent state that is identical to that when the mechanical loading is initially applied.

4.2. The effect of initial electrical polarization on toughening. Within this model it is assumed that crack growth occurs when G_{tip} reaches the intrinsic fracture toughness of the material G_0 . Hence the ratio G_{ss}/G_0 indicates the amount of toughening due to domain switching, with $G_{ss}/G_0 = 1$ corresponding to no toughening enhancement or R -curve behavior. With regard to R -curve behavior, G_0 should be interpreted as the applied energy release rate where crack growth first begins, and G_{ss} is the steady state or plateau level of the applied energy release rate after sufficiently large amounts of crack growth. Figure 4 shows the ratio of G_{ss}/G_0 versus the level of the initial remanent polarization under plane strain conditions. Electric field is first applied to pole the material to a given level and then removed. Thereafter, no electric field is applied. The cases for the material poled in the x_3 direction are taken from [Wang and Landis 2004] for comparison to the in-plane cases.

Prior to discussing the results for the initially poled cases, it is informative to construct a reasonable hypothesis for the qualitative behavior of the relative toughening, taking the toughening in the unpoled case as a reference. Since crack tips tend to cause higher stresses in the x_2 direction (for most polar

angles around the tip) it is reasonable to assume that the material's propensity for remanent straining in the x_2 direction will lead to greater toughening. For example, when a material is poled by an electric field in the x_1 direction, domains switch from being aligned closely to the x_2 and x_3 direction to the x_1 direction. Then, when a crack tip passes through with an accompanying large σ_{yy} component, the domains can switch back to the x_2 direction causing dissipation and toughening. In contrast, a material poled by an electric field in the x_2 direction will have most domains initially aligned closely with the x_2 direction. When a crack tip passes, nearby domains cannot switch again towards the x_2 -axis and hence the dissipation due to domain switching will be relatively small. Applying these considerations, one would expect the following qualitative behaviors of the toughening: toughening should increase as the polarization in the x_1 or x_3 direction increases, and toughening should decrease as the polarization in the x_2 direction increases.

Figure 4 illustrates that as the initial remanent polarization increases the toughening, G_{ss}/G_0 , will increase for poling parallel to the crack surface (x_1), decrease for poling perpendicular to the crack surface (x_2), and have little effect for poling parallel to the crack front (x_3). Hence, the qualitative hypotheses on toughening were correct for the x_1 and x_2 poling cases but incorrect for the x_3 case. It has been shown by Wang and Landis [2004], that the relatively weak dependence of the toughening ratio on the level of poling in the x_3 direction can be explained by considering the out-of-plane constraint imposed by the plane strain conditions. The qualitative explanation is as follows. If domains were to switch completely from being oriented towards the x_3 direction to an in-plane direction then this would cause a large negative remanent strain component ε'_{33} . In order to maintain a total out-of-plane strain of zero, the elastic strain must then be positive and have the same magnitude as ε'_{33} . This elastic strain component must arise from an out-of-plane stress component of a magnitude approximately equal to $E\varepsilon'_{33}$. Therefore, if $|\varepsilon'_{33}| > \sigma_0/E$, then the out-of-plane stress will be close to σ_0 and there will be a tendency for the domains to switch *back* towards the out-of-plane direction. The actual events do not proceed by switching in-plane and then switching back out-of-plane, but rather by switching only a relatively small amount. Hence, the out-of-plane constraint will negate the expected toughening effect described previously. This behavior has been verified experimentally by Hackemann and Pfeiffer [2003] who observed that samples poled parallel to the crack front had practically identical toughening to unpoled samples.

4.3. Effect of applied electric field on toughening: the perpendicular case. In this section, the results for the case when the electric field is applied perpendicular to the crack surface (in the x_2 direction) will be discussed in detail. Figure 5 shows the ratio of G_{ss}/G_0 versus the applied electric field in the x_2 direction for a range of initial poling states. The cases associated with the solid red and blue curves will be discussed first, as these cases essentially envelop the others and form an inverted butterfly loop. The red and blue regions of the inserted hysteresis and butterfly loops in the upper left and right hand corners correspond to the red and blue portions of the inverted toughness butterfly loop.

The results for fracture toughening can be explained qualitatively by considering the competing or complementary effects of the applied electric field and stress on domain switching near the crack tip. In general it is valid to assume that the crack tip stress field will tend to elongate the material in the x_2 direction and will tend to cause domain switching that will produce such an elongation. First, consider a thermally depolarized material poled by a strong uniaxial electric field in the x_2 direction. The states of

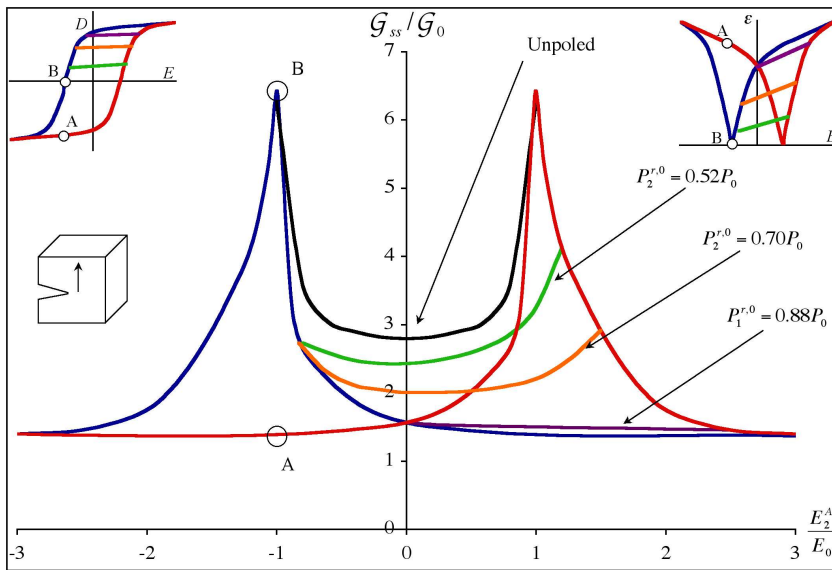


Figure 5. The normalized toughness enhancement G_{ss}/G_0 versus the applied electric field E_2 for a range of initial poling states for plane-strain conditions. The colored lines on the main plot correspond to the colored lines on the hysteresis and butterfly loops depicted in the inserts at the upper left and right corners. Points A and B are highlighted to indicate the relationships between the electromechanical constitutive response and the fracture toughness predictions.

electric displacement and strain for this material can be found at the upper right corners of the hysteresis loops in Figures 2a and 2b while the field is applied. If this level of applied electric field is held fixed at $3E_0$, steady crack growth occurs at an applied energy release rate of $G_{ss} = 1.4G_0$. This level of toughening is the lowest depicted on Figure 5. However, if the applied electric field was even greater, then the steady state toughness would continue to decrease, approaching G_0 as $E_2 \rightarrow \infty$. The qualitative reason for this behavior is that both the applied electric field and the stresses near the crack tip tend to cause domain switching towards the x_2 direction. If the initially applied electric field is sufficiently high, then almost all of the domains that can switch towards the x_2 direction will have done so prior to the growth of the crack. Thereafter, due to the lack of “switchable” domains, the mechanical loads cannot cause any additional switching and it is as if the crack is running through a linear, nondissipative, piezoelectric material. Since it is the domain switching process that gives rise to the dissipation of energy and the increase in fracture toughness, any phenomenon that inhibits any additional switching during crack growth, will also tend to decrease the fracture toughness. In contrast, applied electric field and initial poling states that allow the crack tip fields to cause additional switching will enhance the fracture toughening.

The remainder of the blue portion of the curve is obtained by first poling the material with a strong electric field, then reversing the electric field to a lower or negative applied electric field level of E_2^A , and finally applying the in-plane mechanical loading to produce steady crack growth. During this type

of initial electrical loading the electric displacement and strain behavior of the material traces out the outmost hysteresis loops depicted in Figures 2a and 2b and in the inserted plots in the upper left and right hand corners of Figure 5. As the electric field is removed, the inhibiting effect of the field on domain switching decreases and hence the fracture toughness increases. For positive levels of E_2^A , since most domains remain aligned in the x_2 direction, the increase in toughening remains small. However, when the applied electric field is reversed, some domains will switch towards the x_1 direction. Then, when the crack passes by, the crack tip fields will switch these domains back towards the x_2 direction creating both dissipation and fracture toughening. The most dramatic increase in the toughening occurs very close to $E_2^A = -E_0$, where reverse domain switching due to the applied electric field peaks. In fact, the spikes or “butterfly legs” of the toughness versus electric field curve in Figure 5 correspond to the legs of the butterfly loops in Figure 2b and the steep regions of the hysteresis loop in Figure 2a.

If the reversal of the initial applied electric field is large enough, that is, for $E_2^A < -E_0$, then the initial polarization of the material will be reversed as well, and the case where the remanent polarization and electric field are aligned is revisited. Hence, as the initial electric field is driven to large negative levels, it will again align domains in the x_2 direction, leaving little potential for switching due to the crack tip fields, which in turn causes low values of the steady state fracture toughening. Finally, the red curve is a mirror image of the blue curve and is obtained by poling in the negative x_2 direction first. Notice that points A and B are denoted on the three loops in this figure in order to aid in the understanding of the correlation between the fundamental electromechanical constitutive behavior and the fracture toughening predictions.

Also plotted Figure 5 are the cases where the material is partially poled by a moderate electric field, then the electric field is removed, a new electric field E_2^A is applied, and finally steady crack growth proceeds due to in-plane mechanical loading. For all of the partially poled cases negative E_2^A levels have similar trends with the fully poled, bold dashed curve described above. The differences between the partially poled cases and the fully poled cases are evident at intermediate levels of E_2^A . These levels of E_2^A correspond to the linear unloading regions indicated with the arrows on Figures 2a and 2b. At the same level of E_2^A , the toughening decreases with increasing initial remanent polarization if $-E_0 < E_2^A < E_0$. For large levels of E_2^A the partially poled cases eventually merge with the outer red and blue curves that represent the situations where the material has been initially poled by a strong electric field. The regions of similar toughening behavior between the partially and fully poled cases can be understood by considering the hysteresis and butterfly loops of Figure 2a and 2b. Specifically, the levels of applied electric field where the toughness curves merge in Figure 5 coincide with the electric field levels where the linear unloading segments for the partially poled materials meet the outer hysteresis and butterfly loops in Figure 2. At these levels of electric field, the partially poled materials commence additional nonlinear behavior.

4.4. Effect of applied electric field on toughening: parallel case. Figure 6 shows the ratio of G_{ss}/G_0 versus the applied electric field in x_1 direction for a range of initial poling states. Again, the cases associated with the red and blue curves will be discussed first. The red and blue regions of the inserted hysteresis and butterfly loops in the upper left and right hand corners correspond to the red and blue portions of the toughness butterfly loop. The similarities and differences between the perpendicular and parallel electrical loading cases will be explained in the following discussion.

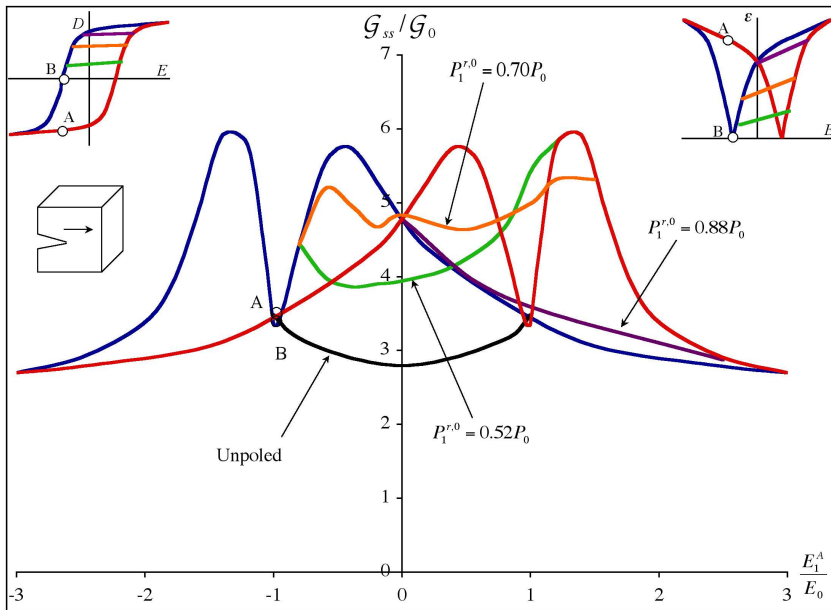


Figure 6. The normalized toughness enhancement G_{ss}/G_0 versus the applied electric field E_1 for a range of initial poling states for plane-strain conditions. The colored lines on the main plot correspond to the colored lines on the hysteresis and butterfly loops depicted on the inserts in the upper left and right corners. Points A and B are highlighted to indicate the relationships between the electromechanical constitutive response and the fracture toughness predictions.

First, consider a material poled by a strong uniaxial electric field of magnitude in the x_1 direction. As for the perpendicular poling case, if the applied electric field is sufficiently strong, it will be able to impede domain switching with the result that the fracture toughening is small. The primary difference between the parallel and perpendicular cases for this strong electrical loading scenario is that for the parallel case there will always be domains available to switch towards the x_2 direction. Then, unless the applied electric field E_1^A is extraordinarily strong, the singular crack tip fields will be able to switch domains towards the x_2 direction creating some toughening enhancement. In fact, for an applied electric field level of $E_1^A = 3E_0$ the simulations predict that crack growth occurs at an applied energy release rate of $G_{ss} = 2.7G_0$ for applied field in the x_1 direction as compared to $G_{ss} = 1.4G_0$ for applied field in the x_2 direction. To summarize, the primary reason why toughening is low for strong electric fields applied perpendicular to the crack is that there is a dearth of domains available for switching towards the x_2 direction. Whereas for strong fields in the x_1 direction, domains are available for switching but the electric field prevents the domain switching towards the x_2 direction. In either case, the fracture toughening decreases as the applied electric field continues to increase.

Next consider the region of the blue curve on Figure 6 for the region $0 \leq E_1^A < 3E_0$. This region of the curve is obtained by first poling the material with a strong electric field, then partially removing the field to a lower level of E_1^A . Thereafter, the in-plane mechanical loading is applied to produce steady

crack growth. As the electric field is removed, the inhibiting effects of the electric field on domain switching towards the x_2 direction decreases and the fracture toughening increases. The region of the blue toughening curve with $0 \leq E_1^A < 3E_0$ can be relatively well understood because the initial polarization state is similar for all cases within this range and only the tendency for the applied electric field to align the polarization (and hence the strain) in the x_1 direction needs to be considered. In contrast, a qualitative description of the behavior in the range of $-1.4E_0 < E_1^A < 0$ is considerably more difficult to construct due to the competing effects of differing potential for change in axial strain in the x_2 direction and the tendency for the applied electric field to align the polarization in the x_1 direction. The model results for the specific material properties applied in the simulations indicate that the toughening increases in the range $-0.5E_0 < E_1^A < 0$, decreases for $-E_0 < E_1^A < -0.5E_0$, increases again for $-1.4E_0 < E_1^A < -E_0$, and finally decreases when $E_1^A < -1.4E_0$. First note that as the applied electric field traverses the range from $E_1^A = 0$ to $E_1^A = -E_0$ the remanent strain in the x_1 direction goes from approximately $\varepsilon_{11}^r = 1.1\varepsilon_c$ to $\varepsilon_{11}^r = 0$. Therefore, the case with the greatest potential for remanent straining towards the x_2 direction is at $E_1^A = 0$ and decreases until $E_1^A = -E_0$. Thereafter, the possible change of remanent strain towards the x_2 direction increases again as $E_1^A \rightarrow -\infty$. Hence, the toughening due to the potential remanent strain contribution should take the same shape as the strain-electric field butterfly loop. The fact that the x_1 toughening curve does not take this shape is due to the competing effect of the applied electric field tending to align the strain in the x_1 direction. The strength of this competing “force” is best quantified by the energetic term $E_1^A P_1^{r,0}$. In the range from $-E_0 < E_1^A < 0$, this quantity will actually be negative suggesting that the applied electric field “helps” the strain reorient towards the x_2 direction. At $E_1^A = 0$ this quantity will obviously be zero and at $E_1^A = -E_0$ this quantity will also be close to zero due to the fact that $P_1^{r,0} \approx 0$ when $E_1^A = -E_0$. For $E_1^A < -E_0$, both E_1^A and $P_1^{r,0}$ will be less than zero causing $E_1^A P_1^{r,0}$ to be positive indicating that these levels of applied electric field inhibit the toughening. Then, when the competing effects of potential strain and applied electric field are added together, an oversimplified but qualitatively valid understanding of the toughening curve of Figure 6 is obtained. Instead of the butterfly shaped toughening loop that would be expected if only the potential for remanent straining in the x_2 direction governed the behavior, the quantitative results predict that the effects of the applied electric field “fold” the butterfly loop “in half”. Specifically, the tips of the “wings” at high applied electric field are inverted, but the “legs” remain in the same orientation.

Also shown on Figure 6 are the cases where the material is initially unpoled or partially poled by a moderate electric field, the electric field is removed, a new electric field E_1^A is applied, and finally steady crack growth proceeds due to in-plane mechanical loading. Of special interest is the behavior of the material near zero electric field for partial poling levels of $P_1^{r,0} = 0.52P_0$ and $P_1^{r,0} = 0.7P_0$. Note that the toughening trend near zero electric field for $P_1^{r,0} = 0.52P_0$ increases with applied electric field, whereas the trend is the opposite for a fully poled material. Also, the toughening behavior is relatively flat for the partial poling case of $P_1^{r,0} = 0.7P_0$. These intermediate poling cases illustrate the sensitivity of the toughening behavior to the initial polarization state of the material for crack growth along the applied electric field direction. Furthermore, it is our opinion that modest changes in the shapes of the hysteresis and butterfly loops of the material will also have a significant effect on the shape of the x_1 toughening curve. Specifically, changes in the material behavior will likely cause a shift in the location of the “fold” in the x_1 toughening curve.

5. Discussion

The model presented here differs from previous theoretical explanations of the effects of electric field and polarization on the fracture toughness of ferroelectrics in that an incremental, microelectromechanically tested, phenomenological constitutive law has been applied instead of a discrete switching law. Additionally, in contrast to applying simplifying assumptions associated with most transformation toughening models, the details of the electromechanical fields have been obtained from finite element computations. The fields computed in this work include both the perturbing influences of ferroelectric switching and the change of the piezoelectric effect that results from such switching. The detailed constitutive model applied in this work has allowed for both qualitative and quantitative characterizations of the effects of electric field on the toughening due to domain switching in ferroelectric ceramics. The model predicts a range of phenomena that indicate that the toughening is dependent on both the level of electric field, its direction of application, and on the initial polarization state.

The predictions of the present model are in qualitative accord with several different experimental observations. First, the model predictions displayed in Figure 4 indicate that the toughening is greater for crack growth parallel to the poling direction than for crack growth perpendicular to the poling direction for the in-plane cases. This prediction is in agreement with the observations of Tobin and Pak [1993] and Lucato et al. [2002]. When the polarization is parallel to the crack front, then the model predicts that there is little to no variation in the toughness with changes in the polarization. Again, this prediction is in agreement with the experimental observations of Hackemann and Pfeiffer [2003]. Additionally, the model results illustrated in Figure 3 indicate that domain switching is intense near the tip of the crack but diffuse towards the outer boundary of the switching zone. This prediction is also in agreement with the observations of Hackemann and Pfeiffer [2003]. Lastly, the model predictions shown in Figure 5, indicating that a positive electric field reduces toughening and negative electric field increases toughening for polarization perpendicular to the crack, are in agreement with the observations of both Tobin and Pak [1993] and Park and Sun [1995].

As discussed above, the present model is able to explain the experimental results observed by Hackemann and Pfeiffer [2003]. However, previous modeling efforts on the fracture toughness of ferroelectrics are not able to predict or explain such observations. Specifically, the simple model applied to analyze transformation toughening for partially stabilized zirconia [McMeeking and Evans 1982] has been used to determine switching zones and fracture toughening during crack growth in ferroelectrics. These models assume that once a specific switching criterion is met, for example,

$$E_i \Delta P_i^r + \sigma_{ij} \Delta \varepsilon_{ij}^r = G_c,$$

[Hwang and McMeeking 1998] the material attains a finite transformation polarization ΔP_i^r and strain $\Delta \varepsilon_{ij}^r$ that remains fixed and frozen into the material. This is in contrast to the incremental flow rule used in the present model that allows both the polarization and strain to gradually evolve as the crack passes through the material. Therefore, the transformation toughening models predict uniform remanent strain and polarization within the switching zone. Furthermore, since intermediate remanent states are not allowed within the transformation toughening model, it predicts that the out-of-plane poled material is significantly tougher than the unpoled material. Hackemann and Pfeiffer [2003] observed an increased concentration of switched domains close to the crack tip and a lower fraction of switched domains towards

the outer boundary of the switching zone. They also measured nearly identical R -curve behavior for both unpoled and out-of-plane poled material with short-circuited electrodes. The transformation toughening models cannot capture either of these observations, while the present approach does. The favorable comparison of the present model to the experimental observations suggests that ferroelectric switching behavior is more accurately modeled with an incremental plasticity formulation, rather than as an unstable phase transformation.

References

- [Beom and Atluri 2003] H. G. Beom and S. N. Atluri, “Effect of electric fields on fracture behavior of ferroelectric ceramics”, *J. Mech. Phys. Solids* **51**:6 (2003), 1107–1125.
- [Chen and Lu 2002] Y.-H. Chen and T. J. Lu, “Cracks and fracture in piezoelectrics”, *Adv. Appl. Mech.* **39** (2002), 121–215.
- [Fu and Zhang 2000] R. Fu and T.-Y. Zhang, “Effects of an electric field on the fracture toughness of poled lead zirconate titanate ceramics”, *J. Am. Ceram. Soc.* **83**:5 (2000), 1215–1218.
- [Hackemann and Pfeiffer 2003] S. Hackemann and W. Pfeiffer, “Domain switching in process zones of PZT characterization by microdiffraction and fracture mechanical methods”, *J. Eur. Ceram. Soc.* **23**:1 (2003), 141–151.
- [Huber et al. 1999] J. E. Huber, N. A. Fleck, C. M. Landis, and R. M. McMeeking, “A constitutive model for ferroelectric polycrystals”, *J. Mech. Phys. Solids* **47**:8 (1999), 1663–1697. MR 1686648 (2000b:74019)
- [Hutchingson 1974] J. W. Hutchingson, “A course on nonlinear fracture mechanics”, University Report, 1974. Harvard DEAP S-8, Division of Applied Sciences.
- [Hwang and McMeeking 1998] S. C. Hwang and R. M. McMeeking, “The prediction of switching in polycrystalline ferroelectric ceramics”, *Ferroelectrics* **207** (1998), 465–495.
- [Kamlah 2001] M. Kamlah, “Ferroelectric and ferroelastic piezoceramics-modeling of electromechanical hysteresis phenomena”, *Continuum Mech. Therm.* **13**:4 (2001), 219–268.
- [Landis 2002a] C. M. Landis, “Fully coupled, multi-axial, symmetric constitutive laws for polycrystalline ferroelectric ceramics”, *J. Mech. Phys. Solids* **50**:1 (2002), 127–152.
- [Landis 2002b] C. M. Landis, “A new finite-element formulation for electromechanical boundary value problems”, *Int. J. Numer. Methods Eng.* **55**:5 (2002), 613–628.
- [Landis 2003a] C. M. Landis, “On the fracture toughness of ferroelastic materials”, *J. Mech. Phys. Solids* **51**:8 (2003), 1347–1369.
- [Landis 2003b] C. M. Landis, “On the strain saturation conditions for polycrystalline ferroelastic materials”, *J. Appl. Mech. (Trans. ASME)* **70**:4 (2003), 470–478.
- [Landis 2004a] C. M. Landis, “Energetically consistent boundary conditions for electromechanical fracture”, *Int. J. Solids Struct.* **41**:22-23 (2004), 6291–6315.
- [Landis 2004b] C. M. Landis, “In-plane complex potentials for a special class of materials with degenerate piezoelectric properties”, *Int. J. Solids Struct.* **41**:3-4 (2004), 695–715.
- [Landis 2004c] C. M. Landis, “Non-linear constitutive modeling of ferroelectrics”, *Curr. Opin. Solid State Mater. Sci.* **8**:1 (2004), 59–69.
- [Landis et al. 2000] C. M. Landis, T. Pardoan, and J. W. Hutchinson, “Crack velocity dependent toughness in rate dependent materials”, *Mech. Mater.* **32**:11 (2000), 663–678.
- [Landis et al. 2004] C. M. Landis, J. Wang, and J. Sheng, “Micro-electromechanical determination of the possible remanent strain and polarization states in polycrystalline ferroelectrics and the implications for phenomenological constitutive theories”, *J. Intell. Mater. Syst. Struct.* **15**:7 (2004), 513–525.
- [Li et al. 1985] F. Z. Li, C. F. Shih, and A. Needleman, “A comparison of methods for calculating energy release rates”, *Eng. Fract. Mech.* **21**:2 (1985), 405–421.
- [Lucato et al. 2002] S. L. Lucato, J. Lindner, D. C. Lupascu, and J. Rödel, “Influence of electrical and geometrical boundary conditions on crack growth in PZT”, *Key Eng. Mater.* **206**:213 (2002), 609–612.

- [Lynch 1996] C. S. Lynch, "The effect of uniaxial stress on the electro-mechanical response of 8/65/35 PLZT", *Acta Mater.* **44**:10 (1996), 4137–4148.
- [McMeeking 1999] R. M. McMeeking, "Crack tip energy release rate for a piezoelectric compact tension specimen", *Eng. Fract. Mech.* **64**:2 (1999), 217–244.
- [McMeeking and Evans 1982] R. M. McMeeking and A. G. Evans, "Mechanics of transformation toughening in brittle materials", *J. Am. Ceram. Soc.* **65**:5 (1982), 242–246.
- [Park and Sun 1995] S. Park and C.-T. Sun, "Fracture criteria for piezoelectric ceramics", *J. Am. Ceram. Soc.* **78**:6 (1995), 1475–1480.
- [Schneider and Heyer 1999] G. A. Schneider and V. Heyer, "Influence of the electric field on Vickers indentation crack growth in BaTiO₃", *J. Eur. Ceram. Soc.* **19**:6-7 (1999), 1299–1306.
- [Tobin and Pak 1993] A. G. Tobin and E. Pak, "Effect of electric fields on fracture behavior of PZT ceramics", *P. Soc. Photo-Opt. Inst.* **1916** (1993), 78–86.
- [Wang and Landis 2004] J. Wang and C. M. Landis, "On the fracture toughness of ferroelectric ceramics with electric field applied parallel to the crack front", *Acta Mater.* **52**:12 (2004), 3435–3446.
- [Wang and Singh 1997] H. Wang and R. N. Singh, "Crack propagation in piezoelectric ceramics: effects of applied electric fields", *J. Appl. Phys.* **81**:11 (1997), 7471–7479.
- [Yang and Zhu 1998] W. Yang and T. Zhu, "Switch-toughening of ferroelectrics subjected to electric fields", *J. Mech. Phys. Solids* **46**:2 (1998), 291–311.
- [Zeng and Rajapakse 2001] X. Zeng and R. K. N. D. Rajapakse, "Domain switching induced fracture toughness variation in ferroelectrics", *Smart Mater. Struct.* **10** (2001), 203–211.
- [Zhang et al. 2001] T.-Y. Zhang, M. Zhao, and P. Tong, "Fracture of piezoelectric ceramics", *Adv. Appl. Mech.* **38** (2001), 147–289.

Received 5 Jan 2006.

JIANXIN WANG: wjx@rice.edu

Department of Mechanical Engineering and Materials Science, MS 321, Rice University, P.O. Box 1892, Houston, TX 77251-1892, United States

CHAD M. LANDIS: landis@rice.edu

Department of Mechanical Engineering and Materials Science, MS 321, Rice University, P.O. Box 1892, Houston, TX 77251-1892, United States

<http://mems.rice.edu/~landis>

SUBMISSION GUIDELINES

ORIGINALITY

Authors may submit manuscripts in PDF format on-line. Submission of a manuscript acknowledges that the manuscript is *original and has neither previously, nor simultaneously, in whole or in part, been submitted elsewhere*. Information regarding the preparation of manuscripts is provided below. Correspondence by email is requested for convenience and speed. For further information, write to:

Marie-Louise Steele
Division of Mechanics and Computation
Durand Building, Room 262
Stanford University
Stanford CA 94305

LANGUAGE

Manuscripts must be in English. A brief abstract of about 150 words or less must be included. The abstract should be self-contained and not make any reference to the bibliography. Also required are keywords and subject classification for the article, and, for each author, postal address, affiliation (if appropriate), and email address if available. A home-page URL is optional.

FORMAT

Authors are encouraged to use \LaTeX and the standard article class, but submissions in other varieties of \TeX , and, exceptionally in other formats, are acceptable. Electronic submissions are strongly encouraged in PDF format only; after the refereeing process we will ask you to submit all source material.

REFERENCES

Bibliographical references should be listed alphabetically at the end of the paper and include the title of the article. All references in the bibliography should be cited in the text. The use of \BIBTeX is preferred but not required. Tags will be converted to the house format (see a current issue for examples), however, in the manuscript, the citation should be by first author's last name and year of publication, e.g. "as shown by Kramer, et al. (1994)". Links will be provided to all literature with known web locations and authors are encouraged to provide their own links on top of the ones provided by the editorial process.

FIGURES

Figures prepared electronically should be submitted in Encapsulated PostScript (EPS) or in a form that can be converted to EPS, such as GnuPlot, Maple, or Mathematica. Many drawing tools such as Adobe Illustrator and Aldus FreeHand can produce EPS output. Figures containing bitmaps should be generated at the highest possible resolution. If there is doubt whether a particular figure is in an acceptable format, the authors should check with production by sending an email to:

production@mathscipub.org

Each figure should be captioned and numbered so that it can float. Small figures occupying no more than three lines of vertical space can be kept in the text ("the curve looks like this:"). It is acceptable to submit a manuscript with all figures at the end, if their placement is specified in the text by means of comments such as "Place Figure 1 here". The same considerations apply to tables.

WHITE SPACE

Forced line breaks or page breaks should not be inserted in the document. There is no point in your trying to optimize line and page breaks in the original manuscript. The manuscript will be reformatted to use the journal's preferred fonts and layout.

PROOFS

Page proofs will be made available to authors (or to the designated corresponding author) at a web site in PDF format. Failure to acknowledge the receipt of proofs or to return corrections within the requested deadline may cause publication to be postponed.

JOURNAL OF MECHANICS OF MATERIALS AND STRUCTURES

Volume 1 No. 6 June 2006

A new model to predict the behavior at the interfaces of multilayer structures M. KARAMA, K. S. AFAQ AND S. MISTOU	205
A macroscopic model for kink banding instabilities in fiber composites SHILADITYA BASU, ANTHONY M. WAAS AND DAMODAR R. AMBUR	227
Study of viscoelastic and friction damper configurations in the seismic mitigation of medium-rise structures JULIUS MARKO, DAVID THAMBIRATNAM AND NIMAL PERERA	249
The effect of thin film/substrate radii on the Stoney formula for thin film/substrate subjected to nonuniform axisymmetric misfit strain and temperature XUE FENG, YONGGANG HUANG, HANQING JIANG, DUC NGO AND ARES J. ROSAKIS	289
Yield of random elastoplastic materials WEI LI AND MARTIN OSTOJA-STARZEWSKI	303
Effects of in-plane electric fields on the toughening behavior of ferroelectric ceramics JIANXIN WANG AND CHAD M. LANDIS	323



1559-3959(200606)1:6;1-7